



National and Kapodistrian University of Athens

Department of Astrophysics, Astronomy and Mechanics
Faculty of Physics

Studying the effects of interstellar dust in nearby galaxies

Angelos Nersesian

A thesis submitted for the degree of
Doctor of Philosophy

October 2019



NATIONAL AND KAPODISTRIAN
UNIVERSITY OF ATHENS

DEPARTMENT OF ASTROPHYSICS, ASTRONOMY AND MECHANICS
FACULTY OF PHYSICS

PHD THESIS

Studying the effects of interstellar dust in nearby galaxies

by

Angelos NERSESIAN

Supervisors: Dr. Emmanuel M. Xilouris
Prof. Dr. Nektarios Vlahakis
Prof. Dr. Despina Hatzidimitriou

NATIONAL AND KAPODISTRIAN
UNIVERSITY OF ATHENS

DEPARTMENT OF ASTROPHYSICS, ASTRONOMY AND MECHANICS
FACULTY OF PHYSICS

PhD THESIS

submitted for the degree of

DOCTOR OF PHILOSOPHY

IN

—PHYSICS—

by

Angelos NERSESIAN

Studying the effects of interstellar
dust in nearby galaxies

COMMITTEE

<i>Dr.</i>	Emmanuel M. Xilouris	-	NATIONAL OBSERVATORY OF ATHENS
<i>Prof. Dr.</i>	Nektarios Vlahakis	-	UNIVERSITY OF ATHENS
<i>Prof. Dr.</i>	Despina Hatzidimitriou	-	UNIVERSITY OF ATHENS
<i>Dr.</i>	Alceste Z. Bonanos	-	NATIONAL OBSERVATORY OF ATHENS
<i>Prof. Dr.</i>	Kalliopi Dasyra	-	UNIVERSITY OF ATHENS
<i>Prof. Dr.</i>	Apostolos Mastichiadis	-	UNIVERSITY OF ATHENS
<i>Prof. Dr.</i>	Maarten Baes	-	UNIVERSITY OF GHENT

Date of the defense: October 22, 2019

Σύνοψη

Τετρακόσιες χιλιάδες χρόνια μετά τη Μεγάλη Έκρηξη (Big Bang) το Σύμπαν είχε «κρυσώσει» σε τέτοιο βαθμό ώστε να είναι εφικτός ο σχηματισμός ατόμων αερίου. Αρχικά τα άτομα αυτά είχαν την απλούστερη δυνατή μορφή (Υδρογόνο και Ήλιο) με ένα μικρό ποσοστό βαρύτερων στοιχείων («μέταλλα»). Στη συνέχεια, αυτό το αέριο άρχισε να καταρρέει βαρυτικά με αποτέλεσμα να δημιουργηθούν τα πρώτα αστέρια και γαλαξίες. Από τότε τα αστέρια συνεχώς εμπλουτίζουν το μεσοαστρικό χώρο με βαρύτερα μέταλλα με αποτέλεσμα, μέσω της διεργασίας της νουκλεοσύνθεσης, την εμφάνιση μεγαλύτερων σωματιδίων, την κοσμική σκόνη.

Οι γαλαξίες είναι συστήματα τα οποία αποτελούνται από τρία βασικά δομικά στοιχεία: αέριο, αστέρια και σκόνη, ενώ παρουσιάζουν σημαντικές διαφορές μεταξύ τους σε σχέση με το σχήμα και το μέγεθός τους. Η μορφολογία ενός γαλαξία συνδέεται άμεσα με την σχετική περιεκτικότητα των προαναφερθέντων δομικών στοιχείων. Με βάση την οπτική τους εμφάνιση και γεωμετρία, οι γαλαξίες κατανέμονται κατά τον Edwin Hubble (1889-1953) σε ελλειπτικούς (ellipticals, E), φακοειδείς (lenticulars, S0), σπειροειδείς (spirals, S), και ανώμαλους (irregulars, Irr) (Εικ. 1.3). Ένας εύκολος τρόπος να παραμετροποιηθεί κανείς το μορφολογικό τύπο ενός γαλαξία είναι με τη χρήση της παραμέτρου Hubble Stage (T). Σε κάθε μορφολογικό τύπο δίνεται μία συγκεκριμένη τιμή ανάλογα με τον μορφολογικό τύπο (Πίνακας 1.1). Με αρνητικούς αριθμούς από -5 έως -4 δηλώνονται οι ελλειπτικοί γαλαξίες, με αριθμούς από -3 έως 0 οι φακοειδείς, με θετικούς αριθμούς από 1 έως 7 οι σπειροειδείς, και από 8 έως 10 οι ανώμαλοι γαλαξίες.

Οι ελλειπτικοί και φακοειδείς γαλαξίες αποτελούνται κυρίως από γηραιούς αστρικούς πληθυσμούς ($> 5 \text{ Gyr}$), ενώ η περιεκτικότητά τους σε μεσοαστρική ύλη είναι ελάχιστη, γεγονός που σημαίνει ότι δεν υπάρχουν νέοι αστέρες σε αυτούς τους γαλαξίες. Εν αντιθέσει με τους ελλειπτικούς, οι σπειροειδείς γαλαξίες περιέχουν άφθονη μεσοαστρική ύλη, γεγονός που τους επιτρέπει να έχουν μεγαλύτερο πλήθος νεαρών αστέρων. Ανάλογα με τα μορφολογικά τους χαρακτηριστικά οι σπειροειδείς χωρίζονται περαιτέρω σε «κανονικούς» (normal, SA) και «ραβδωτούς» (barred, SB). Οι κανονικοί σπειροειδείς γαλαξίες παρουσιάζουν συνήθως δύο σπείρες οι οποίες εκτυλίσσονται από δύο αντιδιαμετρικά σημεία του πυρήνα, ενώ στους ραβδωτούς οι σπείρες εκτυλίσσονται από τα άκρα μίας ράβδου που διαπερνά τον γαλαξιακό

πυρήνα. Τέλος, οι ανώμαλοι γαλαξίες, όπως προΐδεάζει και το όνομά τους, δεν έχουν κάποια συγκεκριμένη δομή ενώ το μέγεθός τους παραμένει σχετικά μικρό. Οι γαλαξίες αυτοί είναι πλούσιοι σε μεσοαστρική ύλη και συνεπώς σε νεαρούς αστρικούς πληθυσμούς.

Μία άλλη σημαντική κατηγορία γαλαξιών είναι οι λεγόμενοι «ενεργοί» γαλαξίες. Οι πυρήνες αυτού του είδους γαλαξιών ονομάζονται Ενεργοί Γαλαξιακοί Πυρήνες [ΕΓΠ; Active Galactic Nuclei (AGN)]. Για την ερμηνεία της λαμπρότητας ενός ΕΓΠ, προτείνεται ότι είναι προϊόν της συσσώρευσης ύλης γύρω από μία υπερμεγέθη μελανή οπή (δίσκος προσαύξεσης), ενώ η περιοχή γύρω από την μελανή οπή και τον δίσκο προσαύξεσης περιβάλλεται από έναν τόρο ύλης (σκόνη και αέριο). Σε ορισμένες περιπτώσεις, η εκπομπή από έναν ΕΓΠ μπορεί να έχει κυρίαρχο ρόλο στην έκλυση ακτινοβολίας στα υπέρυθρα μήκη κύματος (mid-infrared, far-infrared) του φάσματος ενός γαλαξία. Ο λόγος είναι πως ο τόρος από σκόνη που περικλείει τον δίσκο προσαύξεσης απορροφά την υπεριώδη ακτινοβολία του δίσκου και την επανεκπέμπει στα υπέρυθρα μήκη κύματος.

Μία από τις βασικότερες διεργασίες που επηρεάζει τις χημικές ιδιότητες της μεσοαστρικής ύλης και, κατ' επέκταση, την εξέλιξη ενός γαλαξία είναι ο ρυθμός παραγωγής νέων αστέρων. Πρώτη και άμεση συνέπεια της δημιουργίας νέων αστέρων είναι η κατανάλωση του διαθέσιμου αερίου και η μετατροπή του σε θερμική ακτινοβολία. Οι νεαροί αστέρες εκπέμπουν το μέγιστο της ακτινοβολίας τους στα υπεριώδη μήκη κύματος με αποτέλεσμα να δρουν ως πρώτος μηχανισμός θέρμανσης του μεσοαστρικού υλικού. Η παραγωγή υψηλοενεργειακών φωτονίων ($\lambda < 0.1 \mu\text{m}$) προκαλεί τον ιονισμό των ατόμων του υδρογόνου (HII), κι εξαιτίας της εκπομπής από την επανασύνδεση του ιονισμένου αερίου, είναι δυνατό κανείς να εκτιμήσει έμμεσα τον ρυθμό παραγωγής νέων αστέρων. Ανάλογα με τη μάζα τους οι αστέρες ακολουθούν διαφορετική εξελικτική πορεία. Οι νεαροί, μεγάλης μάζας αστέρες (αστέρες με μάζα μεγαλύτερη από $8 M_{\odot}$) καταναλώνουν το αερίό τους πιο γρήγορα και ο θάνατός τους μπορεί να έρθει με βίαιες υπερκαινοφανείς εκρήξεις. Εικάζεται πως τέτοιου είδους εκρήξεις προκαλούν κύματα σοκ, τα οποία με τη σειρά τους έχουν ως αποτέλεσμα την ενεργοποίηση της κατάρρευσης μοριακών νεφών στο μεσοαστρικό χώρο κι επομένως την έναρξη παράγωγης νέων αστέρων. Ο ρόλος των υπερκαινοφανών εκρήξεων δεν σταματά εκεί, αφού είναι επίσης υπεύθυνες για τον εμπλουτισμό της μεσοαστρικής ύλης με μέταλλα, τα οποία δρουν ως παράγοντες ψύξης του αερίου.

Περίπου 10 εκατομμύρια χρόνια από την γέννηση ενός νέου αστρικού σμήνους, τα νεαρά άστρα, παρά το γεγονός ότι συνεχίζουν να παράγουν ακτινοβολία στα υπεριώδη μήκη κύματος, ικανή να θερμάνει την περιβάλλουσα ύλη, δεν μπορούν να παράξουν ακτινοβολία ώστε να ιονίσει τα άτομα του υδρογόνου. Με το πέρασμα του χρόνου, οι αστέρες κύριας ακολουθίας (αστέρες με μάζα παρόμοια με αυτή του Ήλιου) θα γίνουν η κυρίαρχη πηγή ακτινοβολίας, εκπέμποντας το μέγιστο της ενέργειάς τους στα οπτικά και εγγύς-υπέρυθρα μήκη κύματος. Οι αστέρες της κύριας ακολουθίας συνήθως έχουν μεγάλες και ήρεμες ζωές, και δρουν ως δεύτερος μηχανισμός θέρμανσης του μεσοαστρικού μέσου. Ένα από τα υποπροϊόντα της αστρικής εξέλιξης είναι και η δημιουργία της κοσμικής σκόνης.

Η κοσμική σκόνη που συναντάμε στους γαλαξίες αποτελεί ένα μικρό ποσοστό της

μάζας της μεσοαστρικής ύλης ($\lesssim 1\%$) αλλά, παρόλα αυτά, παίζει σπουδαίο ρόλο στην κατανόηση της δημιουργίας και της εξέλιξης των γαλαξιών. Τα σωματίδια σκόνης ενεργούν ως καταλύτες ως προς τη δημιουργία μοριακού υδρογόνου, ενώ ταυτόχρονα προστατεύουν τα μόρια από την βλαβερή ακτινοβολία των νεαρών αστερών. Ο τρόπος που η σκόνη αλληλεπιδρά με την ακτινοβολία από τα αστερία του γαλαξία παραμένει ακόμα σε μεγάλο βαθμό ανεξερεύνητος. Οι κόκκοι της σκόνης αποτελούνται από στερεά σωματίδια διαφόρων μεγεθών, που κυμαίνονται από 0.3 nm έως 0.3 μm . Η σκόνη απορροφά και σκεδάζει το φως των αστεριών, κάτι που προκαλεί την εξασθένηση του αστρικού φωτός στα υπεριώδη και οπτικά μήκη κύματος, και το κάνει να φαίνεται πιο «κόκκινο». Το φαινόμενο αυτό οφείλεται στο γεγονός ότι το μέγεθος των κόκκων της σκόνης είναι της ίδιας τάξης μεγέθους με το μήκος κύματος της ακτινοβολίας. Επιπλέον, η σκόνη θερμαίνεται (σε θερμοκρασίες 10-100 K) από τους διαφορετικούς αστρικούς πληθυσμούς και εκπέμπει, εκ νέου, την απορροφημένη ακτινοβολία στα υπέρυθρα μήκη κύματος. Τέλος, τα γαλαξιακά μαγνητικά πεδία υποβάλλουν τους κόκκους σκόνης σε συγκεκριμένη κατευθυντικότητα, κάτι που οδηγεί σε πόλωση του φωτός.

Είναι προφανές ότι η κοσμική σκόνη είναι ένα από τα θεμελιώδη συστατικά του μεσοαστρικού μέσου, ενώ είναι υπεύθυνη για πολλές διαδικασίες που διευκολύνουν το σχηματισμό των άστρων. Μία αρκετά αξιόπιστη μέθοδος για να μελετήσει κανείς την αλληλεπίδραση μεταξύ της αστρικής ακτινοβολίας και της σκόνης είναι η μοντελοποίηση της φασματικής ενεργειακής κατανομής (Spectral Energy Distribution; SED) ενός γαλαξία. Οι γαλαξίες αποτελούν ένα σύνολο πολλαπλών βαρυονικών συνιστωσών (δηλ. αστρικοί πληθυσμοί, σκόνη, ιονισμένο αέριο κλπ.). Αυτά τα συστατικά δεν είναι απομονωμένα, αλλά αλληλεπιδρούν συνεχώς μεταξύ τους, τόσο βαρυτικά όσο και ηλεκτρομαγνητικά. Με άλλα λόγια, το SED ενός γαλαξία περιέχει πολύτιμες πληροφορίες για τις διαδικασίες που οδήγησαν στο σχηματισμό και την εξέλιξή του.

Στη παρούσα διατριβή διερευνώ τις ιδιότητες της κοσμικής σκόνης και την αλληλεπίδρασή της με το αστρικό πεδίο ακτινοβολίας (που προέρχεται από διαφορετικούς αστρικούς πληθυσμούς) για 814 γαλαξίες στο κοντινό Σύμπαν (γαλαξίες που βρίσκονται σε απόσταση μικρότερη των 40 Mpc) οι οποίοι έχουν παρατηρηθεί από το διαστημικό τηλεσκόπιο *Herschel* του Ευρωπαϊκού Οργανισμού Διαστήματος. Οι παρατηρήσεις αυτές, στα υπέρυθρα μήκη κύματος, υποδηλώνουν την ύπαρξη της μεσοαστρικής σκόνης στους γαλαξίες, αφού, θερμαινόμενη από την ακτινοβολία των αστεριών, εκπέμπει σε αυτή την περιοχή του φάσματος. Οι παρατηρήσεις αυτές υπάρχουν συγκεντρωμένες σε μια μεγάλη βάση δεδομένων που ονομάζεται «DustPedia» (<http://dustpedia.astro.noa.gr/>). Το «DustPedia» ήταν ένα πρόγραμμα (2014-2018) χρηματοδοτούμενο από την Ευρωπαϊκή Ένωση (EU-FP7 program) με στόχο την αξιοποίηση παρατηρήσεων κοντινών γαλαξιών. Ο φιλόδοξος στόχος του προγράμματος αυτού ήταν να παράσχει απαντήσεις για τις ιδιότητες της κοσμικής σκόνης στο τοπικό Σύμπαν.

Χρησιμοποιώντας τα δεδομένα της βάσης δεδομένων του «DustPedia», και με την εφαρμογή του ευρέως διαδεδομένου κώδικα CIGALE (<https://cigale.lam.fr/>), ο οποίος είναι κατάλληλα διαμορφωμένος ώστε να συμπεριλαμβάνει το προηγμένο μοντέλο για την εκπομπή της σκόνης THEMIS (<https://www.ias.u-psud.fr/>

[themis/THEMIS_model.html](#)), μου επέτρεψε να μοντελοποιήσω τις φασματικές ενεργειακές κατανομές των γαλαξιών. Ο κώδικας CIGALE πραγματοποιεί προσαρμογή στα παρατηρησιακά δεδομένα με τη μέθοδο Bayesian. Με αυτό τον τρόπο μπορούν να προσδιοριστούν οι βασικές ιδιότητες των γαλαξιών, όπως, τη μάζα των αστρικών πληθυσμών και της σκόνης (M_{star} και M_{dust} , αντιστοίχως), τον ρυθμό σχηματισμού νέων αστεριών (Star-Formation Rate; SFR), τη συνολική φωτεινότητα κάθε αστρικού πληθυσμού, καθώς και την ενέργεια που απορροφάται εξαιτίας της σκόνης, τόσο για τους γηραιούς (> 200 Myr) όσο και για τους νεαρούς (≤ 200 Myr) αστρικούς πληθυσμούς. Συγκεκριμένα, ο τρόπος με τον οποίο παραμετροποίησα την διεργασία της αστρογένεσης στους γαλαξίες είναι ένας συνδυασμός από γεγονότα έντονης αστρογένεσης τα οποία έχουν εκθετική εξέλιξη με το χρόνο. Συνήθως, γίνεται υπόθεση για δύο τέτοια γεγονότα, ένα πρόσφατο (το οποίο περιγράφει το μεγαλύτερο ποσοστό της ακτινοβολίας που παρατηρούμε στα υπεριώδη και υπέρυθρα μήκη κύματος) και ένα προγενέστερο (το οποίο περιγράφει την εκπομπή του γαλαξία στο οπτικό και εγγύς-υπέρυθρο μέρος του φάσματος).

Για την κατασκευή του μοντέλου της φασματικής κατανομής ενός γαλαξία, ο κώδικας CIGALE διαθέτει μία πλούσια συλλογή βιβλιοθηκών για την εκπομπή των διαφόρων αστρικών πληθυσμών (για παράδειγμα [Bruzual & Charlot 2003](#); [Maraston 2005](#)) καθώς και για την εκπομπή της σκόνης (για παράδειγμα [Draine & Li 2007](#); [Draine et al. 2014](#); [Dale et al. 2014](#); [Jones et al. 2017](#)). Μάλιστα, η εκπομπή της σκόνης θέτει περιορισμούς ως προς την εφαρμογή του νόμου εξασθένησης του αστρικού φωτός (διαθέσιμοι νόμοι εξασθένησης: [Calzetti et al. 2000](#); [Charlot & Fall 2000](#)). Βασίζομενος σε πρόσφατες μελέτες που κάνουν χρήση του κώδικα CIGALE, χρησιμοποίησα τη βιβλιοθήκη [Bruzual & Charlot \(2003\)](#) για την εκπομπή των διαφόρων αστρικών πληθυσμών, τον νόμο εξασθένησης που περιγράφεται στην εργασία [Calzetti et al. \(2000\)](#), ενώ για την μοντελοποίηση της σκόνης στα υπέρυθρα μήκη κύματος δημιούργησα και εφάρμοσα τη δική μου βιβλιοθήκη, βασισμένη στο μοντέλο για την εκπομπή της σκόνης, THEMIS. Το THEMIS βασίζεται στις οπτικές ιδιότητες της σκόνης (περιέχει χημικές ενώσεις από υδρογονάνθρακες και πυρίτιο) όπως αυτές έχουν παρατηρηθεί στο εργαστήριο (Εικ. 2.3). Το συγκεκριμένο μοντέλο για τη σκόνη περιγράφει ικανοποιητικά την παρατηρούμενη εξασθένηση του φωτός στα υπεριώδη και οπτικά μήκη κύματος καθώς και το σχήμα της θερμικής εκπομπής της σκόνης στα υπέρυθρα μήκη κύματος. Το μοντέλο έχει επίσης συγκριθεί επιτυχώς με τις πιο πρόσφατες παρατηρήσεις εξασθένησης του φωτός και εκπομπής από την διάχυτη σκόνη στον Γαλαξία μας (Milky Way Galaxy; [Ysard et al. 2015](#); [Fanciullo et al. 2015](#)).

Από την έρευνα αυτή προκύπτει ότι η μάζα των αστεριών, της σκόνης και του αερίου, καθώς κι ο ρυθμός σχηματισμού αστεριών και η θερμοκρασία της σκόνης διαφέρουν από γαλαξία σε γαλαξία ανάλογα με τον μορφολογικό τους τύπο (δες Εικ. 5.11, 5.12). Η συνολική μάζα των αστεριών είναι μέγιστη στους ελλειπτικούς γαλαξίες ($T = -5$) και παρουσιάζει μικρές μεταβολές για γαλαξίες με $T < 2$ ενώ για γαλαξίες με $T > 5$ υπάρχει απότομη πτώση, περίπου δύο τάξεις μεγέθους. Η συνολική μάζα του ατομικού αερίου μεταβάλλεται ελαφρώς για τους γαλαξίες με $T < 2$ (παρόμοια με την συνολική μάζα των αστεριών) ακολουθούμενη από μια πτώση, περίπου μιας τάξης μεγέθους, για γαλαξίες με $T > 5$. Η συνολική μάζα της σκόνης και ο ρυθμός αστρογένεσης μεταβάλλονται επίσης με παρόμοιο τρόπο σε σχέση με

τους διαφορετικούς μορφολογικούς τύπους. Και οι δύο ποσότητες παρουσιάζουν μία συνεχή αύξηση για γαλαξίες με $T < 0$ και μία αργή μείωση για τους γαλαξίες με $T > 5$ (περίπου δύο τάξεις μεγέθους και στις δύο περιπτώσεις), με μέγιστη τιμή για τους γαλαξίες με $T = 5$. Η θερμοκρασία της σκόνης υπολογίζεται ότι είναι υψηλότερη στους ελλειπτικούς γαλαξίες (~ 30 K) σε σύγκριση με τους σπειροειδείς όπου παρατηρείται πτώση στη θερμοκρασία κατά ~ 10 K, ακολουθούμενη από μία απότομη αύξηση στους ~ 30 K για τους γαλαξίες μορφολογικού τύπου Sm και Irr.

Η κυρίαρχη πηγή ακτινοβολίας στους ελλειπτικούς γαλαξίες είναι ο γηραιός αστρικός πληθυσμός με λιγότερο από 10% της συνολικής ακτινοβολίας να προέρχεται από τον νεαρό αστρικό πληθυσμό (Εικ. 5.15). Για τους σπειροειδείς γαλαξίες με Hubble Stage μεταξύ 0 και 5 η συνεισφορά του νεαρού αστρικού πληθυσμού στο πεδίο της ακτινοβολίας σταδιακά αυξάνεται στο 25%, ενώ παραμένει σταθερό για γαλαξίες με $T > 5$. Κατά μέσο όρο, για τους 814 γαλαξίες, το ποσοστό απορρόφησης της ακτινοβολίας από την σκόνη (f_{abs}) κυμαίνεται σε 19% ενώ αν ληφθούν υπόψη μόνο οι γαλαξίες με $T > 0$ το ποσοστό αυξάνεται σε 25% (δες εκτενή μελέτη για το f_{abs} σε Bianchi et al. 2018). Συγκεκριμένα, το ποσοστό της ακτινοβολίας που απορροφάται από την σκόνη παίρνει τη μέγιστη τιμή του ($\sim 34\%$) για γαλαξίες με Hubble Stages περίπου 5, ενώ σταδιακά μειώνεται σχεδόν σε $\sim 0\%$ για τους ελλειπτικούς γαλαξίες ($T = -5$) και σε $\sim 10\%$ για τους ανώμαλους γαλαξίες ($T = 10$).

Κατά μέσο όρο, ο νεαρός αστρικός πληθυσμός είναι πολύ πιο αποτελεσματικός στη θέρμανση της σκόνης, ενώ το ποσοστό της απορρόφησης της ακτινοβολίας για τον συγκεκριμένο πληθυσμό φτάνει το $\sim 77\%$. Από την άλλη, το μέγιστο ποσοστό απορρόφησης της ακτινοβολίας του γηραιού αστρικού πληθυσμού είναι $\sim 24\%$ (Εικ. 5.16). Η θέρμανση της σκόνης στους ελλειπτικούς γαλαξίες οφείλεται κυρίως στον γηραιό αστρικό πληθυσμό, μέχρι και $\sim 90\%$. Ο νεαρός αστρικός πληθυσμός συμβάλλει προοδευτικά περισσότερο στους «κανονικούς» σπειροειδείς γαλαξίες και γίνεται η κυρίαρχη πηγή θέρμανσης της σκόνης για τους «ανώμαλους» γαλαξίες μορφολογικού τύπου Sm και Irr, με το 60% της ακτινοβολίας του να συμβάλλει στο σκοπό αυτό (Εικ. 5.17). Τέλος, γίνεται αναφορά της συσχέτισης του ποσοστού θέρμανσης της σκόνης από το νεαρό αστρικό πληθυσμό με τον μορφολογικό τύπο και τον ειδικό ρυθμό σχηματισμού αστέρων [Specific Star-Formation Rate ($\text{SFR}/M_{\text{star}}$); Εικ. 5.18].

Επιπλέον, ένας από τους κύριους στόχους της διατριβής ήταν η δημιουργία τρισδιάστατων μοντέλων διάδοσης ακτινοβολίας για γαλαξίες με υψηλή διακριτική ικανότητα. Με τη συγκεκριμένη μέθοδο επιχείρησα να λύσω το πρόβλημα διάδοσης της ακτινοβολίας. Η λύση στο πρόβλημα επέρχεται με την εύρεση της επίδρασης της ύλης στην ενέργεια μίας δέσμης φωτονίων (ενέργεια μπορεί να προστεθεί ή να αφαιρεθεί από αυτήν με εκπομπή, σκέδαση ή απορρόφηση). Συνολικά, μια δέσμη φωτός που καλύπτει μια φυσική απόσταση s , μπορεί να περιγραφεί από την στατική παγχωματική εξίσωση διάδοσης ακτινοβολίας:

$$\begin{aligned} \frac{dI_\lambda}{ds} = & j_\lambda^{\text{star}} - \rho \kappa_\lambda^{\text{ext}} I_\lambda \\ & + \rho \kappa_\lambda^{\text{sca}} \int_{4\pi} I_\lambda \Phi_\lambda(\mathbf{k}, \mathbf{k}') d\Omega' \\ & + j_\lambda^{\text{dust}} \end{aligned}$$

όπου I_λ είναι η ειδική ένταση της ακτινοβολίας ανά μήκος κύματος λ , j_λ^{star} αναπαριστά την εκπομπή που προέρχεται από τους αστρικούς πληθυσμούς, ρ είναι η πυκνότητα της σκόνης, $\kappa_\lambda^{\text{ext}}$, $\kappa_\lambda^{\text{abs}}$, και $\kappa_\lambda^{\text{sca}}$ είναι οι συντελεστές εξασθένησης, απορρόφησης, και σκέδασης της σκόνης με $\kappa_\lambda^{\text{ext}} = \kappa_\lambda^{\text{abs}} + \kappa_\lambda^{\text{sca}}$, $\Phi_\lambda(\mathbf{k}, \mathbf{k}')$ είναι η συνάρτηση σκέδασης της σκόνης, και j_λ^{dust} είναι η θερμική εκπομπή της σκόνης. Αυτή η εξίσωση λαμβάνει υπόψη τις φυσικές διεργασίες της απορρόφησης, σκέδασης και θερμικής εκπομπής.

Από δισδιάστατες εικόνες παρατηρήσεων στα διάφορα μήκη κύματος, παρήγαγα τις τρισδιάστατες κατανομές των αστεριών και της σκόνης, γεγονός που επιτρέπει μια πιο ρεαλιστική περιγραφή των σύνθετων αστρικών γεωμετριών που βρίσκονται στους γαλαξίες, όπως τις σπειροειδείς δομές ή περιοχές συμπύκνωσης της σκόνης (Εικ. 6.1). Για να μοντελοποιήσω τις σύνθετες γεωμετρίες, χρησιμοποίησα το SKIRT (<http://www.skirt.ugent.be>), έναν σύγχρονο κώδικα Monte Carlo, τρισδιάστατης διάδοσης ακτινοβολίας που σχεδιάστηκε για να προσομοιώνει την απορρόφηση, τη σκέδαση, και τη θερμική εκπομπή από τη σκόνη για αυθαίρετες τρισδιάστατες κατανομές. Οι προσομοιώσεις διάδοσης ακτινοβολίας με το SKIRT, παρέχουν τη μοναδική ευκαιρία για την αναλυτική μελέτη των μηχανισμών θέρμανσης της σκόνης από τους διάφορους αστρικούς πληθυσμούς σε «τοπικό» επίπεδο, δηλαδή σε διαφορετικές περιοχές μέσα στον ίδιο γαλαξία.

Ανέλυσα τη συμβολή των διαφόρων αστρικών πληθυσμών στις διαδικασίες θέρμανσης της σκόνης σε τέσσερις κοντινούς, ραβδωτούς γαλαξίες: NGC 1365, M 83, M 95, και M 100; καθώς κι έναν γαλαξία οποίος διαθέτει έναν ενεργό γαλαξιακό πυρήνα: NGC 1068. Η γωνία κλίσης του επιπέδου των συγκεκριμένων γαλαξιών είναι πολύ μικρή με αποτέλεσμα να φαίνεται όλος ο δίσκος τους. Η επιλογή των συγκεκριμένων γαλαξιών έγινε γιατί, έως και σήμερα, δεν έχουν μελετηθεί τέτοιου είδους γαλαξίες (ραβδωτοί και με ΕΓΠ) με τον συγκεκριμένο τρόπο. Σκοπός της ανάλυσης αυτής ήταν να ποσοτικοποιήσω το ποσοστό που σχετίζεται άμεσα με τον ρυθμό παραγωγής νέων αστερών, καθώς και την έκταση της συνεισφοράς του ενεργού γαλαξιακού πυρήνα στη θέρμανση της διάχυτης σκόνης στις τρεις διαστάσεις.

Για την κατασκευή του τρισδιάστατου μοντέλου για κάθε γαλαξία υπέθεσα τέσσερις γεωμετρικές κατανομές, τρεις κύριους αστρικούς πληθυσμούς και την κατανομή της σκόνης, επί του γαλαξιακού επιπέδου. Συγκεκριμένα, οι αστρικοί πληθυσμοί διαχωρίζονται με βάση την ηλικία τους σε: έναν γηραιό αστρικό πληθυσμό (> 8 Gyr) ο οποίος κατανέμεται ομαλά σε όλη την έκταση του γαλαξιακού επιπέδου, έναν νεαρό αστρικό πληθυσμό (~ 100 Myr) ο οποίος έχει απομακρυνθεί από τις περιοχές της αστρογένεσης, και σε έναν νεότερο αστρικό πληθυσμό (< 10 Myr) ο οποίος βρίσκεται στο ίδιο επίπεδο με τον δίσκο της σκόνης, ενώ η παραγόμενη ακτινοβολία τους μπορεί

να ιονίσει το υλικό στην τοπική τους περιοχή. Για την δημιουργία των ξεχωριστών κατανομών έγινε χρήση αντιπροσωπευτικών εικόνων από παρατηρήσεις στα διάφορα μήκη κύματος. Για την κατανομή του γηραιού αστρικού πληθυσμού χρησιμοποιήσα την εικόνα στα 3.6 μm από το όργανο IRAC του τηλεσκοπίου *Spitzer*, για τον νεαρό αστρικό πληθυσμό πήρα την εικόνα στα 0.1 μm του τηλεσκοπίου GALEX ενώ για τον νεότερο αστρικό πληθυσμό συνδύασα 2 εικόνες, την εικόνα στα 24 μm από το όργανο MIPS του τηλεσκοπίου *Spitzer* με την εικόνα εκπομπής H α . Τέλος, για την κατανομή της σκόνης συνδύασα πολλαπλές εικόνες από τις παρατηρήσεις του τηλεσκοπίου *Herschel* στα 70, 100, και 160 μm . Στη περίπτωση του NGC 1068 έγινε υπόθεση μίας επιπλέον κατανομής για την συνεισφορά του ΕΓΠ επί του γαλαξιακού δίσκου. Για την κατανομή της εκπομπής του ΕΓΠ έγινε χρήση της εικόνας στα 4.6 μm από το τηλεσκόπιο *WISE*. Το τρισδιάστατο στοιχείο για κάθε μία από αυτές τις τέσσερις κατανομές δίνεται με την εφαρμογή ενός τέλει εκθετικού προφίλ, ορισμένο από προηγούμενες μελέτες γαλαξιών των οποίων η γωνία κλίσης του επιπέδου τους προσεγγίζει τις 90° (edge-on).

Από την κατανομή της πυκνότητας της σκόνης σε κάθε γαλαξία παράγεται ένα δίκτυο το οποίο αποτελείται από περίπου 3 εκατομμύρια τρισδιάστατα στοιχεία (dust cells). Έπειτα, αφού οριστεί ο συνολικός αριθμός μηκών κύματος (252), για κάθε μήκος κύματος στο μοντέλο χρησιμοποιούνται 5 εκατομμύρια φωτόνια, τα οποία διαδίδονται μέσω του δικτύου σκόνης. Έτσι λοιπόν, κάνοντας χρήση του κώδικα SKIRT και της μεθόδου Monte Carlo η οποία καθορίζει την πιθανότητα ενός φωτονίου να απορροφηθεί ή να σκεδαστεί από τη σκόνη, γίνεται λύση του προβλήματος διάδοσης ακτινοβολίας στα μελετώμενα συστήματα γαλαξιών. Με αυτό το τρόπο προσδιορίζονται οι ελεύθερες παράμετροι του μοντέλου οι οποίες είναι τρεις: η μάζα της σκόνης, η φωτεινότητα του νεαρού αστρικού πληθυσμού στο υπεριώδες, και η φωτεινότητα του νεότερου αστρικού πληθυσμού στο υπεριώδες. Συνολικά, για κάθε γαλαξία, τρέξαμε κατά μέσο όρο 400 προσομοιώσεις. Στη περίπτωση του NGC 1068 προσδιορίζεται ακόμη μία ελεύθερη παράμετρος η οποία αντιστοιχεί στην εκπομπή του ΕΓΠ στα 4.6 μm . Τα αποτελέσματα των προσομοιώσεων για κάθε γαλαξία είναι εικόνες στα διάφορα μήκη κύματος οι οποίες μπορούν να συγκριθούν άμεσα με τις πραγματικές παρατηρήσεις, και συνεπώς να γίνει η επιλογή του καλύτερου μοντέλου (Εικ. 6.2).

Από τη μελέτη αυτή πραγματοποιήθηκε η μέτρηση ρεαλιστικών νόμων εξασθένησης της ακτινοβολίας για τους γαλαξίες M 83, M 95, M 100, NGC 1068, και NGC 1365, ενώ προκύπτει ότι η μορφή του νόμου εξασθένησης της ακτινοβολίας από τη σκόνη για κάθε γαλαξία συσχετίζεται άμεσα με το βαθμό πολυπλοκότητας της σχετικής γεωμετρίας μεταξύ των αστρικών πληθυσμών και της κατανομής της σκόνης (Εικ. 6.8). Επίσης, παρατηρήθηκε ότι ο ειδικός ρυθμός σχηματισμού αστέρων συνδέεται άμεσα με τη κλίση του νόμου εξασθένησης και με το πόσο ισχυρή είναι η απορρόφηση της ακτινοβολίας στα 0.22 μm (UV bump). Κατά μέσο όρο, το 36.5% της συνολικής ακτινοβολίας ενός γαλαξία απορροφάται από τη σκόνη. Το αποτέλεσμα αυτό συμφωνεί ικανοποιητικά με τη μέση τιμή του ποσοστού απορρόφησης της ακτινοβολίας από την σκόνη για τον αντίστοιχο μορφολογικό τύπο γαλαξιών (Sb-Sc) που παρουσιάζεται στην εργασία των Bianchi et al. (2018).

Τα αποτελέσματα αυτής της εργασίας επιβεβαιώνουν ότι η κεντρική περιοχή κα-

θώς και τα δύο διαμετρικά αντίθετα άκρα της ράβδου είναι τοποθεσίες ενισχυμένου σχηματισμού νέων αστέρων για τους γαλαξίες M 83, M 95, M 100, και NGC 1365, ενώ γίνεται αναφορά για την επίδραση της κεντρικής ράβδου στα ακτινικά προφίλ του ποσοστού θέρμανσης της σκόνης από τους νεαρούς αστρικούς πληθυσμούς (Εικ. 6.10), και της θερμοκρασίας της σκόνης (Εικ. 6.13). Κατά μέσο όρο, η θερμοκρασία της διάχυτης σκόνης στον πυρήνα κάθε γαλαξία είναι υψηλότερη σε σχέση με αυτή στη ράβδο. Πέρα από την περιοχή της ράβδου η θερμοκρασία της σκόνης μειώνεται σταδιακά. Ο γηραιός αστρικός πληθυσμός είναι αποκλειστικά υπεύθυνος για τη θέρμανση της ζεστής σκόνη στο πυρήνα κάθε γαλαξία καθώς και για τη θέρμανση της κρύας διάχυτης σκόνης επί του γαλαξιακού δίσκου. Από την άλλη, οι νεαροί αστρικοί πληθυσμοί είναι, επί το πλείστον, η κύρια πηγή θέρμανσης της ζεστής σκόνης στις σπειρές και στις περιοχές έντονης αστρογένεσης.

Γενικά, διαπιστώνεται ότι οι νεαροί αστρικοί πληθυσμοί είναι οι κύριοι συντελεστές της θέρμανσης της σκόνης για τους τέσσερις ραβδωτούς γαλαξίες, δωρίζοντας, κατά μέσο όρο, το 59% της ακτινοβολίας τους για το σκοπό αυτό σε όλο τον γαλαξία. Το ποσοστό θέρμανσης της σκόνης από τους νεαρούς αστρικούς πληθυσμούς πέφτει στο 53% στην περιοχή των ράβδων και στο 38% στην κεντρική περιοχή όπου ο γηραιός αστρικός πληθυσμός είναι ο κυριότερος συντελεστής της θέρμανσης της σκόνης (Εικ. 6.9). Επιπροσθέτως, επιβεβαιώνεται η ισχυρή συσχέτιση μεταξύ του ποσοστού θέρμανσης της σκόνης από τους νεαρούς αστρικούς πληθυσμούς με τον ειδικό ρυθμό σχηματισμού αστέρων (Εικ. 6.11) και παρατίθεται μία σχέση για τη βαθμονόμηση της συνεισφοράς του γηραιού αστρικού πληθυσμού στη θέρμανση της σκόνης, ιδιαίτερα σημαντική για τη μοντελοποίηση της φασματικής κατανομής των γαλαξιών.

Τέλος, για τον NGC 1068, τον γαλαξία που φιλοξενεί ΕΓΠ βρίσκουμε ότι η διάχυτη σκόνη θερμαίνεται, κατά κύριο λόγο, από το συνεχή σχηματισμό νέων αστέρων. Κατά μέσο όρο, το ποσοστό θέρμανσης της σκόνης από τους νεαρούς αστρικούς πληθυσμούς πλησιάζει το 83%, ενώ το εναπομείναν ποσοστό (~ 17%) προέρχεται σε μεγάλο βαθμό από την συνεισφορά του γηραιού αστρικού πληθυσμού. Η συνεισφορά του ΕΓΠ στη θέρμανση της σκόνης παραμένει αρκετά υψηλή στη κεντρική περιοχή του γαλαξία (~80%) εντός μίας ακτίνας 40 pc. Επί του γαλαξιακού δίσκου, σε ακτίνα 500 pc η συνεισφορά του ΕΓΠ πέφτει στο 10%, ενώ κυμαίνεται μεταξύ μερικών ποσοστιαίων μονάδων σε απόσταση 4 kpc, από τον πυρήνα, γεγονός που υποδεικνύει την συνεισφορά του ΕΓΠ πέρα από τη κεντρική περιοχή του γαλαξία (Εικ. 7.7).

Επιγραμματικά, η διατριβή οδήγησε στην πρώτη συστηματική περιγραφή μεγάλου πλήθους κοντινών γαλαξιών, προσέδωσε σημαντικές πληροφορίες για τις ιδιότητες της κοσμικής σκόνης αλλά και για τις διεργασίες με τις οποίες διαμορφώνονται οι γαλαξίες στην τωρινή τους μορφή και, κατ' επέκταση, για το πως οι γαλαξίες εξελίσσονται στο χρόνο. Τέλος, η διατριβή αυτή επέτρεψε την καλύτερη κατανόηση των μηχανισμών θέρμανσης της σκόνης από τους διάφορους αστρικούς πληθυσμούς εφαρμόζοντας δύο διαφορετικές, ανεξάρτητες μεταξύ τους, μεθόδους: 1) την μοντελοποίηση της φασματικής κατανομής κοντινών γαλαξιών, και 2) την τρισδιάστατη μοντελοποίηση γαλαξιών με χρήση κώδικα διάδοσης ακτινοβολίας.

Abstract

The present thesis investigates the properties of cosmic dust and its interaction with the stellar radiation field (originating from different stellar populations) on global scales, for 814 galaxies in the local Universe, all observed by the *Herschel Space Observatory*. I took advantage of the widely used fitting code CIGALE, properly adapted to include the state-of-the-art dust model THEMIS. Using the DustPedia photometry I have determined the physical properties of the galaxies, such as the dust and stellar mass, the star-formation rate, the bolometric luminosity, the unattenuated and the absorbed by dust stellar light, for both the old (> 200 Myr) and young (≤ 200 Myr) stellar populations. I show how the mass of stars, dust, and atomic gas, as well as the star-formation rate and the dust temperature vary between galaxies of different morphologies and provide recipes to estimate these parameters given their Hubble stage (T). I find a mild correlation between the mass fraction of the small a-C(:H) grains with the specific star-formation rate. On average, young stars are very efficient in heating the dust, with absorption fractions reaching as high as $\sim 77\%$ of the total unattenuated luminosity of this population. On the other hand, the maximum absorption fraction of old stars is $\sim 24\%$. Dust heating in early-type galaxies is mainly due to old stars, up to a level of $\sim 90\%$. Young stars progressively contribute more for “typical” spiral galaxies and they become the dominant source of dust heating for Sm-type and irregular galaxies, with $\sim 60\%$ of their luminosity contributing to that purpose. Finally, we find a strong correlation of the dust heating fraction by young stars with morphology and the specific star-formation rate.

In addition, as one of the main goals of this thesis, is to construct detailed 3D dust radiative transfer models for spatially resolved, nearby galaxies. From 2D images I have derived the 3D distributions of stars and dust. To model the complex geometries, I have used SKIRT, a state-of-the-art 3D Monte Carlo radiative transfer code designed to self-consistently simulate the absorption, scattering, and thermal re-emission by the dust for arbitrary 3D distributions. By analysing the contribution of the different stellar populations to the radiative dust heating processes in four nearby face-on barred galaxies: NGC 1365, M 83, M 95, and M 100; and a galaxy hosting an AGN: NGC 1068, has enabled me to quantify the fraction directly related to star-formation, as well as the extent of the contribution of the AGN to the diffuse dust heating. First, I have derived

global attenuation laws for each galaxy and confirmed that galaxies of high specific star-formation rate have shallower attenuation curves and weaker UV bumps. On average, 36.5% of the bolometric luminosity is absorbed by dust in the galaxy sample. I have reported a clear effect of the bar structure on the radial profiles of the dust-heating fraction by the young stellar populations, and the dust temperature. I have found that the young stellar populations are the main contributors to the dust heating, donating, on average $\sim 59\%$ of their luminosity to this purpose throughout the galaxy. This dust-heating fraction drops to $\sim 53\%$ in the bar region and $\sim 38\%$ in the bulge region where the old stars are the dominant contributors to the dust heating. We also find a strong link between the heating fraction by the young stellar populations and the specific star-formation rate.

Acknowledgements

Writing this thesis is the last stage of a very long journey that started three years ago. The experience of being a PhD student offers many moments of anxiety, agony, doubt, but it also (and most importantly) brings unforgettable moments of joy and excitement. Here, I would like to thank all those people that accompanied me on this journey.

First and foremost, there are not enough words to express how grateful and lucky I am for having Manolis Xilouris as my supervisor. From the first moment we met, Manolis believed in me and my abilities, providing me with his enduring patience and professional guidance since then. Because of him I was able to work alongside top, fellow astronomers on a grand project as the DustPedia, which allowed me to grow as a researcher and to acquire valuable knowledge that will help me pursue a career in astronomy. For that, I am forever thankful. Lastly, without his efforts I would have never had the opportunity to live and work abroad in Ghent. Manolis thank you for everything, you are the best mentor that anyone could have asked for.

Also, I would like to express my sincere gratitude to my supervisor at Ghent University, Maarten Baes. Thanks to his continuous encouragement and cheerful attitude I was able to look on the bright side of every moment even when things looked dim. Maarten thank you for supporting my efforts, inspiring me to constantly try to top myself, and for giving me the chance to become a member of your team. It was an honour.

Furthermore, I would like to thank my advisors at the University of Athens, Nektarios Vlahakis and Despina Hatzidimitriou as well as Prof. Apostolos Mastichiadis, for their support throughout my studies. I would also like to thank all jury members, for reviewing my thesis and helping me to present the results of my research in the best possible way. Besides my advisors, I would like to give a special shout out to the merry group of DustPedians. Thanks goes to each and everyone of you, for your sheer enthusiasm about my work and for all the fun we had together during our meetings.

As in any kind of adventure, you cannot travel far without a fellowship of true friends. First, I would like to thank my officemates at De Sterre, Ana Trčka and Wouter Dobbels for the countless times we spent discussing and laughing about everything. To Ana in particular, I am deeply thankful for enduring my grumpiness and my whining for a whole year, for the many evenings we were working together before deadlines, and of course for

keeping my PC alive in my absence. I couldn't have asked for a better officemate and a friend. I would also like to thank my RT buddies Sam Verstocken and Sébastien Viaene for the stimulating discussions and genuine team work. Special thanks to Sam and Ellen for your hospitality and for the relaxing moments we spent gardening. Thank you both for making me feel Ghent as my second home. Moreover, I would like to thank both Michele Mastropietro and Shivangee Rathi for the always interesting conversations about culture, and for the numerous, pleasant moments we had in Ghent. Finally, I would like to thank Marjorie Declair for her willingness to help me when I needed her aid, for the opportunity she gave me to travel to Tuscon and make observations at Kitt Peak National Observatory, and for the plenty fond memories. Special shout out to the nice people I met in Ghent - Sven De Rijcke, Peter Camps, Ilse De Loose, Dries Van De Putte, Steven Caluwaerts, Michiel Van Ginderachter, Arjen Van Der Wel, Aaron Wilkinson, Caroline Straatman, Francesco D'Eugenio, Inge Van Der Vennet and Gerbrand Nootens.

Last but not least, I am blessed to work daily among so many awesome and admirable people at the National Observatory of Athens. Thank you all for making our work place an environment of joyful weirdness. I appreciate each and everyone of you. An enormous thanks goes to Emmy Paraskeva, Zoi Spetsieri, Ektoras Pouliasis, Sophia Derlopa, Ming Yang, Angel Ruiz, Maria Chira, Vaggelis Paspaliaris, Vasilia Masoura, George Dimopoulos, Frank Trammer, Stephan De Wit, Letizia Cassarà, George Mountrichas, Ioannis Alikakos, Alexis Liakos, Grigoris Maravelias, Michalis Papachristou, Stella Boula, Stavroula Papatheochari, Stavroula Katsioli, Alexandros Chiotelis, Pauline Tsiapi, and Konstantina Varsou. Special thanks to the researchers at NOA – Alceste Bonanos, Antonis Georgakakis, Kalliopi Dasyra, Elias Koulouridis, Tasos Dapergolas, Ioannis Georgantopoulos, Panayotis Boumis, and Ioannis Bellas.

I dedicate this thesis to my parents.

Άγγελος

This research is co-financed by Greece and the European Union (European Social Fund - ESF) through the Operational Programme «Human Resources Development, Education and Lifelong Learning» in the context of the project 'Strengthening Human Resources Research Potential via Doctorate Research' (MIS-5000432), implemented by the State Scholarships Foundation (IKY).

This research was supported partially by DustPedia, a project funded by the EU (grant agreement number 606847) under the heading 'Exploitation of space science and exploration data (FP7-SPACE-2013-1)' and is a collaboration of six European institutes: Cardiff University (UK), National Observatory of Athens (Greece), Istituto Nazionale di Astrofisica (Italy), Universiteit Gent (Belgium), Commissariat à l'énergie atomique (France), Université Paris Sud (France).

Cover – The image used on the cover page of this dissertation is an image of the Elephant's Trunk Nebula in IC 1396 produced by J.C. Canonne, P. Bernhard, D. Chaplain & L. Bourgon. IC 1396 is a young stellar cluster in the constellation of Cepheus. The different colours represent the light emission of different elements, like ionised hydrogen, sulphur, and oxygen atoms, while the dark ridges outline regions of cool interstellar dust and gas clouds, obscuring the light of protostars.

Contents

I	Introduction	1
1	About galaxies and their content	3
1.1	A galaxy's anatomy	3
1.2	Galaxy classification and morphology	5
1.3	Galaxy formation and evolution	8
1.4	The process of star formation	10
1.5	Dust in galaxies	12
1.5.1	Grain production	13
1.5.2	Grain destruction	14
1.5.3	Grain populations	14
1.5.4	Dust effects in galaxies	16
1.6	The SED of a galaxy	19
1.7	Radiative transfer	20
1.8	This thesis	22
2	The DustPedia project	25
2.1	The DustPedia sample of galaxies	25
2.2	THEMIS: a new global physical dust model	27
2.3	The radiative transfer modelling framework	28

II	Astrophysical modelling tools	33
3	Fitting the SEDs with CIGALE	35
3.1	Assumptions on the SFH	35
3.2	Dust attenuation laws	37
3.3	Implementing THEMIS to CIGALE	37
3.4	Deriving the integrated properties of galaxies	38
4	Radiative transfer modelling with SKIRT	41
4.1	SKIRT concepts	41
4.1.1	Wavelength grid	42
4.1.2	Spatial geometries	42
4.1.3	Dust grid	43
4.1.4	Instruments	44
III	Global SED fitting	45
5	Old and young stellar populations and their role in dust heating	47
5.1	Introduction	47
5.2	The sample	49
5.3	Fitting the SEDs with CIGALE	50
5.3.1	The parameter space	51
5.3.2	Quality of the fit	51
5.4	Mock analysis	55
5.5	CIGALE modelling using the DL14 dust model and comparison with the THEMIS model	58
5.6	Comparison with different recipes used in the literature	59
5.7	Fitting the FIR with MBB	63
5.8	Comparison between CIGALE and MBB	65
5.9	Physical parameters as a function of the Hubble stage	67
5.10	Evolution of small a-C(:H)	71
5.11	The stellar populations and the dust content in nearby galaxies	73
5.11.1	Old and young stellar populations in galaxies	76

5.11.2	The heating of dust by the different stellar populations	76
5.12	Recipes to estimate physical properties of galaxies as a function of Hubble stage	81
5.13	Summary and conclusions	81
IV	High-resolution, 3D radiative transfer modelling of nearby galaxies	85
6	The DustPedia barred galaxies	87
6.1	Introduction	87
6.2	Galaxy sample and data	89
6.3	Radiative transfer simulations with SKIRT	93
6.3.1	Modelling approach	93
6.4	Model validation	97
6.4.1	Global SEDs	97
6.4.2	Image comparison	100
6.5	Discussion	106
6.5.1	Attenuation law	106
6.5.2	Dust heating	108
6.5.3	Correlation between young heating fraction and sSFR	113
6.5.4	Dust temperature	117
6.6	Conclusions	120
7	AGN-powered dust heating in NGC 1068	123
7.1	Introduction	123
7.2	Data	126
7.3	Model preparation	126
7.4	Radiative transfer SED fitting	129
7.5	A 3D high-resolution model for NGC 1068	132
7.6	Dust heating sources	137
7.7	Discussion and summary	140

V	Summary and conclusions	143
8	Summary and conclusions	145

List of Figures

1.1	All sky view of the Milky Way	4
1.2	Image of M 51 taken from <i>Hubble Space Telescope</i>	5
1.3	The Hubble-de Vaucouleurs galaxy classification scheme	6
1.4	The ATLAS ^{3D} galaxy classification scheme	7
1.5	The ‘Main sequence’ of galaxies	10
1.6	The Eagle Nebula	11
1.7	The life cycle of dust	12
1.8	Dust grain examples	15
1.9	Dust extinction curves	17
1.10	Dust attenuation curves	18
1.11	SED examples of different galaxy types	20
2.1	The DustPedia sample of galaxies	26
2.2	Multi-band images of NGC 3198	27
2.3	Schematic of dust properties in the THEMIS dust model	28
2.4	Standard geometric model of spiral galaxies	29
2.5	Schematic of the radiation transfer modelling framework	31
3.1	CIGALE workflow schematic	36
3.2	SED examples of DustPedia galaxies from CIGALE	39
4.1	SKIRT workflow schematic	42
4.2	Example of a dust grid used in SKIRT	44

5.1	Reduced χ^2 distribution of the DustPedia galaxies using CIGALE-THEMIS	53
5.2	Ratios of observed fluxes to the modelled fluxes	54
5.3	Best-fitted and mock parameters comparison using CIGALE-THEMIS	56
5.4	Best-fitted and mock parameters comparison using CIGALE-DL14	57
5.5	Reduced χ^2 distribution of the DustPedia galaxies using CIGALE-DL14	59
5.6	Comparison between SFR, T_{dust} , M_{star} , and M_{dust}	60
5.7	Comparison between M_{star} and SFR	61
5.8	Average absorption coefficient for the THEMIS dust model	64
5.9	Reduced χ^2 distribution of the DustPedia galaxies using MBB-THEMIS	65
5.10	Comparison of M_{dust} and T_{dust}	66
5.11	Scaling relations versus morphological type	69
5.12	T_{dust} versus morphological type	71
5.13	Small a-C(:H) mass fraction versus sSFR	72
5.14	Median SEDs for six main morphological classes as derived from CIGALE	74
5.15	Relative stellar luminosity ratios versus morphological type	75
5.16	Mean values of stellar luminosity ratios versus morphological type	78
5.17	Mean dust heating fractions versus morphological type	79
5.18	Correlation between $S_{\text{young}}^{\text{abs}}$ and sSFR	80
6.1	2D maps of different components for each barred galaxy	91
6.2	Panchromatic SED of each barred galaxy	98
6.3	PDFs of the three free parameters in the model optimisation	99
6.4	Observations versus simulations in selected wavebands for M 83	101
6.5	Observations versus simulations in selected wavebands for NGC 1365	102
6.6	Observations versus simulations in selected wavebands for M 95	103
6.7	Observations versus simulations in selected wavebands for M 100	104
6.8	Compilation of attenuation laws derived from 3D radiation transfer models	107
6.9	Young heating fraction map and distribution of each barred galaxy	110
6.10	Distribution of f_{young} versus galactocentric distance	112
6.11	Relation between sSFR and f_{young}	114
6.12	Relations between sSFR and f_{young}	115

6.13	Distribution of T_{dust} versus galactocentric distance and T_{dust} maps . . .	118
7.1	2D maps of different components for NGC 1068	127
7.2	PDFs of the free parameters in the model optimisation of NGC 1068 . . .	131
7.3	SEDs from the best-fit model for NGC 1068	132
7.4	Observations versus simulations in selected wavebands for NGC 1068 . . .	135
7.5	AGN emission fraction per wavelength for NGC 1068	136
7.6	f_{young} and f_{AGN} maps and distributions of NGC 1068	138
7.7	Distribution of f_{young} and f_{AGN} versus galactocentric distance	139

List of Tables

1.1	Numerical Hubble Stage	7
5.1	Parameter grid used for the CIGALE templates	51
5.2	Mean values of physical properties of the DustPedia galaxies	52
5.3	Mean values of normalised physical properties of DustPedia galaxies	68
5.4	Mean values of luminosity ratios	77
5.5	Recipes to estimate galaxy properties given their Hubble stage	82
6.1	Basic properties of 4 barred face-on galaxies	89
6.2	Integrated flux densities for our galaxy sample	92
6.3	Overview of the different components in the radiation transfer model	94
6.4	Overview of the model parameters for all four galaxies	95
6.5	Number of simulations for each barred galaxy	96
6.6	Mean values of f_{abs} and f_{young} for each barred galaxy	109
6.7	Relations between sSFR and f_{young}	116
7.1	Model overview for NGC 1068	133

List of Abbreviations

AGB	Asymptotic Giant Branch stars
AGN	Active Galactic Nuclei
DGS	Dwarf Galaxy Survey
DL14	Draine & Li (2007) ; Draine et al. (2014) dust model
ETGs	Early-Type Galaxies
FIR	Far-Infrared regime
FITS	Flexible Image Transport System
FUV	Far-Ultraviolet waveband
HRS	<i>Herschel</i> Reference Survey
HSA	<i>Herschel Science Archive</i>
HST	<i>Hubble Space Telescope</i>
IMF	Initial Mass Function
IR	Infrared regime
ISM	Interstellar Medium
ISRF	Interstellar Radiation Field
KINGFISH	Key Insights on Nearby Galaxies: A Far-Infrared Survey with <i>Herschel</i>
KDE	Kernel Density Estimation
LMC	Large Magellanic Cloud
LTE	Local Thermal Equilibrium
LTGs	Late-Type Galaxies
MBB	Modified Black-Body emission
MIR	Mid-Infrared regime

List of Abbreviations

MW	Milky Way Galaxy
NIR	Near-Infrared regime
NLTE	Non-Local Thermal Equilibrium
NUV	Near-Ultraviolet waveband
PAH	Polycyclic Aromatic Hydrocarbon
PDR	Photo-Dissociation Regions
PSF	Point Spread Function
PTS	Python Toolkit for SKIRT
RSRF	Relative Spectral Response Function
RT	Radiative Transfer
SED	Spectral Energy Distribution
SFH	Star-Formation History
SFR	Star-Formation Rate
SMC	Small Magellanic Cloud
SP	Stellar Population
sSFR	Specific Star-Formation Rate
SSP	Single Stellar Population
submm	Sub-millimetre regime
S/N	Signal-to-Noise ratio
UV	Ultra-violet regime

List of Publications

Refereed

A. Nersesian, E. M. Xilouris, S. Bianchi, F. Galliano, A. P. Jones, M. Baes, V. Casasola, L. P. Cassará, C. J. R. Clark, J. I. Davies, M. Declair, W. Dobbels, I. De Looze, P. De Vis, J. Fritz, M. Galametz, S. C. Madden, A. V. Mosenkov, A. Trčka, S. Verstocken, S. Viaene, and S. Lianou, 2019, ‘Old and young stellar population in DustPedia galaxies and their role in dust heating’, [A&A, 624, A80](#)

A. Nersesian, S. Verstocken, S. Viaene, M. Baes, E. M. Xilouris, S. Bianchi, V. Casasola, C. J. R. Clark, J. I. Davies, I. De Looze, P. De Vis, W. Dobbels, J. Fritz, M. Galametz, F. Galliano, A. P. Jones, S. C. Madden, A. V. Mosenkov, A. Trčka, and N. Ysard, 2019, ‘High-resolution, 3D radiative transfer modelling III. The DustPedia barred galaxies’, [A&A, Forthcoming](#)

S. Viaene, **A. Nersesian**, J. Fritz, S. Verstocken, M. Baes, S. Bianchi, V. Casasola, L. P. Cassará, C. J. R. Clark, I. De Looze, P. De Vis, W. Dobbels, M. Galametz, F. Galliano, A. P. Jones, S. C. Madden, A. V. Mosenkov, A. Trčka, E. M. Xilouris, and N. Ysard, 2019, ‘High-resolution, 3D radiative transfer modelling IV. AGN-powered dust heating in NGC 1068’, [A&A, submitted](#)

S. Verstocken, M. Baes, **A. Nersesian**, S. Viaene, S. Bianchi, V. Casasola, C. J. R. Clark, J. I. Davies, I. De Looze, P. De Vis, W. Dobbels, F. Galliano, A. P. Jones, S. C. Madden, A. V. Mosenkov, A. Trčka, and E. M. Xilouris, 2019, ‘High-resolution, 3D radiative transfer modelling II. The early-type spiral galaxy M 81 and a modelling framework’, [A&A, submitted](#)

W. Dobbels, M. Baes, S. Viaene, S. Bianchi, J. I. Davies, V. Casasola, C. J. R. Clark, J. Fritz, M. Galametz, F. Galliano, A. V. Mosenkov, **A. Nersesian**, and A. Trčka, 2019, ‘Predicting the global far-infrared emission of galaxies via machine learning techniques’, [arXiv:1910.06330](#)

S. Bianchi, V. Casasola, M. Baes, C. J. R. Clark, E. Corbelli, J. I. Davies, I. De Looze, P. De Vis, W. Dobbels, M. Galametz, F. Galliano, A. P. Jones, S. C. Madden, L. Magrini, A. Mosenkov, **A. Nersesian**, S. Viaene, E. M. Xilouris, and N. Ysard, 2019, ‘Dust emissivity

and absorption cross-section in DustPedia late-type galaxies', [arXiv:1909.12692](https://arxiv.org/abs/1909.12692)

J. I. Davies, **A. Nersesian**, M. Baes, S. Bianchi, V. Casasola, L. P. Cassar, C. J. R. Clark, I. De Looze, P. De Vis, R. Evans, J. Fritz, M. Galametz, F. Galliano, A. P. Jones, S. Lianou, S. C. Madden, A. V. Mosenkov, M. W. L. Smith, S. Verstocken, S. Viaene, M. Vika, E. Xilouris, and N. Ysard, 2019, 'DustPedia: the relationships between stars, gas, and dust for galaxies residing in different environments', *A&A*, **626**, A63

M. Declair, I. De Looze, M. Boquien, M. Baes, S. Verstocken, D. Calzetti, L. Ciesla, J. Fritz, R. Kennicutt, **A. Nersesian**, and M. Page, 2019, 'Revealing the dust attenuation properties on resolved scales in NGC 628 with SWIFT UVOT data', *MNRAS*, **486**, 743D

M. Baes, A. Trcka, P. Camps, **A. Nersesian**, J. Trayford, T. Theuns, and W. Dobbels, 2019, 'The cosmic spectral energy distribution in the EAGLE simulation', *MNRAS*, **484**, 4069B

P. De Vis, A. P. Jones, S. Viaene, V. Casasola, C. J. R. Clark, M. Baes, S. Bianchi, L. P. Cassar, J. I. Davies, I. De Looze, M. Galametz, F. Galliano, S. Lianou, S. C. Madden, A. Manilla-Robles, A. V. Mosenkov, **A. Nersesian**, S. Roychowdhury, E. M. Xilouris, and N. Ysard, 2019, 'A systematic metallicity study of DustPedia galaxies reveals evolution in the dust-to-metal ratios', *A&A*, **623**, A5

A. V. Mosenkov, M. Baes, S. Bianchi, V. Casasola, L. P. Cassar, C. J. R. Clark, J. Davies, I. De Looze, P. De Vis, J. Fritz, M. Galametz, F. Galliano, A. P. Jones, S. Lianou, S. C. Madden, **A. Nersesian**, M. W. L. Smith, A. Trcka, S. Verstocken, S. Viaene, M. Vika, and E. M. Xilouris, 2019, 'Dust emission profiles of DustPedia galaxies', *A&A*, **622**, A132

S. Bianchi, P. De Vis, S. Viaene, **A. Nersesian**, A. V. Mosenkov, E. M. Xilouris, M. Baes, V. Casasola, L. P. Cassar, C. J. R. Clark, J. I. Davies, I. De Looze, W. Dobbels, M. Galametz, F. Galliano, A. P. Jones, S. Lianou, S. C. Madden, and A. Trcka, 2018, 'The fraction of bolometric luminosity absorbed by dust in DustPedia galaxies', *A&A*, **620**, A112

Submitted

V. Casasola, S. Bianchi, P. De Vis, L. Magrini, E. Corbelli, C. J. R. Clark, J. Fritz, **A. Nersesian**, S. Viaene, M. Baes, L. P. Cassar, J. I. Davies, I. De Looze, W. Dobbels, F. Galliano, A. P. Jones, S. C. Madden, A. V. Mosenkov, A. Trcka, and E. M. Xilouris, 2019, 'The ISM scaling relations in DustPedia late-type galaxies: a benchmark study for the Local Universe', *A&A*, *submitted*

Proceedings

A. Nersesian, S. Verstocken, S. Viaene, M. Baes 2019, 'High-resolution radiation transfer modelling of barred galaxies', IAU...PanModel2018, in press

Part I

Introduction

CHAPTER 1

About galaxies and their content

Cosmic dust. Seemingly insignificant in the grand scheme of things, yet so pivotal for the evolution of galaxies. Although it constitutes only but a small fraction of the interstellar medium (ISM), dust is ubiquitous. It was first revealed to us from images taken in the optical wavelengths of our Galaxy (Fig. 1.1), and of other galaxies, as dark regions along the galactic plane. The background, diffuse starlight is dimmed by clumps of dust (see Sect. 1.5.4), which lie in between the light sources and our line-of-sight. Dust grains are made of solid particles of varying sizes, ranging from 0.3 nm to 0.3 μm (mean radius 0.1 μm , Hildebrand 1983). Regardless of its relatively small abundance ($\lesssim 1\%$ of the ISM mass), dust has a major impact on galaxy physics. Dust causes the extinction of ultra-violet (UV) and optical ($\lambda < 1 \mu\text{m}$) starlight due to the fact that the size of the dust grains is of the same order as the wavelength of the radiation field. Furthermore, dust is heated by the different stellar populations, and re-radiates the absorbed stellar energy in the infrared (IR) wavelengths. A detailed knowledge of the dust heating mechanisms and dust properties are necessary to study the lifecycle of the ISM and galaxy evolution.

1.1 A galaxy's anatomy

Galaxies are gravitationally bound systems made of several building blocks: gas, stars, and dust (see Fig. 1.2). Much of the space between the stars is filled with atomic and molecular gas accounting for $\sim 99\%$ ($\sim 74\%$ of hydrogen in either molecular, neutral or ionised form, $\sim 24\%$ of helium, and $\sim 1\%$ of heavier elements) of the baryonic mass of a galaxy. Gas is the fuel that drives the formation of new stars in galaxies, and depending on the properties of the local environment, it manifests in different phases. The hot ionised phase takes place at the lowest densities, in which hot gas is produced by supernova explosions and gas temperatures can reach up to 10^7 K. Gas also appears in two warm phases; the warm neutral and warm ionised phase. Typical temperatures of the former phase are greater than 6000 K, while for the latter phase temperatures reach

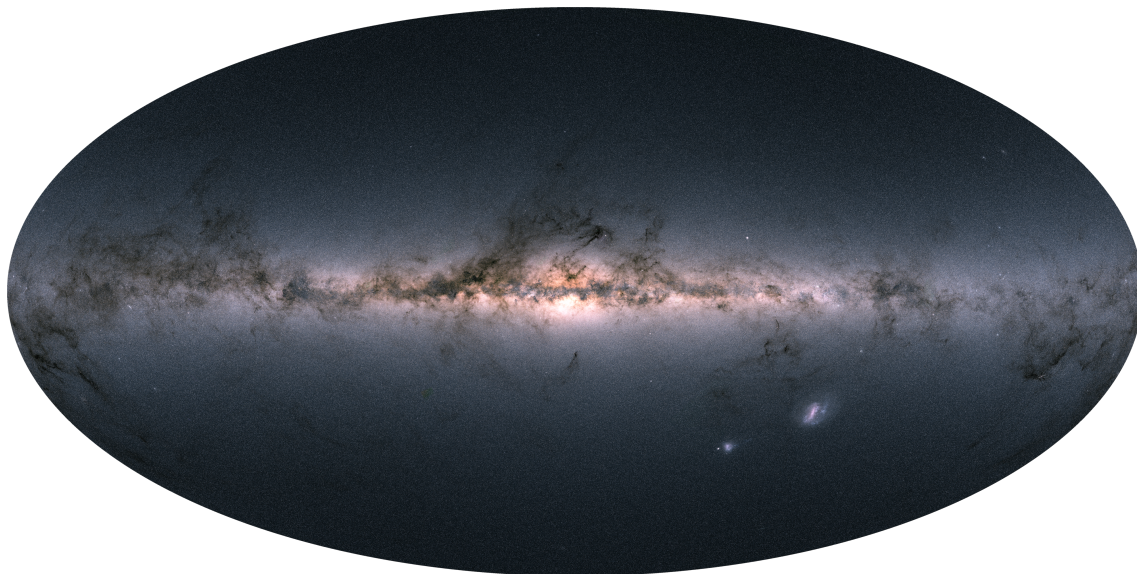


Figure 1.1: An all sky view map of the Milky Way (MW). The map is a composition of three other maps, combining the fluxes measured in the Gaia G, G_{BP} and G_{RP} photometric bands. Dust clouds cause the starlight-obscuration and appear as voids and rifts along the galactic plane. *Image Credit: ESA, Gaia, DPAC.*

as high as 8000 K. These two phases are associated with HI and HII regions, respectively. Eventually the gas cools down, it is distributed in dense filaments, and becomes part of the cold neutral medium (~ 100 K), traced by HI measured in absorption. Finally, at the most dense regions of the ISM, typical gas temperatures range from 10-20 K. These temperature conditions allow gases to transition to the molecular phase (H₂).

Stars are born in the dense, cold, molecular clouds that collapse due to their own internal gravity. In the stellar cores, gas is transformed into heavier elements through thermonuclear fusion. Stars are the primary source of radiation in galaxies, dominating the UV, optical and near-infrared (NIR) regions of the electromagnetic spectrum. Depending on the mass, age and metallicity (fraction of heavy elements) of a star, the wavelength of the peak of the emission shifts. Low-mass stars ($\leq 0.8 M_{\odot}$) radiate most of their energy in the NIR, intermediate stars (like our Sun) are brightest in the optical regime, whereas high-mass stars ($\geq 8 M_{\odot}$) live relatively short lives and dominate the UV spectrum. Likewise, the different stellar populations can be distinguished by their age and metallicity. Typically, old (metal-rich) stellar populations have a distinct red colour, since they are more luminous at longer wavelengths. On the other hand, young (metal-poor) stellar populations are relatively more luminous at shorter wavelengths, causing them to appear more blue.

The final and most relevant component for our research, is dust. Dust is made of small grains of various sizes, composed of a mix of heavy elements (for example, C, O, Si, Mg, Fe), which are available in the ISM (see Sect. 1.5.3). In fact, dust grains regulate many chemical and physical processes in the ISM (see Sect. 1.5.4). Dust is responsible for the extinction of background UV, optical, and NIR light, and the emission in the mid-infrared (MIR), far-infrared (FIR) and sub-millimetre (submm) regime. A more detailed



Figure 1.2: An image of M 51 (NGC 5194) and its companion NGC 5195 taken with *Hubble Space Telescope* (HST) in optical and near-infrared filters. The blue light originates from stars in its spiral arms, where young stars reside, and yellow light comes from its central core, a home of older, evolved stars. Stars are partially obscured by the dark dust features. Clouds of ionised gas are shown in bright pink colours. *Image Credit: NASA, ESA, S. Beckwith (STScI), and The Hubble Heritage Team (STScI/AURA).*

description of the properties and effects of dust is given in Sect. 1.5.

1.2 Galaxy classification and morphology

Galaxies come in different shapes and sizes. Their morphology is linked to the relative fraction of their main building blocks, described in the previous section. Despite the plethora of morphological types, it is still possible to group galaxies by shape, size or other properties. Edwin Hubble (1889-1953) classified galaxies into different categories depending on their visual appearance. The outcome of this classification was the famous ‘Hubble Tuning Fork’ or ‘Hubble diagram’ (Hubble 1982). de Vaucouleurs (1959) revised the tuning fork, and it is still widely used today to group galaxies. Figure 1.3 shows an example of such a classification with galaxies selected from the DustPedia (Davies et al. 2017) galaxy sample. The left side of the diagram (base of the fork) is occupied by galaxies that exhibit a smooth ellipsoidal shape, and have a distinct, featureless brightness profile (ellipticals; E). On the right side, the spiral galaxies were placed at the branches of the fork. They were divided according to their morphological characteristics

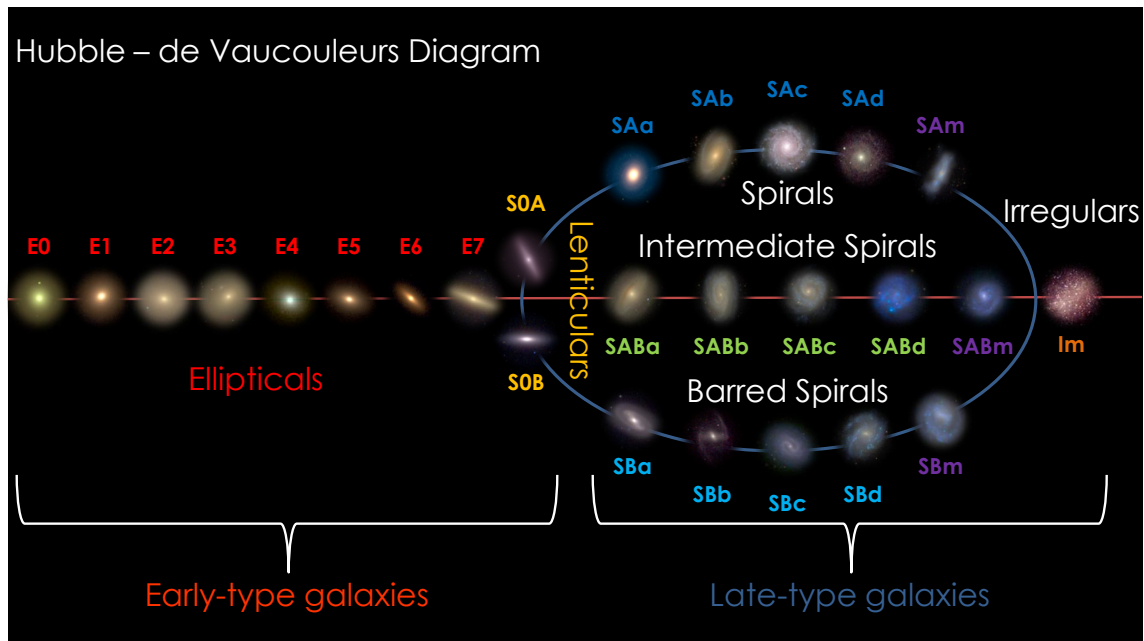


Figure 1.3: A ‘Hubble-de Vaucouleurs Tuning Fork’ with a selection of galaxies from the DustPedia (Davies et al. 2017) sample. The images are a compilation of the g , r , and i images taken from SDSS observations. Morphological classifications range from pure elliptical (E), lenticular (S0A, S0B) to spiral (SA, SAB, SAB) and irregular (Irr) morphologies. The letter ‘B’ infers the presence of a central bar structure.

to normal (SA), intermediate (SAB), and barred (SB) spirals. Finally, galaxies that do not have a specific structure, either elliptical or spiral, were put on the right edge of the fork (irregulars; Irr). The irregular shape of these galaxies is probably the result of a past or ongoing interaction with another galaxy. In the middle of the diagram, between elliptical and spiral galaxies there is another category called lenticulars (S0). These galaxies are some kind of hybrid since they exhibit a smooth brightness profile like the ellipticals, and a clear disk shape, but without a sign of spiral arms. The most likely explanation is that lenticular galaxies are in a transition phase between spirals and ellipticals.

Hubble erroneously thought that galaxies evolve from ellipticals to spirals. For that reason, he labelled elliptical and lenticular galaxies as early-type galaxies (ETGs) while spirals and irregulars as late-type galaxies (LTGs). In addition, de Vaucouleurs also assigned numerical values to each class of galaxy in his scheme. Values of the numerical Hubble stage T range from -5 to $+10$, with negative numbers corresponding to ETGs and positive numbers to LTGs (Table 1.1). Hereafter and throughout the text, we parametrize the galaxy morphology of the DustPedia sample by the Hubble stage (T), the values of which have been retrieved from the HyperLEDA database (Makarov et al. 2014)¹. A morphological classification in six main sub-classes (E, S0, Sa-Sab, Sb-Sc, Scd-Sdm, and Sm-Irr) is also used wherever specifically indicated.

In recent years, several studies have proposed different ways to categorise galaxies or have

¹<http://leda.univ-lyon1.fr/>

Table 1.1: Numerical Hubble Stage T .

	Numerical Hubble stage															
Hubble stage T	-5	-4	-3	-2	-1	0	1	2	3	4	5	6	7	8	9	10
de Vaucouleurs class	E	E ⁺	S0 ⁻	S0 ⁰	S0 ⁺	S0a	Sa	Sab	Sb	Sbc	Sc	Scd	Sd	Sdm	Sm	Irr
Hubble class	E		S0			S0a	Sa	Sa-b	Sb	Sb-c	Sc			Sc-Irr	Irr	

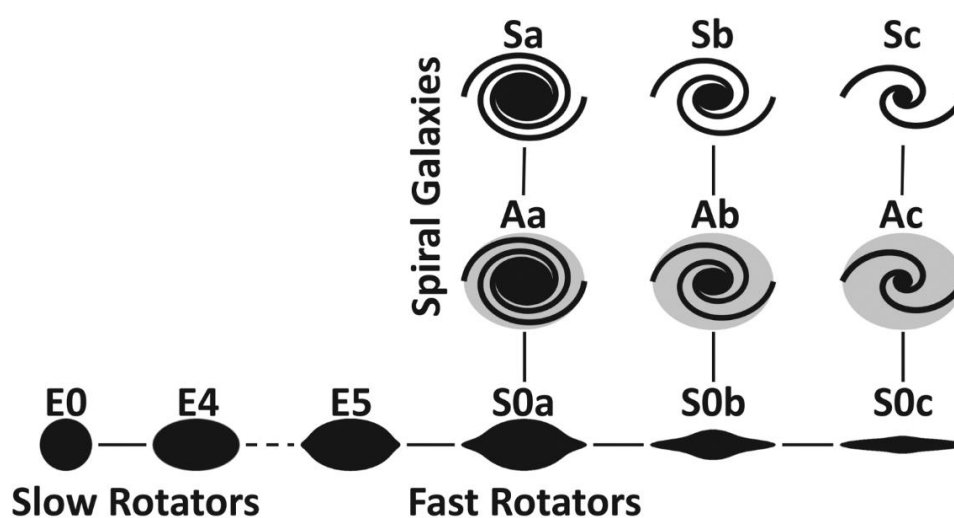


Figure 1.4: The ATLAS^{3D} ‘comb’ diagram. Based on their stellar kinematics, galaxies are divided in two main groups: slow rotators and fast rotators. Fast rotators are subdivided into three groups: lenticular (S0), anaemic (A), and spirals (S) galaxies. *Image Credit: Cappellari et al. (2011).*

tried to revision the ‘Hubble-de Vaucouleurs Tuning Fork’ in order to classify galaxies in a more natural and physically orientated way. For example, the ATLAS^{3D} project used a classification based on the kinematics of stars within galaxies. They grouped galaxies into two categories: fast rotators, with regular velocity fields, and slow rotators, with complex stellar velocity fields and often kinematically distinct stellar cores (see Fig. 1.4; Cappellari et al. 2011). The diagram resembles a ‘comb’, with ellipticals and lenticulars arranged on the handle, while spirals were placed along three teeth. Now, fast-rotating galaxies can be further divided by the status of their spiral structure. Thus, the class of fast-rotators includes bulge-dominated systems (lenticular galaxies), an intermediate stage called anaemic spirals, and a stage of fast-rotating spiral galaxies.

1.3 Galaxy formation and evolution

In the previous section we have outlined how galaxies can be classified according to different schemes. The various possible ways of classifying galaxies not only highlights their extreme diversity, but also provides significant insights into their formation and evolution through cosmic time. It is generally assumed that galaxy evolution is driven by two processes: star formation and merging events. A satisfactory theory on galaxy formation, that matches observations reasonably well, is the hierarchical structure formation model. In the primordial Universe, small objects made out of dark matter collapse to form haloes. As time goes by, these haloes would provide the gravitational potential wells necessary for the infall of baryonic matter (gas) and eventually the formation of disc-like proto-galaxies (White & Rees 1978). Stars drive the evolution of galaxies and act as cosmic factories, which convert the available gas into heavier elements through nuclear fusion. These heavier elements are the building blocks of cosmic dust in galaxies. Eventually, gas-rich proto-galaxies collapse due to their internal gravity, resulting to the formation of flattened disc structures. Due to the conservation of angular momentum, these systems rotate faster, and in combination with the feedback of stellar evolution, the formation of the spiral structures in galaxies becomes possible.

Merging events have a major impact on the evolution of galaxies. Galaxies have the ability to grow and evolve through the consumption of neighbouring galaxies (Springel et al. 2005), and by enriching their ISM with gas inflows. As galaxies age they interact more and more with their local environment, and therefore the galaxies we observe today should to some extent be a reflection of that environment. Numerical simulations are in favour of this scenario, indicating that the environment can have a large influence on the physical properties of galaxies (De Lucia et al. 2012; Wang et al. 2018). For example, the likelihood of galaxy interactions was much higher in the early days of the Universe, because it was significantly more dense than today and the distance between galaxies was shorter. In present day, merging interactions can often be observed between members of a galaxy cluster.

The process of star formation could either be activated or ceased by these merging interactions. Furthermore, mergers have the potential to severely fracture the galactic discs and cause disturbances to their rotation pattern. Thus, it is expected that events of such intensity could accelerate the evolution of disc galaxies towards bulge-dominated systems. Consequently, the distinct morphologies of galaxies we observe today, are the result of the relationship between environment and a galaxy's physical properties. A large fraction of ETGs lie in the centre of galaxy clusters, whereas LTGs are more in the outskirts (Oemler 1974). Dressler (1980) further confirmed that a relationship exists between the local galaxy density and the morphological mix of galaxies in clusters, i.e. environments of higher density lead to a larger fraction of early types. Both of these works made a comparison between galaxies that reside in clusters and those that lie in the general field.

Follow up studies have firmly established the strong correlation of the environment with many global physical parameters, such as the stellar mass, galaxy colour, star-formation rate (SFR) and gas content (Ostriker & Tremaine 1975; Dressler 1980; Giovanelli &

Haynes 1985; Kodama et al. 2001; Gavazzi et al. 2002; Kauffmann et al. 2004; Casasola et al. 2004; Baldry et al. 2006; Fumagalli et al. 2009; Peng et al. 2010). However, an open question still remains of whether this is an environmental effect or the result of the galaxy morphology density relation. In dense environments, such as clusters, the fraction of quiescent ETGs is greater than LTGs, which by definition have depleted most of their gas content and therefore have lower SFRs (Dressler et al. 1985). The galaxy population is clearly evolving with many less massive galaxies at high redshift and an apparent lack of the Hubble sequence beyond a redshift of 2 (Conselice et al. 2005; Buitrago et al. 2013). However, it is still not known whether morphology once obtained is fixed over a long period of time or whether morphological transformation occurs, and if so how many changes in morphology may occur (Conselice 2014).

Morphology does appear to be linked to other galaxy properties as well. For example more massive galaxies tend to be more spheroidal and star-forming galaxies tend to have more prominent discs (Gadotti 2009; Whitaker et al. 2015). Probably related to this is the high abundance of generally spheroidal red and/or gas deficient galaxies in higher density environments, particularly galaxy clusters (Visvanathan & Sandage 1977; Giovanelli & Haynes 1985) and the bimodality of the SFR. This bimodality leads to a clear distinction between galaxies that are actively star forming ('main sequence of star-forming galaxies'; Noeske et al. 2007), and those that are 'quenched' and their corresponding disc or spheroidal structure (Strateva et al. 2001; Blanton et al. 2005, see Fig. 1.5). These two populations are clearly evolving as the relative numbers of quenched galaxies has increased since a redshift of one (Tomczak et al. 2014).

With regard to the SFR of cluster galaxies compared to the field, the situation is less clear. There is evidence for the suppression of star formation in clusters when compared to the field, even when the morphological mix is taken into account (Kennicutt 1983; Dressler et al. 1985; Bamford et al. 2009). On the other hand the interaction of LTGs with the cluster environment may lead to enhanced star formation (Kennicutt et al. 1984; Moss & Whittle 1993). Willett et al. (2015) found no difference in the SFR- M_{star} relation for star-forming galaxies of different morphological types suggesting that galaxies are strongly self-regulated. Davies et al. (2019), investigated the role of the environment for a subset of the DustPedia galaxies (grouped into field and cluster members) by examining their stellar, dust and gas content. They found that the physical properties of galaxies of the same morphological type do not vary significantly with environment suggesting that the intrinsic properties of the galaxies are determined mainly by their internal physical processes.

Galaxy interactions have become more rare, due to the expansion of the Universe. A recent review of the star-formation history (SFH) of the observable Universe, showed that the present Universe is rather calm, and its most violent phases of galaxy evolution are left behind (Madau & Dickinson 2014). In fact, Madau & Dickinson (2014) confirmed that the star formation of the Universe peaked around redshifts 2-3, in line with previous results suggesting that the Universe had higher amounts of dust in the past (Dunne et al. 2011; Rowlands et al. 2014). Concerning the majority of nearby galaxies, they are actively star forming but at a slower rate than in the past, or the process of star formation has ceased altogether. Of course, galaxies that host an active galactic nuclei (AGN) or strong bursts of star formation still exist, but they are less common. Consequently, in

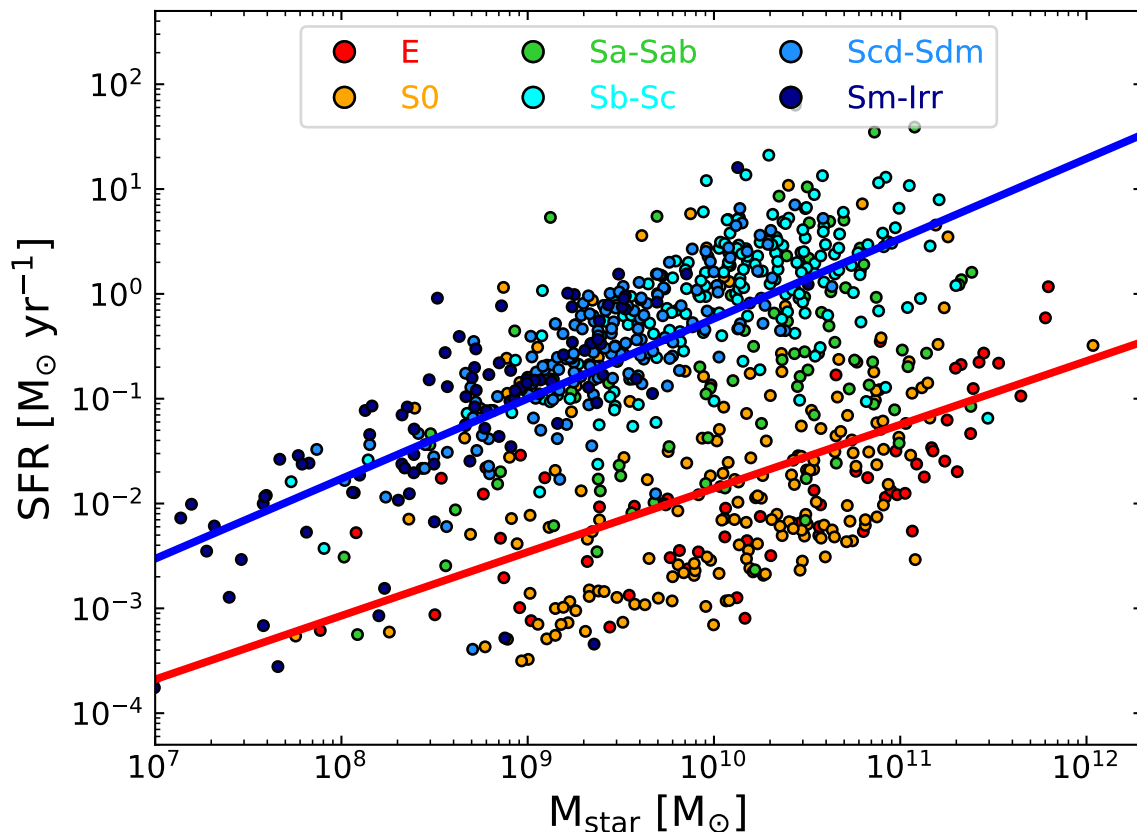


Figure 1.5: The ‘Main sequence’ for the 814 DustPedia galaxies defined by the stellar mass (M_{star}) and SFR. Galaxies are distinguished by their morphological type T into six groups. The thick blue line is the locus of the galaxy main sequence (star-forming galaxies) and the red line the locus of ‘non-star forming’ galaxies.

this study we examine the properties of nearby, ‘typical’ galaxies, because they are the most common objects in the local Universe.

1.4 The process of star formation

Atomic hydrogen is the most abundant element in the Universe. Depending on the phase of the gas, temperatures range from ~ 100 K (cold phase) to ~ 8000 K (warm phase). In the former case, the atomic hydrogen is converted into molecular hydrogen (H_2). Throughout the life of a galaxy, the ISM is enriched with heavy elements (metals), such as carbon and oxygen. These metals cool down the gas, allowing it to form dense regions of molecular structures within galaxies (Fig. 1.6). Young stars are forming out of these giant molecular clouds in interstellar space (usually referred to as ‘star-forming regions’), when they collapse under their internal gravity (Stahler & Palla 2005).

Although the process of star formation is qualitatively well understood (and summarised in Fig. 1.7), a handful of open questions still remain. For example, how gas cooling actually works, what are the exact mechanisms that initialise the collapse of molecular clouds, and how important are the roles of turbulence and magnetic fields. Quantitatively,



Figure 1.6: Newborn stars are forming in the Eagle Nebula. Gigantic pillars of dense gas and dust surround the newly-formed bright stars, the intense radiation of which is causing surrounding material to vaporise. This image, taken with the *Hubble Space Telescope* in NIR light, allows the viewer to see through much of the thick dust that makes the pillars opaque in visible light. The giant, pillar-shaped structures are dubbed informally as the *Pillars of Creation*. Image Credit: NASA, ESA, Hubble, HLA; Processing: Lluís Romero.

we can estimate how much star formation is to be expected from the gas surface density through the Kennicutt-Schmidt law (Schmidt 1959; Kennicutt 1998). The formation of new stars in galaxies depends on the amount of their gas content, and it may be triggered by internal events (e.g. supernova shock waves), as well as external events (e.g. mergers, tidal interactions).

When modelling galaxies, it is important to consider the stellar mass distribution in a newborn stellar population. A way to estimate the number of newly-formed stars is an initial mass function (IMF). Several IMFs exist and applied depending on the environment that galaxies find themselves within. For example, IMFs can vary from bottom-heavy (more low-mass stars are formed) to top-heavy (more high-mass stars are formed). Recent observations have shown that the IMF depends on metallicity (Marks et al. 2012) and star-formation density (Zhang et al. 2018). Among the most popular IMF models are those proposed by Salpeter (1955), Kroupa (2001), and Chabrier (2003). Throughout this thesis, we make use of both the Salpeter (1955) (bottom-heavy) and Chabrier (2003) (top-heavy) IMFs.

Star formation has a huge impact on the composition of the ISM in galaxies. First and foremost, a direct consequence of star formation is the consumption of a galaxy's gas content and its conversion into thermal radiation. Young ionising stellar populations emit most of their energy in the UV regime, acting as a first heating mechanism for the ISM. The production of high-energetic photons ($\lambda < 0.1 \mu\text{m}$) leads to the ionisation of hydrogen atoms (HII). Due to the emission from the recombination of the ionised gas,

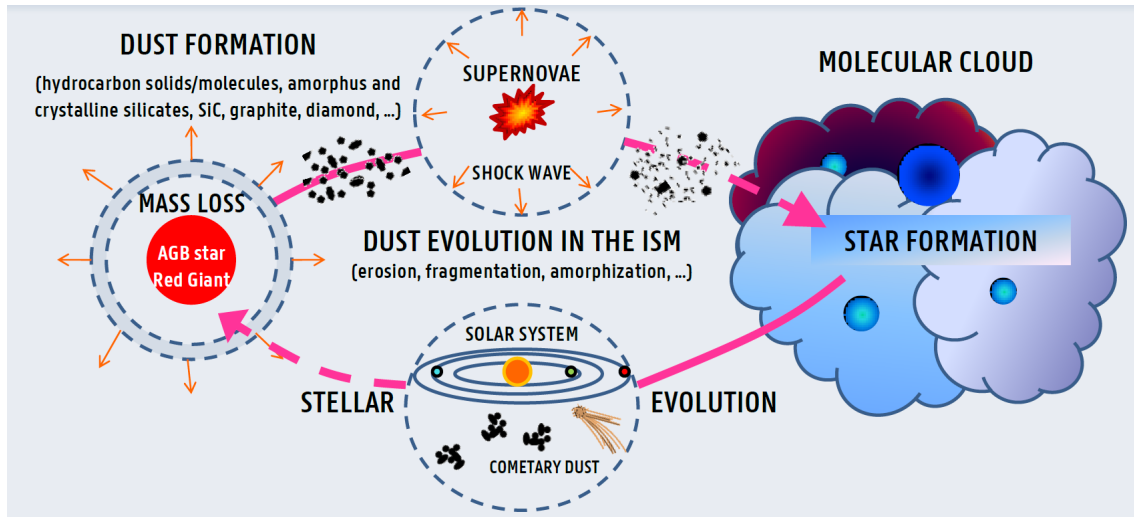


Figure 1.7: The life cycle of dust in the ISM.

it is possible to indirectly trace the star-formation rate. Stars evolve depending on their mass. Young, massive stars live fast and die young in violent supernova explosions. It is assumed that shocks generated by supernovae may trigger the collapse of the molecular clouds and hence activate the process of star formation. The extent of the role of supernovae does not stop there, since they are also responsible of enriching the gas with metals, which act as cooling agents of the gas.

Approximately 10 Myr after the birth of a new stellar population, young non-ionising stars dominate the radiation field of the whole population, still producing enough UV photons capable to warm up their surrounding environment. With the passage of time, the main sequence stars (intermediate and solar mass stars) will become the dominant sources of radiation, emitting most of their energy in the optical and NIR wavelengths. These kind of stars live long and act as a second heating mechanism for the ISM. Of course, a by-product of star formation is interstellar dust, which we will discuss in more detail in the following sections (see Sect. 1.5).

In conclusion, the process of star formation is quite crucial for the chemical evolution of a galaxy. Through that process, the immense amount of gas in the ISM transforms to a chemically rich and complex environment. Furthermore, star formation shapes the observed properties of a galaxy, and has severe consequences on their appearance. Therefore, one of the main topics of our research is to study the influence of light emitted from the different stellar populations on dust and vice versa.

1.5 Dust in galaxies

As we have already mentioned, dust is but a small fraction of the mass of a galaxy, yet it plays a crucial role in galactic evolution. It is on the surface of dust grains that molecules form, and dust grains help to prevent subsequent dissociation by high energy stellar photons. This gives rise to the giant molecular clouds which are such a prominent

component of the ISM in galaxies. Thus, the study of how much dust there is in a galaxy and how it interacts with the interstellar radiation field, forms a key part of any detailed study of galactic evolution, since the star-forming process is so fundamental. Dust can absorb up to 25%-30% of the starlight in LTGs, resulting in the observed attenuation and reddening effects at UV and optical wavelengths (Nersesian et al. 2019b; Bianchi et al. 2018; Viaene et al. 2016). The energy absorbed by dust, is then re-emitted in the MIR, FIR and submm wavelengths (Soifer & Neugebauer 1991). Although dust emission is often linked to the star formation (i.e. young stars of age < 100 Myr; Devereux & Young 1990; Buat & Xu 1996; Kennicutt 1998; Kennicutt et al. 2009), the contribution of the old stellar populations (i.e. stars of age > 2 Gyr) to the dust heating can be non-negligible (De Looze et al. 2014). It is, therefore, essential to decouple the effects of the relative contribution of the different stellar populations, and draw robust conclusions on their impact to dust heating.

Figure 1.7 schematically outlines the life cycle of dust. New dust is formed in the circumstellar shells of evolved stars, such as asymptotic giant branch (AGB) and red giant stars. Then, dust is released into the ISM through outflows during the final stages of stellar evolution, where it can be re-processed by shock waves from supernova events or by the strong diffuse radiation field. Finally, interstellar dust is concentrated into clouds that are then cooled down by their radiative processes. Cold, dense molecular clouds are quite important for the whole process of star formation, the growth of dust grains through coagulation, as well as the formation of comets, asteroids, and planets (e.g. Draine 2003; Dwek et al. 2009). The cycle commences again when the next generation of stars evolves off the main sequence.

1.5.1 Grain production

Over the years, several mechanisms have been proposed to explain the observable amount of dust in galaxies (e.g. AGB, red giants, M giants, etc.; Morgan & Edmunds 2003; Gail et al. 2009; Rowlands et al. 2014). The primary dust factories are the circumstellar shells around evolved stars. Small sized grains may form in the cool carbon-rich (Mattsson & Höfner 2011), and oxygen-rich (Norris et al. 2012) atmospheres of AGB stars. These kind of environments offer the perfect conditions for metals to get trapped into dust grains.

There is evidence of another dust production mechanism that occurs during supernovae explosions (Todini & Ferrara 2001; Gomez et al. 2012; Matsuura et al. 2015). Huge amount of material is ejected into the ISM during those events, including many heavy elements that can be converted into dust grains. By now, it is well established that core-collapse supernovae can produce large amounts of dust, quite efficiently (see e.g. Rho et al. 2009; Kamenetzky et al. 2013).

Furthermore, the ISM is enriched with metals due to stellar winds and supernovae. The ISM is a turbulent environment, so the chance for these elements to collide and stick together is quite high. The result of these collisions is the formation of complex molecules and eventually of small grains. Dust grains can build up and grow into larger sizes through grain coagulation (Ossenkopf 1993; Stepnik et al. 2003; Ormel et al. 2009;

Hirashita & Kuo 2011; Köhler et al. 2012, 2015).

1.5.2 Grain destruction

ETGs usually are low on dust content, or are even devoid of dust entirely. For example, Smith et al. (2012b) only detected dust in 24% out of a sample of 23 elliptical galaxies. The lack of dust in those systems could only mean one thing, that dust must have been destroyed somehow (for a review, see Jones 2004). Indeed, the ISM can be a violent and hostile environment. Dust is constantly bombarded with high-energetic particles (e.g. cosmic rays, atoms, ions, and electrons), that propagate through the ISM. This process is referred to as sputtering (see e.g. Jones 2004; Serra Díaz-Cano & Jones 2008; Bocchio et al. 2012, 2014). Moreover, shocks can further aggravate these violent collisions, by shattering the dust grains instead of coagulating them. Eventually, dust grains get destroyed over a time scale of few Myrs, depending on the environment (see e.g. Jones 2004; Bocchio et al. 2014). The fact that dust is still so abundant and visible in all active galaxies is actually a clear case for its efficient production, or less efficient dust destruction.

The dust destruction efficiency in supernova-triggered shock waves was recently re-estimated using the model developed by Jones et al. (2017) to evaluate the role of dust mantles, and to calculate the emission and extinction from shocked dust (Bocchio et al. 2014). Further constraints were put on the silicate destruction time, using hydrodynamical simulations (Slavin et al. 2015). The main conclusions of these studies are the following: (1) a-C(:H) grains are quickly destroyed, even in a slow propagating shock wave (50 km s^{-1}). This implies that the re-formation of carbonaceous dust in the dense regions of the ISM is a strong requirement. (2) Silicate grains appear to be more resilient, with a mean lifetime of $\sim 2\text{-}3 \text{ Gyr}$ (Slavin et al. 2015).

1.5.3 Grain populations

Dust grains in the ISM come in different sizes and chemical compositions. The first kind of dust expected to found in the ISM, are very small particles of elements heavier than helium (metals essentially). Metals such as carbon, oxygen, magnesium, silicon, sulphide, and iron are in abundance, and they can get trapped into dust grains. Due to their extremely small size, metals have discrete energy levels and therefore are not able to re-process the starlight continuum. On the other hand, abundant hydrogen and helium atoms can excite metals through collisional heating. In that way, metals act as cooling agents for the gas in the ISM, by radiating this collisional energy away.

Now, to explain the extinction in the UV and optical wavelengths, as well as the emission in the MIR and FIR regime, Desert et al. (1990) proposed an empirical dust model that contains three broad dust populations. Big grains make the first dust population. Big grains are quite efficient at absorbing and scattering radiation from the visible to NIR (a power-law NIR continuum, see Fig. 1.9). The grains can be made of silicates and/or carbon-dominated materials, with typical radii varying from 10 nm to 3000 nm, and a size distribution peaking at 150 nm (Zubko et al. 2004; Draine & Li 2007; Jones et al.

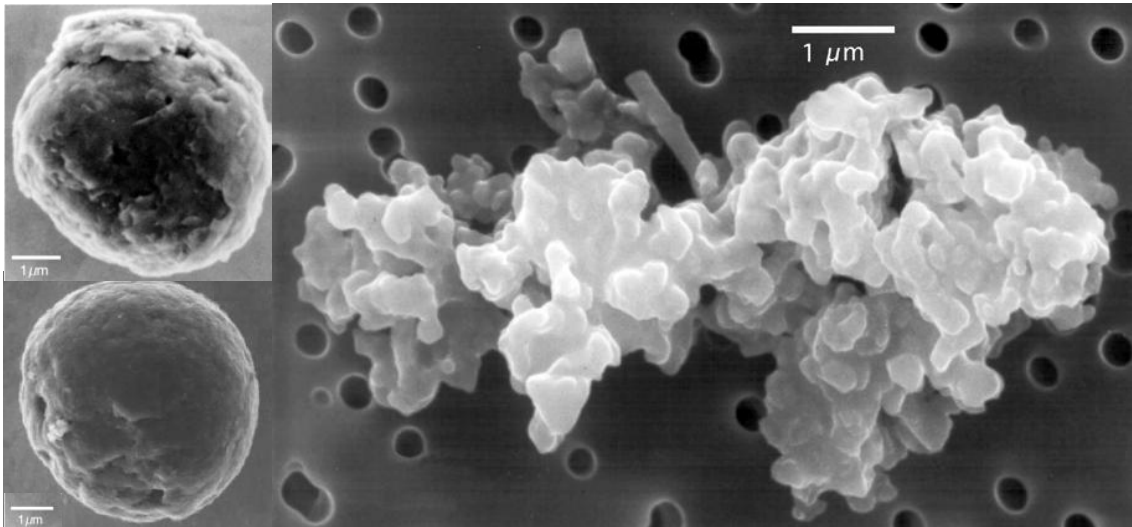


Figure 1.8: Images of dust grains from electron microscope scans. On the left side, two examples of spherical graphite grain are shown that were found in pre-solar meteorites (Clayton & Nittler 2004). *Image Credit: S. Amari.* On the right side, an example of a porous chondrite interplanetary dust particle is shown collected from Earth’s stratosphere. *Image Credit: D. E. Brownlee and E. Jessberger.*

2013, 2017). In the dense regions of the ISM, silicate grains can be enhanced with a mantle of ice or carbon particles around them, accreted through dust coagulation. Big grains are needed to explain the thermal equilibrium in the FIR.

The second dust population is that of small grains (typical radii 1 – 20 nm). In the early dust models, small grains were thought to be made of small graphite molecules. Although, rare pre-solar graphite grains exist in meteorites, follow up studies showed no evidence of graphite being the most abundant carbon dust material (Dartois et al. 2004b, 2005; Serra Díaz-Cano & Jones 2008; Compiègne et al. 2011). Other studies support that amorphous hydrocarbon grains appear to be a prominent dust component in the MW (e.g. Pendleton & Allamandola 2002) and in other galaxies (e.g. Dartois et al. 2004a).

The third and final population of dust is that of Polycyclic Aromatic Hydrocarbons or PAHs. PAHs are the smallest species of dust grains (typical radii < 1nm), and consist mainly out of aromatic molecules of hydro-carbonaceous nature. The peaks of emission in the MIR were entirely attributed to these kind of molecules (Smith et al. 2007; Tielens 2008). Alternatively, recent studies (Jones et al. 2013, 2017) suggested that other aromatic molecules, like the hydrocarbon solids (i.e., a-C:H and a-C, also known as HAC), could also be responsible for the MIR emission.

Small grains and PAHs are pure absorbers, responsible for: (1) the FUV rise in the extinction curve (Fig. 1.9), and (2) the bump feature in the extinction curve at 0.22 μm (Fig. 1.9). Both kinds of grains are heated stochastically, i.e a single energetic photon can excite a small grain to a higher state than its surrounding environment. In other words, these grains are not in local thermal equilibrium. Stochastic heating poses a difficult challenge to model accurately (Camps & Baes 2015).

If we put aside the chemical composition, dust grains come also in various shapes. When modelling dust grains, it is often assumed that their shape is spherical or spheroidal. Of course, this is a rough, first order approximation. Due to the different processes that take place in the ISM (radiative or collisional), it is expected that dust grains may be amorphous or ‘fluffy’. Figure 1.8 shows three examples of dust grains found in meteorites or on the Earth’s stratosphere. On the left images, dust grains have an almost spherical shape and these type of grains are considered to be pre-solar (Clayton & Nittler 2004). On the right side, an example of interplanetary dust is shown. It is rather porous or fluffy, and has a size larger than $1 \mu\text{m}$. This kind of grain is seemingly formed by the aggregation of other smaller sized particles. Unfortunately, we cannot have information about the composition of interstellar dust grains, and therefore dust models rely on empirical models. An additional caveat is that dust properties can vary from galaxy to galaxy, even within different regions of a particular galaxy (Declair et al. 2019). This caveat adds an extra factor of uncertainty on the use of a single dust model in galaxies, and extra care is needed when investigating dust in the local Universe.

1.5.4 Dust effects in galaxies

Our understanding of galactic structure is biased by dust. Dust is responsible for causing many effects which are pivotal for the evolution of a galaxy. As we already mentioned, short-wavelength photons ($\lambda < 0.4 \mu\text{m}$) interact with dust grains. Dust grains absorb and scatter UV and optical photons, resulting to the attenuation of the stellar spectrum. Actually, several studies have shown that dust attenuates roughly one third of the starlight (Nersesian et al. 2019b; Bianchi et al. 2018; Viaene et al. 2016; Skibba et al. 2011; Popescu & Tuffs 2002). In general, dust alters the observed intensity of a source of radiation either by absorbing or scattering out light from the line-of-sight of an observer, while it is still possible for radiation to be scattered into the line-of-sight.

The amount of radiation that is absorbed or scattered out of the line-of-sight of an observer by dust is referred to as extinction. As mentioned in the previous section, the extinction of UV and visible light depends on the intrinsic properties of dust grains (size and composition). For example, the probability of an incoming photon to be absorbed or scattered depends on the specific properties of dust grains such as the absorption coefficient and the scattering albedo. The absorption of photons by dust grains leads to their heating and their related emission, while scattering events cause the incident radiation to re-direct along different directions.

We can measure the extinction on the galaxy’s luminosity for the specific geometry of a star that lies behind a screen of dust. An extinction curve can only be measured for the MW, as well as for other nearby galaxies like, the Small Magellanic Cloud (SMC), Large Magellanic Cloud (LMC), or the Andromeda galaxy (M 31), where single stars can be resolved. An extinction curve shows the wavelength dependence of extinction (Fig. 1.9), and it is often characterised by strong FUV extinction, a UV bump feature at $0.22 \mu\text{m}$, and moderate extinction in the optical and NIR. In Fig. 1.9, it is evident that the extinction curves for the MW (Jones et al. 2013, 2017; Köhler et al. 2014), SMC and LMC (Gordon et al. 2003), have differences either in the global slope or in the UV

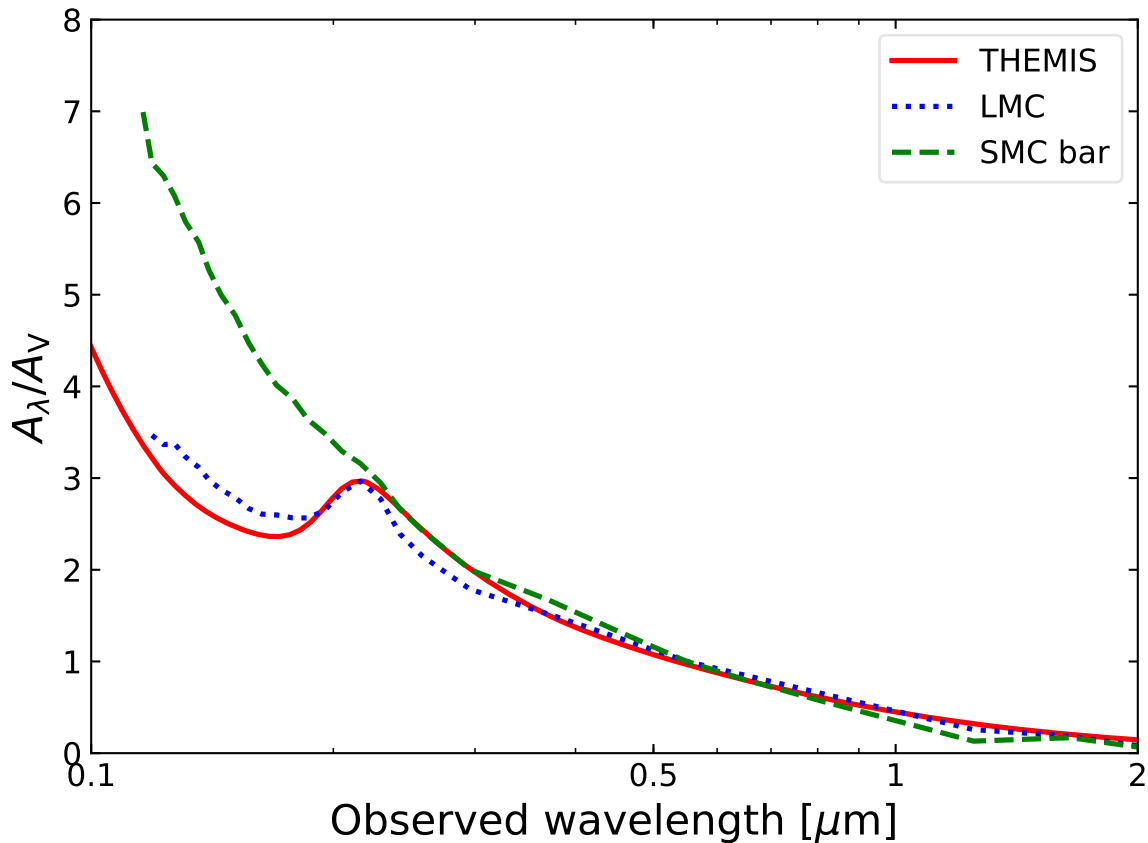


Figure 1.9: Examples of extinction curves. Wavelength-dependent extinction for the SMC (bar region) and LMC (average) from [Gordon et al. \(2003\)](#), and the average MW model from [Jones et al. \(2013, 2017\)](#); [Köhler et al. \(2014\)](#).

bump feature. This is a strong clue that dust properties vary from galaxy to galaxy, and even within galaxies ([Decleir et al. 2019](#)).

Dust attenuation refers to the net effect that dust has on the total spectrum of a galaxy. The term attenuation is generally used to describe a complex geometrical distribution, where the light sources are distributed within the dust, while the dust itself can be smooth, clumpy, or anything in between ([Calzetti 2013](#)). Compared to the extinction, attenuation includes two additional effects: (1) scattering of photons into the line-of-sight, and (2) sources extinguished by different columns of dust. Therefore, attenuation can be considered as the combined effect of extinction and the relative geometry of dust and stars. These two additional effects make the measurement of attenuation much more complex than for extinction. Despite the inherent difficulty, it is possible to calculate the attenuation curves from theory or by using radiation transfer simulations. Few examples of such attenuations are shown in Fig. 1.10 for a sample of nearby galaxies ([Verstocken et al. 2019](#); [Nersesian et al. 2019a](#); [Viaene et al. 2019](#)). Deriving realistic attenuation curves in galaxies is of great importance, leading towards accurate estimates of physical properties in galaxies like, the intrinsic stellar emission, stellar mass, age, metallicity, and SFR.

Beyond the extinction of stellar light, dust affects significantly many other physical or

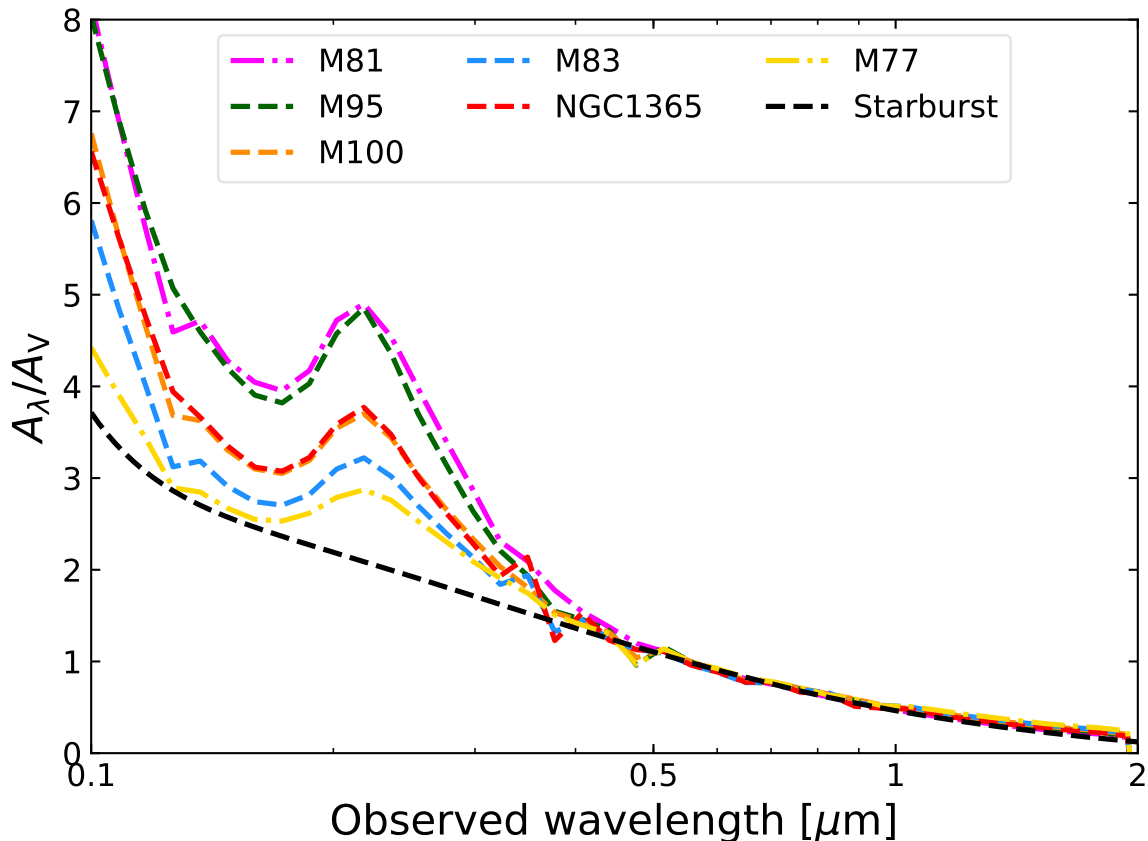


Figure 1.10: Examples of attenuation curves. Wavelength-dependent attenuation for a sample of nearby galaxies as determined from 3D radiation transfer simulations (Verstocken et al. 2019; Nersesian et al. 2019a; Viaene et al. 2019). The attenuation law for a sample of starburst galaxies from Calzetti et al. (2000) is given as well.

chemical processes in the ISM. Dust grains catalyse the formation of molecular hydrogen (H_2), an important ingredient of star formation. In the cold gas phase, hydrogen atoms can stick on a dust grain and merge to form H_2 molecules (Vidali et al. 2004; Bron et al. 2014). Besides their role as catalysts of H_2 , dust grains protect the already formed molecules (shielding) from the strong radiation field of young stars. This process allows the gas to cool down. However, high-energy photons may ionise the gas in the ISM. Then, the free electrons in the gas can interact with dust grains through the photoelectric effect, resulting in heating the gas (Croxall et al. 2012; Hughes et al. 2015). Last but not least, another effect caused by dust is polarisation. The *Planck* satellite mission (Planck Collaboration et al. 2011a) revealed that high levels of polarised emission originates from Galactic dust (Planck Collaboration et al. 2015) by acquiring highly sensitive submm observations. Dust grains align with the Galactic magnetic field leading the polarisation of starlight. The same grains that radiate polarised emission in the infrared and submm regimes also induce starlight polarisation in the optical, and thus the two effects are tightly coupled.

1.6 The SED of a galaxy

So far, we have shown that dust is a fundamental ingredient of the ISM, and a vital component for many processes that facilitate star formation. Without a doubt, the presence of dust defines how we see galaxies today. Hence, it is of uttermost importance to continuously improve our understanding about dust and how it interacts with light originating from different stellar populations, especially in different astrophysical environments. A reliable method to investigate the starlight-dust interaction, is to model the spectral energy distribution (SED) of a galaxy. As we discussed in Sect. 1.1, galaxies are an ensemble of multiple baryonic components (i.e. stellar populations, dust, ionised gas etc.). These components are not isolated, but they constantly interact with each another, both electromagnetically and gravitationally. In other words, the SED of a galaxy contains valuable information about the processes that drove its formation and evolution through cosmic times.

Modelling the SEDs of galaxies across the electromagnetic spectrum, still poses a difficult challenge. In the last decade, serious efforts have been made to create SED fitting codes that can model multi-wavelength datasets by enforcing an energy balance between the absorbed stellar energy and the thermal re-emission by dust at longer wavelengths. Codes such as CIGALE (Code Investigating GALaxy Emission; [Noll et al. 2009](#); [Boquien et al. 2019](#)) and MAGPHYS ([da Cunha et al. 2008](#)), among many others, employ a Bayesian analysis and make use of a plethora of libraries that account for the stellar and dust emission in galaxies. In particular, CIGALE is among the most popular codes in the community and has been applied in many studies (e.g. [Boquien et al. 2015](#); [Vika et al. 2017](#); [De Vis et al. 2017](#); [Buat et al. 2018](#); [Małek et al. 2018](#); [Bianchi et al. 2018](#); [Baes et al. 2019](#); [Declair et al. 2019](#)), providing information about the stellar and dust content, star formation, and dust attenuation.

The shape of the SEDs depends on the morphological type of a galaxy and the relative abundance of its components. Figure 1.11 presents three SED examples of galaxies of various types: a quiescent ETG (red line), a star-forming LTG (blue line), and a galaxy hosting an AGN (green line) ([Nersesian et al. 2019b](#)). The wavelength coverage of different space or ground-based telescopes is given as well. Stellar populations of different ages radiate energy in the UV-NIR regime, whereas dust reveals itself by emitting in the MIR-submm wavelengths. From this plot, it is evident that the SED of ETGs is dominated by emission from evolved stars and low dust emission, while the emission of young stars and dust is more prominent for the LTGs. Stellar populations are usually modelled as a single stellar population (SSP). The most popular SSP models are those developed by [Bruzual & Charlot \(2003\)](#) and [Maraston \(2005\)](#). An SSP template is created by assuming a specific IMF, a certain age and metallicity. Then, the SED of an SSP is computed based on emission models of the individual stars evolved in time. The result of this computation is the intrinsic emission of the stellar population.

As seen in Fig. 1.11, AGN emission can dominate the MIR and FIR regimes. A galaxy hosting an AGN has an additional source of UV-optical radiation (accretion disk) and FIR-submm emission (dusty torus around the accretion disk). Many studies (e.g. [Wu et al. 2007](#); [Bendo et al. 2012](#); [Kirkpatrick et al. 2012, 2015](#); [Verstappen et al. 2013](#);

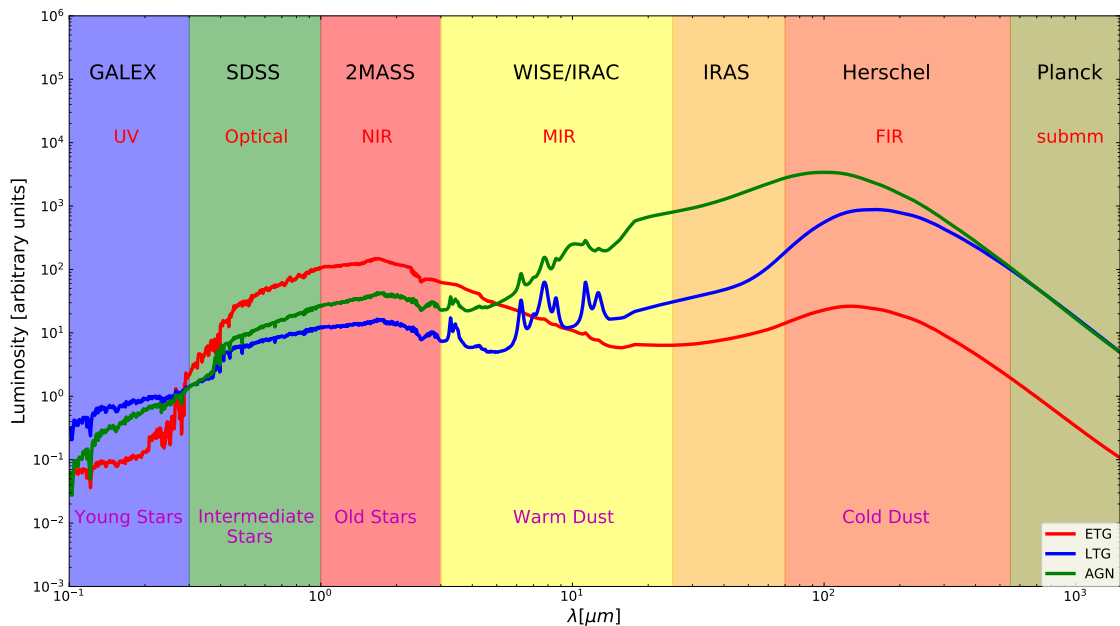


Figure 1.11: SED examples of different galaxy types.

Schneider et al. 2015; Roebuck et al. 2016) have presented evidence that AGN may have a significant contribution to the dust heating, even beyond the central regions of the galaxy. We investigate if this is true by creating a 3D radiative transfer model of NGC 1068 (see Chap.7). However, the bulk of local galaxies do not host AGN. For example, only 19% of the DustPedia galaxies host an AGN. Including the emission of the AGN in our sample by adding an extra SED component would increase the number of degeneracies between the properties the host galaxy and the AGN. With that in mind, we chose to study the global SEDs of galaxies without modelling the AGN contribution, so we can derive the intrinsic properties of the different stellar populations and cosmic dust (see Chap. 5).

In addition, gas in galaxies can be detected in emission, in the X-rays and radio wavelengths through processes such as synchrotron and bremsstrahlung radiation. Although gas can absorb the stellar radiation in discrete wavelengths, the effect is negligible compared to the continuous absorption caused by dust grains. Studying gas emission or absorption is beyond the scope of this investigation and we will no longer consider the effects of gas in our modelling. Therefore we limit our study to the UV-submm spectral region and investigate the interaction between the stellar radiation and dust (dust heating).

1.7 Radiative transfer

Another method to tackle the interplay between starlight and dust is through radiative transfer simulations. Several models are available in the literature trying to solve the radiative transfer problem for dusty systems. The problem is as follows: if a ray

of photons passes through matter, then energy may be added or subtracted from it by emission or absorption, respectively. Scattering of photons in and out of the beam significantly affects the intensity, making the radiative transfer problem even more complicated. Overall, a beam of light that covers a physical distance s , can be described by the static, panchromatic radiative transfer equation:

$$\begin{aligned} \frac{dI_\lambda}{ds} = & j_\lambda^{\text{star}} - \rho \kappa_\lambda^{\text{ext}} I_\lambda \\ & + \rho \kappa_\lambda^{\text{sca}} \int_{4\pi} I_\lambda \Phi_\lambda(\mathbf{k}, \mathbf{k}') d\Omega' \\ & + j_\lambda^{\text{dust}} \end{aligned} \quad (1.1)$$

where I_λ is the *specific intensity* or *brightness* at wavelength λ , j_λ^{star} represents the stellar emission, ρ is the dust density, $\kappa_\lambda^{\text{ext}}$, $\kappa_\lambda^{\text{abs}}$, and $\kappa_\lambda^{\text{sca}}$ are the extinction, absorption, and scattering coefficients of the dust with $\kappa_\lambda^{\text{ext}} = \kappa_\lambda^{\text{abs}} + \kappa_\lambda^{\text{sca}}$, $\Phi_\lambda(\mathbf{k}, \mathbf{k}')$ is the scattering phase function of the dust, and j_λ^{dust} is the thermal emission by the dust. This equation takes into account the physical processes of absorption, scattering, and thermal emission.

We are interested to uncover the properties of dust, and we are able to do so by looking at its emission. As previously mentioned, dust is heated by the diffuse stellar radiation and re-emits the absorbed energy in the IR regime. We can approximate the dust emission by assuming two main states: local thermal equilibrium (LTE) and non-local thermal equilibrium (NLTE). In the limit of LTE, large grains will reach a thermal equilibrium with their environment. In this case, dust grains will absorb the UV-optical radiation of the local interstellar radiation field (ISRF) and re-radiate at FIR-submm wavelengths as a modified black body (MBB; [Hildebrand 1983](#)). Therefore, j_λ^{dust} can be approximated with:

$$j_\lambda^{\text{dust}} = \rho \kappa_\lambda^{\text{abs}} B_\lambda(T_{\text{dust}}) \quad (1.2)$$

where $B_\lambda(T_{\text{dust}})$ is the Planck function, and T_{dust} is the average temperature of the bulk of the large dust grains.

In the case of NLTE emission, very small grains and PAHs are heated stochastically and their state can no longer be characterised by a single temperature. This type of emission dominates the MIR regime of a galaxy's spectrum. Calculating the NLTE emission spectrum of small grains is a difficult endeavour, especially for radiative transfer simulations. SED fitting codes deal with dust emission from stochastic heating by employing theoretical template spectra ([Dale et al. 2001](#); [Draine & Li 2007](#); [da Cunha et al. 2008](#); [Noll et al. 2009](#); [Boquien et al. 2019](#)). On the other hand, stochastic heating in radiative transfer simulations can be computed directly based on the intrinsic properties and size distributions of dust grains, along with the conditions of their local environment (see [Camps et al. 2015](#)).

Over the years, many different approaches have been constructed to tackle the radiative transfer problem. The first radiative transfer models of galaxies used forward radiative

transfer and simple analytical forms for the geometries between stars and dust (e.g. *screen* model, *slab* model, *sandwich* model, etc.). These kind of models were able to generate artificial images of galaxies, allowing for the investigation of dust attenuation in galactic environments (Witt & Gordon 2000; Baes & Dejonghe 2001). Furthermore, Disney et al. (1989) presented a review of those simple models. Thanks to the ever increasing computing power and development of new techniques, radiative transfer codes were able: (1) to test more complex geometries which stressed the importance of multiple stellar populations and clumping, (e.g. Misiriotis & Bianchi 2002; Gadotti et al. 2010; Pastrav et al. 2013a,b), and (2) to produce realistic 2D and 3D models of galaxies (e.g. Xilouris et al. 1999; Popescu et al. 2000; Steinacker et al. 2003; Bianchi 2008; Pinte et al. 2006).

Another interesting technique that is used to model the spectral and morphological appearance of galaxies is that of inverse radiative transfer. In this case, either an observed image or a set of images is used as a reference for the spatial distribution of stars and dust in a galaxy. Several teams led the way, applying this technique in edge-on spiral galaxies to study the extinction and scattering of optical light by the dust (Kylafis & Bahcall 1987; Xilouris et al. 1999; Bianchi 2007). Edge-on galaxies are excellent objects to study the effects of dust since it is clearly visible in extinction, and their geometry is quite simple. It is typical to model edge-on galaxies by assuming a simple exponential disk composed by dust and stars, and a central Sérsic bulge (Sérsic 1963) made of stars.

In the last decade, even more nuanced geometries were introduced to model edge-on galaxies which gave new insights in the distribution and mass of dust in edge-on spirals (e.g. Bianchi 2008; Baes et al. 2010b; De Looze et al. 2012b,a, and references therein). An interesting outcome noted in many studies of edge-on galaxies, is the notorious *dust energy balance* problem (Bianchi et al. 2000; Misiriotis et al. 2001; Bianchi 2008; Baes et al. 2010b; De Geyter et al. 2015; Mosenkov et al. 2016). Due to the assumed dust energy balance, the absorbed energy in the UV-optical regime should match the re-emitted energy in the FIR-submm wavelengths. However, the FIR emission predicted by the radiation transfer models underestimates the observed measurements by a factor of 2-4 (Misiriotis et al. 2001; De Geyter et al. 2015; Mosenkov et al. 2016). The reason behind this is the lack of information about the actual stellar and dust distributions in edge-on galaxies. It is possible to solve this problem if we consider face-on galaxies. Indeed, De Looze et al. (2014) constructed a 3D radiative transfer model of NGC 5194 (M 51), by considering multiple stellar components (young ionising stars, young non-ionising stars, and old stars), and one dust component. The distribution of each component was derived from observed images, while the 3D feature was added by deprojecting them and by applying an exponential vertical profile. The authors of this study were able to reproduce the observed FIR-submm emission. We present the method developed by De Looze et al. (2014) and perfected by Verstocken et al. (2019) in Sect. 2.3.

1.8 This thesis

As mentioned earlier in this chapter, dust in LTGs is responsible for absorbing approximately one third of the energy emitted by stars. It is often assumed that dust heating is

mainly attributable to the absorption of UV and optical photons emitted by the youngest (≤ 100 Myr) stars. Consequently, thermal re-emission by dust at FIR is often linked to the star-formation activity of a galaxy. However, several studies argue that the contribution to dust heating by much older stellar populations might be more significant than previously thought. The goal of this thesis is to investigate the properties of cosmic dust and its interaction with stellar radiation (originating from different stellar populations), in a variety of galactic environments. Our analysis covers both global and local scales in nearby galaxies.

Specifically, we take advantage of the DustPedia sample (Davies et al. 2017) of galaxies. The DustPedia project² contains the largest sample of nearby galaxies (875 galaxies), all observed by the *Herschel Space Observatory*. In Part II, we present the essential modelling tools that were used for the purposes of this investigation. We aim to determine the global properties of the DustPedia galaxies, such as the dust and stellar mass, the SFR, the bolometric luminosity, and the attenuation levels for both the old (> 200 Myr) and young (≤ 200 Myr) stellar populations. We are also interested to determine, for the first time, the contribution and the efficiency of the different stellar components to dust heating, in galaxies of various morphological stages. Towards that goal, we explore the capabilities of panchromatic SED fitting (Part III), by employing the widely used fitting code CIGALE, properly adapted to include the state-of-the-art dust model THEMIS.

Furthermore, we have developed a framework to construct detailed 3D stellar and dust radiative transfer models for nearby galaxies. In this study, for the first time, we aim to analyse the contribution of the different stellar populations to the dust heating in four nearby face-on barred galaxies: NGC 1365, M 83, M 95, and M 100 (see Chap. 6). Our goal is to quantify the fraction directly related to young stellar populations, both globally and on local scales, and to assess the influence of the bar on the heating fraction. It is also our goal to measure the effect of diffuse dust heating by AGN (beyond the torus). To this end, we focus on NGC 1068 and we try to fit a realistic model to its observations, as well as to quantify the contribution of the several dust heating sources (see Chap. 7). In Part V, we present our main conclusions.

²See Sect. 2.1 for the full characteristics of the sample.

The DustPedia project

DustPedia¹ is a EU-FP7 funded project aiming to exploit existing observations of nearby galaxies, all having been observed at FIR and submm wavelengths by the *Herschel Space Observatory*. These observations are publically available from the *Herschel Science Archive* (HSA). The ambitious goal of the project was to provide definitive answers about the properties of cosmic dust in the local Universe, and to develop a coherent interpretation of recent state-of-the-art observations, particularly those that are now available after the successful *Herschel Space Telescope* mission (Pilbratt et al. 2010). Complementary observations various wavelengths from numerous other databases, were combined with those from HSA, extending the wavelength range from the UV to radio.

2.1 The DustPedia sample of galaxies

The DustPedia sample consists of 875 nearby galaxies with recessional velocities of $< 3000 \text{ km s}^{-1}$ (or within ~ 40 Mpc of the Sun), all observed by *Herschel* (Pilbratt et al. 2010). Galaxies at that distance can be considered ‘local’, yet still reside far enough that the larger-scale structure and hence different galactic environments are satisfactorily sampled. The sample includes galaxy-members of the Virgo, Fornax, and Ursa Major clusters, as well as ‘field’ galaxies that lie at the Super-Galactic plane (see Fig. 2.1). Furthermore, objects were primarily selected according to their stellar mass. The best indicator of stellar mass is the flux density in NIR wavelengths (Eskew et al. 2012; Meidt et al. 2014). Consequently, galaxies were chosen with a WISE 3.4 μm signal-to-noise ratio (S/N) > 5 . An additional requirement was the inclusion of galaxies with large

¹<http://www.dustpedia.com>. Dustpedia is a collaborative focused research project supported by the European Union under the Seventh Framework Programme (2007-2013) call (grant agreement no. 606847). The participating institutions are: Cardiff University, UK; National Observatory of Athens, Greece; Ghent University, Belgium; Université Paris Sud, France; National Institute for Astrophysics, Italy and CEA, France.

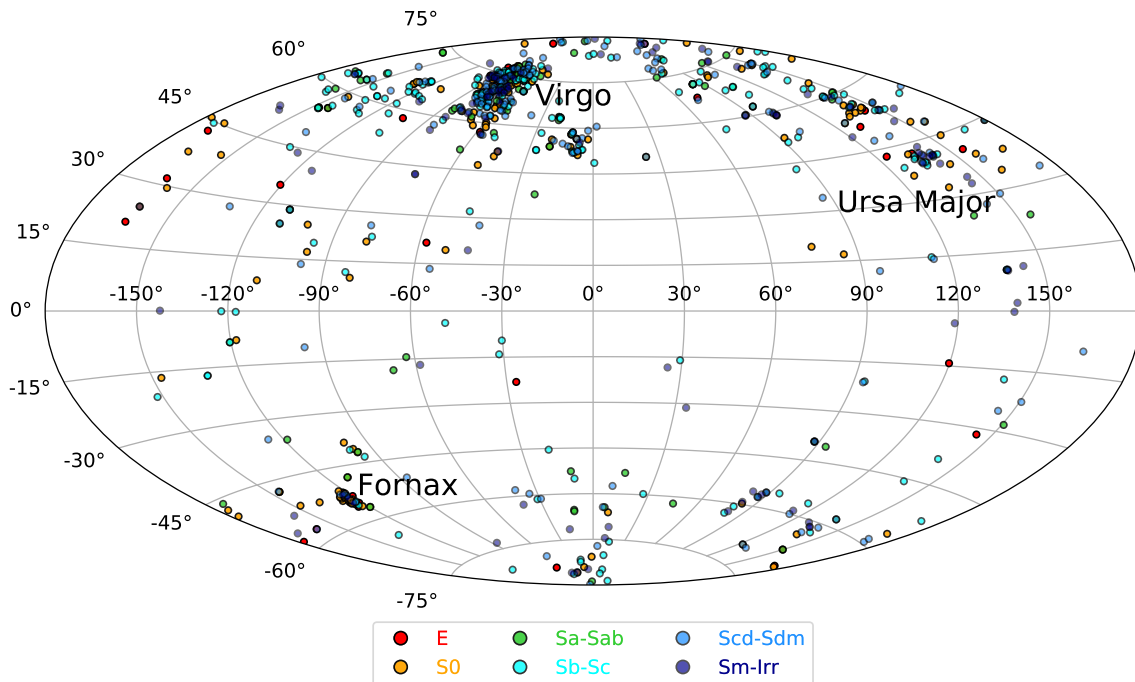


Figure 2.1: Spatial distribution of galaxies in Galactic coordinates but plotted so that for $l > 180^\circ$ the plotted value is $l - 360^\circ$.

optical diameters $D_{25} > 1'$. Finally, studying the very large angular-size local group galaxies like M 31 (and its companions), M 33, LMC, and SMC was outside the scope of the project, given the very different nature of working with such extended systems.

Moving on to the photometry, imaging data is available in the DustPedia archive². These datasets are a combination of images observed by ground-based and space telescopes: GALaxy Evolution eXplorer (GALEX; [Morrissey et al. 2007](#)), Sloan Digital Sky Survey (SDSS; [York et al. 2000](#); [Eisenstein et al. 2011](#)), 2 Micron All-Sky Survey (2MASS; [Skrutskie et al. 2006](#)), Wide-field Infrared Survey Explorer (WISE; [Wright et al. 2010](#)), *Spitzer* ([Werner et al. 2004](#)); *Herschel* ([Pilbratt et al. 2010](#)); InfraRed Astronomical Satellite (IRAS; [Neugebauer et al. 1984](#)); and *Planck* ([Planck Collaboration et al. 2011a](#)), covering a broad wavelength range from the UV to the submm wavelength domain. The DustPedia archive contains aperture-matched estimates for 875 galaxies. A new pipeline was developed within the project to carry out the aperture-matched photometry for all observations (up to 41 bands from the FUV to the submm wavelengths). The pipeline is called CAAPR (Comprehensive & Adaptable Aperture Photometry Routine [Clark et al. 2018](#)), and it was designed to produce uniform and consistent photometry as well as cross-compatible uncertainty calculations for all bands. An example of the final aperture for a given source, applied to all bands, is shown in Fig. 2.2 for NGC 3198.

²<http://dustpedia.astro.noa.gr>

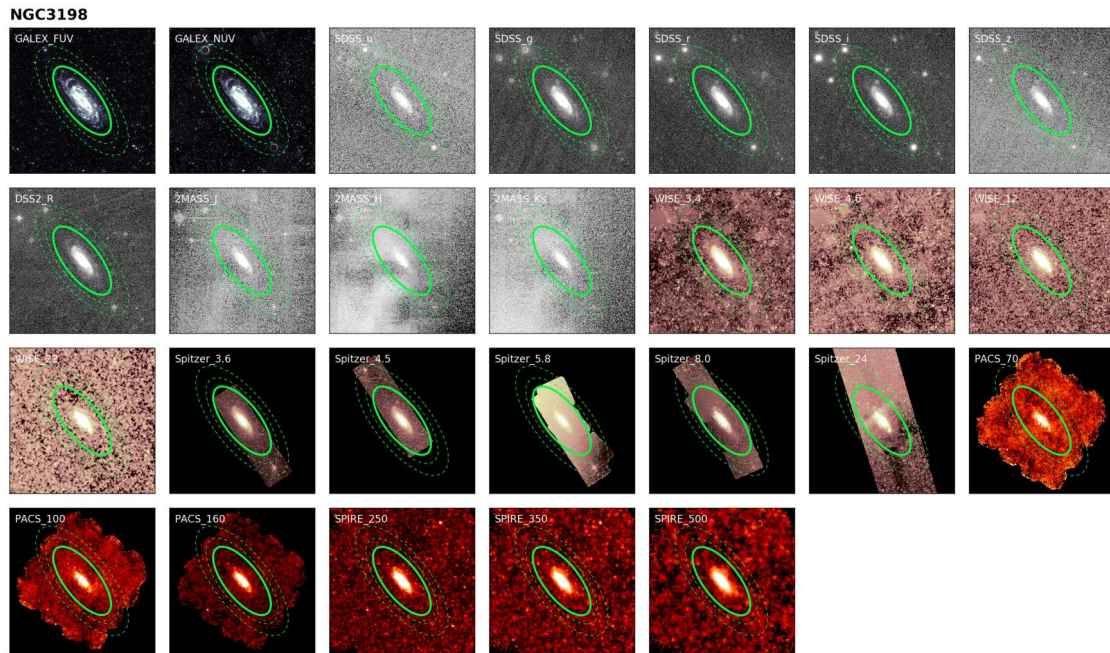


Figure 2.2: Multi-band images of NGC 3198 depicting the apertures used for photometry. The solid lines show the main aperture, while dashed lines denote the background annulus. *Image Credit: Clark et al. (2018)*

2.2 THEMIS: a new global physical dust model

One of the many ambitious goals of the DutPedia project was to develop a self-consistent, unifying, and global dust modelling framework. This framework is called THEMIS (The Heterogeneous Evolution Model for Interstellar Solids Jones et al. 2017). THEMIS advantage over other dust models is that is based upon laboratory-measured properties of interstellar dust analogue materials, such as amorphous hydrocarbon and amorphous silicate materials (Jones et al. 2013, 2014). Special care was taken to consider how the chemical composition, shape and dust-size distribution of these materials evolve in a self-consistent manner within a given region of the ISM, as it continuously interacts with the its local environment (Bocchio et al. 2012, 2013, 2014; Jones et al. 2013, 2014; Jones & Habart 2015; Köhler et al. 2015). In particular, accretion and coagulation or irradiation are processes that can directly alter the optical properties of dust, i.e. the absorption and scattering cross-sections. Figure 2.3 shows a schematic representation of the different evolution stages of dust particles and the associated grain compositions, following a transition towards denser regions of the ISM.

THEMIS successfully explains the observed FUV-NIR extinction and the shape of the IR to mm dust thermal emission. The model has also been successfully compared to the latest available estimates of the diffuse ISM dust extinction and emission in the MW (Ysard et al. 2015; Fanciullo et al. 2015). Furthermore, it is able to predict the observed relationship between the $E(B-V)$ colour excess and the inferred submm opacity derived from *Planck*-HFI observations (Ysard et al. 2015; Fanciullo et al. 2015).

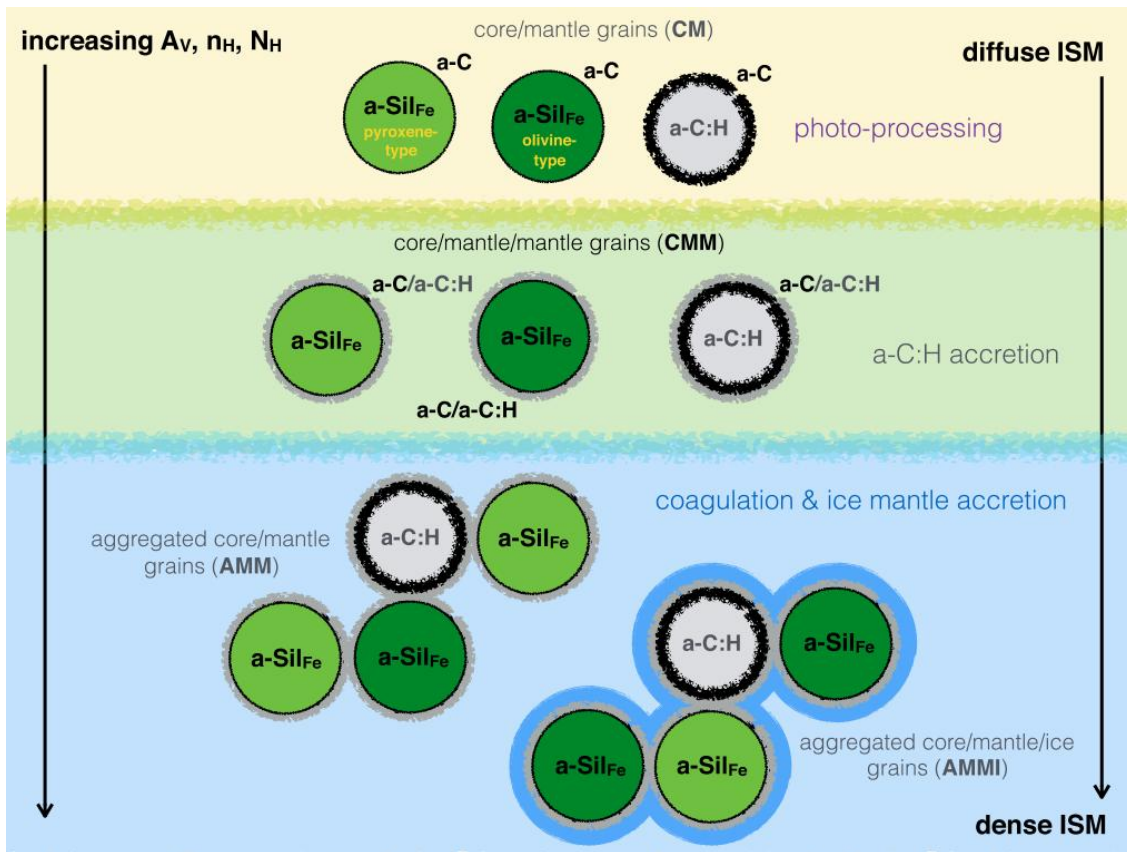


Figure 2.3: Schematic of dust properties in the THEMIS dust model. *Image Credit: Jones et al. (2017).*

2.3 The radiative transfer modelling framework

Within the scope of DustPedia (Davies et al. 2017), we have constructed a framework for creating high-resolution, 3D radiative transfer models of nearby face-on galaxies based on observations. In this framework, we have put together several modelling tools into a software package called PTS³ (Python Toolkit for SKIRT⁴; Verstocken et al. 2019). PTS is designed to manage the observed images of a large sample of face-on galaxies, and to create their 3D radiative transfer models, with consistency and reproducibility in mind.

With PTS, it is possible to pre-process the observed images of a galaxy, using an automatic procedure as developed in our modelling framework. First, PTS identifies the foreground stars from the 2MASS All-Sky Catalog of Point Sources (Cutri et al. 2003), and it removes them from the GALEX, SDSS, 2MASS, WISE, and *Spitzer* images. Then, a correction is applied to all images for background emission and Galactic extinction. Furthermore, depending on the position of the modelling galaxy, PTS determines the attenuation in the UV bands from the V-band attenuation (A_V ; obtained by querying

³http://www.skirt.ugent.be/pts8/_p_t_s.html

⁴<http://skirt.ugent.be>

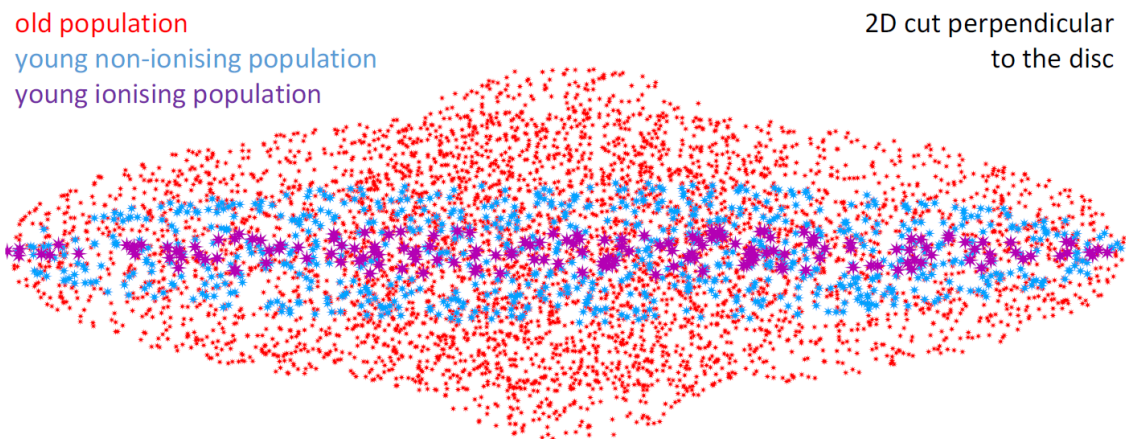


Figure 2.4: Schematic of the standard geometric model of spiral galaxies adopted by the framework. The old stellar population (> 100 Myr) consists of a bulge and a disc component. The young stellar population (100 Myr) resides in a thinner disc compared to the old stars, and the young ionising population (10 Myr) is concentrated to the mid-plane of the galaxy. The dust distribution exhibits the same vertical extent as the young non-ionising stellar population. *Image Credit: Verstocken et al. (2019).*

the IRSA Dust Extinction Service⁵), and by assuming an average extinction law in the MW, $R_V = 3.1$ (Cardelli et al. 1989).

After the preparation stage, images are ready to be used as input geometries for the 3D model. In particular, different images are combined to produce physical maps that represent the distribution of the dust or the various stellar populations within the galaxy. The modelling strategy that we apply is presented in Verstocken et al. (2019), and is the following. First, we build a 3D model for a galaxy, assuming several stellar components and a dust component. We define three stellar populations based on their group of age: an old stellar population (bulge and disc), a young non-ionising stellar disc, and a young ionising disc. The standard model with three distinct stellar populations is depicted in Fig. 2.4 (Verstocken et al. 2019).

To be more specific, the old stellar population contains stars of age > 100 Myr. To retrieve the distribution of the old stellar population in the disc a bulge-to-disc decomposition needs to be performed, using the InfraRed Array Camera (IRAC; Fazio et al. 2004) $3.6 \mu\text{m}$ image. $3.6 \mu\text{m}$ emission is indicative of the older, more evolved stars in the galaxy. The bulge is modelled with a flattened Sérsic profile and the total luminosity is fixed such that it corresponds to the bulge luminosity. The decomposition parameters of the Sérsic geometry are available in the S⁴G database (Spitzer Survey of Stellar Structure in Galaxies: Sheth et al. 2010; Salo et al. 2015), for 2,300 nearby galaxies. Then, the old stellar population disc is obtained by subtracting the bulge from the total observed $3.6 \mu\text{m}$ emission. For this procedure it is assumed that the contribution from the young non-ionising and young ionising stellar populations, as well as the contamination from dust emission in the central region is negligible.

⁵<https://irsa.ipac.caltech.edu/applications/DUST>

To get the distribution of the young non-ionising stellar population in the disc (100 Myr), the GALEX FUV image is used, since young stars dominate this particular spectral range. To retrieve the intrinsic FUV emission of the young stars, a correction is applied for dust attenuation, by employing a FUV attenuation map and a total infrared (TIR) map, based on the prescriptions of Cortese et al. (2008) and Galametz et al. (2013), respectively. A correction was also applied for the UV light emitted by the old stellar population. Regarding the young ionising stellar population in the disc (10 Myr), a Multiband Imager for *Spitzer* (MIPS; Rieke et al. 2004) 24 μm image is combined with an $\text{H}\alpha$ map (if it is available), relying on the prescription derived by Calzetti et al. (2007). The MIPS 24 μm image was also corrected for emission originating from old stars. Finally, the diffuse dust component in the disc is constrained through the FUV attenuation map, while for the dust composition the DustPedia reference dust model THEMIS⁶ (Jones et al. 2013, 2017; Köhler et al. 2014) is used.

The next step is to de-project these 2D maps on the sky to a 3D distribution. To create the 3D distribution of the disc components an exponential profile of different scale heights (h_z) is assigned to each one of them, based on previous estimates of the vertical extent of edge-on galaxies (De Geyter et al. 2014). Then a dust grid is generated based on the dust component map through which the photons propagate in the simulations. Apart from the geometrical distribution, for each stellar component an intrinsic SED and a total luminosity is assigned, that is either fixed or a free parameter in the model. The different combinations of the free parameters generate a 3D radiative transfer simulation that takes into account the emission of the different stellar components as well as the absorption, scattering and thermal re-emission by dust. The output of each simulation includes the SED of the galaxy and a set of broadband images that can directly be compared to the observed images. Additional information is also available: images of the galaxy at any viewing angle and any wavelength can be retrieved, and most importantly the effects of the interaction between the ISRF and the diffuse dust can be studied in 3D. Global luminosities are distributed on the 3D pixels (voxels) according to the density distributions as prescribed by the physical maps. Figure 2.5 summarises the general 3D radiative transfer modelling framework we have adopted. It shows the key steps that are involved in the modelling, such as the image preparation, the map making, the decomposition, and the fitting steps.

⁶https://www.ias.u-psud.fr/themis/THEMIS_model.html

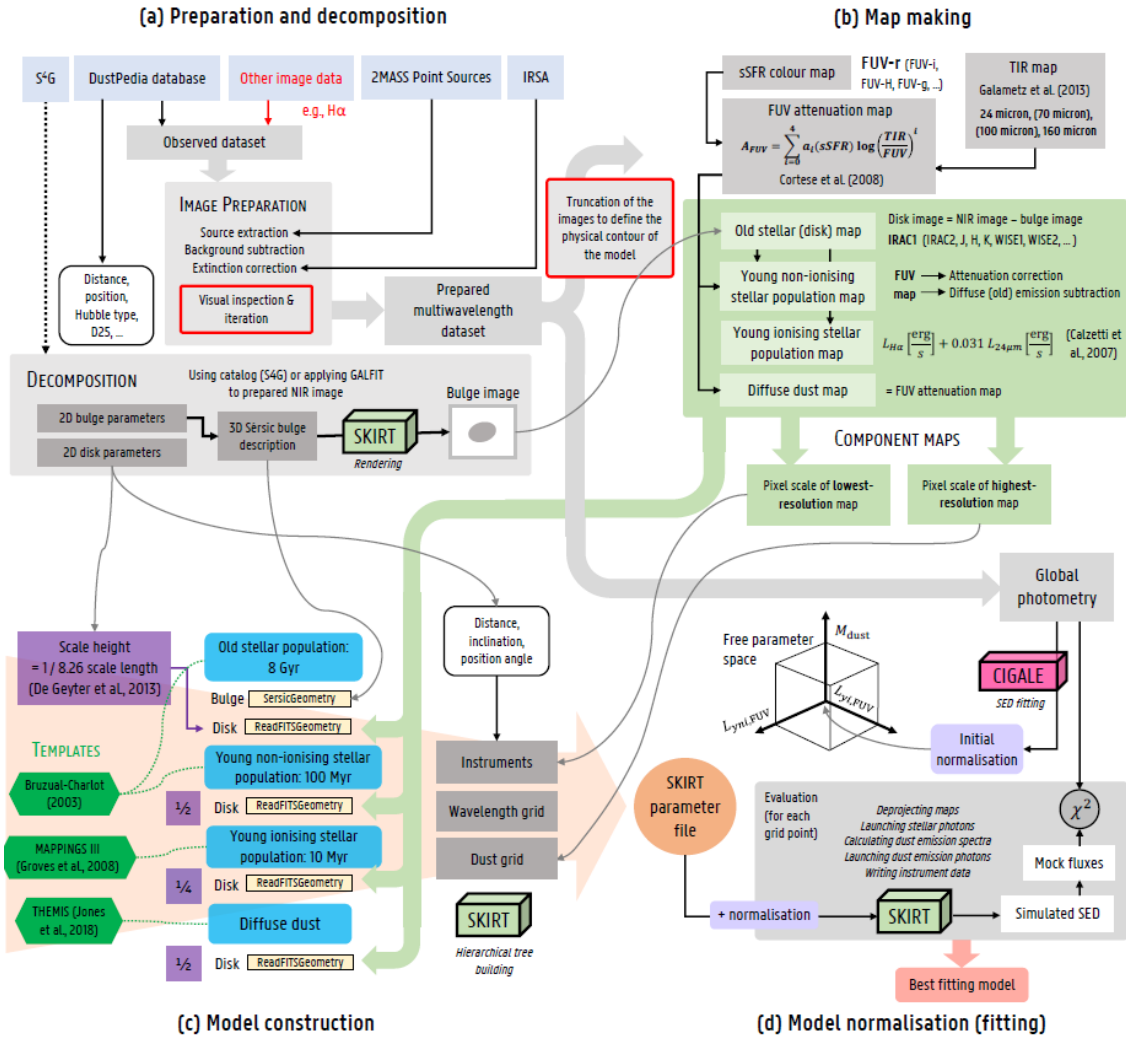


Figure 2.5: Schematic of the radiation transfer modelling framework, as implemented in PTS. Image Credit: Verstocken et al. (2019).

Part II

Astrophysical modelling tools

Fitting the SEDs with CIGALE

CIGALE¹ (Noll et al. 2009; Boquien et al. 2019), is an SED-modelling tool that allows the user to build galaxy SEDs (in the UV to the submm wavelength range) assuming energy conservation between the energy absorbed by the dust and the energy emitted by stars. The SED reconstruction is made by assuming appropriate stellar population libraries for the emission of different stellar populations (e.g. Bruzual & Charlot 2003; Maraston 2005), an IMF (e.g. Salpeter 1955; Chabrier 2003), and a SFH. The dust emission puts constraints on the assumed dust attenuation law (e.g. Calzetti et al. 2000; Charlot & Fall 2000), and the grain emission parameters (Draine & Li 2007; Draine et al. 2014; Dale et al. 2014; Jones et al. 2017). In addition, nebular line and continuum emission are also included in the UV-NIR wavelength range (Inoue 2011), while the contribution of an AGN in the UV, optical and IR can be modelled from various libraries (e.g. Fritz et al. 2006; Casey 2012; Dale et al. 2014). Finally, a module exists to fit the synchrotron radio emission, relying on the radio-IR correlation (Helou et al. 1985). Figure 3.1 depicts a schematic of the general workflow of CIGALE for performing the SED fitting and for estimating the integrated parameters.

3.1 Assumptions on the SFH

To model the SED of a galaxy with CIGALE, a parametric SFH must be assumed. Several types have been proposed (and described with simple analytic functions) to account for the evolution of the stellar content of the galaxies with time. In Ciesla et al. (2015), three SFHs (an exponentially decreasing SFH (1τ -dec) of e-folding time τ , a combination of two exponentially decreasing SFHs (2τ -dec) and a delayed SFH) are discussed and compared with simulated SFHs from GALFORM SAM (Cole et al. 2000) concluding that the delayed SFH is the better choice for estimating SFR, M_{star}

¹<https://cigale.lam.fr>; v2018.0

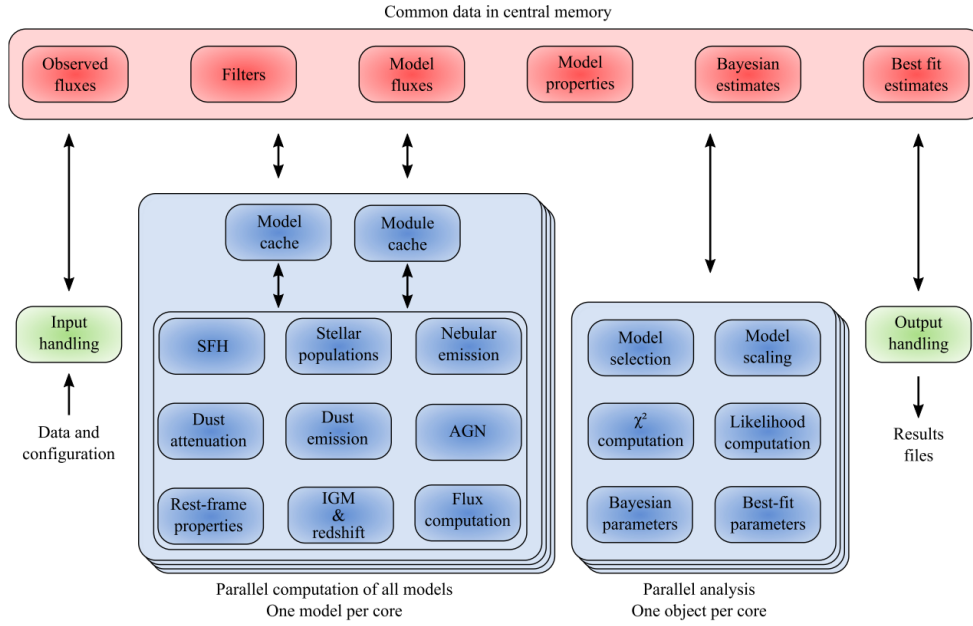


Figure 3.1: A schematic representation of CIGALE's workflow for SED fitting and parameter estimation. *Image Credit:Boquien et al. (2019)*

and age of galaxies. Recently, [Ciesla et al. \(2016, 2017\)](#) suggested that a flexible-delayed SFH is able to accurately describe both field and cluster spirals as well as galaxies with recent starburst activity or SFR decline. Four parameters are used to describe the specific type of SFH, namely the e-folding time of the main stellar population model (τ_{main}), the age of the oldest stars in the galaxy (t_{gal}), the age of the significant drop or rise in the star-formation activity (t_{flex}), and the ratio r_{SFR} of the SFR after quenching or bursting over the SFR at the time of t_{flex} of the star-formation. The SFR as a function of time is then given by:

$$\text{SFR}(t) \propto \begin{cases} t \times \exp(-t/\tau_{\text{main}}) & , \text{ for } t \leq t_{\text{flex}} \\ r_{\text{SFR}} \times \text{SFR}(t = t_{\text{flex}}) & , \text{ for } t > t_{\text{flex}} , \end{cases} \quad (3.1)$$

([Ciesla et al. 2016, 2017](#)). The SFH implemented in CIGALE is the combination of two stellar components resembling an old and a young stellar population. The two populations roughly represent a burst or quench of star-formation in addition to a more passively evolving stellar component. The old stellar component is modelled with an exponentially decreasing SFR with various values of the e-folding rate τ_{main} and age t_{gal} . The young stellar component consists of a burst or decline of constant star-formation starting at time t_{flex} whose amplitude is adjustable and scaled with the ratio r_{SFR} . In what follows, SFR refers to the current SFR (see Equation 3.1). The stellar spectrum of a galaxy is then calculated by convolving the assumed SSP with the SFH, assuming an IMF and a metallicity.

3.2 Dust attenuation laws

Dust is quite efficient at absorbing short-wavelength radiation and then re-radiating this energy back in the MIR and FIR. The energy balance principle lies at the core of CIGALE, hence the attenuation needs to be properly modelled. Several studies showcased that attenuation in galaxies comes in a large variety (e.g. [Lo Faro et al. 2017](#); [Buat et al. 2018](#); [Salim et al. 2018](#); [Decleir et al. 2019](#)). Therefore, attenuation laws need to be flexible to adopt the observations. CIGALE utilises two methods of computing the attenuation: (1) the age-dependent attenuation model of [Charlot & Fall \(2000\)](#), and (2) a flexible attenuation law inspired by the starburst curve of [Calzetti et al. \(2000\)](#).

In our investigation we used the latter. The stellar and nebular emissions are attenuated using a power-law-modified starburst curve ([Calzetti et al. 2000](#)), extended with the [Leitherer et al. \(2002\)](#) curve:

$$A(\lambda) = (A(\lambda)_{\text{SB}} \times (\lambda/550 \text{ nm})^\delta + D_\lambda) \times \frac{E(B-V)_{\delta=0}}{E(B-V)_\delta}, \quad (3.2)$$

([Noll et al. 2009](#); [Boquien et al. 2019](#)), where D_λ is a Lorentzian-like Drude profile modelling the UV bump at 217.5 nm in the attenuation curve, with δ being a free parameter modifying the slope of the attenuation curve and the last term in Equation 3.2 being an attenuation-reduction factor for the old stellar population (older than 10 Myr).

3.3 Implementing THEMIS to CIGALE

Various models have been developed for interstellar dust during the last few decades. Two widely used examples are the silicate-graphite-PAH model ([Desert et al. 1990](#); [Siebenmorgen & Kruegel 1992](#); [Dwek et al. 1997](#); [Li & Draine 2001, 2002](#); [Draine & Li 2001, 2007](#); [Draine et al. 2014](#)) and the silicate-core carbonaceous-mantle model ([Desert et al. 1990](#); [Jones et al. 1990](#); [Li & Greenberg 1997](#)). The latter model has recently been updated resulting in the THEMIS² dust model ([Jones et al. 2013, 2017](#); [Köhler et al. 2014](#)). THEMIS was built upon the optical properties of amorphous hydrocarbon and amorphous silicate materials that have been measured in the laboratory ([Jones 2012a,b,c](#); [Jones et al. 2013, 2017](#); [Köhler et al. 2014](#)). Within this framework, dust is mainly comprised of large carbon-coated amorphous silicate grains and small hydrocarbonaceous grains. The primary goal of the model is to explain the nature of dust in the diffuse ISM.

CIGALE includes numerous model libraries to fit the dust emission in galaxies. Among those models are the models of [Draine & Li \(2007\)](#); [Draine et al. \(2014, hereafter DL14\)](#), and the dust model of [Dale et al. \(2014\)](#). Within the DustPedia framework, we modified CIGALE accordingly to include THEMIS as a separate module for the dust emission parameters. Our approach to generate the template files is similar to the DL14 model.

²https://www.ias.u-psud.fr/themis/THEMIS_model.html

We compute the moments of the average starlight intensity U using a delta function component and a power-law distribution:

$$\begin{aligned} \langle U \rangle = & (1 - \gamma) \int_{U_{\min}}^{U_{\min} + \Delta U} U \times \delta(U_{\min} - U) dU \\ & + \gamma \int_{U_{\min}}^{U_{\min} + \Delta U} U^{1-\alpha} \times \frac{\alpha - 1}{(U_{\min}^{1-\alpha} - U_{\max}^{1-\alpha})} dU, \text{ for } \alpha \neq 1, \end{aligned} \quad (3.3)$$

([Draine & Li 2007](#)), where γ is the fraction of the dust heated in PDRs. We created a library of templates based on three parameters: (1) the mass fraction of aromatic feature emitting grains, q_{hac} (i.e., a-C(:H) smaller than 1.5 nm), (2) the minimum intensity value of the stellar radiation field that heats the dust, U_{\min} , and (3) the power-law index, α . U_{\min} shares the same parameter space as the DL14 model (0.1-50), with an additional upper limit for THEMIS at $U_{\min} = 80$ to cover the most extreme cases, whereas α is fixed to two in both cases. The maximum cutoff for the starlight intensity distribution, U_{\max} , is fixed at 10^7 . The small a-C(:H) component has the same effect as the PAH component in the DL14 model. In the diffuse Galactic ISM, $q_{\text{PAH}} = 7.7\%$ ([Compiègne et al. 2011](#)), and $q_{\text{hac}} = 17\%$ ([Jones et al. 2017](#)). The only difference between a-C(:H) and PAHs is a scaling factor between the two quantities: $q_{\text{PAH}} \sim q_{\text{hac}}/2.2$. Finally, in order to retrieve the total dust mass from the SED templates we normalise with $M_{\text{dust}}/M_{\text{H}} = 7.4 \times 10^{-3}$ ([Jones et al. 2017](#)).

3.4 Deriving the integrated properties of galaxies

CIGALE uses a Bayesian analysis to derive the galaxy properties. The modelled SEDs are integrated into a set of filters and compared directly to the observations. The observations are assigned with an extra 10% uncertainty (added quadratically to the measured uncertainty) to allow for unknown systematic errors in the photometry of the object and the model (see [Noll et al. 2009](#)). For each parameter, a probability distribution function (PDF) analysis is carried out. Given the observed SED of a galaxy, CIGALE derives the posterior probability distribution of the physical parameters. The posterior probability is simply the dot product of the prior, that is, the probability of a model being used before fitting the data, and the likelihood that the data match the model created by the parameter grid. The result of the analysis is the likelihood-weighted mean value of the PDF while the associated error is the likelihood-weighted standard deviation ([Boquien et al. 2019](#)). Figure 3.2 illustrates few SED examples of DustPedia galaxies fitted with CIGALE (see results and analysis in Chap. 5).

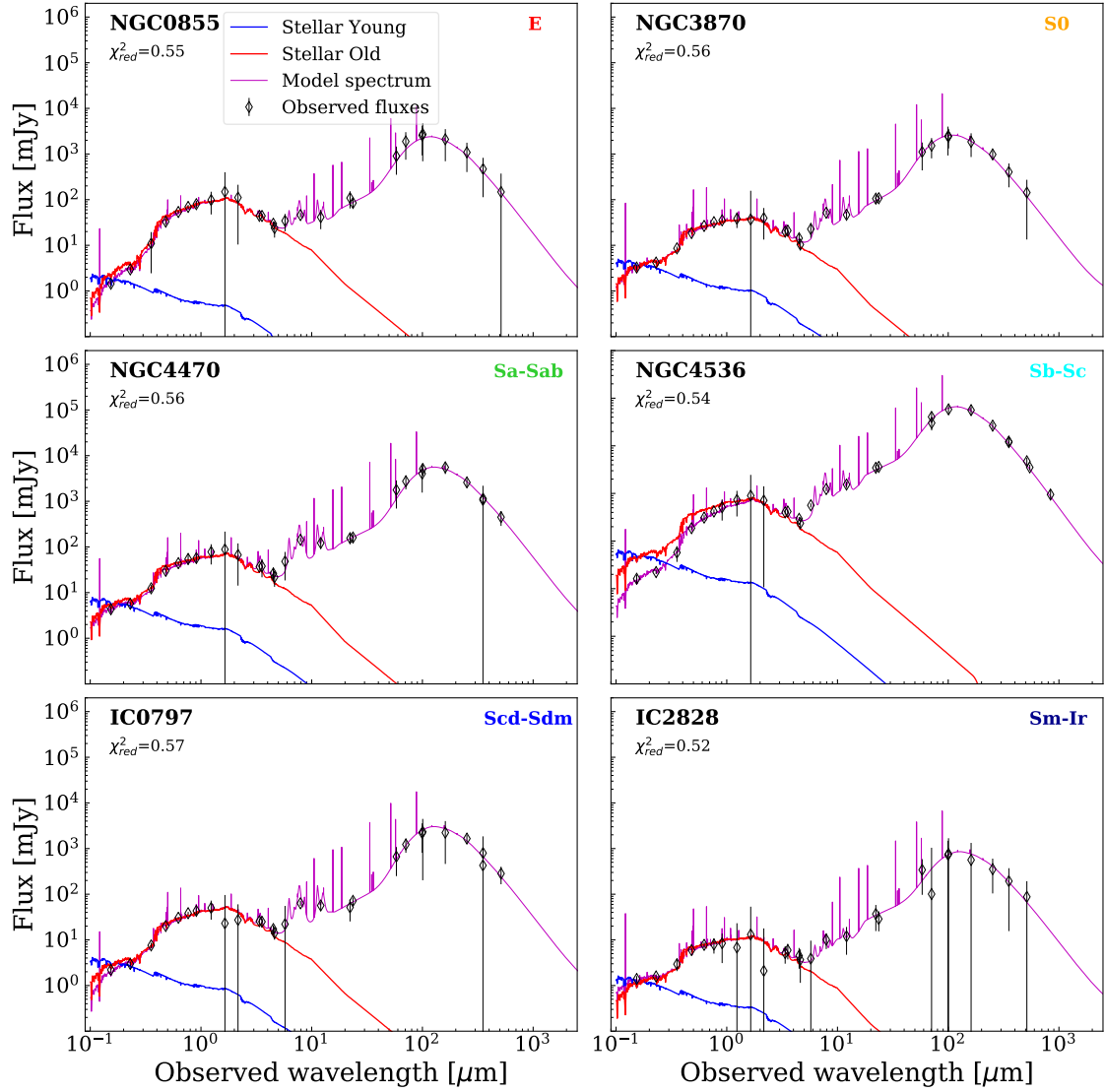


Figure 3.2: Examples of best SED models as derived by CIGALE fitting (Nersesian et al. 2019b). This figure depicts galaxy SEDs according to their respective morphological group. Diamond symbols are the observations. The blue and red lines show the intrinsic luminosity of the young and old stellar populations, respectively. The magenta line is the total SED model as computed by CIGALE.

Radiative transfer modelling with SKIRT

To generate a 3D radiative transfer model simulation for a given galaxy, we used the code SKIRT¹ (Baes et al. 2011; Camps & Baes 2015). SKIRT is a state-of-the-art radiative transfer code that allows the construction of 3D panchromatic models by using a Monte Carlo approach. The code is designed in a way that it can take into account all relevant physical processes such as scattering, absorption, and thermal re-emission by dust, for a wide variety of environments. SKIRT is equipped with a large collection of possible geometries and geometry decorators (Baes & Camps 2015). There are three main geometries used in SKIRT: (1) a pure analytical, (2) a semi-analytical, and (3) one derived from smooth particle hydrodynamics (SPH) simulations. The purpose of decorators is to enable the user to construct realistic models of galaxies, modifying an existing geometry by adding spiral arms, clumps, offsets and so forth. SKIRT is further equipped with efficient hierarchical grid structures such as k -d trees (Saftly et al. 2013, 2014) and Voronoi grids (Camps et al. 2013), and hybrid parallelisation techniques (Verstocken et al. 2017). De Looze et al. (2014) implemented a new feature in the code that allows the construction of the complex 3D structures seen in galaxies, from 2D images. The 2D geometry is deprojected and then according to a vertical exponential profile it is smeared out in the vertical direction, so that the flux density is conserved during the conversion from 2D to 3D. Figure 4.1 depicts a schematic of the general workflow of SKIRT for configuring either an oligochromatic or a panchromatic simulation.

4.1 SKIRT concepts

Solving the radiation transfer problem still remains a difficult task, with many physical processes amounting for a very complex and non-local radiative transfer equation. For example, let us assume an observer of a particular field of view. The observer will only

¹<http://skirt.ugent.be>; v8.0

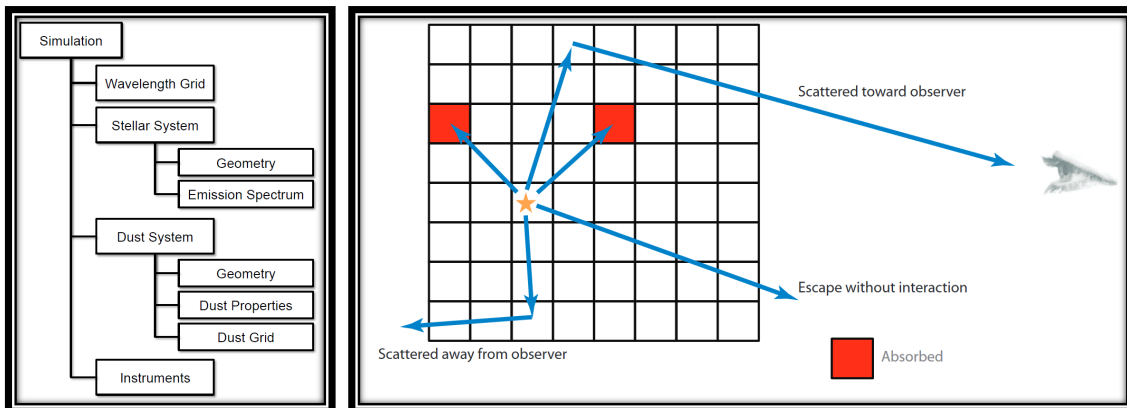


Figure 4.1: On the left side, a schematic representation of SKIRT's workflow for the items to be configured for either an oligochromatic or a panchromatic SKIRT simulation. *Image Credit: Camps & Baes (2015)*. On the right side, a schematic representation of a basic process of Monte Carlo radiative transfer. *Image Credit: Steinacker et al. (2013)*.

detect photons that fall along his line-of-sight. However, these photons have a different origin as they are emitted from various sources and processes, or scattered by dust into the line-of-sight. Of course, photons could either be absorbed or scattered out of the line-of-sight of the observer. The common approach to tackle the radiative transfer problem is by simulating the different processes of emission, absorption, and scattering as photons propagate through the dusty medium. There are two main methods to accomplish that: (1) by tracing the rays of light originating from the various sources (ray-tracing method), and (2) by using random numbers, sampled from probability distributions, to simulate the scattering and absorption events (Monte Carlo method). SKIRT simulations adopt the Monte Carlo method, which is the most popular and more efficient method to model galaxies (see Steinacker et al. 2013, for a review of the available radiative transfer codes).

4.1.1 Wavelength grid

In SKIRT, two types of simulations are available: oligochromatic and panchromatic. As evident from their respective names, oligochromatic simulations could operate at a grid of just one or a small number of distinct wavelengths, whereas panchromatic simulations operate over a broad grid of wavelengths that typically ranges from UV to submm. An oligochromatic simulation can be employed to study simple cases of absorption and scattering events by the dust in the optical regime, since thermal dust emission is not supported for this kind of simulation. On the other hand, the thermal dust emission as well as the absorption and scattering can be handled by a panchromatic simulation.

4.1.2 Spatial geometries

One of the fundamental aspects of a SKIRT simulation is the spatial distribution of the radiation sources and dust components. SKIRT offers a plethora of predefined

geometries which characterise a spatial density distribution for the radiation sources and dust. The available geometries include point-like sources as well as various analytical functions that generate spherical, cylindrical or asymmetrical distributions. Furthermore, it is possible to construct complex model by combining multiple geometries, and to add a decorator to an already defined geometry, hence altering for example a spherical geometry into a spheroidal distribution, or by including clump-like structures in random locations. A feature also exists that imports a density distribution from 2D images.

Now, the main sources of radiation in the simulation are the stellar populations defined by the stellar system. A stellar system can have multiple components and geometrical features. To each stellar geometry a built-in SED is assigned that is characteristic of the emission spectrum. SKIRT includes many parameterised SED families, such as [Bruzual & Charlot \(2003\)](#), [Maraston \(2005\)](#), and MAPPINGS III ([Groves et al. 2008](#)). The amount of radiation can be specified through the bolometric luminosity or through the spectral luminosity at the centre of a standard wavelength band, for example by using a [Bruzual & Charlot \(2003\)](#) model based on stellar age and metallicity.

In a similar fashion, the dust system includes information about the spatial distribution and properties of the dust in the model. Again, each dust component may have its own characteristic geometry and properties. The total dust mass can be used to constrain the amount of dust in the model, while the optical and chemical properties can be handled using various built-in dust mixes. SKIRT includes several dust mixes such as the [Zubko et al. \(2004\)](#) model, the [Draine & Li \(2007\)](#) model, and the THEMIS model ([Jones et al. 2017](#)).

4.1.3 Dust grid

The most efficient way to run a Monte Carlo radiative transfer simulation for astrophysical objects as complex as galaxies, is by constructing a discrete dust grid through which light can travel (see [Fig. 4.2](#)). This can be accomplished by subdividing the dusty medium into a large number of 3D dust cells. The size of the grid cells depends on the dust density; grid cells are small where locations require high resolution, whereas cells can be much bigger elsewhere. This kind of configuration is beneficial for the computational time and the memory requirements of the simulation, since both increase significantly with the increasing number of cells. In each dust cell all physical properties (e.g. optical properties, dust density, radiation field) are considered constant. When running a simulation photon packages are randomly placed inside the grid according to the density profile of the stellar distribution. A photon package propagates through the grid until it crosses a cell with a non-negligible amount of dust, and then interacts with that particular cell according to randomly generated events (i.e. it is randomly determined whether the photon package is absorbed or scattered).

Once all stellar photons are simulated, SKIRT computes the radiation field in every dust cell according to the respective absorbed energy. As we discussed in [Sect. 1.7](#), dust grains absorb the UV and optical photons emitted by stars. The absorbed energy heats up the dust grains causing them to emit at longer wavelengths. At this stage of the simulation, a new batch of photon packages is emitted by the dust cells. Effects like

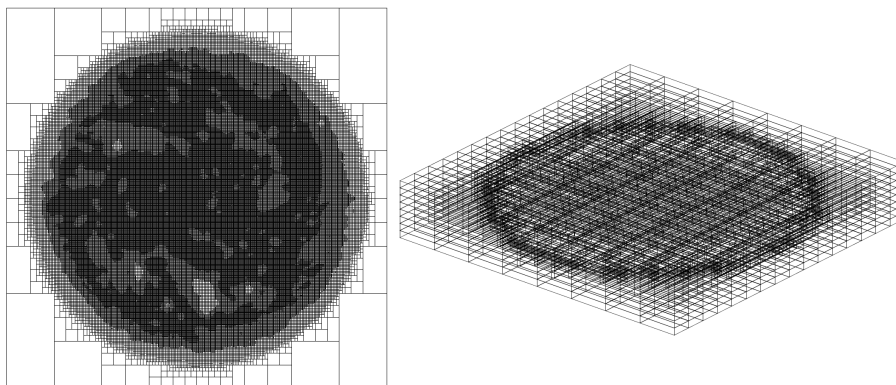


Figure 4.2: Example of a dust grid used in SKIRT. On the left side, a mid-plane cut through a k -d tree grid is depicted, while on the right side the 3-dimensional grid is illustrated. The grid was constructed based on the dust distribution of the barred spiral galaxy NGC 5236.

dust self-absorption and scattering are negligible and thus not simulated (however the option to include them is available).

4.1.4 Instruments

The output of a SKIRT simulation is retrieved with the use of synthetic instruments. These instruments collect and write down the simulated data of the radiation field at any given viewing angle, and can be placed even inside the model. There two main instruments: (1) the frame instrument, and (2) the SED instrument. The frame instrument creates a 3D data cube that includes 2D images at each simulated wavelength, and outputs the results as a FITS file (Flexible Image Transport System). The SED instrument outputs the spectral energy distribution of the detected flux as a text file that can easily be plotted. The option to record the radiation from different sources is also available (i.e. direct radiation, scattered radiation and dust emission).

Part III

Global SED fitting

Old and young stellar populations and their role in dust heating

The analysis and results of this chapter appear in **A. Nersesian**, E. M. Xilouris, S. Bianchi, F. Galliano, A. P. Jones, M. Baes, V. Casasola, L. P. Cassará, C. J. R. Clark, J. I. Davies, M. Declair, W. Dobbels, I. De Looze, P. De Vis, J. Fritz, M. Galametz, S. C. Madden, A. V. Mosenkov, A. Trčka, S. Verstocken, S. Viaene, and S. Lianou, 2019, ‘Old and young stellar population in DustPedia galaxies and their role in dust heating’, *A&A*, 624, A80.

5.1 Introduction

The SED of galaxies holds much information on their stellar and dust content. Space observatories such as *Herschel* (Pilbratt et al. 2010) and *Spitzer* (Werner et al. 2004) provide deep and spatially resolved observations of galaxies in the local Universe, at IR and submm wavelengths, revealing their dust content. Dust has a profound role in shaping the observed SED. In LTGs, dust is found to absorb between roughly one quarter and one third of the total energy emitted by stars in the UV, optical and NIR wavelengths (Soifer & Neugebauer 1991; Xu & Buat 1995; Popescu & Tuffs 2002; Skibba et al. 2011; Viaene et al. 2016) while redistributing this energy into the MIR, FIR and submm regimes. Bianchi et al. (2018) investigated the bolometric attenuation by dust, for 814 galaxies of the DustPedia¹ sample (Davies et al. 2017; Clark et al. 2018), as a function of morphological type and luminosity. They found that dust absorbs on average 19% of the total stellar energy budget. However, if only LTGs are considered, the average value increases to 25%, which is more in line with previous works in the literature.

The various stellar populations contribute to the heating of the dust grains in a different

¹<http://www.dustpedia.com>

way. There are two main factors that regulate the level of efficiency with which the stellar populations affect the dust heating. One has to do with the spatial distribution of the stars of a specific population with respect to the dust distribution. The general picture for unperturbed ETGs is that all components (young stars, old stars, and dust) are distributed in a similar way, with a high concentration in the centre of the galaxy and a gradual decrease of the components towards its extremities. Late-type galaxies on the other hand show a central distribution of the old stars in the bulge with the young stars mostly tracing the spiral arms. The second factor is the effective temperature of the stars and their efficiency at heating up the dust in their neighbourhood. These factors build up the ISRF of a galaxy which is responsible for the dust heating.

An important reason to study the radiation and energy balance of galaxies over the total wavelength range on which they emit, is to learn about their formation and evolution. Physical properties such as the SFR, the stellar mass (M_{star}), and the dust mass (M_{dust}) provide valuable information that can be used to constrain the SFH and to determine how the baryonic content of galaxies evolved through cosmic time. Many studies have shown that it is possible to approximately estimate the intrinsic physical properties of galaxies with only single-band photometry. Measurements in the NIR wavelengths for example, being less affected by dust extinction, can be used as proxies for the estimation of the total M_{star} of a galaxy (Wen et al. 2013). Similarly, measurements in the MIR can trace the SFR adequately (Calzetti et al. 2007; Chang et al. 2015; Davies et al. 2016), while FIR emission can provide estimates of M_{dust} (Smith et al. 2010; Davies et al. 2012; Galametz et al. 2012; Auld et al. 2013; Cortese et al. 2014). However, using single-band proxies may lead to misleading results if samples of galaxies with mixed morphologies are considered. Accurate determination of these parameters is more complicated and requires a more sophisticated and self-consistent approach. An estimation of galactic properties may be more challenging if objects with entirely different physical parameters show similar SEDs in a given wavelength range. Thus, more advanced methods of SED modelling, that take advantage of the full range of observations from the UV to submm wavelengths are necessary.

Several codes have been developed in order to model the panchromatic SEDs of galaxies. Such codes (e.g., CIGALE (Noll et al. 2009; Roehlly et al. 2014; Boquien et al. 2019), MAGPHYS (da Cunha et al. 2008), PROSPECTOR- α (Leja et al. 2017), BEAGLE (Chevallard & Charlot 2016), and BAYESED (Han & Han 2014)), take advantage of Bayesian analysis to fit the SEDs of galaxies providing significant information on the actual stellar and dust content, their ability to form stars, and the efficiency of the ISRF in heating the dust grains. These codes ensure conservation of energy by allowing re-emission of the stellar light, absorbed by the dust grains, at longer wavelengths. In this work we use the most recent version of CIGALE² (version 2018.0) to model the SEDs and to extract the physical properties for the DustPedia galaxies. The code is able to provide both the attenuated and the unattenuated contributions of the different stellar populations (old and young) allowing us to study the fraction of energy that is absorbed by dust for each stellar component. We take advantage of this information to investigate how the stellar populations of galaxies with different morphologies contribute to the dust heating. In addition to CIGALE, we fit single MBBs to the FIR-submm observations

²<https://cigale.lam.fr>

as an alternative way to estimate the dust temperature and mass.

The data used in this study come from the DustPedia archive³. The archive was developed within the framework of the DustPedia project (an FP7-funded EU project) providing access to multi-wavelength imagery and photometry for 875 nearby galaxies. In addition to the imagery and the aperture-matched photometry that was applied to all available maps (Clark et al. 2018), additional data such as redshift-independent distances, HI masses (De Vis et al. 2019), H2 masses (Casasola et al. 2019), optical line and metallicity measurements (De Vis et al. 2019), and information based on 2D photometric fitting (Sérsic indices, effective radii, inclination angles, etc.; Mosenkov et al. 2019) are also available in the DustPedia archive.

5.2 The sample

In our study we make use of multi-wavelength observations of galaxies available in the DustPedia archive (Davies et al. 2017; Clark et al. 2018). For the full description of our photometry pipeline we refer the reader to Clark et al. (2018).

The SED fitting routines that we present in the following section require the average flux densities over the relative spectral response function (RSRF) of the filter as input. Therefore, we make sure that this requirement is met. The DustPedia photometry conforms to the original pipeline outputs of each instrument/filter combination (or catalogue). For UV/optical/NIR data the SED is assumed to be constant over the (relatively narrow) filter bandwidth, hence the flux densities are indeed the average over the filter RSRF. However, for most of the longer-wavelength data points (starting from those of WISE; Wright et al. 2010) a spectral shape for the SED is assumed, while for the IRAS (Neugebauer et al. 1984) bands, a SED with $\nu \times F_\nu = \text{const.}$. The same convention is used for other bands, with the exception of WISE and MIPS (Rieke et al. 2004) bands. We first corrected WISE and MIPS data points from their own colour correction to the IRAS constant-energy convention. We then removed this further colour correction in all long-wavelength bands, so that all flux densities give the average over their respective filter RSRF. In most cases, the correction is smaller than a few percent, with the exception of the WISE 12 μm band (whose DustPedia flux densities must be multiplied by 1.05), MIPS bands (an increase by factors 1.03 and 1.07 at 24 and 70 μm , respectively), and the IRAS 60 μm band (a correction of 0.95).

Before using this photometric dataset we applied several rejection criteria following the guidelines and flagging codes given in Clark et al. (2018) to ensure that only good-quality measurements are fed into our modelling. First, we used all bands from GALEX-FUV up to *Planck*-850 μm , excluding all photometric measurements flagged as contaminated from a nearby galactic or extragalactic source, determined upon visual inspection by Clark et al. (2018). We furthermore excluded all photometric entries with significant artefacts in the imagery or insufficient sky coverage (leading to a poor background estimate). IRAS and *Planck* data were also checked and measurements where a fraction of the extended emission might have been missed were excluded. Finally, galaxies with

³<http://dustpedia.astro.noa.gr>

insufficient coverage of the SED (i.e. galaxies without fluxes in the wavelength range $0.35 \leq \lambda/\mu\text{m} \leq 3.6$, and those without fluxes around the peak of the dust emission in the wavelength range $60 \leq \lambda/\mu\text{m} \leq 500$) were also excluded. With 61 galaxies rejected, our final sample consists of 814 galaxies with the majority (94%) having more than 15 photometric measurements available to constrain the SED modelling performed with CIGALE.

Galaxies hosting an AGN require extra treatment with CIGALE (depending on the strength of the AGN emission and on the level that this emission may affect the SED of the galaxy, especially in MIR wavelengths; Ciesla et al. 2015). Inclusion of AGN templates would significantly increase the required computing time prohibiting us from constructing a dense grid for the rest of the parameters that are significant for the majority of the galaxies in the sample. An assessment on whether or not a galaxy hosts an AGN can be made by using the method described in Satyapal et al. (2018) and Assef et al. (2018). The latter method uses a 90%-confidence criterion based on the WISE 3.4 and 4.6 μm bands to disentangle the galaxies that host an AGN component. Bianchi et al. (2018), using this method on the DustPedia galaxies, found that 19 objects out of the total 814 galaxies, show a significant probability of hosting an AGN. These 19 galaxies are: ESO 434-040, IC 0691, IC 3430, NGC 1068, NGC 1320, NGC 1377, NGC 3256, NGC 3516, NGC 4151, NGC 4194, NGC 4355, NGC 5347, NGC 5496, NGC 5506, NGC 7172, NGC 7582, UGC 05692, UGC 06728, and UGC 12690. Since this is only a small fraction ($\sim 2\%$) of the DustPedia galaxies we did not use AGN templates in our modelling (in the plots that follow however we mark these galaxies with an 'X' symbol). Furthermore, we searched for jet-dominated radio galaxies in our sample since synchrotron and free-free emission can be the dominant component in the FIR-submm region of the spectrum. Four such galaxies (NGC 1399, NGC 4261, NGC 4374, and NGC 4486) were found by cross-matching the DustPedia galaxies with the all-sky catalogue of radio-galaxies in the local Universe (van Velzen et al. 2012) and marked with a '+' in subsequent plots. In the characteristic case of NGC 4486 (M 87), the FIR-submm SED is completely dominated by synchrotron emission (Baes et al. 2010a).

5.3 Fitting the SEDs with CIGALE

For the purpose of this work, we make use of the SED fitting code CIGALE to model and interpret the SEDs of the DustPedia galaxies. The code fits the multi-wavelength spectrum of each galaxy in order to derive global properties such as the SFR, the stellar mass M_{star} , the lower cutoff of the ISRF intensity U_{min} and the dust mass $M_{\text{dust}}^{\text{CIGALE}}$. Furthermore, the stellar component is described by providing the relative contribution of both the young and the old stellar components to the total SED of the galaxy. Complementary to CIGALE we approximate the FIR-submm spectrum of the galaxies with the traditionally used MBB approach with the dust grain properties accordingly scaled to match the THEMIS dust properties. This provides us with an independent estimate of the total dust mass and dust temperature for each galaxy.

Table 5.1: Parameter grid used for computing the CIGALE templates. A total of 80,041,500 models were produced.

Parameter	Value
Star-Formation History	Flexible Delayed ^(a)
e-folding time, τ_{main} (Myr)	500, 750, 1100, 1700, 2600, 3900, 5800, 8800, 13000, 20000
galaxy age, t_{gal} (Myr)	2000, 4500, 7000, 9500, 12000
quenching or bursting age, t_{flex} (Myr)	200
r_{SFR}	0.01, 0.0316, 0.1, 0.316, 1.0, 3.16, 10.0
Stellar population model	BC03 ^(b)
IMF	Salpeter ^(c)
Metallicity	0.02
Dust attenuation	Calzetti ^(d)
color excess of the young stars, $E(B-V)$	0.0, 0.005, 0.0075, 0.011, 0.017, 0.026, 0.038, 0.058, 0.087, 0.13, 0.20, 0.29, 0.44, 0.66, 1.0
Reduction factor for $E(B-V)$, $E(B-V)_{\text{old}}/E(B-V)_{\text{young}}$	0.25, 0.50, 0.75
δ	-0.5, -0.25, 0.0
Dust grain model	THEMIS ^(e) ; DL14 ^(f)
Fraction of small hydrocarbon solids (THEMIS), q_{hac}	0.02, 0.06, 0.10, 0.14, 0.17, 0.20, 0.24, 0.28, 0.32, 0.36, 0.40
PAH abundance [%] (DL14), q_{PAH}	0.47, 1.12, 1.77, 2.50, 3.19, 3.90, 4.58, 5.26, 5.95, 6.63, 7.32
U_{min}	0.1, 0.15, 0.3, 0.5, 0.8, 1.2, 2.0, 3.5, 6, 10, 17, 30, 50, 80
α	2.0
γ	0.0, 0.001, 0.002, 0.004, 0.008, 0.016, 0.031, 0.063, 0.13, 0.25, 0.5

References: (a) Ciesla et al. (2016). (b) Bruzual & Charlot (2003). (c) Salpeter (1955). (d) Calzetti et al. (2000). (e) Jones et al. (2017). (f) Draine et al. (2014).

5.3.1 The parameter space

We adopted a similar parameter grid to the one used by Hunt et al. (2019) to fit the SEDs of 61 galaxies from the KINGFISH⁴ sample (Kennicutt et al. 2011). In Table 5.1 we give the parameter space used by CIGALE to calculate the SED templates to be fitted to the actual datasets. Two sets of templates were produced, one including the dust parameters given by the THEMIS model and, for comparison, another one including the DL14 dust model characteristics (the latter is briefly discussed in Sect. 5.5). In total, 80,041,500 such templates were created with CIGALE running on the high-performance cluster of Ghent University. The parameters derived for each galaxy are provided in the DustPedia archive while the mean values per morphological type for SFR, M_{star} , and $M_{\text{dust}}^{\text{CIGALE}}$ are given in Table 5.2.

5.3.2 Quality of the fit

With the current setup of CIGALE we can derive estimates of several parameters, such as the SFR, the FUV attenuation (A_{FUV}), the minimum ISRF intensity (U_{min}), the stellar mass (M_{star}), the bolometric luminosity (L_{bolo}), the dust mass and luminosity ($M_{\text{dust}}^{\text{CIGALE}}$ and L_{dust} respectively), the mass fraction of hydrocarbon solids (q_{hac} ; the PAH abundance q_{PAH} in the case of DL14), and the fraction of the dust luminosity coming from PDRs (γ), to name a few. To examine how well these parameters can be constrained from the multi-wavelength SED fitting that CIGALE performs, and to monitor accuracy and precision expected for each parameter, we made use of the

⁴Key Insights on Nearby Galaxies: A Far-Infrared Survey with *Herschel*.

Table 5.2: Mean values of various physical properties of the DustPedia galaxies, for different morphological sub-classes. M_{dust} and T_{dust} are derived by CIGALE and MBB modelling, SFR and M_{star} by CIGALE, while the mass of atomic hydrogen (M_{HI}) is obtained from the literature (see [De Vis et al. 2019](#)). The number of objects per morphological bin (N_{obj}) refers to the parameters derived with CIGALE. In total, 814 galaxies were modelled with CIGALE, 678 out of 814 with a single MBB, and 711 have M_{HI} measurements.

T	Type	N_{obj}	$\log(\langle \text{SFR} \rangle)$ [M_{\odot}/yr]	$\log(\langle M_{\text{star}} \rangle)$ [M_{\odot}]	$\log(\langle M_{\text{HI}} \rangle)$ [M_{\odot}]	$\log(\langle M_{\text{dust}}^{\text{CIGALE}} \rangle)$ [M_{\odot}]	$\log(\langle M_{\text{dust}}^{\text{MBB}} \rangle)$ [M_{\odot}]	$\langle T_{\text{dust}}^{\text{CIGALE}} \rangle$ [K]	$\langle T_{\text{dust}}^{\text{MBB}} \rangle$ [K]
-5	E	51	-1.27 ± 0.21	10.92 ± 0.05	8.53 ± 0.01	6.15 ± 0.38	6.55 ± 0.42	27.59 ± 4.91	18.62 ± 5.06
-4	E ⁺	20	-1.05 ± 0.14	10.94 ± 0.05	9.95 ± 0.01	6.60 ± 0.27	6.66 ± 0.36	26.85 ± 5.77	19.29 ± 6.95
-3	S0 ⁻	34	-0.59 ± 0.14	10.35 ± 0.09	8.51 ± 0.04	5.95 ± 0.28	6.11 ± 0.31	26.70 ± 4.23	21.87 ± 5.26
-2	S0 ⁰	83	-0.61 ± 0.23	10.48 ± 0.07	8.86 ± 0.02	6.12 ± 0.22	6.27 ± 0.30	26.89 ± 4.10	21.88 ± 5.65
-1	S0 ⁺	43	-0.36 ± 0.14	10.46 ± 0.06	8.55 ± 0.04	6.46 ± 0.13	6.56 ± 0.18	24.75 ± 4.71	22.00 ± 4.76
0	S0a	37	-0.40 ± 0.09	10.74 ± 0.04	9.24 ± 0.02	6.74 ± 0.16	6.84 ± 0.16	24.63 ± 4.87	20.50 ± 4.34
1	Sa	50	0.03 ± 0.08	10.65 ± 0.08	9.37 ± 0.02	7.00 ± 0.09	7.01 ± 0.13	23.23 ± 4.34	22.89 ± 4.30
2	Sab	40	0.42 ± 0.11	10.48 ± 0.08	9.26 ± 0.02	7.01 ± 0.07	7.02 ± 0.10	22.79 ± 4.22	22.63 ± 3.65
3	Sb	58	0.36 ± 0.13	10.55 ± 0.08	9.45 ± 0.02	7.23 ± 0.07	7.23 ± 0.11	22.62 ± 3.45	22.48 ± 3.24
4	Sbc	63	0.47 ± 0.10	10.40 ± 0.10	9.62 ± 0.04	7.31 ± 0.06	7.33 ± 0.09	21.82 ± 3.00	21.45 ± 3.82
5	Sc	70	0.31 ± 0.07	10.28 ± 0.09	9.66 ± 0.03	7.29 ± 0.07	7.30 ± 0.11	22.09 ± 2.64	21.70 ± 2.34
6	Scd	84	-0.05 ± 0.09	9.83 ± 0.11	9.40 ± 0.02	6.94 ± 0.09	6.96 ± 0.14	21.03 ± 3.30	20.21 ± 2.66
7	Sd	46	-0.14 ± 0.05	9.62 ± 0.11	9.42 ± 0.01	6.81 ± 0.11	6.84 ± 0.19	20.92 ± 3.29	19.65 ± 2.77
8	Sdm	32	-0.56 ± 0.05	9.27 ± 0.11	9.13 ± 0.02	6.46 ± 0.14	6.53 ± 0.22	21.05 ± 3.94	19.17 ± 3.54
9	Sm	36	-0.14 ± 0.04	9.24 ± 0.12	9.15 ± 0.02	6.25 ± 0.17	6.42 ± 0.25	24.32 ± 5.15	20.87 ± 5.51
10	lrr	67	-0.77 ± 0.16	9.08 ± 0.14	8.88 ± 0.02	5.93 ± 0.25	6.21 ± 0.44	25.11 ± 5.21	19.62 ± 5.05
$[-5.0, -3.5)$	E	71	-1.20 ± 0.18	10.92 ± 0.05	9.36 ± 0.01	6.33 ± 0.32	6.59 ± 0.40	27.38 ± 5.18	19.09 ± 5.71
$[-3.5, 0.5)$	S0	197	-0.50 ± 0.16	10.52 ± 0.06	8.89 ± 0.02	6.38 ± 0.17	6.51 ± 0.21	25.96 ± 4.54	21.51 ± 5.16
$[0.5, 2.5)$	Sa-Sab	90	0.25 ± 0.10	10.58 ± 0.08	9.32 ± 0.02	7.00 ± 0.08	7.01 ± 0.12	23.03 ± 4.29	21.92 ± 4.03
$[2.5, 5.5)$	Sb-Sc	191	0.38 ± 0.10	10.42 ± 0.09	9.59 ± 0.03	7.28 ± 0.07	7.29 ± 0.10	22.16 ± 3.04	21.64 ± 2.83
$[5.5, 8.5)$	Scd-Sdm	162	-0.14 ± 0.07	9.70 ± 0.11	9.37 ± 0.01	6.84 ± 0.10	6.87 ± 0.16	21.00 ± 3.43	20.09 ± 2.91
$[8.5, 10.0]$	Sm-lrr	103	-0.44 ± 0.07	9.14 ± 0.13	9.00 ± 0.02	6.07 ± 0.21	6.30 ± 0.35	24.83 ± 5.21	20.55 ± 5.27

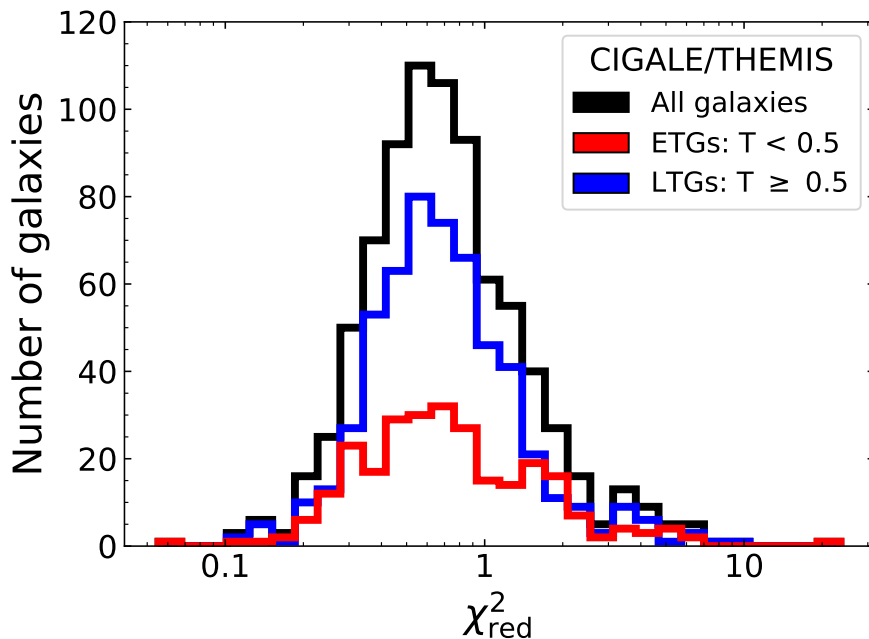


Figure 5.1: Distribution of the reduced χ^2 for the 814 galaxies modelled with CIGALE and with the THEMIS dust model (black line). The distributions for the LTG and ETG subsamples are shown with blue and red lines respectively.

CIGALE module that performs a mock analysis. This module creates a mock SED for each galaxy based on the best fitted parameters, allowing the fluxes to vary within their measured uncertainties. By modelling these mock SEDs with CIGALE we can then retrieve the best set of the mock fitted parameters and compare them with those used as an input. This provides us with a direct measure of how accurately one can retrieve specific parameters for a specific sample of galaxies. The results of the mock analysis can be found in Sect. 5.4.

To explore the overall quality of the fits to the observations we examine the distribution of the reduced χ^2 values (χ^2_{red} ; the χ^2 values divided by the number of observations minus the number of free parameters). The χ^2_{red} distribution is shown in Fig. 5.1 (black line). The χ^2_{red} distributions for the two main morphological classes of galaxies in the DustPedia sample (ETGs ($T < 0.5$) and LTGs ($T \geq 0.5$)), are also shown (red and blue lines, respectively). For the full sample modelled with CIGALE (814 galaxies) we find that the median value of the histogram is 0.66, while it gets to 0.67 when only considering the 546 LTGs and drops down again to 0.66 for the 268 ETGs. Out of the 814 modelled galaxies, there are 60 ($\sim 7\%$) with $\chi^2_{\text{red}} > 2$ and only 22 ($\sim 3\%$) with $\chi^2_{\text{red}} > 4$. Similar distributions for the χ^2_{red} are obtained when using the DL14 dust model (see Fig. 5.5 in Sect. 5.5), although the values are slightly lower compared to THEMIS. A possible explanation is that THEMIS has on average a flatter FIR-submm slope ($\beta = 1.79$) than the DL14 model ($\beta = 2$). With a distribution of ISRF such as that assumed here, it is always possible to fit an observed slope that is flatter than the slope of the intrinsic grain properties, simply by adding colder temperatures. This means that the model with the highest β (DL14) has the highest fitting flexibility,

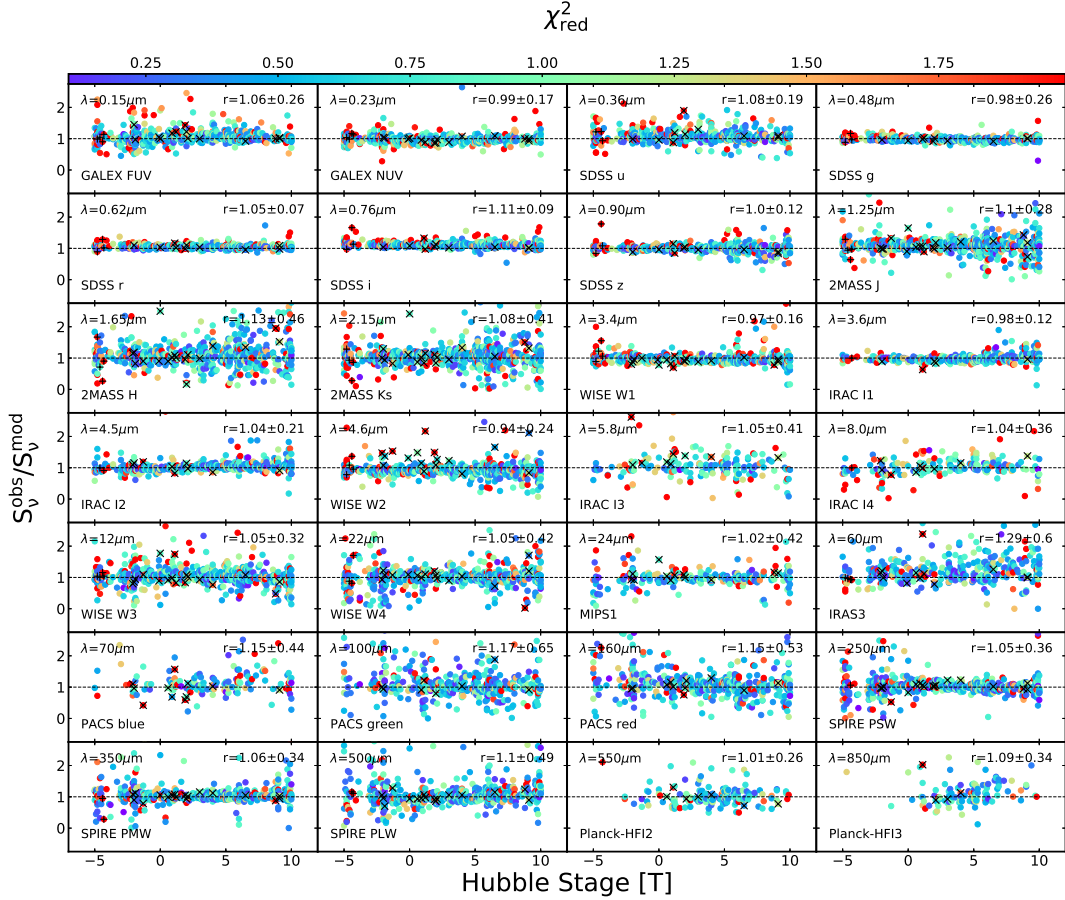


Figure 5.2: Ratios of the observed fluxes to the modelled (CIGALE) fluxes at specific wavelengths, from the FUV ($0.15 \mu\text{m}$) to the submm ($850 \mu\text{m}$), as a function of Hubble stage (T). The wavelength indication (in μm) is given in the top-left corner of each panel, and the name of the survey/band is provided in the bottom-left corner. The ratios are colour-coded with the χ^2_{red} of the fit as indicated in the colour-bar at the top of the plot. Galaxies hosting an AGN or strong radio-jets are marked with an 'X' or a '+' respectively. In the top-right corner of each panel, the mean value of the ratio and the standard-deviation are also provided.

and will thus result in lower χ^2_{red} values.

As a further check of the goodness of the fit to the observations we examined how the ratios of the observed-to-modelled flux densities compare for galaxies of different Hubble stages. The model flux densities in each waveband were calculated by CIGALE. A systematic trend in these ratios in a given band could help reveal potential weaknesses in our modelling. This is shown in Fig. 5.2 with the ratios at wavelengths ranging from the FUV ($0.15 \mu\text{m}$; top-left panel) to the submm ($850 \mu\text{m}$; bottom-right panel) with the wavelength indicated in the top-left corner in each panel. Each point represents a galaxy colour-coded with its χ^2_{red} . Overall we see that despite the large scatter in some cases the ratio of the observed-to-modelled flux densities remains around unity (horizontal dashed line) indicating that CIGALE is able to adequately fit the SED of the galaxy in the full wavelength range considered. The χ^2_{red} values (as indicated with the different colours)

show a general picture where many ETGs and irregular galaxies (the two extremes in the x -axis) are either on the higher (red colour) or lower (blue colour) end on the χ_{red}^2 scale, while the galaxies with intermediate Hubble stages lead to χ_{red}^2 values closer to one (cyan and green colours).

For each waveband we calculated (and presented in the top-right corner in each panel) the mean value of the ratio as well as the standard-deviation. We see that there are 14 wavebands which show deviations from the mean of less than or equal to 5% (0.23, 0.48, 0.62, 0.90, 3.4, 3.6, 4.5, 5.8, 8.0, 12, 22, 24, 250, and 550 μm), 8 with deviations larger than 5% and less than or equal to 10% (0.15, 0.36, 1.25, 2.15, 4.6, 350, 500 and 850 μm), and a remaining 6 with deviations larger than 10% (0.76, 1.65, 60, 70, 100, and 160 μm). In all six cases with the largest deviations from unity ($> 10\%$) the model under-predicts the observed fluxes. With the exception of the SDSS i -band (0.76 μm) with a scatter of 0.09, the rest of the bands show large scatter (> 0.4) and especially for Hubble stages $T < 0$ and $T > 5$ which also drives the underestimation of the modelled fluxes. At submm wavelengths and especially at 500 and 850 μm there seems to be a mild trend of increasing of the observed-to-modelled flux ratios with increasing Hubble stage. Such a trend has already been reported in other studies (Ciesla et al. 2014) with a possible interpretation being the submm excess observed in low-metallicity systems (Galametz et al. 2009, 2010; Ciesla et al. 2014).

5.4 Mock analysis

In this section we present the results of the mock analysis. The results of this procedure are shown in Fig. 5.3 with the input values of each parameter plotted on the x -axis and the probability-weighted mean value along with the associated standard-deviation of the fitted values (error bars) on the y -axis. The data are colour-coded with the number of fluxes available for each galaxy (see the inset of the panel in the middle for the explanation of the colours). There are 17, 86, 134, 337, 152, and 88 galaxies with their available number of observations between [10,13), [13,17), [17,20), [20,24), [24,27), and [27,30], respectively.

In general, most of the parameters are well correlated with the input parameters but there is significant scatter in the cases of $M_{\text{dust}}^{\text{CIGALE}}$, A_{FUV} , q_{hac} , U_{min} and γ . Galaxies with large deviations from the one-to-one relation usually have red, gold or green colors indicating that the lack of observations is an important cause of this discrepancy. In most cases the linear fit is very close to the one-to-one relation indicating the ability of CIGALE to retrieve the input values. The exceptions are the values of q_{hac} , and U_{min} with their linear regression fits deviating significantly from the one-to-one relation. This is also shown with the Spearman's coefficient, $\rho = 0.32$ and $\rho = 0.57$ respectively. The linear regression improves when only galaxies with a sufficient number of observations (more than 20) are considered (green dashed lines) with the associated Spearman's coefficients being slightly higher ($\rho = 0.45$ and $\rho = 0.69$ for q_{hac} , and U_{min} respectively).

To understand the nature of these deviations, we performed a series of tests. First, a visual inspection of the fitted SEDs of the galaxies that are the most deviant from the

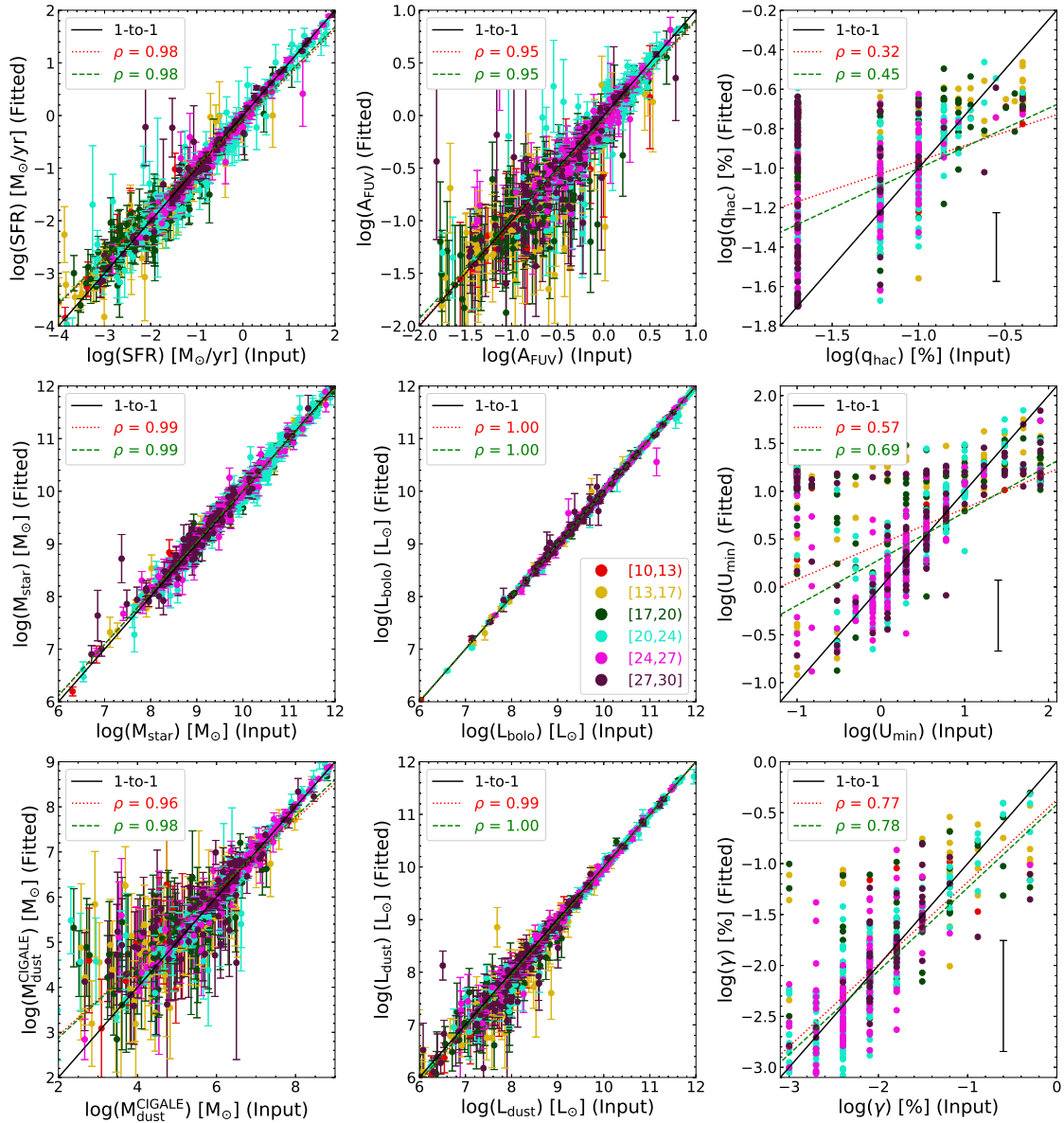


Figure 5.3: Comparison between the best fitted parameters (input values; x-axis) and the mock parameters (fitted values; y-axis) estimated from the CIGALE fitted PDFs for each parameter (SFR, A_{FUV} , q_{hac} , M_{star} , L_{bolo} , U_{min} , $M_{\text{dust}}^{\text{CIGALE}}$, L_{dust} , and γ , from top to bottom). For each galaxy the probability-weighted mean value along with the associated standard deviation of the mock values (error bars) are plotted on the y-axis. In the cases of q_{hac} , U_{min} , and γ , the average standard deviation is plotted in the bottom-right corner of each panel in order to avoid confusion. The data are colour-coded with the number of observations available for each galaxy (see the inset of the panel in the middle for the explanation of the colours). The solid black line is the one-to-one relation, the red dotted line is the linear regression to the full set of data, while the green dashed line is the linear regression to the galaxies with more than 20 observations available. The Spearman's coefficient (ρ) of the linear regression fits is also provided in each panel.

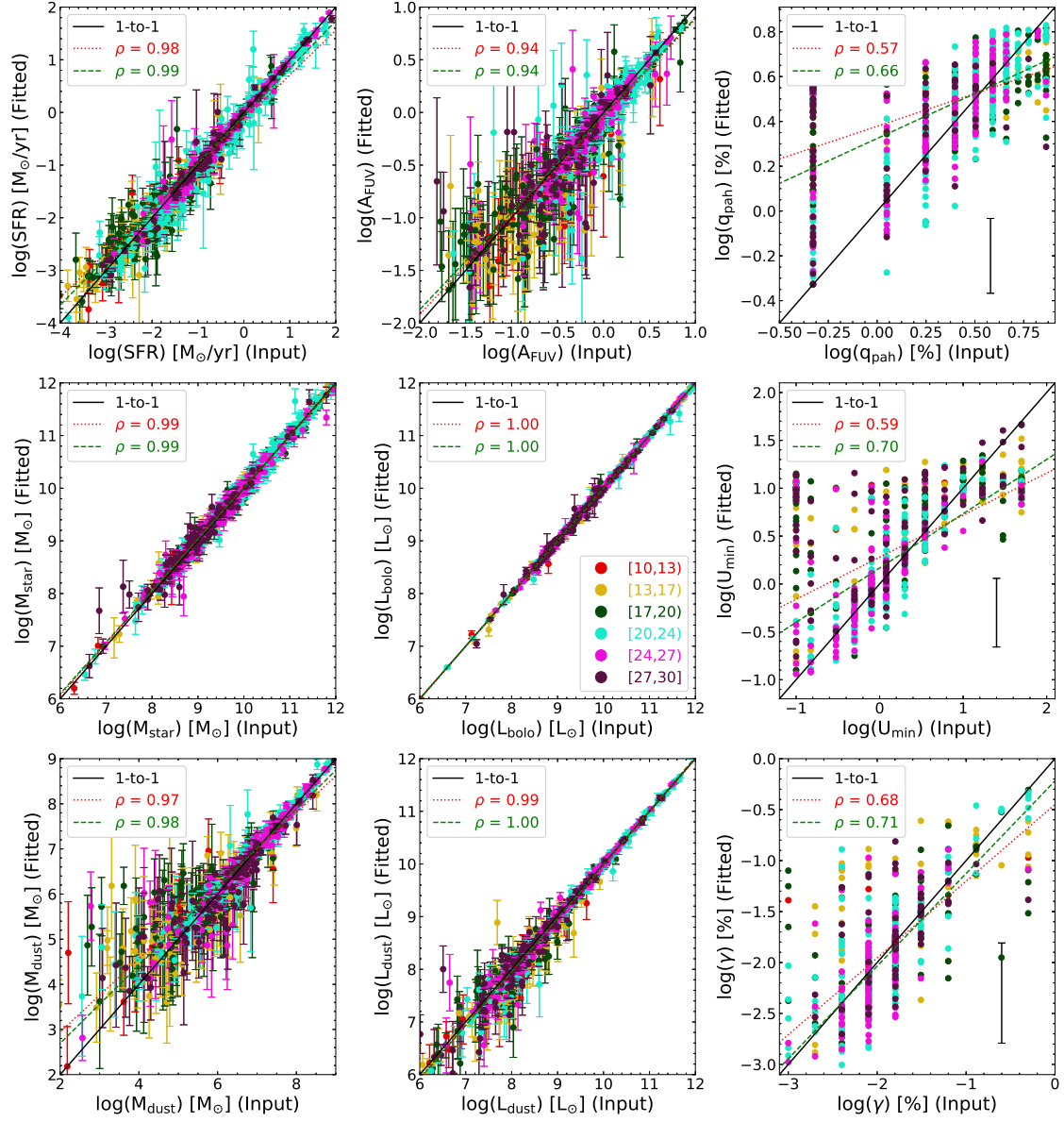


Figure 5.4: As in Fig. 5.3 but for the DL14 dust model. In DL14, the PAH abundance (q_{PAH}) is substituting the fraction of hydrocarbon solids (q_{hac}).

one-to-one relation in the mock analysis revealed that most of these objects lack crucial photometric data near the peak of the dust emission (just left or right from the peak), making it relatively difficult to constrain the dust parameters. Moreover, many of these deviant galaxies have large uncertainties on their FIR-submm flux measurements which also adds up to the poor constraint of U_{\min} .

Finally, our CIGALE setup, with the specific parameter grid used for this study, was also used by Trčka et al. (2019) to fit synthetic SEDs (from the FUV to the submm wavelengths) of galaxies from the EAGLE (Evolution and Assembly of GaLaxies and their Environments; Schaye et al. 2015) simulations. In this sample a complete set of measurements of 29 bands were available for CIGALE to fit resulting in a very accurate recovery of the input values for each parameter (Trčka et al. 2019). From the above tests it becomes evident that the most important cause of the large uncertainties observed in some of the derived parameters is the poor wavelength coverage for these galaxies.

5.5 CIGALE modelling using the DL14 dust model and comparison with the THEMIS model

Since Draine et al. (2007) (updated in Draine et al. 2014, DL14) is a widely adopted model that describes the dust properties, we performed an additional fitting run with CIGALE using this model, instead of THEMIS (Sect. 5.3.1). The parameter grid is the same as in the case of THEMIS, with only the PAH abundance (q_{PAH}) substituting the fraction hydrocarbon solids (q_{hac} ; see Table 5.1).

In Fig. 5.4 we show the results of the relevant mock analysis obtained from CIGALE with the input values of each parameter plotted on the x -axis and the mock fitted values on the y -axis. Similarly to Fig. 5.3, data are colour-coded according to the number of observations available for each galaxy (see the inset of the panel in the middle for the explanation of the colours). As in the case where the THEMIS model is used, most of the input values of the parameters are well correlated with the values derived from the mock analysis with the exception of q_{PAH} , and U_{\min} that show a similar scatter. The Spearman's coefficients for these parameters are $\rho = 0.57$ and $\rho = 0.59$ respectively. The linear regression improves when only galaxies with a sufficient number of observations (more than 20) are considered (green dashed lines) with the associated Spearman's coefficients being slightly higher ($\rho = 0.66$ and $\rho = 0.70$ for q_{pah} and U_{\min} respectively).

As for the THEMIS model we provide here the χ_{red}^2 distribution in Fig. 5.5 (to be compared with Fig. 5.1). In the DL14 case the median value of χ_{red}^2 is 0.58 for the full sample, with 0.56 for the LTGs only and 0.61 for the ETGs. There are 57 ($\sim 7\%$) galaxies with $\chi_{\text{red}}^2 > 2$ and 19 ($\sim 2\%$) with $\chi_{\text{red}}^2 > 4$.

In Fig. 5.6 we compare the results obtained by fitting CIGALE with the DL14 dust model (x -axis) and the THEMIS model (y -axis) for four parameters (SFR, T_{dust} , M_{star} , and M_{dust} , from top to bottom respectively). In each panel the galaxies modelled by CIGALE are plotted, colour-coded with their morphology (see the inset in the top-left panel). It immediately becomes evident that parameters that are constrained mainly from

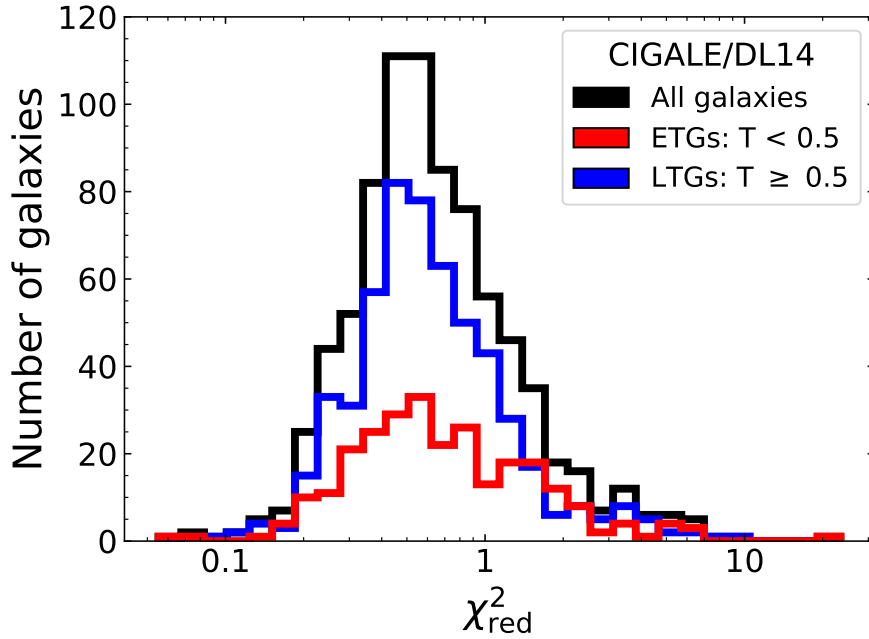


Figure 5.5: Distribution of the reduced χ^2 of the 814 galaxies modelled with CIGALE and with the DL14 dust model (black line). The distributions for the LTGs and the ETGs are also shown (blue and red lines respectively).

the optical part of the SED of the galaxy (SFR and M_{star}) are in very good agreement, and they are almost unaffected by the choice of the dust model. The dust parameters on the other hand, T_{dust} ⁵ and M_{dust} , depend on the choice of the dust model used and this is revealed by an offset from the one-to-one relation for all morphologies. In particular, DL14 predicts higher dust masses with a percentage difference of $\sim 42\%$ and lower dust temperatures of $\sim 5\%$. This offset is due to the fact that THEMIS is more emissive than DL14. THEMIS has both a lower β and a higher κ_0 value (e.g. Fig. 4 of Galliano et al. 2018).

5.6 Comparison with different recipes used in the literature

Here we investigate how the parameters derived from CIGALE compare with values obtained from recipes, widely used in the literature. To obtain an alternative estimate of stellar mass we have used the formula derived in Wen et al. (2013):

$$\log\left(\frac{M_{\text{star}}}{M_{\odot}}\right) = (-0.040 \pm 0.001) + (1.120 \pm 0.001) \times \log\left(\frac{\nu L_{\nu}(3.4 \mu\text{m})}{L_{\odot}}\right), \quad (5.1)$$

⁵See Sect. 5.8, Equation 5.8 on how we derived T_{dust} .

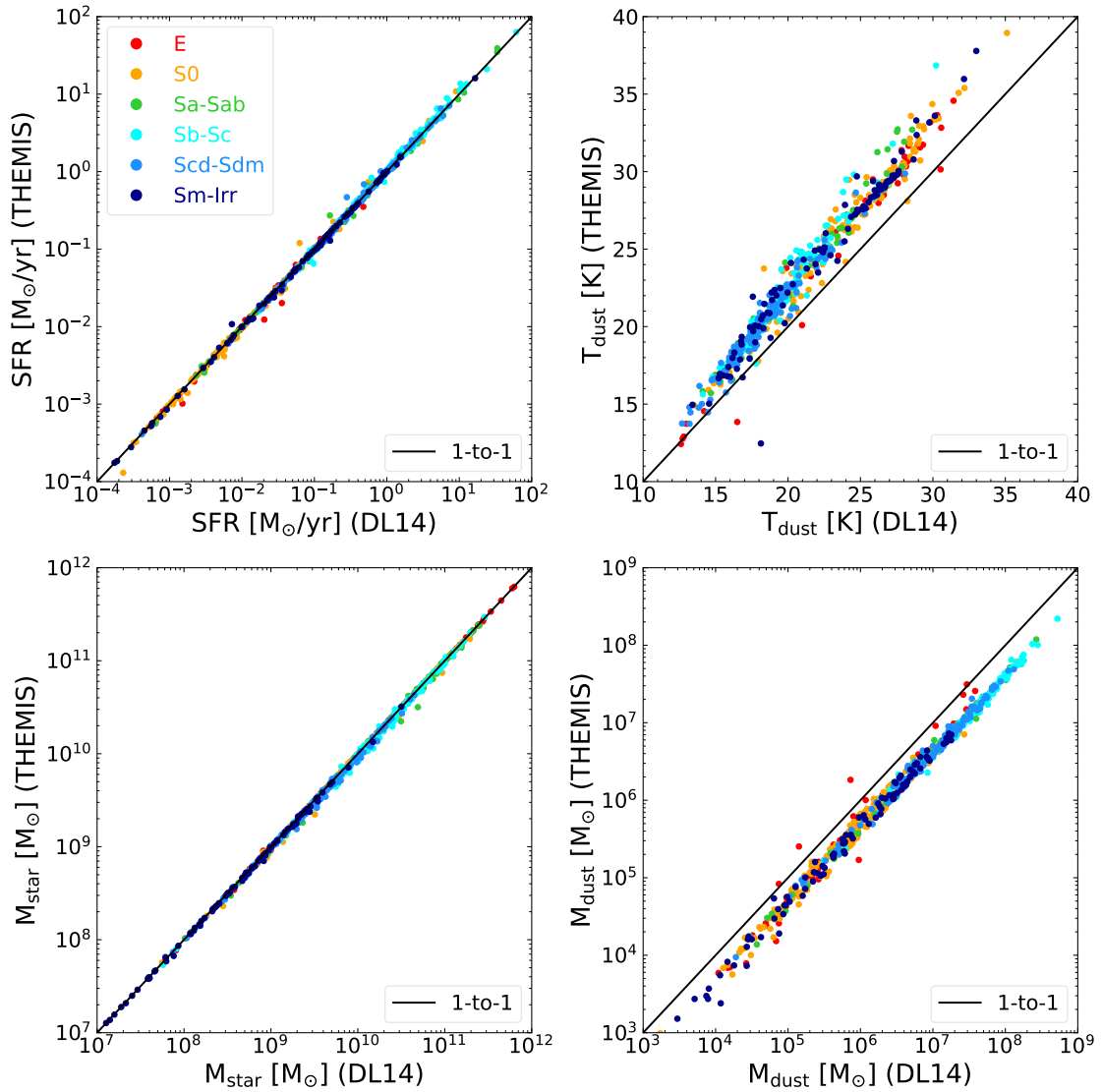


Figure 5.6: Comparison between SFR, T_{dust} , M_{star} , and M_{dust} (from top-left to bottom-right respectively), as derived from CIGALE, assuming two different dust grain models (DL14 on x-axis and THEMIS on y-axis). The points are colour-coded according to the six main morphological types (see the inset in the top-left panel). The black solid line is the one-to-one relation.

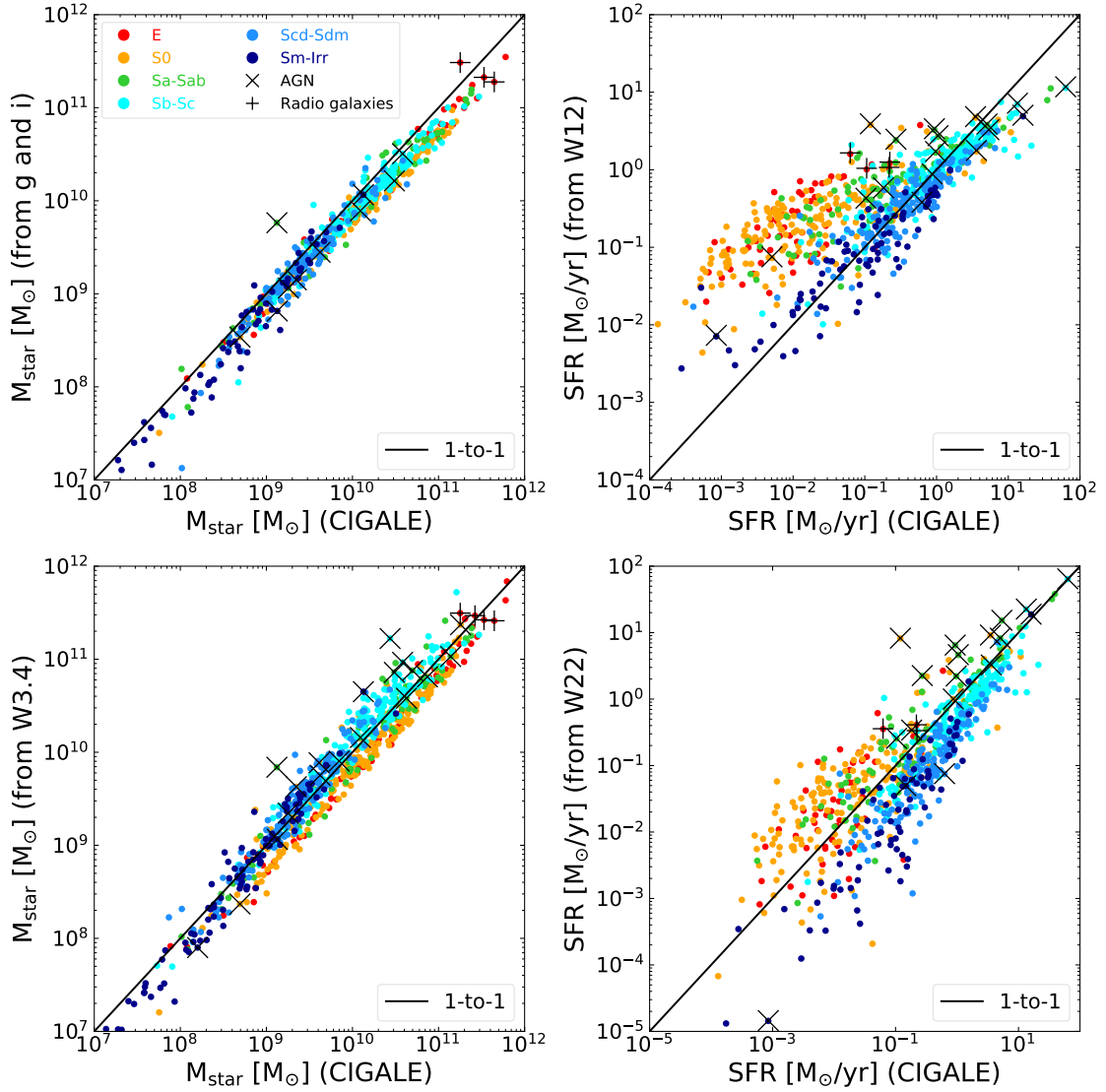


Figure 5.7: Comparison between M_{star} (left panels) and SFR (right panels) derived from CIGALE (x -axis), and other recipes widely used in the literature (y -axis). The formulas used in the literature are given in the text. The points are colour-coded according to the morphological type, while galaxies hosting AGNs and strong radio-jets are marked with an 'X' or a '+', respectively. The black solid line is the one-to-one relation.

where $L_\nu(3.4 \mu\text{m})$ is the WISE 3.4 μm luminosity in L_\odot . Another recipe we used to determine the stellar mass was the formula derived in [Taylor et al. \(2011\)](#):

$$\log\left(\frac{M_{\text{star}}}{M_\odot}\right) = 1.152 + 0.7(g - i) - 0.4M_i, \quad (5.2)$$

where g and i are the apparent magnitudes derived from our photometry of SDSS data in the respective bands and M_i is the absolute i -band magnitude. Stellar masses derived from the above are compared with those obtained from CIGALE in Fig. 5.7 (left panels). In all panels of Fig. 5.7, the circles are individual galaxies colour-coded with their morphology, as shown in the inset in the top-left panel, while the 'X' and '+' symbols indicate AGN and strong radio galaxies, respectively; in many cases these are extreme outliers in the correlations under investigation. Even though [Taylor et al. \(2011\)](#) assumed a [Chabrier \(2003\)](#) IMF to retrieve the stellar masses, the comparison with CIGALE is fairly good but with a small offset. On the other hand, the stellar masses derived from the WISE 3.4 μm band agree to an even greater degree with the stellar masses derived from CIGALE. Therefore, we can confirm that the recipe of [Wen et al. \(2013\)](#) is a good proxy for the stellar mass of a galaxy.

We used the WISE 12 μm and WISE 22 μm data to make alternative estimates of the SFR of the galaxies. Before calculating the SFR we subtracted an estimate of the stellar continuum emission in the 12 μm and 22 μm bands using the data in Table B1 of [Ciesla et al. \(2014\)](#). They calculate the contamination separately for early and late-type galaxies based on fits to the stellar continuum at shorter wavelengths. We used the values normalised to the IRAC 3.6 μm band. [Cluver et al. \(2014\)](#) used the WISE 12 μm data calibrated against $\text{H}\alpha$ to derive SFRs for GAMA sample galaxies matched to the WISE data ([Driver et al. 2011](#)). These galaxies have a wide range of morphological types, though of course the initial calibration does require a measured $\text{H}\alpha$ flux. Typically, the strongest individual contributor to the WISE 12 μm pass band is the 11.3 μm PAH feature, which is predominantly excited by UV radiation from young stars, hence the link to the SFR ([Kaneda et al. 2008](#)). [Houck et al. \(2007\)](#) and [Farrah et al. \(2007\)](#) have previously shown that PAH features can be used as indicators of the current SFR. To this end we use the re-calibration of the [Cluver et al. \(2014\)](#) WISE 12 μm flux density SFR relation given in [Davies et al. \(2016\)](#):

$$\log\left(\frac{\text{SFR}}{M_\odot\text{yr}^{-1}}\right) = (0.66 \pm 0.01) [\log(L_{12}) - 22.25] + (0.160 \pm 0.004), \quad (5.3)$$

where L_{12} is the WISE 12 μm flux density in W Hz^{-1} . This calibration has been updated to a common standard for various SFR indicators. We note that the re-calibration is based on the properties of 'typical' spiral galaxies (disk galaxies of stellar mass $9 < \log(M_{\text{star}}/M_\odot) < 11$), though the original data and calibration include galaxies with a larger range of morphological types.

[Chang et al. \(2015\)](#) also provided calibrations for the star-formation by analysing the MIR properties of the full SDSS spectroscopic galaxy sample. From that work we used

the WISE 22 μm band SFR proxy:

$$\log\left(\frac{\text{SFR}}{M_{\odot}\text{yr}^{-1}}\right) = \log(L_{22}/L_{\odot}) - 9.08, \quad (5.4)$$

The comparison of calculated SFRs is shown in Fig. 5.7 (right panels). The fit is clearly good for the later types, but not so good for the early type galaxies. The 12 μm flux calibration clearly overestimates the SFR of the ETGs compared to that obtained from CIGALE. Compared to literature values, such as those from Davis et al. (2014), the 12 μm values for ETGs are high, thus the CIGALE values are consistent with previous measures and so we accept and use these. On the other hand, the 22 μm calibration underestimates the SFR of the latest type of galaxies while it also overestimates the SFR of the early types, however to a lesser extent than for the 12 μm . In both cases, it is apparent that MIR monochromatic band proxies, despite the fact that they trace the warm dust and consequentially SFR, are not sufficient to obtain a good estimate of the current SFR.

5.7 Fitting the FIR with MBB

The emission from dust in thermal equilibrium with the radiation field can be approximated using MBBs with flux densities given by:

$$S(\lambda, T_{\text{dust}}^{\text{MBB}}) \propto \lambda^{-\beta} B(\lambda, T_{\text{dust}}^{\text{MBB}}), \quad (5.5)$$

where β is the grain emissivity index, usually taking values between 1 and 2 (Hildebrand 1983; Draine & Lee 1984; Boselli et al. 2012; Auld et al. 2013), and $B(\lambda, T_{\text{dust}}^{\text{MBB}})$ is the Planck function at a given temperature $T_{\text{dust}}^{\text{MBB}}$.

Integrating the flux density over a certain wavelength range provides the luminosity emitted by the dust at those wavelengths. For consistency we calculate the dust luminosity in the wavelength range from 8 to 1000 μm as usually used (Kennicutt 1998). Assuming an opacity $\kappa(\lambda)$ for the average dust grain mix, the dust mass can then be derived by:

$$M_{\text{dust}}^{\text{MBB}} = \frac{D^2}{\kappa(\lambda)} \frac{S(\lambda, T_{\text{dust}}^{\text{MBB}})}{B(\lambda, T_{\text{dust}}^{\text{MBB}})}, \quad (5.6)$$

(Hildebrand 1983) with D being the distance to the galaxy (in Mpc).

The opacity is usually approximated by a power-law over the IR wavelengths (see, e.g., Alton et al. 2004; Galliano et al. 2018). In our case, in order to be consistent with the grain physics of the THEMIS model, we fitted a power-law to the average opacity inferred by THEMIS (see Fig. 5.8), in the wavelength range $70 \leq \lambda/\mu\text{m} \leq 700$. We find that the opacity scales with wavelength as:

$$\kappa(\lambda) = \kappa_{250} (250/\lambda)^{1.790}, \quad (5.7)$$

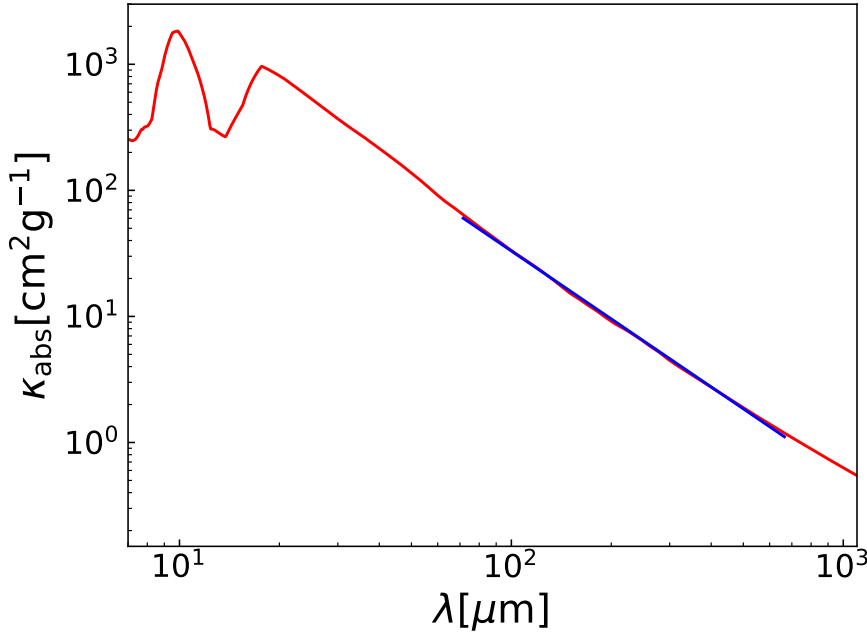


Figure 5.8: The average absorption coefficient calculated within the THEMIS dust model (red line). For the wavelength range $70 \leq \lambda/\mu\text{m} \leq 700$ we approximated the extinction law with a power-law (blue line) so that it can be used in the MBB calculations (see text for more details).

with λ given in μm and $\kappa_{250} = 6.40 \text{ cm}^2 \text{ g}^{-1}$.

We modelled the DustPedia galaxies with a single MBB using data at wavelengths $\lambda \geq 100 \mu\text{m}$, that is, every available observation among the IRAS (100 μm), PACS (100, 160 μm), MIPS (160 μm), SPIRE (250, 350, 500 μm) and *Planck* (350, 550 μm) wavebands. We avoided using fluxes below 100 μm in order to prevent the fitted SED from being polluted by emission from dust grains in non-thermal equilibrium. We also avoided fluxes above 550 μm so as to exclude possible contamination from synchrotron and free-free emission from low-luminosity radio galaxies. As in the case of CIGALE, a 10% uncertainty was added quadratically to the measured flux uncertainties (see Sect. 5.3.1). The fit was made using standard χ^2 minimisation techniques (Levenberg-Marquardt) allowing the dust temperature ($T_{\text{dust}}^{\text{MBB}}$) to range between 10 and 40 K. The SED of the MBB was convolved to the RSRF of each filter. In the case of the SPIRE bands, the RSRF for extended emission was used. An estimate of the uncertainty on the derived parameters is provided by performing a bootstrap analysis to our datasets by fitting 1000 SEDs for each galaxy. The mock fluxes are randomly drawn from a Gaussian distribution centred on the observed flux and with a standard-deviation identical to those observed. The uncertainty assigned to each of the two parameters ($T_{\text{dust}}^{\text{MBB}}$ and $M_{\text{dust}}^{\text{MBB}}$) is then defined as the standard deviation of the 1000 values derived from this procedure.

Out of the 875 DustPedia galaxies, 802 have at least three reliable measurements (with no major flags associated) in the wavelength range under consideration (100-600 μm) and could be fitted with a MBB. Out of these 802 galaxies, only 678 galaxies fulfilled our

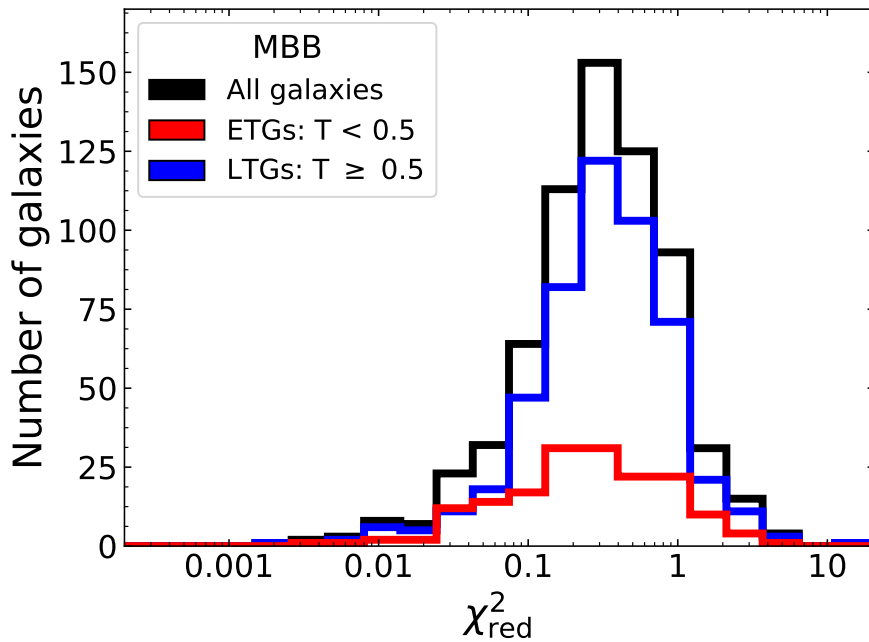


Figure 5.9: Distribution of the reduced χ^2 of the 678 galaxies modelled with a MBB scaled to the THEMIS dust model (black line). The distributions for the LTG and the ETG subsamples are also shown (blue and red lines respectively).

temperature boundary conditions (10-40 K) and gave a reasonable fit. The parameters derived for each galaxy are provided in the DustPedia archive while the mean values, per morphological type, for $M_{\text{dust}}^{\text{MBB}}$, and $T_{\text{dust}}^{\text{MBB}}$ are given in Table 5.2.

As in CIGALE, we explore the overall quality of the fits to the observations by examining the distribution of the χ_{red}^2 values. The χ_{red}^2 distribution is shown in Fig. 5.9. We find that the median value of the distribution (for the 678 modelled galaxies) is at 0.31 while it rises to 0.32 when only considering the 506 LTGs and drops down to 0.25 for the 172 ETGs. Out of the 678 modelled galaxies there are 22 ($\sim 3\%$) with $\chi_{\text{red}}^2 > 2$ and only four galaxies with $\chi_{\text{red}}^2 > 4$. Here, the small values of χ_{red}^2 (much smaller than unity) indicate that the model is ‘over-fitting’ the data. This is mainly due to the fact that the number of available observations is in many cases small, but also that the noise assigned to the fluxes is sufficiently large to allow for a poorly constrained model.

5.8 Comparison between CIGALE and MBB

While CIGALE does not provide a direct estimate for T_{dust} , it allows us to approximate it using the strength of the ISRF parametrized by U_{min} . Assuming that dust is heated by an ISRF with a MW like spectrum (Mathis et al. 1983), we can approximate T_{dust} by:

$$T_{\text{dust}}^{\text{CIGALE}} = T_{\text{o}} U_{\text{min}}^{(1/(4+\beta))}, \quad (5.8)$$

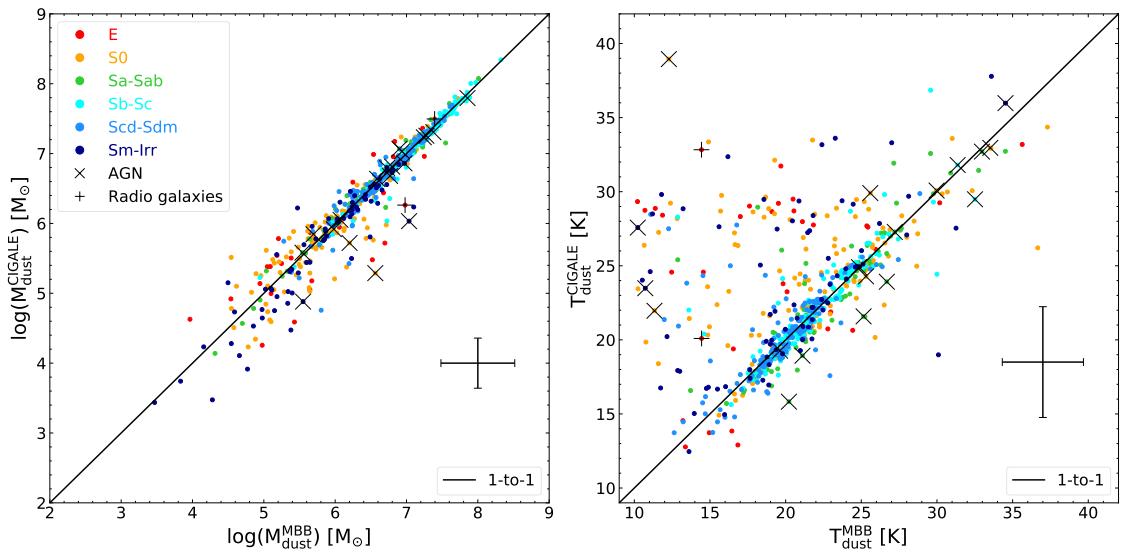


Figure 5.10: Comparison of M_{dust} (left panel) and T_{dust} (right panel), as derived from CIGALE (y-axis) and MBB (x-axis) modelling. The points are colour-coded according to the morphological type, while ‘+’ and ‘X’ symbols indicate strong radio jet galaxies and AGNs, respectively (see the inset in the left panel for the explanation of the different colours and symbols). The solid black line indicates the one-to-one relation. The average uncertainty is indicated in the lower-right corner of each plot.

(Aniano et al. 2012). Here, U_{min} is the minimum ISRF level heating the diffuse dust, $T_{\odot} = 18.3 \text{ K}$ is the dust temperature measured in the solar neighbourhood, and β is the dust emissivity index, which, for the THEMIS dust model, gets the value of 1.79 (see Sect. 5.7). The values of $T_{\text{dust}}^{\text{CIGALE}}$ derived for each galaxy are provided in the DustPedia archive while the mean values, per morphological type, are given in Table 5.2.

Having derived the dust masses and temperatures using the two methods described above (CIGALE and MBB) we can directly compare them for the 678 galaxies in common in the two sub-samples. We do so in Fig. 5.10, with the comparison of M_{dust} in the left panel and that of T_{dust} in the right panel. In each panel the symbols are colour-coded according to the morphological class.

The two different methods for estimating the dust properties compare fairly well, with the scatter generally increasing for less dusty objects (ETGs). This is evident in the dust masses (left panel of Fig. 5.10), with most of the deviant cases showing MBB dust masses higher than those derived by CIGALE. Differences become more prominent in the dust temperatures (right panel of Fig. 5.10) with CIGALE systematically estimating higher values compared to MBB for these galaxies. Some of the galaxies identified as AGNs and strong radio-sources are amongst the outliers, indicating that the models were not able to adequately fit the observations; there are only a few cases however.

For the majority of the most deviant cases, a visual inspection of the SEDs reveals that discrepancies are mainly due to a combination of two effects. First, the FIR-submm measurements, especially for the ETGs, come with large uncertainties due to the low level of emission. This allows CIGALE, which is constrained from a large

multi-wavelength dataset, greater ‘flexibility’ in fitting this part of the SED, in most cases ‘over-weighting’ MIR and FIR against submm measurements. This results in a bias favouring high temperatures for CIGALE compared to MBB modelling where only a small number of FIR-submm data points are fitted. Furthermore, a single MBB component fitted to the FIR-submm fluxes is only sensitive to the colder dust, missing a large fraction of dust heated to warmer temperatures. These are the effects that we see in Fig. 5.10 but also looking at the mean values of the dust temperature in Table 5.2. For galaxies with $0 < T < 8$ there is very good agreement between the two methods, well within the uncertainties, while the differences progressively become larger for earlier- and later-type galaxies. Overall, we conclude that the dust temperatures derived from CIGALE are more accurate than those from the MBB fitting. The dust temperatures obtained by CIGALE ($T_{\text{dust}}^{\text{CIGALE}}$) as a function of morphological type are discussed in more detail in Sect. 5.9.

5.9 Physical parameters as a function of the Hubble stage

The abundance of dust and gas in galaxies can reveal valuable information about their star-formation cycle and chemical evolution. The local environment is expected to play a significant role however, affecting the chemical evolution and the ISM content in individual galaxies (e.g., Casasola et al. 2004; Baldry et al. 2006; Fumagalli et al. 2009; Peng et al. 2010; De Lucia et al. 2012).

Although the general picture that local ETGs are poor in ISM (dust and gas) compared to less-evolved galaxies is widely accepted (e.g., Bettoni et al. 2003; Casasola et al. 2004; Boselli et al. 2014), a more detailed analysis is needed of the variation of the ISM content among galaxies of different morphological stages. The DustPedia sample is ideal for carrying out this analysis since it contains the most complete collection of local galaxies to date, spanning the full range of morphologies with sufficient multi-wavelength coverage such that an SED fitting analysis can be applied in a uniform way. Furthermore, measurements of the atomic hydrogen mass (M_{HI}) for a significant fraction of the DustPedia galaxies (711 out of 814 galaxies; see Table 5.2) allow us to investigate how the gas content of galaxies varies with morphology.

In the first three panels of Fig. 5.11 we investigate how the specific mass of dust ($M_{\text{dust}}^{\text{CIGALE}}/M_{\text{star}}$) and atomic gas ($M_{\text{HI}}/M_{\text{star}}$), as well as the specific star-formation rate (sSFR; $\text{SFR}/M_{\text{star}}$), vary with the morphology of the galaxy. In each panel the orange circles show the values of individual galaxies while the red diamonds and blue squares show the mean (also given in Table 5.3) and the median values for each morphological bin, respectively. The fourth panel from the top shows the variation of the dust-to-atomic-gas mass ratio as a function of morphological type. We see that $M_{\text{dust}}^{\text{CIGALE}}/M_{\text{star}}$, $M_{\text{HI}}/M_{\text{star}}$, and $\text{SFR}/M_{\text{star}}$ vary by about two orders of magnitude, whereas $M_{\text{dust}}^{\text{CIGALE}}/M_{\text{HI}}$ varies by one order of magnitude. Finally, the bottom panel shows the change in M_{star} , $M_{\text{dust}}^{\text{CIGALE}}$, M_{HI} , and SFR with Hubble stage as a fifth-order polynomial regression through the median values per Hubble stage bin. M_{star} , $M_{\text{dust}}^{\text{CIGALE}}$,

Table 5.3: Mean values of $M_{\text{dust}}^{\text{CIGALE}}$, M_{HI} , and SFR normalised to the M_{star} , as well as the $M_{\text{dust}}^{\text{CIGALE}}/M_{\text{HI}}$ ratio together with their associated standard deviation for different morphological bins.

T	$\log \langle \langle M_{\text{dust}}^{\text{CIGALE}}/M_{\text{star}} \rangle \rangle$	$\log \langle \langle M_{\text{HI}}/M_{\text{star}} \rangle \rangle$	$\log \langle \langle SFR/M_{\text{star}} \rangle \rangle$	$\log \langle \langle M_{\text{dust}}^{\text{CIGALE}}/M_{\text{HI}} \rangle \rangle$
-5	-4.23 ± 0.33	-2.00 ± 0.08	-11.70 ± 0.42	-2.31 ± 0.45
-4	-4.51 ± 0.52	-1.23 ± 0.05	-11.84 ± 0.48	-2.10 ± 0.41
-3	-4.02 ± 0.42	-1.76 ± 0.05	-11.29 ± 0.57	-2.15 ± 0.34
-2	-4.06 ± 0.35	-1.24 ± 0.09	-11.29 ± 0.17	-2.36 ± 0.20
-1	-3.75 ± 0.19	-1.29 ± 0.08	-11.02 ± 0.18	-1.84 ± 0.15
0	-3.67 ± 0.30	-1.04 ± 0.16	-10.72 ± 0.18	-1.93 ± 0.25
1	-3.57 ± 0.15	-1.14 ± 0.11	-10.37 ± 0.14	-1.86 ± 0.11
2	-3.39 ± 0.15	-1.29 ± 0.09	-10.32 ± 0.16	-1.67 ± 0.07
3	-3.13 ± 0.13	-0.78 ± 0.11	-10.10 ± 0.13	-2.04 ± 0.06
4	-3.02 ± 0.14	-0.62 ± 0.10	-10.07 ± 0.14	-2.16 ± 0.07
5	-2.90 ± 0.15	-0.48 ± 0.12	-9.86 ± 0.13	-2.28 ± 0.08
6	-2.77 ± 0.19	-0.20 ± 0.11	-9.83 ± 0.14	-2.29 ± 0.12
7	-2.73 ± 0.21	-0.02 ± 0.13	-9.78 ± 0.13	-2.53 ± 0.11
8	-2.77 ± 0.19	-0.07 ± 0.10	-9.85 ± 0.12	-2.46 ± 0.13
9	-2.96 ± 0.30	0.20 ± 0.15	-9.65 ± 0.14	-2.63 ± 0.36
10	-2.95 ± 0.39	0.41 ± 0.17	-9.54 ± 0.19	-2.41 ± 0.39
[-5.0, -3.5)	-4.29 ± 0.36	-1.66 ± 0.06	-11.73 ± 0.43	-2.24 ± 0.44
[-3.5, 0.5)	-3.88 ± 0.30	-1.23 ± 0.11	-11.06 ± 0.21	-2.05 ± 0.20
[0.5, 2.5)	-3.48 ± 0.15	-1.20 ± 0.10	-10.35 ± 0.15	-1.77 ± 0.09
[2.5, 5.5)	-3.00 ± 0.14	-0.60 ± 0.11	-9.99 ± 0.13	-2.15 ± 0.07
[5.5, 8.5)	-2.76 ± 0.20	-0.11 ± 0.11	-9.82 ± 0.13	-2.38 ± 0.12
[8.5, 10.0]	-2.95 ± 0.36	0.34 ± 0.17	-9.58 ± 0.18	-2.48 ± 0.39

M_{HI} , and SFR have been normalised to the maximum value obtained from each polynomial regression by: $3.9 \times 10^{10} M_{\odot}$, $1.2 \times 10^7 M_{\odot}$, $2.6 \times 10^9 M_{\odot}$ and $1.08 M_{\odot}/\text{yr}$, respectively.

From the bottom panel of Fig. 5.11, we see that the stellar mass (red line) takes its maximum value for E-type galaxies and varies slightly for galaxies with $T < 2$. For galaxies with $T > 2$, a sharp drop in stellar mass (of about two orders of magnitude) is observed. The HI mass (magenta line) varies slightly for galaxies with $T < 2$ (in a similar way as stellar mass), followed by a rise (of about one order of magnitude) and then a drop for galaxies with $T > 5$. The dust mass (orange line) and the SFR (cyan line) vary in a similar way with a continuous increase for ETGs and a decrease for later-type galaxies with a peak value for Sc-type galaxies. However, the real variation of the ISM content between different galaxies can only be appreciated if we consider galaxies of the same stellar mass. This is what we present in the first three panels by normalising $M_{\text{dust}}^{\text{CIGALE}}$, M_{HI} , and SFR, to the stellar mass of each galaxy.

A continuous increase of the dust mass (about two orders of magnitude, on average) is

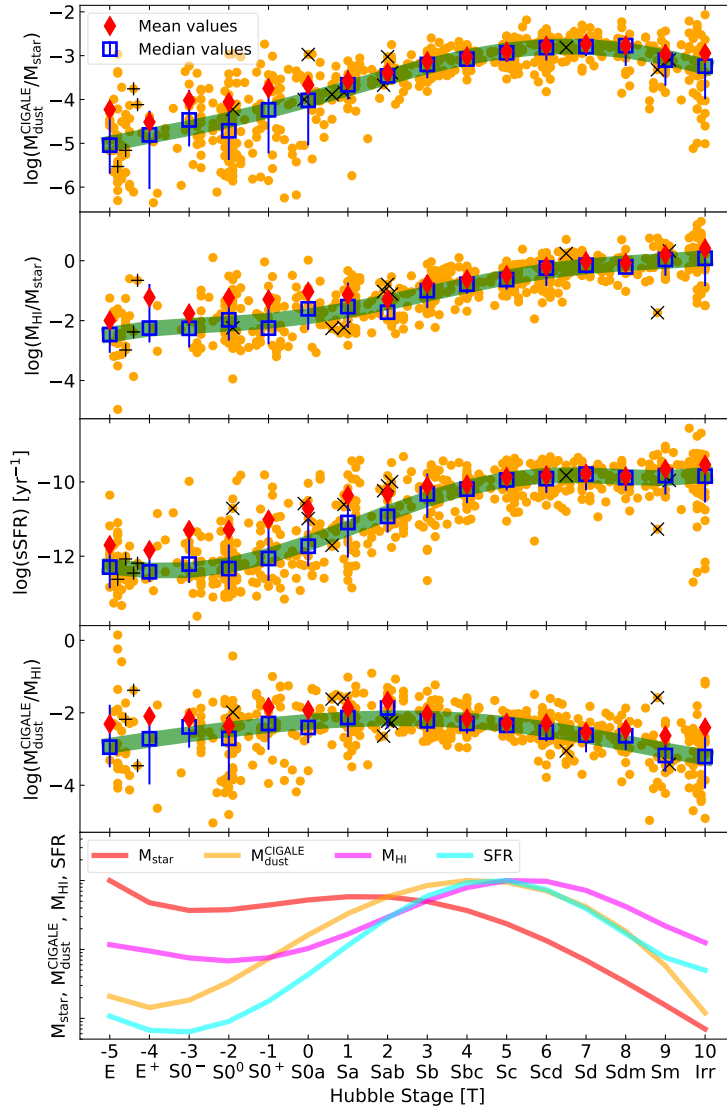


Figure 5.11: From top to bottom (first four panels): $M_{\text{dust}}^{\text{CIGALE}}/M_{\text{star}}$, $M_{\text{HI}}/M_{\text{star}}$, sSFR and $M_{\text{dust}}^{\text{CIGALE}}/M_{\text{HI}}$ as a function of Hubble stages (T). In each panel orange circles are individual galaxies, red diamonds are the mean values for each morphological bin, while blue squares are the median values. Error bars bracket the range between the 16th and 84th percentiles from the median. The green curves are fifth-order polynomial regressions to the median values (see Table 5.5 for the polynomial regression parameters). In each of these panels '+' and 'X' symbols indicate strong radio jet galaxies and AGNs, respectively. The last panel shows the variation in M_{star} , $M_{\text{dust}}^{\text{CIGALE}}$, M_{HI} , and SFR (red, orange, magenta, and cyan lines respectively) with morphology as being fitted with a fifth-order polynomial regression through the median values (see Table 5.5).

observed for galaxies with Hubble stages from -5 up to around 7, where $M_{\text{dust}}^{\text{CIGALE}}/M_{\text{star}}$ peaks, and then drops at larger Hubble stages (top panel). The continuous increase of the ratio is mainly due to the sharp increase in dust mass from $T = -5$ to $T = 5$ while from $T = 5 - 7$ it is mainly the drop in the stellar mass that causes the ratio to continue increasing. Subsequently, from $T = 7$ onwards, it is mainly the dust mass that takes over again with a sharp drop (see the orange and red lines in the bottom panel for the dust and the stellar mass changes).

The specific mass of the atomic gas content, on the other hand, shows a relatively flat behaviour for ETGs (being roughly constant and around 0.01 for galaxies with $T \sim 2$). This is mainly because both the stellar mass and the HI mass show similar trends for these types of galaxies. Meanwhile, the decrease in stellar mass and a mild increase of the atomic gas mass for galaxies with $2 < T < 7$ is the main driver of the increase of the $M_{\text{HI}}/M_{\text{star}}$ ratio of about one order of magnitude. The sharp decrease in the stellar mass for galaxies beyond $T > 7$ then compensates the drop in the gas mass causing the $M_{\text{HI}}/M_{\text{star}}$ ratio to continue increasing (to about unity) but with a slower rate.

The sSFR remains approximately constant for earlier-type galaxies ($T < -2$). This is because, as we see from the bottom panel, M_{star} and SFR follow roughly the same trend. For galaxies up to $T = 5$ though, a sharp increase in SFR and a mild decrease in M_{star} (cyan and red lines, respectively, in the bottom panel) results in a sharp increase in sSFR. For later morphological types, M_{star} and SFR follow similar trends resulting in a roughly constant sSFR. The dust-to-gas mass ratio obtains its maximum value around $T = 2$. The rise in the earlier types of galaxies comes from the sharp increase in the dust mass compared to the gas mass which remains approximately constant. Beyond $T = 5$, both the dust and the gas mass drop, but it is the dust mass that drops faster causing the slow drop in the $M_{\text{dust}}^{\text{CIGALE}}/M_{\text{HI}}$ ratio. This behaviour is similar to the results previously presented for the atomic gas mass as a function of morphology in [Draine et al. \(2007\)](#) and [Cortese et al. \(2012\)](#) for SINGS ([Kennicutt et al. 2003](#)) and *Herschel* Reference Survey (HRS, [Boselli et al. 2010b](#)) galaxies respectively. In these studies, the ratio $M_{\text{dust}}/M_{\text{HI}}$ peaks for Sab galaxies (around $T = 2$) and decreases when going either to ETGs or irregular galaxies.

In [Fig. 5.12](#) we show how dust temperature, as obtained by CIGALE, varies with morphology. Although a large scatter is present in each morphological bin, a clear trend is evident with ETGs heating the dust up to higher temperatures (~ 30 K) compared to LTGs where a drop in dust temperature (by ~ 10 K) is observed. These results compare fairly well with the findings of [Skibba et al. \(2011\)](#) for ten ETGs from KINGFISH, where these latter authors found an average dust temperature of 30 K. A sharp rise in temperature (back to ~ 30 K) is then seen for Sm-Irr galaxies. Here, we basically see the effect of the intense ISRF seen in ETGs being very efficient in heating the dust up to high temperatures. This is easy to achieve in ETGs since dust, in most cases, is found in the very centre of the galaxies where the ISRF intensity is very strong. In LTGs with $0 < T < 8$ on the other hand, dust found in the disk of the galaxies is distributed in a more diffuse way, away from the heating sources, keeping the dust at low temperatures (see, e.g., [Xilouris et al. 2012](#)). For Sm-Irr galaxies, where merging processes shape the morphology and trigger star-formation activity, dust is found in the vicinity of star-forming sites giving rise to the higher dust temperatures ([Boselli et al. 2010a](#);

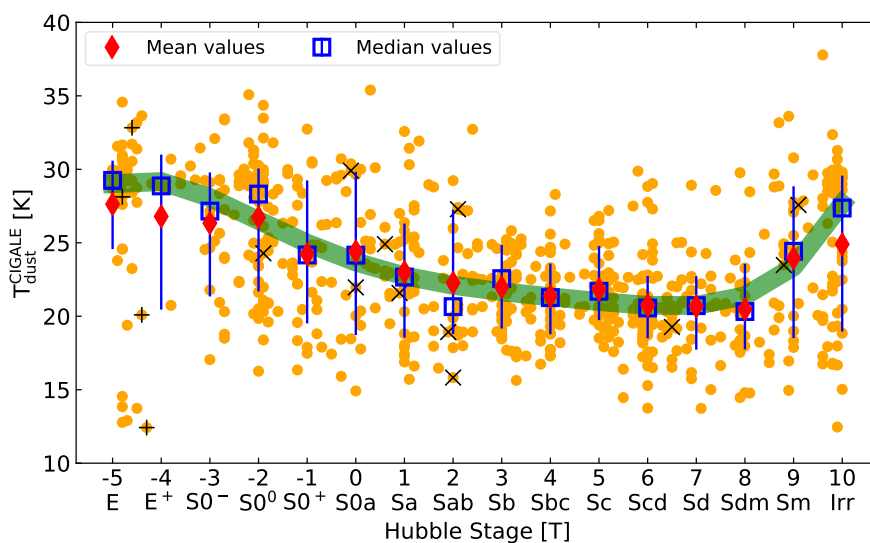


Figure 5.12: Dust temperature for galaxies of different Hubble stages, as derived from CIGALE. Orange circles are individual galaxies, red diamonds are the mean values for each morphological bin, while blue open squares are the median values. Error bars bracket the range between the 16th and 84th percentiles from the median. The thick green curve is a fifth-order polynomial regression to the median values (see Table 5.5). The ‘+’ and ‘X’ symbols indicate strong radio jet galaxies and AGNs respectively.

Rémy-Ruyer et al. 2015). For these galaxies a potential submm excess is detected (500 and 850 μm residuals in Fig. 5.2). This effect is expected to account for some extra amount of cold dust (Galametz et al. 2009, 2010; Ciesla et al. 2014), undetected by the CIGALE SED fitting.

5.10 Evolution of small a-C(:H)

Dust forms and grows in the circumstellar shells of evolved stars, for example asymptotic giant branch (AGB) and red giant stars or in the ejecta of core-collapse supernovae (Galliano et al. 2018), whilst acting as a catalyst for molecular hydrogen (H_2) formation. On the other hand, the smallest grains, which are primarily carbonaceous nanoparticles, are much more susceptible to local conditions. This can result in their (photo/thermal) processing and possibly their complete destruction if the local physical conditions (gas temperature and density, radiation field hardness and intensity) are extreme enough (see Jones 2004, for a review). Understanding the link between the dust properties and star-formation can provide useful information for galaxy evolution studies. From CIGALE, we were able to obtain an estimate of the mass fraction of small a-C(:H) grains, q_{hac} , for our galaxy sample. We note however that since this parameter may not be well constrained in some cases (see the mock analysis in Sect. 5.4), interpretation of the results should be considered with caution. Figure 5.13 shows how q_{hac} varies with the sSFR and morphological type. The q_{hac} mass fraction is normalised to the fraction estimated for the diffuse Galactic ISM ($\sim 17\%$, Compiègne et al. 2011), and varies by

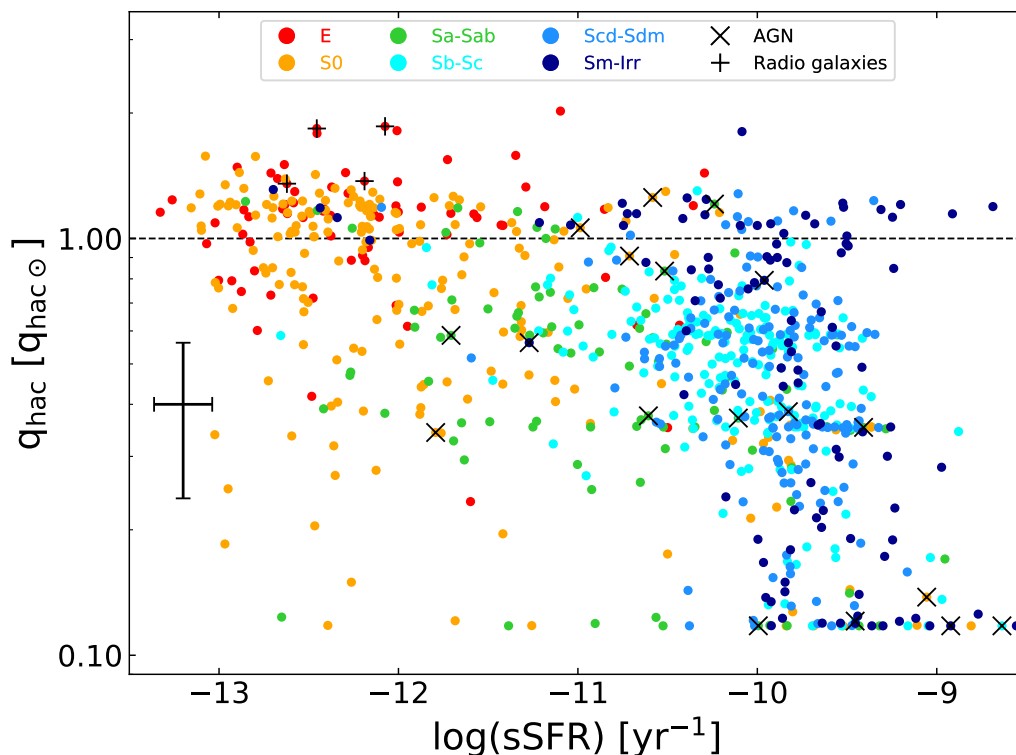


Figure 5.13: The small a-C(:H) mass fraction (q_{hac}) as a function of sSFR. The parameter q_{hac} is expressed in units of $q_{\text{hac}\odot}$, $q_{\text{hac}\odot} = 17\%$. Each point represents a galaxy and is colour-coded according to morphology type, while galaxies hosting AGNs or strong radio-jets are indicated with an 'X' or a '+', respectively. The large cross is the typical uncertainty on the data.

one order of magnitude, with a typical error of 16%. Despite the large scatter, we find a mild correlation between q_{hac} and sSFR ($\rho = -0.57$). Galaxies with low sSFR up to $\log(\text{sSFR}) \sim -10.5$ have roughly constant q_{hac} values, with fractions similar or slightly higher than the one estimated for the Galactic ISM. Subsequently, q_{hac} drops very fast for galaxies with high sSFR, $\log(\text{sSFR}) > -10.5$. Rémy-Ruyer et al. (2015) found a similar decreasing trend between the PAH abundance and the sSFR for two samples of late-type galaxies (109 in total), DGS (Dwarf Galaxy Survey, Madden et al. 2013) and KINGFISH.

The behaviour seen in Fig. 5.13 indicates that galaxies at the beginning of their evolutionary stage have low mass fractions of small grains, and that as galaxies evolve, more metals become available in the ISM resulting in more efficient grain growth, and thus higher q_{hac} fractions. The majority of low-mass LTGs (Sm-Irr) in Fig. 5.13 have on average higher sSFRs (see Table 5.3), and significantly lower q_{hac} values. In this case, galaxies with high sSFR possess stronger UV radiation fields, often resulting in the efficient destruction of the small grains in the ISM. As 'typical' spiral galaxies grow in stellar mass and gas, their a-C(:H) mass fractions also increase, with q_{hac} reaching values as high as $q_{\text{hac}\odot}$, and then remain roughly constant for the later evolutionary stages. This behaviour indicates a balance between dust destruction and dust growth

([Mattsson et al. 2014](#)), consistent with the findings of [De Vis et al. \(2019\)](#), who studied the variation of the dust-to-metal ratio for a subsample of ~ 500 DustPedia galaxies. They found that a chemical evolution model with a significant contribution from grain growth describes DustPedia galaxies fairly well, with the more evolved galaxies having a constant dust-to-metal ratio, while less evolved galaxies have on average 2.5 times lower dust-to-metal ratios.

5.11 The stellar populations and the dust content in nearby galaxies

Knowledge of the different components of the stellar populations in galaxies and the way their released energy interacts with the dust particles is a crucial in understanding the full picture of galaxy formation and evolution ([Smith et al. 2012b](#); [Boquien et al. 2014](#); [Bendo et al. 2015](#)). Here we explore the importance of the old and the young stellar components of the galaxies as parametrized by CIGALE. CIGALE distinguishes between two classes of stars, one of a variable age accounting for the average old stellar population and one of a younger age (t_{flex} as parametrized in the case of a flexible-delayed SFH used here) accounting for the young stellar population. The old stellar population was given the freedom to obtain values between five different ages ranging from 2 to 12 Gyr (see [Table 5.1](#), t_{gal}) while the age of 200 Myr was fixed for the young stellar population. The choice of a fixed young stellar age was dictated by the need to keep the total number of parameters in CIGALE to a minimum and from the fact that varying the age will not significantly alter the shape of the SED and thus the luminosity of this component (see [Ciesla et al. 2016](#), and their [Fig. 3](#) where SEDs of a range of t_{trunc} values are plotted).

In [Fig. 5.14](#) we present the median SEDs fitted by CIGALE for six main morphological types. In each panel the median SED for each Hubble type is indicated as a black solid curve. The red and blue curves in the optical part of the SED are the median SEDs of the unattenuated old and young stellar populations, respectively, while the orange and green curves in the MIR-submm part are the median SEDs indicating the diffuse dust and the dust in PDRs, respectively. In all curves the shaded areas bracket the 16th and 84th percentiles around the median. A first visual inspection of the SEDs of different Hubble types shows that the young stellar population becomes less dominant in comparison to the old stellar population, when following the evolutionary track from the late-type and irregular galaxies to the ETGs. This can be quantified by calculating the relative contribution of each component to the total bolometric luminosity of each galaxy, something that we discuss in [Sect. 5.11.1](#).

In the FIR-submm part of the spectrum, we see that for all types of galaxies the emission is dominated by the diffuse dust component (orange curve) with the PDR dust (green curve) making up only a small fraction and mainly contributing to the MIR emission. In the cases of E- and Sm-Irr-type galaxies in particular, the PDR dust emission is negligible with the MIR emission composed mainly of the superposition of the diffuse dust emission and the emission originating from the old stellar population. The diffuse dust emission progressively becomes a significant part of the bolometric luminosity of the

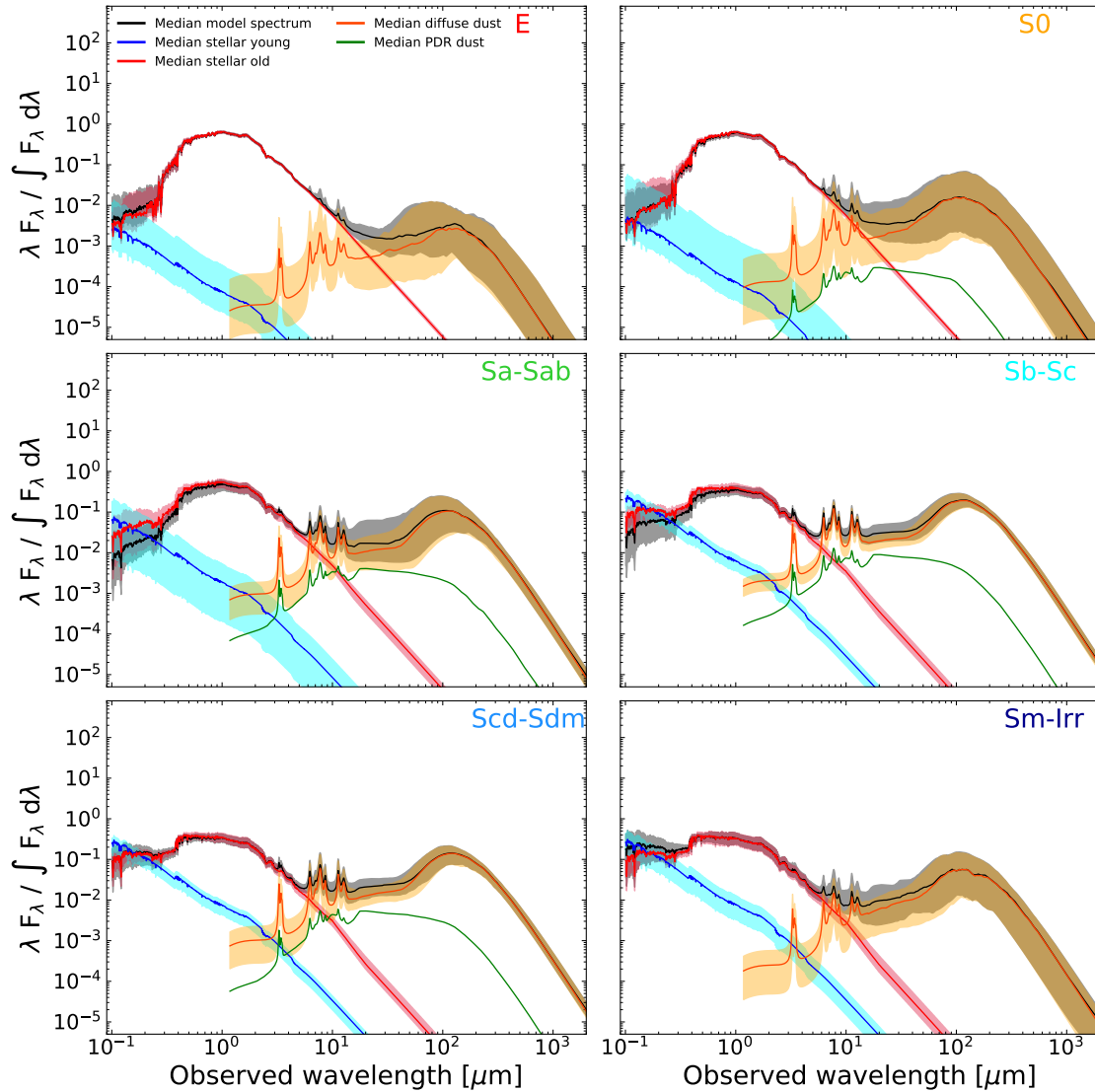


Figure 5.14: Template SEDs for the six main morphological classes as derived by CIGALE. The median SED of each sub-class is shown as a black curve while the unattenuated SEDs of the old and the young stars are shown as red and blue curves, respectively. The orange curve indicates the median spectrum of the diffuse dust, while the green curve shows the emission from PDRs. The shaded areas represent the range of the 16-84th percentiles to the median value (except for the case of the PDR spectra, where for clarity we refrain from presenting the full range of SEDs). For each subsample, the 10% most deviant SEDs have been excluded (see also the template SEDs presented in [Bianchi et al. 2018](#)).

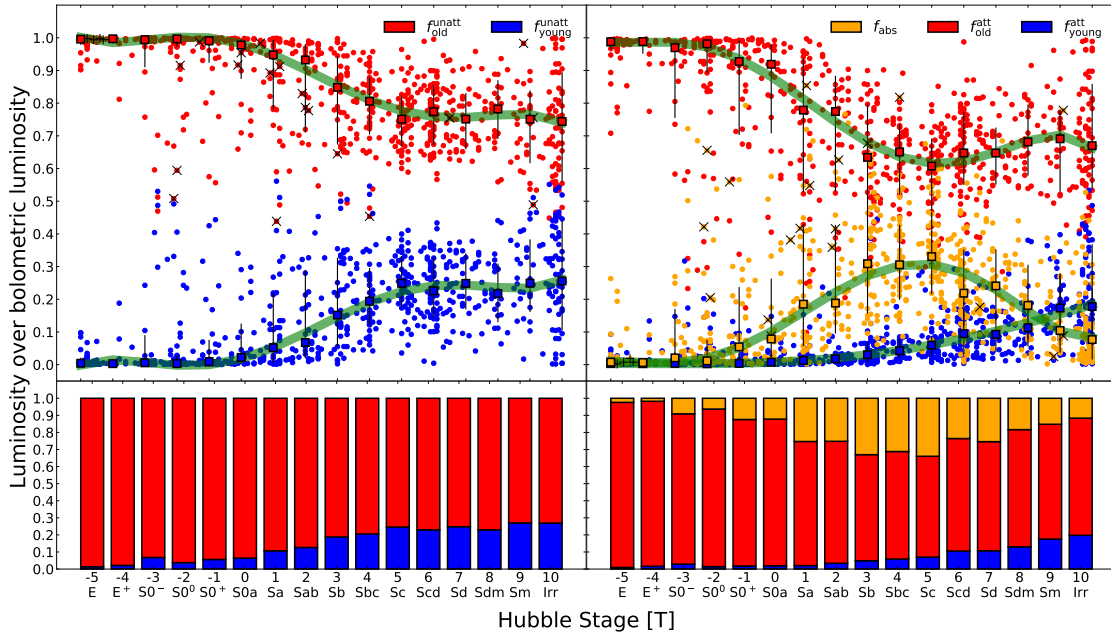


Figure 5.15: Left: Ratio of the unattenuated luminosity of the old and the young stellar components to the bolometric luminosity (red and blue circles, respectively; top-left panel) along with the respective stacked-bar plots of the mean values (bottom-left panel). Right: Ratio of the attenuated luminosity of the old and the young stellar components to the bolometric luminosity (red and blue circles, respectively) together with the ratio of the dust luminosity to the bolometric luminosity (orange circles; top-right panel) along with the respective stacked-bar plots of the mean values (bottom-right panel). Square symbols in the top panels are the median values for a specific Hubble stage bin while the bars indicate the 16th and 84th percentiles range. The thick green curves are the fifth-order polynomial regression to the median values (see Table 5.5 for the polynomial regression parameters). Galaxies hosting an AGN or strong radio jets are marked with an 'X' or a '+', respectively, for the old stellar population only (red circles) in the top-left panel, and for the dust luminosity only (orange circles) in the top-right panel.

galaxy when moving along the evolutionary track from E to Sb-Sc but then it becomes less prominent in later-type galaxies. As a result of the large quantities of dust grain material in these galaxies a severe extinction is observed (especially evident in the UV wavelengths, below $\sim 0.4 \mu\text{m}$). This is a striking feature in the SEDs of Sa-Sab, and Sb-Sc galaxies where the unattenuated SEDs of both the old and the young components (red and blue, respectively) exceed the 'observed' SED of the galaxy (black curve). In E and S0 galaxies the extinction is minimal with both unattenuated curves being found to be below the observed SED, while for Scd-Sdm and Sm-Irr galaxies it is only the young stars that suffer from significant attenuation at UV wavelengths below $\sim 0.2 \mu\text{m}$.

5.11.1 Old and young stellar populations in galaxies

Investigating the relative contribution of the old and the young stellar components to the bolometric luminosity for galaxies of different morphological types as well as the effect of the different stellar populations in the dust heating is a difficult task. This is because the light originating from the stars cannot be observed directly due to its attenuation by the dust. The only way to overcome this problem is by exploiting the information hidden in the SEDs using appropriate methods that simultaneously treat the stellar and dust emission. We do this based on the parametrization of the stellar populations and the dust emission obtained by fitting CIGALE to the DustPedia galaxies. This is shown in the top-left panel of Fig. 5.15 with the ratio of the unattenuated luminosities (i.e., the intrinsic luminosities) of the two stellar components (old and young) to the bolometric luminosity ($f_{\text{old}}^{\text{unatt}} = L_{\text{old}}^{\text{unatt}}/L_{\text{bolo}}$, $f_{\text{young}}^{\text{unatt}} = L_{\text{young}}^{\text{unatt}}/L_{\text{bolo}}$) plotted as red and blue circles respectively. What is immediately evident is the dominant role of the old, more evolved, stars in the total luminosity. Independent of the morphology of the galaxy, on average, the old stellar component dominates the bolometric luminosity of the galaxy, contributing more than $\sim 75\%$. The luminosity of the ETGs ($T < 0.5$) is the most extreme example, dominated by the emission of the old stars and with only a small contribution (maximum of $\sim 10\%$ at $T = 0$) from the young stars (see Table 5.4). For a detailed discussion on the contribution of old and young stars on the luminosity of ETGs (focusing on the different behaviours of the two ‘classical’ subsamples of elliptical and lenticular galaxies) we refer to [Cassarà et al. \(2019\)](#)). For morphological types in the range $T = 0 - 5$, there is a gradual rise in the contribution of the young stars to the bolometric luminosity reaching about 25%, while this value remains practically constant for morphological types $T > 5$. The scatter in each morphological bin is relatively significant, though a clear trend is visible, as discussed above.

Some galaxies, of various Hubble stages, show values of the relative luminosities of the different stellar components to the bolometric luminosities, reaching up to 50%; for example NGC 1222, NGC 1377, ESO 097-013, ESO 493-016, NGC 2993, NGC 4194, NGC 6300, and NGC 7714. These are all galaxies showing extreme values of SFR, well above the average value for each morphological bin. The bottom-left panel in Fig. 5.15 shows the stacked bars of the mean values per Hubble stage with the exact mean values provided in Table 5.4 (columns $f_{\text{old}}^{\text{unatt}}$ and $f_{\text{young}}^{\text{unatt}}$).

5.11.2 The heating of dust by the different stellar populations

The presence of large quantities of dust material throughout the galaxy affects how the galaxy is observed, by extinguishing the light originating from the different stellar populations. The lost energy is deposited into the dust giving rise to the luminosity at FIR wavelengths. This interplay between stars and dust is presented in the top-right panel of Fig. 5.15, in its simplest way, for galaxies of different Hubble stages. The red and blue circles now indicate the luminosity attenuated by dust, normalised to the bolometric luminosity of each galaxy, for the old and the young stars, respectively ($f_{\text{old}}^{\text{att}} = L_{\text{old}}^{\text{att}}/L_{\text{bolo}}$, $f_{\text{young}}^{\text{att}} = L_{\text{young}}^{\text{att}}/L_{\text{bolo}}$). Comparing with the top-left panel of Fig. 5.15, a decrease in luminosity is observed for both stellar populations, which is most important

Table 5.4: Mean luminosity ratios of the stellar and dust components of galaxies with different Hubble stages (T). Given that L_{bolo} is the bolometric luminosity, L_{dust} the dust luminosity, $L_{\text{old}}^{\text{unatt}}$ and $L_{\text{young}}^{\text{unatt}}$ the unattenuated luminosity of the old and the young stars, $L_{\text{old}}^{\text{att}}$ and $L_{\text{young}}^{\text{att}}$ the attenuated luminosity of the old and the young stars, and $L_{\text{old}}^{\text{abs}}$ and $L_{\text{young}}^{\text{abs}}$ are the luminosities of the old and the young stars absorbed by dust, we define the following fractions: $f_{\text{old}}^{\text{unatt}} = \frac{L_{\text{old}}^{\text{unatt}}}{L_{\text{bolo}}}$, $f_{\text{young}}^{\text{unatt}} = \frac{L_{\text{young}}^{\text{unatt}}}{L_{\text{bolo}}}$, $f_{\text{old}}^{\text{att}} = \frac{L_{\text{old}}^{\text{att}}}{L_{\text{bolo}}}$, $f_{\text{young}}^{\text{att}} = \frac{L_{\text{young}}^{\text{att}}}{L_{\text{bolo}}}$, $f_{\text{abs}} = \frac{L_{\text{dust}}}{L_{\text{bolo}}}$, $F_{\text{old}}^{\text{att}} = \frac{L_{\text{old}}^{\text{att}}}{L_{\text{unatt}}^{\text{old}}}$, $F_{\text{old}}^{\text{abs}} = \frac{L_{\text{old}}^{\text{abs}}}{L_{\text{unatt}}^{\text{old}}}$, $F_{\text{young}}^{\text{att}} = \frac{L_{\text{young}}^{\text{att}}}{L_{\text{unatt}}^{\text{young}}}$, $F_{\text{young}}^{\text{abs}} = \frac{L_{\text{young}}^{\text{abs}}}{L_{\text{unatt}}^{\text{young}}}$, $S_{\text{old}}^{\text{abs}} = \frac{L_{\text{old}}^{\text{abs}}}{L_{\text{dust}}}$, and $S_{\text{young}}^{\text{abs}} = \frac{L_{\text{young}}^{\text{abs}}}{L_{\text{dust}}}$.

T	$f_{\text{old}}^{\text{unatt}}$	$f_{\text{young}}^{\text{unatt}}$	$f_{\text{old}}^{\text{att}}$	$f_{\text{young}}^{\text{att}}$	f_{abs}	$F_{\text{old}}^{\text{att}}$	$F_{\text{old}}^{\text{abs}}$	$F_{\text{young}}^{\text{att}}$	$F_{\text{young}}^{\text{abs}}$	$S_{\text{old}}^{\text{abs}}$	$S_{\text{young}}^{\text{abs}}$
-5	0.99	0.01	0.97	0.01	0.02	0.98	0.02	0.84	0.16	0.91	0.09
-4	0.98	0.02	0.97	0.01	0.02	0.99	0.01	0.87	0.13	0.90	0.10
-3	0.93	0.07	0.88	0.03	0.09	0.93	0.07	0.66	0.34	0.84	0.16
-2	0.96	0.04	0.92	0.02	0.06	0.95	0.05	0.73	0.27	0.88	0.12
-1	0.94	0.06	0.86	0.02	0.12	0.90	0.10	0.55	0.45	0.84	0.16
0	0.94	0.06	0.86	0.02	0.12	0.91	0.09	0.52	0.48	0.79	0.21
1	0.89	0.11	0.73	0.02	0.25	0.79	0.21	0.31	0.69	0.76	0.24
2	0.87	0.13	0.72	0.03	0.25	0.80	0.20	0.30	0.70	0.69	0.31
3	0.81	0.19	0.62	0.05	0.33	0.76	0.24	0.23	0.77	0.59	0.41
4	0.79	0.21	0.63	0.06	0.31	0.79	0.21	0.28	0.72	0.54	0.46
5	0.75	0.25	0.59	0.07	0.34	0.78	0.22	0.28	0.72	0.48	0.52
6	0.77	0.23	0.65	0.11	0.24	0.85	0.15	0.45	0.55	0.47	0.53
7	0.75	0.25	0.64	0.11	0.25	0.85	0.15	0.42	0.58	0.44	0.56
8	0.77	0.23	0.69	0.13	0.18	0.89	0.11	0.55	0.45	0.44	0.56
9	0.73	0.27	0.67	0.18	0.15	0.91	0.09	0.67	0.33	0.40	0.60
10	0.73	0.27	0.68	0.20	0.12	0.94	0.06	0.74	0.26	0.44	0.56
[-5.0, -3.5)	0.98	0.02	0.97	0.01	0.02	0.98	0.02	0.85	0.15	0.90	0.10
[-3.5, 0.5)	0.95	0.05	0.89	0.02	0.09	0.93	0.07	0.64	0.36	0.85	0.15
[0.5, 2.5)	0.88	0.12	0.72	0.03	0.25	0.80	0.20	0.31	0.69	0.73	0.27
[2.5, 5.5)	0.78	0.22	0.61	0.06	0.33	0.78	0.22	0.27	0.73	0.53	0.47
[5.5, 8.5)	0.77	0.23	0.66	0.11	0.23	0.86	0.14	0.46	0.54	0.45	0.55
[8.5, 10.0]	0.73	0.27	0.68	0.19	0.13	0.93	0.07	0.72	0.28	0.42	0.58

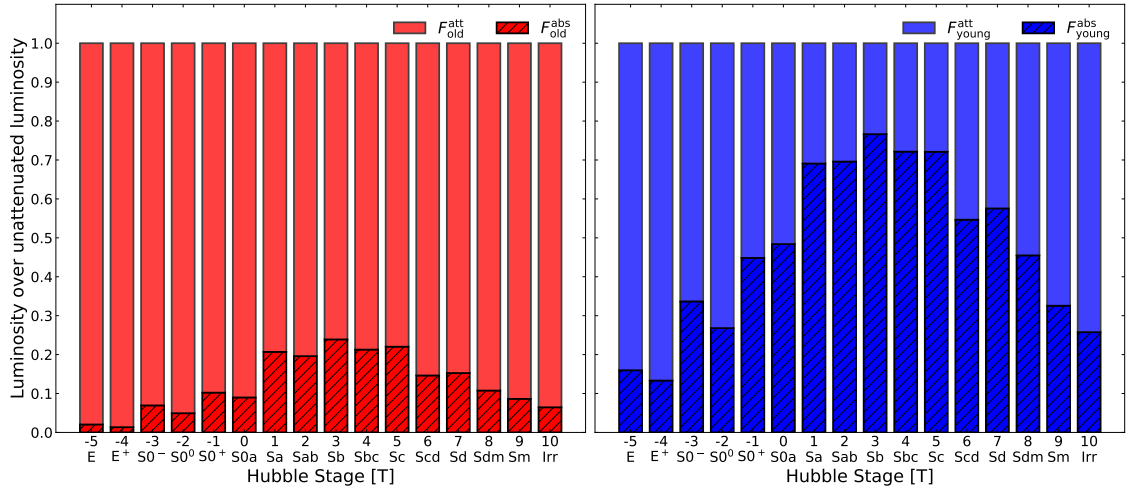


Figure 5.16: Mean values, per Hubble stage bin, of the fraction of the luminosity of the old and the young stellar components (left and right panels, respectively) used for the dust heating. In each panel the mean value of the ratio of the luminosity absorbed by the dust to the unattenuated luminosity of the specific stellar component (F_{old}^{abs} , F_{young}^{abs}) is shown as crossed bars, while the mean value of the ratio of the attenuated luminosity of the specific stellar component to the unattenuated luminosity (F_{old}^{att} , F_{young}^{att}) is shown as solid bars. The mean values are provided in Table 5.4.

in intermediate Hubble stages ($1 \leq T \leq 7$). This energy is absorbed by the dust and re-emitted in the IR and submm wavelengths giving rise to the dust luminosity (orange circles; $f_{abs} = L_{dust}/L_{bolo}$).

The bottom-right panel in Fig. 5.15 shows the stacked bars of the mean value per Hubble stage for the three components (old stars, young stars and dust) with the exact mean values provided in Table 5.4 (columns f_{old}^{att} , f_{young}^{att} and f_{abs}). What is interesting to notice from this plot is the continuous, monotonic increase of f_{young}^{att} when following the Hubble sequence from E to Irr galaxies reaching maximum mean values of 20% for Irr galaxies. Both the young and the old stars are mostly affected by dust in intermediate spiral galaxies ($1 \leq T \leq 7$) with a drop of more than 15% in their intrinsic luminosities.

To further investigate the efficiency of the two stellar populations in the heating of the dust, we calculated the ratios of the attenuated and the absorbed (by the dust) luminosities in each stellar component to the unattenuated luminosity of the specific component ($F_{old}^{att} = L_{old}^{att}/L_{old}^{unatt}$ and $F_{old}^{abs} = L_{old}^{abs}/L_{old}^{unatt}$ for the old stellar population and $F_{young}^{att} = L_{young}^{att}/L_{young}^{unatt}$ and $F_{young}^{abs} = L_{young}^{abs}/L_{young}^{unatt}$ for the young stellar population). This is presented in the stacked bar graphs of Fig. 5.16, with the left panel for the relative contribution of the old stars and the right panel for the young stars. In each panel the shaded bars show the fraction of the luminosity of each stellar component that is absorbed by the dust and contribute to its heating, while the remaining is the fraction of the luminosity that is left as direct light emitted by the stars. For the case of the old stellar population, up to $\sim 24\%$ of the luminosity of the stars of Sb galaxies contributes to heating dust, with a very small fraction of their luminosity (below $\sim 10\%$) contributing to this heating for the two extremes of the Hubble stages (E and Irr). In the

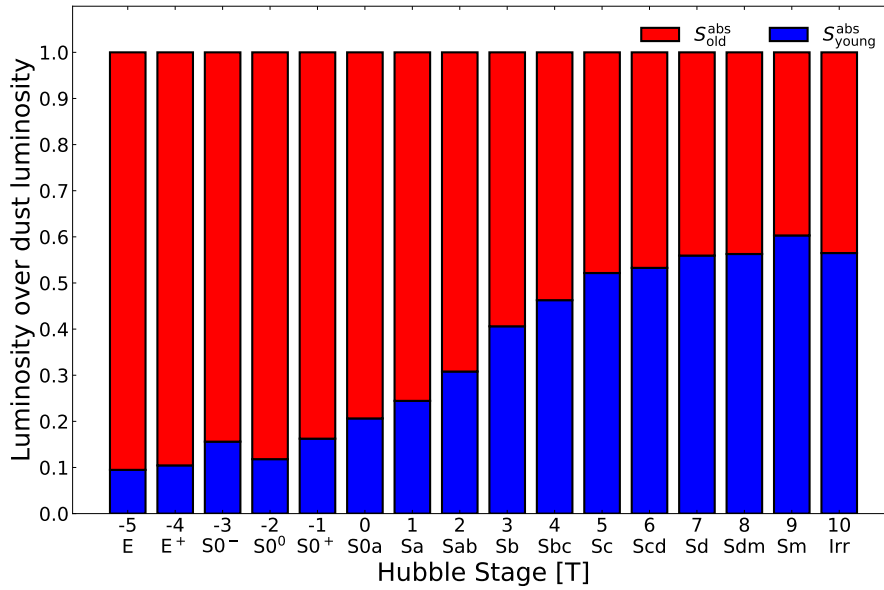


Figure 5.17: The mean values per Hubble stage bin, of the ratios of the luminosity absorbed by dust, for a specific stellar component to the dust luminosity. Red and blue bars refer to the old and the young stellar components ($S_{\text{old}}^{\text{abs}}$ and $S_{\text{young}}^{\text{abs}}$), respectively. The mean values are provided in Table 5.4.

case of young stars on the other hand, a higher, significant fraction of their luminosity contributes to dust heating, which can be up to $\sim 77\%$, again for Sb galaxies, with more than $\sim 15\% - 20\%$ of their luminosity going into dust heating for the extreme Hubble stages.

The relative contribution of the old and the young stars to the dust heating is shown in Fig. 5.17 with the absorbed luminosities to the dust luminosity ($S_{\text{old}}^{\text{abs}} = L_{\text{old}}^{\text{abs}}/L_{\text{dust}}$, and $S_{\text{young}}^{\text{abs}} = L_{\text{young}}^{\text{abs}}/L_{\text{dust}}$ for the old and the young stellar populations respectively) plotted as stacked bars (red and blue, respectively). Here, it is interesting to notice the gradual increase in the contribution of the young stars to the dust heating from only $\sim 10\%$ for E galaxies to $\sim 60\%$ for later-type galaxies (see Table 5.4 for the exact values). To obtain a clearer view of the dust-heating processes, we look at the relation between the $S_{\text{young}}^{\text{abs}}$ and the sSFR. The sSFR is sensitive to the different heating sources in galaxies and can adequately trace the hardness of the UV radiation field (Ciesla et al. 2014).

Figure 5.18 shows the correlation between the sSFR and $S_{\text{young}}^{\text{abs}}$. We find a tight correlation with a Spearman's coefficient of $\rho = 0.95$. The relation between the two quantities can be approximated with a power-law function:

$$\log S_{\text{young}}^{\text{abs}} = 0.44 \times \log \text{sSFR} + 6.06, \quad (5.9)$$

Galaxies with $\log \text{sSFR} > -10.5$ have high $S_{\text{young}}^{\text{abs}}$ fractions, indicating that dust is mainly heated by UV radiation emitted by the young stellar population, whereas galaxies with low $\log \text{sSFR}$ have extremely low heating fractions. A similar correlation was reported by De Looze et al. (2014) and Viaene et al. (2017). They used radiation transfer simulations

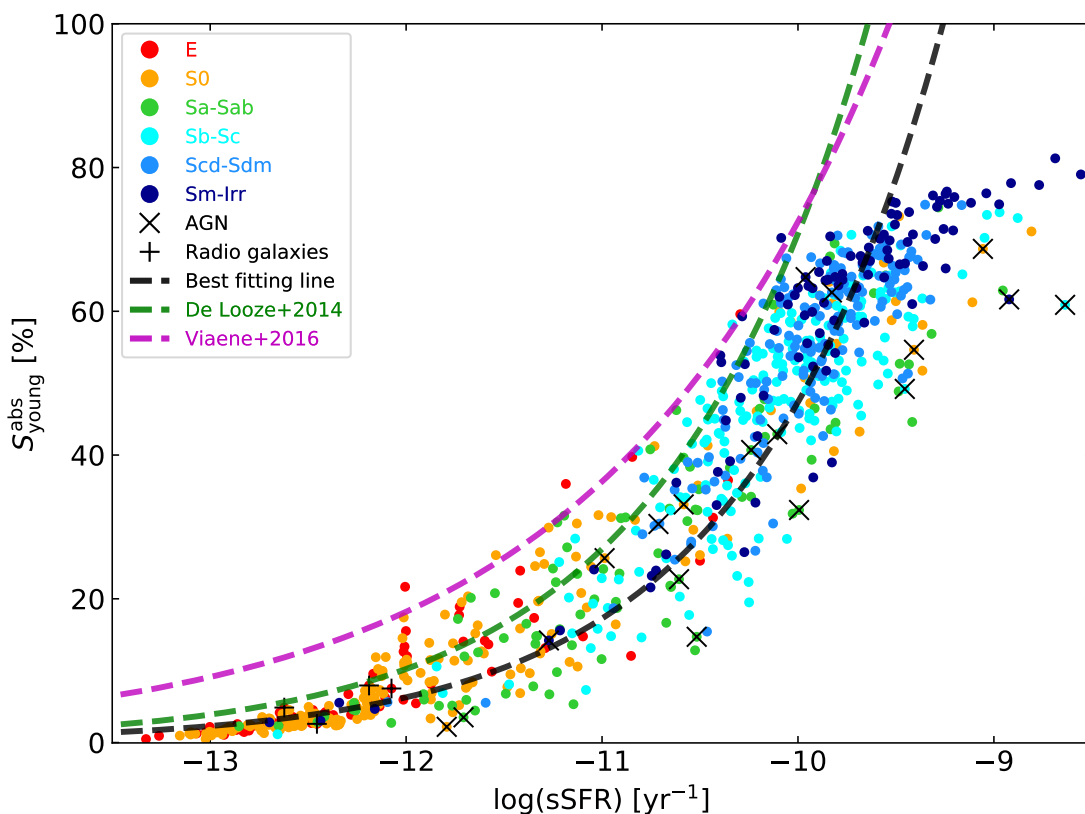


Figure 5.18: Correlation between $S_{\text{young}}^{\text{abs}}$ and sSFR. Each point represents a galaxy and is colour-coded according to morphological type. Galaxies hosting AGNs and strong radio jets are marked with an 'X' or a '+', respectively. The black dashed line is the best fitted powerlaw. For comparison, the best fitted lines for M 51 (green line: [De Looze et al. 2014](#)) and HRS (magenta line: [Viaene et al. 2016](#)) are shown.

to quantify the dust heating fraction due to the young stellar population (≤ 100 Myr) for M 51 and the Andromeda galaxy, respectively. They found that high heating fractions correspond to high levels of sSFR. Furthermore, [Viaene et al. \(2016\)](#) also reported a similar trend between the UV dust heating fraction and the sSFR for 239 LTGs of the HRS sample. A clear offset can be seen in Fig. 5.18 between the results of this work (black line) and the work of [De Looze et al. \(2014\)](#) (green line) and [Viaene et al. \(2016\)](#) (magenta line). We attribute this offset to the different methods used to estimate the sSFR and the heating fraction. [De Looze et al. \(2014\)](#) estimated the SFR of M 51 on a pixel-by-pixel basis, using the MAPPINGS ([Groves et al. 2004](#)) SED templates of the ionizing stars (≤ 10 Myr), while [Viaene et al. \(2016\)](#) used MAGPHYS to derive the sSFR. Furthermore, we also notice a correlation of the heating fraction with morphology, with LTGs having the highest heating fractions. From this analysis, it is evident that dust heating is driven globally and locally, by the ratio of ongoing star-formation to past star-formation.

The approach we used in this study to determine the dust heating due to the different stellar populations is only a rough approximation given the perplexing interaction among the stellar radiation field and the dust. Other sources not treated here could potentially

contribute to the dust heating (e.g., the X-ray emission from a hot halo gas (Natale et al. 2010) or an AGN). Thus, a more sophisticated approach is needed to describe the complicated processes that contribute to the heating of dust in galaxies that take into account the effect of non-local heating. Such approaches include detailed treatment of the 3D morphology of galaxies through radiative-transfer modelling. Following previous studies by De Looze et al. (2014) and Viaene et al. (2017), several DustPedia galaxies have been modelled using the SKIRT radiative-transfer code (Baes et al. 2011; Camps & Baes 2015). These galaxies include the most extended, face-on galaxies in our sample (e.g., NGC 3031, NGC 1365, NGC 5236, NGC 3351, NGC 4321, and NGC 1068) with a variety of morphologies (grand design spirals, lenticulars, barred, AGNs). Although the heating of the dust (attributed to old and young stars) in these studies is investigated on local scales, our results on global scales agree fairly well (details of this analysis are presented in Verstocken et al. (2019), Chap. 6, and Chap. 7).

5.12 Recipes to estimate physical properties of galaxies as a function of Hubble stage

As already discussed in this chapter, we interpolated the median values, per morphological bin, of several physical parameters with a fifth-order polynomial (see Figs. 5.11 and 5.15). In Table 5.5 we provide the exact values of the coefficients of the polynomial regression. This allows us, for a galaxy of a given Hubble stage (T), to estimate the values of M_{star} , M_{dust} , M_{HI} , SFR, $T_{\text{dust}}^{\text{CIGALE}}$, the fractions of the stellar populations $f_{\text{old}}^{\text{unatt}}$, $f_{\text{young}}^{\text{unatt}}$, as well as the fractions of the attenuated luminosities of the old and the young stellar components $f_{\text{old}}^{\text{att}}$, $f_{\text{young}}^{\text{att}}$ and the fraction of the absorbed, by the dust, luminosity f_{abs} . The typical uncertainty values of each polynomial coefficient was derived through bootstrapping the data. More specifically, for every relation we created 100 new datasets by randomly varying the original values within their typical uncertainties. For every new dataset we computed the median values per morphological bin and fitted a fifth-order polynomial through them. By calculating the standard deviation of these 100 fitted lines we were then able to get a measurement of the typical errors. The values are also provided in Table 5.5.

5.13 Summary and conclusions

We have used photometric measurements of a sample of 814 local galaxies, drawn from the DustPedia archive, to construct their multi-wavelength SEDs (from the UV to the submm). This is the first dedicated study of dust heating for such a large, statistically significant sample. More than 15 such measurements are available for the majority of these objects (94%; with a minimum of 10 and a maximum of 30 for the entire sample). The galaxies span a variety of morphologies parametrized with their Hubble stage (T) on a scale from -5 to 10 (from pure ellipticals to irregular galaxies, respectively) with an average of 50 objects in each morphology class. In order to extract information

Table 5.5: Recipes to estimate the integrated physical properties of galaxies given their Hubble stage (T).

y	α_0	α_1	α_2	α_3	α_4	α_5
	$y = \alpha_0 + \alpha_1 \times T + \alpha_2 \times T^2 + \alpha_3 \times T^3 + \alpha_4 \times T^4 + \alpha_5 \times T^5$					
$\log(M_{\text{dust}}/M_{\text{star}})$	-4.01 ± 0.07	0.25 ± 0.03	0.01 ± 0.01	$(-2.06 \pm 1.20) \times 10^{-3}$	$(-2.52 \pm 3.70) \times 10^{-4}$	$(1.93 \pm 2.85) \times 10^{-5}$
$\log(M_{\text{HI}}/M_{\text{star}})$	-1.86 ± 0.10	0.18 ± 0.04	0.03 ± 0.02	$(-0.68 \pm 1.84) \times 10^{-3}$	$(-6.30 \pm 5.80) \times 10^{-4}$	$(4.15 \pm 4.40) \times 10^{-5}$
$\log(\text{SFR}/M_{\text{star}})$	$[-\text{yr}^{-1}]$ -11.65 ± 0.06	0.38 ± 0.02	0.03 ± 0.01	$(-6.89 \pm 1.12) \times 10^{-3}$	$(-2.50 \pm 3.50) \times 10^{-4}$	$(4.66 \pm 2.70) \times 10^{-5}$
$\log(M_{\text{dust}}/M_{\text{HI}})$	-2.25 ± 0.10	0.08 ± 0.04	-0.01 ± 0.02	$(-1.07 \pm 1.77) \times 10^{-3}$	$(-0.10 \pm 5.60) \times 10^{-4}$	$(0.79 \pm 4.30) \times 10^{-5}$
$\log(M_{\text{star}})$	$[M_{\odot}]$ 10.31 ± 0.10	0.07 ± 0.04	-0.01 ± 0.02	$(-4.71 \pm 1.90) \times 10^{-3}$	$(5.30 \pm 6.00) \times 10^{-4}$	$(-1.65 \pm 4.60) \times 10^{-5}$
$\log(M_{\text{dust}})$	$[M_{\odot}]$ 6.28 ± 0.12	0.33 ± 0.05	-0.02 ± 0.02	$(-5.96 \pm 2.20) \times 10^{-3}$	$(6.36 \pm 6.80) \times 10^{-4}$	$(-3.03 \pm 5.20) \times 10^{-5}$
$\log(M_{\text{HI}})$	$[M_{\odot}]$ 8.44 ± 0.15	0.18 ± 0.06	0.04 ± 0.02	$(-4.77 \pm 2.60) \times 10^{-3}$	$(-6.26 \pm 8.14) \times 10^{-4}$	$(5.70 \pm 6.20) \times 10^{-5}$
$\log(\text{SFR})$	$[M_{\odot}/\text{yr}]$ -1.33 ± 0.10	0.42 ± 0.05	0.02 ± 0.02	$(-10.10 \pm 2.00) \times 10^{-3}$	$(-1.25 \pm 6.20) \times 10^{-4}$	$(5.40 \pm 4.80) \times 10^{-5}$
$T_{\text{dust}}^{\text{CIGALE}}$	$[\text{K}]$ 24.47 ± 0.52	-1.01 ± 0.21	0.10 ± 0.08	$(0.66 \pm 9.12) \times 10^{-3}$	$(-2.84 \pm 2.87) \times 10^{-3}$	$(3.14 \pm 2.20) \times 10^{-4}$
$f_{\text{unatt}}^{\text{old}}$	0.98 ± 0.01	-0.030 ± 0.004	-0.010 ± 0.002	$(5.22 \pm 1.70) \times 10^{-4}$	$(1.74 \pm 0.54) \times 10^{-4}$	$(-1.43 \pm 0.41) \times 10^{-5}$
$f_{\text{unatt}}^{\text{young}}$	0.02 ± 0.01	0.030 ± 0.004	0.010 ± 0.002	$(-5.22 \pm 1.70) \times 10^{-4}$	$(-1.74 \pm 0.54) \times 10^{-4}$	$(1.43 \pm 0.41) \times 10^{-5}$
$f_{\text{att}}^{\text{old}}$	0.88 ± 0.02	-0.063 ± 0.006	-0.007 ± 0.003	$(1.45 \pm 0.28) \times 10^{-3}$	$(1.29 \pm 0.88) \times 10^{-4}$	$(-1.69 \pm 0.68) \times 10^{-5}$
$f_{\text{att}}^{\text{young}}$	0.01 ± 0.02	0.004 ± 0.002	0.001 ± 0.001	$(0.07 \pm 0.10) \times 10^{-3}$	$(-0.04 \pm 0.31) \times 10^{-4}$	$(-0.01 \pm 0.24) \times 10^{-5}$
f_{fals}	0.10 ± 0.02	0.056 ± 0.007	0.005 ± 0.003	$(-1.43 \pm 0.31) \times 10^{-3}$	$(-1.18 \pm 0.97) \times 10^{-4}$	$(1.51 \pm 0.74) \times 10^{-5}$

on their baryonic content (stars and dust) we use the advanced fitting tool CIGALE adapted so as to include the recently developed dust model THEMIS (Jones et al. 2017), which successfully explains the observed FUV-NIR extinction, the IR to submm dust thermal emission and the shape of the infrared emission bands. For each galaxy we obtain accurate measurements of the stellar mass, the current SFR, the dust mass, and the dust temperature, while the stellar populations in each galaxy and their role in the dust heating is investigated by deriving the luminosity produced by the old and the young stars separately. Additional information on the atomic gas mass (M_{HI}) for a subsample of 711 galaxies is also provided for each galaxy (De Vis et al. 2019). For comparison, we derived the global dust properties (mass and temperature) in an independent way, by fitting the FIR-submm part of the SED ($\lambda \geq 100 \mu\text{m}$) with a MBB properly scaled to account for the THEMIS dust physics. Our analysis indicates that:

- ◆ The stellar mass is maximal for pure ellipticals ($T = -5$) and presents small variations for galaxies of $T < 2$ with a sharp drop (of about two orders of magnitude) for later-type galaxies. The atomic gas mass varies slightly for galaxies with $T < 2$ (very similar to the stellar mass) followed by a drop (of about an order of a magnitude) for later-type galaxies. The dust mass and SFR change in a similar way, between different morphological classes, with a continuous increase for earlier types and a decrease for later-type galaxies (of about two orders of magnitude in both cases), with a peak value for galaxies around $T = 5$.
- ◆ Normalisation to the stellar mass of the galaxy shows an increasing trend (from $T = -5$ to $T = 10$) for both the dust and the gas content as well as the SFR with $M_{\text{dust}}^{\text{CIGALE}}/M_{\text{star}}$ obtaining its maximum value at $T = 7$, $M_{\text{HI}}/M_{\text{star}}$ increasing continuously from $T = -5$ to $T = 10$ and with sSFR being roughly constant for ETGs with $T < -2$, increasing rapidly for galaxies with Hubble stages up to $T = 5$, followed by a mild increase for later-type galaxies. The dust-to-gas mass ratio ($M_{\text{dust}}^{\text{CIGALE}}/M_{\text{HI}}$) obtains its maximum value at around $T = 2$ with lower values (by about two orders of magnitude) for earlier- and later-type galaxies.
- ◆ The dust temperature, calculated by scaling the strength of the ISRF intensity derived by CIGALE, is higher for ETGs (~ 30 K) compared to LTGs where a drop by ~ 10 K is observed, followed by a sharp rise back to ~ 30 K for Sm-Irr type galaxies. The dust temperatures compare fairly well with those derived by fitting a single MBB in the wavelength range 100-600 μm , especially for LTGs.
- ◆ The mass fraction of aromatic feature emitting grains q_{hac} , correlates with sSFR and morphology. Galaxies with a high sSFR have low dust mass fractions and as galaxies grow in stellar mass and gas content, q_{hac} rises up to values close to that estimated for the Galactic ISM ($\sim 17\%$). For galaxies with sSFR $> 10^{-10} \text{ yr}^{-1}$, q_{hac} was found to be roughly constant.
- ◆ ETGs mainly contain old stars with only a small fraction of the bolometric luminosity ($< 10\%$) originating from young stars. For spiral galaxies with Hubble stages from 0-5 the fraction of young stars gradually increases up to $\sim 25\%$, while it stays roughly constant for galaxies with Hubble stages larger than 5.

- ◆ The dust luminosity normalised to the bolometric luminosity of the galaxy (f_{abs}) gets its maximum value ($\sim 34\%$) for galaxies with Hubble stages around stage 5, while it progressively decreases down to almost zero for ellipticals ($T = -5$) and to $\sim 10\%$ for irregulars ($T = 10$) (see [Bianchi et al. 2018](#), for a complete review on f_{abs}).
- ◆ On average, young stars are heating the dust more efficiently with the absorbed (by the dust) luminosity reaching as high as $\sim 77\%$ (at $T = 3$) of the total unattenuated luminosity of the young stars. On the other hand, the maximum luminosity of the old stars contributing to the heating of dust is $\sim 24\%$, again at $T = 3$.
- ◆ The heating of the dust in ETGs is dominated by the old stars to a level of up to $\sim 90\%$ while the young stars progressively contribute more to the dust heating for galaxies with Hubble stages from 0 to 5, while they become the dominant source of dust heating for galaxies with Hubble stages greater than stage 5, contributing $\sim 60\%$ of their luminosity to dust heating.
- ◆ The dust heating fraction by young stars is strongly correlated with the sSFR, with higher heating fractions corresponding to higher sSFR. There is also a clear trend between the heating fraction and the morphological type with significantly higher fractions in late-type galaxies.

Recipes to estimate physical properties of galaxies, as a function of the Hubble stage of the galaxy are provided in Table 5.5. The results of the CIGALE and the MBB modelling, presented in this study are provided in the DustPedia archive for every galaxy modelled.

Part IV

High-resolution, 3D radiative transfer modelling of nearby galaxies

The DustPedia barred galaxies

The analysis and results of this chapter appear in **A. Nersesian**, S. Verstocken, S. Viaene, M. Baes, E. M. Xilouris, S. Bianchi, V. Casasola, C. J. R. Clark, J. I. Davies, I. De Looze, P. De Vis, W. Dobbels, J. Fritz, M. Galametz, F. Galliano, A. P. Jones, S. C. Madden, A. V. Mosenkov, A. Trčka, and N. Ysard, 2019, ‘High-resolution, 3D radiative transfer modelling III. The DustPedia barred galaxies’, *A&A*, *Forthcoming*.

6.1 Introduction

Cosmic dust is one of the fundamental ingredients of the ISM, and considerably affects many physical and chemical processes. Although dust makes up a small fraction of the total mass of a galaxy, it is responsible for the attenuation and reddening effects at UV and optical wavelengths (Galliano et al. 2018). In ‘typical’ modern late-type galaxies, dust absorbs roughly 30% of the total starlight (Popescu & Tuffs 2002; Skibba et al. 2011; Viaene et al. 2016; Bianchi et al. 2018), and converts this energy to radiation at the MIR, FIR, and submm wavelengths (Soifer & Neugebauer 1991). Dust emission in those regimes is often used to trace star-formation activity either from MIR and FIR measurements alone (Calzetti et al. 2007; Chang et al. 2015; Davies et al. 2016), or from FIR measurements combined with UV and optical data (Kennicutt 1998; Kennicutt et al. 2009; Kennicutt & Evans 2012). However, the contribution of the old, more evolved, stars to the dust heating can be non-negligible (e.g. Hinz et al. 2004; Calzetti et al. 2010; Bendo et al. 2010, 2015; Boquien et al. 2011; Bendo et al. 2012; Smith et al. 2012a; De Looze et al. 2014; Viaene et al. 2017; Leja et al. 2019; Nersesian et al. 2019b) and therefore needs to be taken into account while estimating the SFR of a galaxy.

In the last decade, SED fitting codes that use Bayesian analysis and cover broader wavelength ranges rose in number and popularity. SED fitting codes can model panchromatic datasets by enforcing an energy conservation between the absorbed starlight and

the re-emitted photons by dust, at longer wavelengths. Codes such as CIGALE (Code Investigating GALaxy Emission; [Noll et al. 2009](#); [Boquien et al. 2019](#)) and MAGPHYS ([da Cunha et al. 2008](#)), among many others, make use of libraries and templates that account for the stellar and dust emission of galaxies, providing information about the stellar and dust content, and the efficiency of the ISRF to heat the dust. Despite their rise in popularity, an important caveat of SED fitting still remains: the use of empirical attenuation laws that lack any constraints on the 3D geometry of stars and dust in galaxies. Some codes use different attenuation for young and old stellar populations (SP), but this leads to extra parameters and consequently to degeneracies.

For an accurate and self-consistent representation of the dust-heating processes in galaxies, high-resolution, 3D radiative transfer (RT) modelling is required. Such simulations take into account the complex geometrical distribution of stars and dust (constrained by well-resolved imaging observations), while creating a realistic description of the ISRF as it propagates through the dusty medium. Previous 3D radiative transfer studies have also stressed the importance of non-local dust heating (e.g. [De Looze et al. 2012b, 2014](#); [Viaene et al. 2017](#); [Williams et al. 2019](#)), an effect that is not considered in global SED fitting methods or in pixel-by-pixel SED fits. Quantifying the relative contribution of the dust-heating sources through radiation transfer will enable us to obtain an indicative estimation of the current star-forming activity and a better insight on the dust properties in nearby galaxies.

The first detailed radiation transfer models were performed for a slew of edge-on galaxies, using axially symmetric models. Edge-on galaxies offer valuable information on the vertical and radial distribution of their stellar and dust components ([Xilouris et al. 1999](#); [Bianchi 2007](#); [Baes et al. 2010b](#); [De Looze et al. 2012a,b](#); [De Geyter et al. 2014, 2015](#); [Mosenkov et al. 2016, 2018](#)). While edge-on galaxies provide significant insight on the vertical and radial structures of galaxies, their main drawback is the lack of insight in the spatial distribution of star-forming regions and the clumpiness of the ISM ([Saftly et al. 2015](#)). In that sense, well-resolved, face-on galaxies are excellent objects to study since we can identify with great detail the star-forming regions as well as recover the asymmetric stellar and dust geometries.

A novel technique was developed by [De Looze et al. \(2014\)](#) for the panchromatic radiative transfer modelling of well-resolved face-on galaxies. They used observational images to derive the stellar and dust distributions, and then accurately described the starlight-dust interactions. The authors applied this technique to the grand-design spiral galaxy M 51 (NGC 5194). They found that the contribution of the older stellar population to the dust heating is significant, with an average contribution to the TIR emission reaching up to 37%. [Viaene et al. \(2017\)](#) and [Williams et al. \(2019\)](#) adopted the same technique and built a radiative transfer model of the Andromeda galaxy (M 31) and the Triangulum Galaxy (M 33), respectively. [Williams et al. \(2019\)](#) found that dust in M 33 absorbs 28% of the energy emitted by the old stellar population, while in M 31 the old stellar population is the dominant dust-heating source with the average contribution being around 91% ([Viaene et al. 2017](#)). Furthermore, those three studies have shown that the relative contribution of the young stars to the dust heating varies strongly with location and wavelength.

Table 6.1: Basic properties of the galaxies in our sample.

Galaxy ID	Hubble stage ^(a) [T]	Type ^(b)	Nuclear activity	Distance ^(c) [Mpc]	Apparent size [arcmin]	Position angle	Inclination ^(d)
NGC 1365	3.2	SB(s)b	Seyfert 1.8	17.9 ± 2.7 ($1'' = 86$ pc)	11.2×6.2	$132^\circ.0$	$54^\circ.5$
M 83 (NGC 5236)	5.0	SAB(s)c	Starburst	7.0 ± 4.1 ($1'' = 34$ pc)	12.9×11.5	$137^\circ.0$	$19^\circ.5$
M 95 (NGC 3351)	3.1	SB(r)	Starburst	10.1 ± 1.0 ($1'' = 49$ pc)	7.4×5.0	$101^\circ.2$	$45^\circ.5$
M 100 (NGC 4321)	4.1	SAB(s)	HII/LINER	15.9 ± 2.5 ($1'' = 77$ pc)	7.4×6.3	$84^\circ.1$	$34^\circ.9$

^(a) From Makarov et al. (2014). ^(b) From de Vaucouleurs et al. (1995). ^(c) From Sheth et al. (2010). ^(d) From Mosenkov et al. (2019).

Within the scope of the DustPedia¹ (Davies et al. 2017) project, we have developed a framework to construct detailed 3D panchromatic radiative transfer models for nearby galaxies with the SKIRT Monte Carlo code (Baes et al. 2011; Camps & Baes 2015). Where previous works (e.g. De Looze et al. 2014; Viaene et al. 2017; Williams et al. 2019) dealt with single individual galaxies, each with their own modelling strategy, here we take advantage of the standardised multi-wavelength imagery data available in the DustPedia archive² (Clark et al. 2018), and we apply a uniform strategy for the 3D radiative transfer modelling to a small sample of face-on galaxies with different characteristics. The full description and strategy of our modelling framework is presented in Verstocken et al. (2019). The authors applied this state-of-the-art modelling approach to the early-type spiral galaxy M 81 (NGC 3031). In this work we continue this kind of analysis by modelling four late-type barred galaxies; NGC 1365, NGC 5236 (M 83), NGC 3351 (M 95), and NGC 4321 (M 100). Barred galaxies are of particular interest since bars have a strong impact on the physical and chemical evolution of the ISM. It is generally considered that bars funnel molecular gas from the disc toward the central regions of galaxies, fuelling active nuclei and central starbursts (e.g. Casasola et al. 2011; Combes et al. 2013, 2014). The 3D distribution of stars and dust in the bars of galaxies could shed light on the physics of the dominant stellar component in both discs and bars.

6.2 Galaxy sample and data

For the purposes of this work, we selected galaxies from the DustPedia sample (Davies et al. 2017) with large angular diameters, so that they are well-resolved even at infrared and submm wavelengths. The sample consists of four nearby, spiral galaxies with a prominent bar in their centres; NGC 1365, M 83, M 95, and M 100. All four galaxies have a small or moderate inclination and optical discs larger than 7 arcmin in diameter. We also selected these galaxies to be roughly representative of early-, mid-, and late-type barred spirals, with the basic properties of each galaxy given in Table 6.1. For two of them (NGC 1365 and M 83) a detailed analysis of the radial distribution of stars, gas, dust, and SFR is presented in Casasola et al. (2017).

NGC 1365 (Fig. 6.1a), also known as the *Great Barred Spiral Galaxy*, is one of the best studied barred galaxies in the nearby Universe and is located in the Fornax cluster at a

¹<http://www.dustpedia.com>

²<http://dustpedia.astro.noa.gr>

distance of 17.9 Mpc (Sheth et al. 2010). NGC 1365 has been classified as an SB(s)b type galaxy by de Vaucouleurs et al. (1995) with a Hubble stage of $T = 3.2$. This truly impressive galaxy, with a major axis twice as large as of the Milky-Way (~ 60 kpc), displays strong ongoing star formation in the centre (Lindblad 1999) and hosts a bright Seyfert 1.8 nucleus (Véron-Cetty & Véron 2006). Two massive prominent dust lanes along the nuclear bar can be seen in optical images (Teuben et al. 1986), while the well developed spiral arms extend from the bar edges with the tendency to turn inwards at the outer edges of the galaxy (Lindblad et al. 1996). According to Nersesian et al. (2019b), this massive galaxy contains more than $8 \times 10^{10} M_{\odot}$ of stars, $10^8 M_{\odot}$ of dust, and shows a SFR of $13 M_{\odot} \text{ yr}^{-1}$. Its HI gas mass is measured to be $9.5 \times 10^9 M_{\odot}$ (De Vis et al. 2019) and its H2 gas mass $3 \times 10^9 M_{\odot}$ (Zabel et al. 2019).

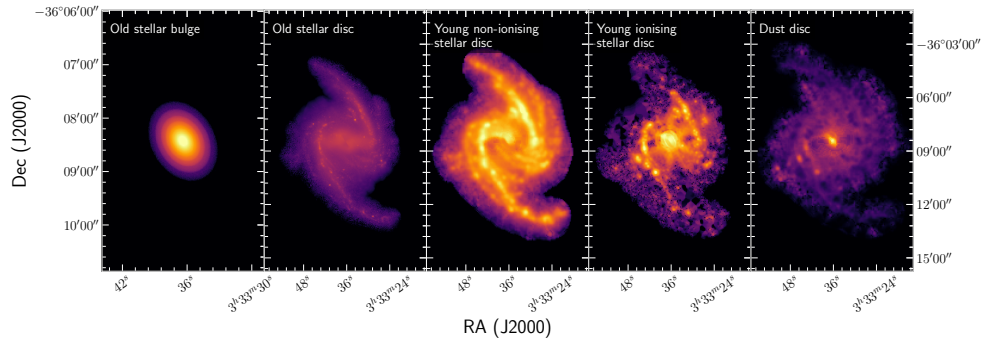
M 83 (NGC 5236, Fig. 6.1b) is a grand-design spiral galaxy, with a strong bar in the centre and prominent dust lanes connecting the central region to the disc. M 83 is an SAB(s)c ($T = 5$) galaxy as classified by (de Vaucouleurs et al. 1995), representing a ‘typical’ nearby grand-design Sb-Sc galaxy, and is located at a distance of 7.0 Mpc (Sheth et al. 2010). It has a nearly face-on orientation, with an estimated inclination of $19^{\circ}.5$. The nuclear region is a site of strong starburst activity (Telesco & Harper 1980; Turner et al. 1987), with dynamical studies showing that gas is funnelled along the bar producing high rates of star formation at the centre (Knapen et al. 2010). According to Nersesian et al. (2019b), M 83 has a stellar mass, dust mass, and integrated SFR of $3 \times 10^{10} M_{\odot}$, $2 \times 10^7 M_{\odot}$, and $6.7 M_{\odot} \text{ yr}^{-1}$, respectively. Its HI gas mass is measured to be more than $2 \times 10^9 M_{\odot}$ (De Vis et al. 2019).

M 95 (NGC 3351, Fig. 6.1c) is a nearby early-type barred spiral galaxy, located at a distance of 10.1 Mpc (Sheth et al. 2010). The morphological classification of the galaxy is SB(r) (de Vaucouleurs et al. 1995), with a Hubble stage of $T = 3.1$. M 95 is the host of a compact star-forming circumnuclear ring with a diameter approximately 0.7 kpc, and a larger ring of molecular gas regions surrounding the stellar bar of the galaxy (Knapen et al. 2002). Multi-wavelength, sub-kpc studies have shown that the central region is mainly populated by young stars (Mazzalay et al. 2013), whereas the bar region mainly hosts an older stellar population (James & Percival 2016). According to Nersesian et al. (2019b), M 95 contains a stellar mass, dust mass, and SFR of $3 \times 10^{10} M_{\odot}$, $8 \times 10^6 M_{\odot}$, and $1.1 M_{\odot} \text{ yr}^{-1}$, respectively. According to De Vis et al. (2019), this galaxy has an HI gas mass of $10^9 M_{\odot}$.

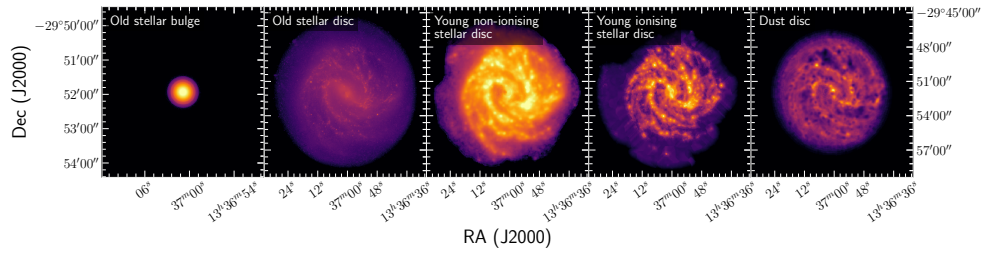
M 100 (NGC 4321, Fig. 6.1d) is located at a distance of 15.9 Mpc (Sheth et al. 2010) and it is a member of the Virgo Cluster. M 100 has been classified as SAB(s) by de Vaucouleurs et al. (1995), with two well-defined, symmetrical spiral arms emerging from the bar in the galactic centre. M 100 also hosts a circumnuclear ring with a diameter of 2 kpc. Ho et al. (1997) classified the nucleus as HII/LINER. The present-day SFR is estimated to be around $6 M_{\odot} \text{ yr}^{-1}$ (Nersesian et al. 2019b). M 100 has approximately $5 \times 10^{10} M_{\odot}$ of stars, $4 \times 10^7 M_{\odot}$ of dust (Nersesian et al. 2019b), and $3 \times 10^9 M_{\odot}$ of HI gas (De Vis et al. 2019).

For each galaxy, we automatically retrieved more than 24 images from the DustPedia archive through our modelling pipeline PTS³ (Verstocken et al. 2019). Since SDSS data

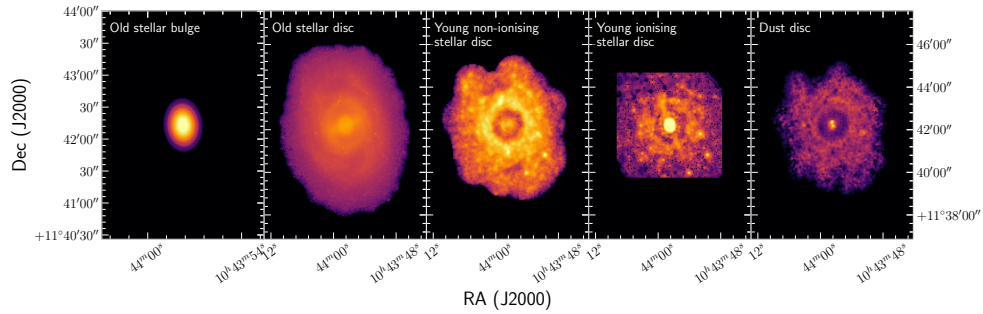
³http://www.skirt.ugent.be/pts8/_p_t_s.html



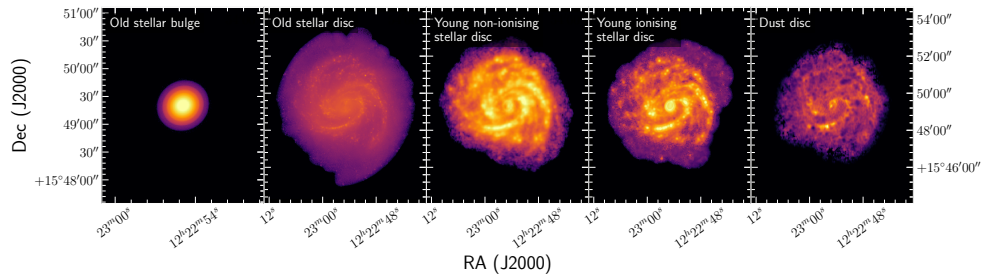
(a) NGC 1365.



(b) M 83.



(c) M 95.



(d) M 100.

Figure 6.1: 2D maps of different components of each galaxy. The model includes an old stellar bulge and disc component, a young non-ionising and ionising stellar disc, as well as a dust disc. The bulge image has been generated with SKIRT using a Sérsic profile geometry. The resolution of each map is based on the respective observations. The extent of the different components is due to the exclusion of unphysical pixels based on the different S/N in each band. The colour coding is in log scale and reflects a normalised flux density.

were not available for NGC 1365 and M 83, we manually downloaded and processed an R_C -band image (Lauberts & Valentijn 1989) for each galaxy from the NASA Extragalactic Database (NED)⁴. Supplementary to those images, properly processed (stellar continuum-subtracted) $H\alpha$ images were retrieved from NED for all galaxies.

Table 6.2: Integrated flux densities for our galaxy sample in this paper, listed by increasing central wavelength. The bands not used in our modelling are indicated in boldface.

Instrument	Band	λ_{eff} [μm]	NGC 1365	M 83	M 95	M 100
			Flux density [Jy]	Flux density [Jy]	Flux density [Jy]	Flux density [Jy]
GALEX	FUV	0.154	0.043 ± 0.002	0.287 ± 0.013	0.016 ± 0.001	0.031 ± 0.002
GALEX	NUV	0.227	0.061 ± 0.002	0.470 ± 0.013	0.027 ± 0.001	0.054 ± 0.002
SDSS	u	0.359	–	–	0.081 ± 0.001	0.202 ± 0.003
SDSS	g	0.464	–	–	0.340 ± 0.003	0.498 ± 0.004
SDSS/Other	r/ R_C	0.612	0.907 ± 0.007	5.455 ± 0.044	0.632 ± 0.005	0.815 ± 0.006
SDSS	i	0.744	–	–	0.896 ± 0.006	1.134 ± 0.008
SDSS	z	0.890	–	–	1.007 ± 0.008	1.237 ± 0.010
2MASS	J	1.235	1.796 ± 0.050	9.818 ± 0.275	1.470 ± 0.041	1.681 ± 0.047
2MASS	H	1.662	1.710 ± 0.050	11.870 ± 0.332	1.946 ± 0.054	2.117 ± 0.059
2MASS	Ks	2.159	1.698 ± 0.050	8.350 ± 0.234	1.573 ± 0.044	1.430 ± 0.040
WISE	W1	3.352	1.214 ± 0.035	6.113 ± 0.180	0.814 ± 0.024	0.922 ± 0.027
IRAC	I1	3.508	1.170 ± 0.035	6.295 ± 0.190	0.805 ± 0.024	0.967 ± 0.030
IRAC	I2	4.437	0.884 ± 0.027	4.124 ± 0.124	0.498 ± 0.015	0.628 ± 0.020
WISE	W2	4.603	0.885 ± 0.030	3.818 ± 0.130	0.439 ± 0.015	0.519 ± 0.018
IRAC	I3	5.628	2.190 ± 0.066	12.400 ± 0.370	0.820 ± 0.025	1.314 ± 0.040
IRAC	I4	7.589	5.210 ± 0.156	30.051 ± 0.901	1.612 ± 0.048	3.318 ± 0.010
WISE	W3	11.56	4.164 ± 0.192	21.105 ± 0.971	1.080 ± 0.050	2.452 ± 0.113
WISE	W4	22.09	12.472 ± 0.698	45.804 ± 2.565	2.690 ± 0.151	3.690 ± 0.207
MIPS	24	23.21	8.853 ± 0.443	39.885 ± 1.994	2.387 ± 0.119	3.318 ± 0.166
MIPS	70	68.44	–	306.368 ± 30.640	–	35.647 ± 3.565
PACS	70	68.92	138.496 ± 9.695	448.555 ± 31.398	25.907 ± 1.813	42.932 ± 3.005
PACS	100	100.8	214.973 ± 15.048	–	49.566 ± 3.470	87.256 ± 6.108
MIPS	160	152.6	–	756.137 ± 90.740	–	117.714 ± 14.126
PACS	160	153.9	204.472 ± 14.313	834.000 ± 58.380	54.741 ± 3.832	115.215 ± 8.065
SPIRE	PSW	247.1	99.620 ± 5.480	371.240 ± 20.420	29.693 ± 1.633	63.481 ± 3.491
SPIRE	PMW	346.7	43.280 ± 2.380	148.972 ± 8.194	13.183 ± 0.725	26.801 ± 1.474
HFI	857	349.9	37.410 ± 2.390	134.040 ± 8.578	9.535 ± 0.610	16.454 ± 1.053
SPIRE	PLW	496.1	15.085 ± 0.830	50.356 ± 2.770	4.804 ± 0.264	9.054 ± 0.498
HFI	545	550.1	11.470 ± 0.700	34.851 ± 2.126	2.544 ± 0.155	4.753 ± 0.300
HFI	353	849.3	2.424 ± 0.020	3.900 ± 0.030	0.766 ± 0.006	1.056 ± 0.008

⁴<https://ned.ipac.caltech.edu>

Although multi-wavelength global photometry (Clark et al. 2018) is available in the DustPedia archive for all 875 DustPedia galaxies, we performed our own custom aperture photometry using PTS. The reason behind this choice was to ensure that the measurement of the flux densities between observed and simulated images is consistent. The measured flux densities and uncertainties of the observed images are given in Table 6.2. The bands that were not used in our modelling are indicated in boldface. The morphological type of each galaxy has been retrieved from the HyperLEDA database (Makarov et al. 2014)⁵. The inclination angle of each galaxy was estimated based on the method described in Mosenkov et al. (2019).

6.3 Radiative transfer simulations with SKIRT

In this section we briefly lay out the steps we followed to construct our model galaxies. To generate a 3D radiative transfer model of each galaxy, we used the code SKIRT (Baes et al. 2011; Camps & Baes 2015). Our purpose is to apply the same systematic approach, introduced in Verstocken et al. (2019), for a sample of barred galaxies. For the complete description of our modelling procedure and strategy we refer the reader to Verstocken et al. (2019, see also Sect. 2.3).

6.3.1 Modelling approach

The model for every galaxy consists of four stellar components and a dust component. We considered an old stellar bulge, an old stellar disc, a young non-ionising stellar disc, a young ionising stellar disc, and a dust disc. We modelled the old and young non-ionising stellar populations using the Bruzual & Charlot (2003) SSP templates of solar metallicity $Z = 0.02$, typical ages of 8 Gyr and 100 Myr, respectively, and a Chabrier (2003) IMF. For the young ionising population we adopted the SED templates from MAPPINGS III (Groves et al. 2008) assuming an age of 10 Myr. There are five parameters that define the MAPPINGS III templates, namely: the mean cluster mass (M_{cl}), the gas metallicity (Z), the compactness of the clusters (C), the pressure of the surrounding ISM (P_0), and the covering fraction of the molecular cloud photo-dissociation regions (f_{PDR}). The following parameters were used as our default values: $Z = 0.02$, $M_{cl} = 10^5 M_{\odot}$, $\log C = 6$, $P_0/k = 10^6 K \text{ cm}^{-3}$, and $f_{PDR} = 0.2$ (Verstocken et al. 2019). Despite the fact that all four galaxies have a prominent bar in their central region, we did not treat the bar as a separate component here. Instead we treated the bar and the galactic disc as a single structure to keep the modelling procedure in line with the DustPedia standard.

Based on the observed images of the individual galaxies at different wavelengths, we were able to generate the geometrical distribution of each of the input components. We modelled the bulge of each galaxy with a flattened Sérsic profile. The decomposition parameters of the Sérsic geometry were retrieved from the S⁴G database⁶ (Spitzer Survey

⁵<http://leda.univ-lyon1.fr>

⁶https://www.oulu.fi/astronomy/S4G_PIPELINES4/MAIN

Table 6.3: Overview of the different stellar populations and dust components in our model.

Component	2D geometry	Vertical dimension	SED template	Normalisation
Bulge				
Old SP (8 Gyr)	Sérsic profile geometry ^(a)		Bruzual & Charlot (2003)	3.6 μm
Disc				
Old SP (8 Gyr)	IRAC 3.6 μm ^(b)	Exponential profile ($h_{\text{disc}, z}$) ^(f)	Bruzual & Charlot (2003)	3.6 μm
Young non-ionising SP (100 Myr)	GALEX FUV ^(c)	$h_{\text{yni}, z} = 1/2 \times h_{\text{disc}, z}$	Bruzual & Charlot (2003)	FUV
Young ionising SP (10 Myr)	$\text{H}\alpha + 0.031 \times \text{MIPS } 24 \mu\text{m}$ ^(d)	$h_{\text{yi}, z} = 1/4 \times h_{\text{disc}, z}$	MAPPINGS III ^(g)	FUV
Dust	FUV attenuation map ^(e)	$h_{\text{dust}, z} = 1/2 \times h_{\text{disc}, z}$	THEMIS ^(h) dust mix	Total dust mass

^(a) The parameters of the flattened Sérsic profile, like the effective radius R_e , Sérsic index n , and intrinsic flattening factor q , were retrieved from the S⁴G database (Sheth et al. 2010; Salo et al. 2015). ^(b) Image corrected for bulge emission. ^(c) Image corrected for old SP emission and dust attenuation (Cortese et al. 2008; Galametz et al. 2013), using images from IRAC 3.6 μm , SDSS r , MIPS 24 μm , and PACS 70-, 100-, 160 μm . ^(d) Image corrected for old SP emission. The map was constructed based on the prescription of Calzetti et al. (2007). ^(e) The dust map was constructed based on the prescriptions of Cortese et al. (2008) and Galametz et al. (2013). We used images from GALEX FUV, SDSS r , MIPS 24 μm , and PACS 70-, 100-, 160 μm . ^(f) We assumed an exponential distribution with a scale height h_z in the vertical direction. The scale height for the old SP is, $h_{\text{disc}, z} = 1/8.26 \times h_R$ (De Geyter et al. 2014), where h_R is the scale length. ^(g) Groves et al. (2008). ^(h) Jones et al. (2017).

of Stellar Structure in Galaxies: Sheth et al. 2010; Salo et al. 2015) and we fixed the total luminosity such that it corresponds to the bulge luminosity, measured from the IRAC (Fazio et al. 2004) 3.6 μm image. To derive the stellar and dust geometries in the disc of each galaxy, we combined different images to create physical maps that characterise, for example, the density distribution of the diffuse dust or old stellar population on the galaxy. The different components can be seen in Fig. 6.1, while in Table 6.3 we provide an overview of the images and templates used for the different stellar and dust components in our model. The details on how we generated these physical maps are presented in Verstocken et al. (2019).

For the dust composition we used the DustPedia reference dust model THEMIS⁷ (The Heterogeneous Evolution Model for Interstellar Solids; Jones et al. 2013, 2017; Köhler et al. 2014). The adopted THEMIS model is for the MW diffuse ISM and even though we know that the dust evolves (e.g. Fitzpatrick & Massa 2007, 2009; Planck Collaboration et al. 2011b,a; Liszt 2014b,a; Ysard et al. 2015; Reach et al. 2015, 2017b,a; Lenz et al. 2017; Nguyen et al. 2018), this is not taken into account in the current modelling. The dust around star forming regions is introduced in our model through subgrid models that rely on the MAPPINGS III SED templates for the young ionising stellar population (which account for the combined emission from HII regions and their surrounding PDRs).

To create the 3D distribution of the disc components we assigned to each of them an exponential profile of different scale heights, $h_{z,i}$, based on previous estimates of the vertical extent of edge-on galaxies (De Geyter et al. 2014). Then we generated a dust grid based on the dust component map through which the photons propagate in our simulations. For that purpose, a binary tree dust grid (Saftly et al. 2014) was employed with approximately 2.8 million dust cells for each galaxy.

Apart from the geometrical distribution, for each stellar component we assigned an intrinsic SED and a total luminosity, that is either fixed or a free parameter in the

⁷https://www.ias.u-psud.fr/themis/THEMIS_model.html

Table 6.4: Overview of the model parameters for all four galaxies.

	Description	Parameters	NGC 1365	M 83	M 95	M 100
Fixed parameters	Sérsic parameters ^(a)	n	0.857	0.664	0.563	0.639
		q	0.577	0.897	0.256	0.795
		R_e [pc]	826	236	314	557
	Scale heights ^(b)	$h_{\text{disc}, z}$ [pc]	1000	436	344	572
		$h_{\text{yni}, z}$ [pc]	500	218	172	286
		$h_{\text{yi}, z}$ [pc]	250	109	86	143
		$h_{\text{dust}, z}$ [pc]	500	218	172	286
	Old SP luminosity	$L_{\text{bulge}, 3.6}$ [$10^9 L_\odot$]	2.60	0.68	0.35	0.67
$L_{\text{disc}, 3.6}$ [$10^9 L_\odot$]		7.52	7.54	1.87	5.96	
Free parameters	Initial guess	$L_{\text{yni}, \text{FUV}}^{\text{init}}$ [$10^{10} L_\odot$]	3.82	4.26	0.29	1.81
		$L_{\text{yi}, \text{FUV}}^{\text{init}}$ [$10^{10} L_\odot$]	2.45	1.26	0.20	1.13
		$M_{\text{dust}}^{\text{init}}$ [$10^7 M_\odot$]	10.1	2.01	0.82	3.70
	Best-fit	$L_{\text{yni}, \text{FUV}}$ [$10^{10} L_\odot$]	1.21 ± 0.70	2.40 ± 0.83	0.04 ± 0.01	1.02 ± 0.37
		$L_{\text{yi}, \text{FUV}}$ [$10^{10} L_\odot$]	1.83 ± 0.60	0.71 ± 0.57	0.20 ± 0.04	0.36 ± 0.23
		M_{dust} [$10^7 M_\odot$]	18.0 ± 4.87	4.76 ± 0.98	1.68 ± 0.27	6.60 ± 1.64

^(a) Bulge parameters: n is the Sérsic index, q is the intrinsic flattening factor, and R_e is the effective radius. ^(b) Disc parameters.

model. The different combinations of the free parameters generate a 3D radiative transfer simulation that takes into account the emission of the different stellar components as well as the absorption, scattering, and thermal re-emission by dust. The output of each simulation includes the SED of the galaxy and a set of broadband images that can directly be compared to the observed images. Additional information is also available: images of the galaxy at any viewing angles and any wavelengths can be retrieved, and most importantly the effects of the interaction between the ISRF and the diffuse dust can be studied in 3D. Global luminosities are distributed on the 3D pixels (voxels) according to the density distributions as prescribed by the physical maps. The $3.6 \mu\text{m}$ luminosity of the old stellar population ($L_{\text{bulge+disc}, 3.6}$) was fixed a priori.

In Table 6.4 we list the main parameters that were used to model each galaxy. We distinguish between the parameters that were kept fixed and those that were left free. We left three parameters in our model free and they are determined via a χ^2 optimisation procedure. These parameters are the intrinsic FUV luminosity of the young non-ionising stellar population ($L_{\text{yni}, \text{FUV}}$), the intrinsic FUV luminosity of the young ionising stellar population ($L_{\text{yi}, \text{FUV}}$), and the total dust mass (M_{dust}). In a similar fashion as in CIGALE, we added quadratically an extra 10% of the observed flux to the measured uncertainty, to account for systematic errors in the photometry and the models (Noll et al. 2009). For the free parameters we provide the initial guess values retrieved from global SED fitting with CIGALE, performed by Nersesian et al. (2019b, see also Chap. 5) for the DustPedia galaxies, as well as the best-fitting values retrieved from our simulations.

In order to determine the best-fitting model of each galaxy, we set up two batches of simulations. The first batch acts as an exploratory step of the parameter space. We first generated a broad parameter grid, considering 5 grid points for $L_{\text{yni}, \text{FUV}}$ and

M_{dust} , and 7 grid points for $L_{\text{yi, FUV}}$. The choice of extending the range of $L_{\text{yi, FUV}}$ was made because of the difficulty to constrain this particular parameter (Viaene et al. 2017). We ran the first batch of simulations with a low-resolution wavelength grid of 115 wavelengths between 0.1 and 1000 μm , and without the requirement of spectral convolution of the simulated fluxes and images to the filter response curves. For each wavelength we used 10^6 photon packages, which was sufficient enough to reconstruct the global SEDs. In total, SKIRT created 175 simulated SEDs for each galaxy, and by directly comparing them with the observed SED we were able to narrow down the possible best-fitting parameter ranges. Based on those best-fitting values of the first batch, we generated a refined parameter grid space for the second batch of simulations.

For the second batch, we used a high-resolution wavelength grid (252 wavelength points) distributed in a non-uniform way over the entire UV-submm wavelength range. Furthermore, we used 5×10^6 photon packages per wavelength to ensure more accurate sampling of emission, extinction, and scattering, while we enabled spectral convolution. Despite the fact that we started the second batch of simulations with the same number of parameters for all galaxies –5 grid points for each free parameter–, in the cases of NGC 1365 and M 83, the expansion of the parameter space was necessary due to the difficulty in constraining the best-fitting values of $L_{\text{yi, FUV}}$ and $L_{\text{yni, FUV}}$, respectively. The number of simulations for the first and second batch are given in Table 6.5.

We ran our simulations on the high-performance cluster of Ghent University. For every galaxy here, each simulation of the first batch consumes approximately 22 h of (single-core) CPU time, amounting to 15,400 CPU hours. For the second batch of high-resolution simulations, the average CPU time for each simulation is about 312 h. In total, all simulations together consumed about 26 CPU years.

Table 6.5: Number of grid points for each free parameter ($L_{\text{yni, FUV}}$, $L_{\text{yi, FUV}}$ and M_{dust}), and for each batch of simulations. The last column gives the total number of simulations we ran for each galaxy.

Galaxy ID	Number of simulations		
	1st batch	2nd batch	Total
NGC 1365	$5 \times 7 \times 5 = 175$	$6 \times 8 \times 6 = 288$	463
M 83	$5 \times 7 \times 5 = 175$	$7 \times 5 \times 7 = 245$	420
M 95	$5 \times 7 \times 5 = 175$	$5 \times 5 \times 5 = 125$	300
M 100	$5 \times 7 \times 5 = 175$	$5 \times 5 \times 5 = 125$	300

6.4 Model validation

6.4.1 Global SEDs

We perform a series of quality checks on our results. The best simulated SEDs are shown in Fig. 6.2 along with the observed photometry derived from our pipeline. The total model SED is indicated by the black line, whereas the coloured lines represent the contribution of the different stellar components. We would like to point out that the dust emission of the individual SEDs does not add up to the total SED (black line), because the dependence of dust emission on the absorbed energy is non-linear. On the other hand, the sum of the (attenuated) stellar emission of each component equals the total stellar emission (black line). A weight was assigned to each filter depending on the wavelength regime that it belongs to (we define six regimes: UV, optical, NIR, MIR, FIR, and submm), such that each wavelength regime is equally important. Overall, and in all cases, the simulation agrees with the observations notably well within the uncertainties.

In all galaxies, a systematic deviation between model and observation is evident for the GALEX FUV and NUV bands, with the model always overestimating the FUV luminosity and underestimating the NUV luminosity. The most notable differences are around -0.12 dex for the GALEX FUV band of M 83 and 0.17 dex for the GALEX NUV band of M 95, while for M 100 there is an equal absolute deviation of 0.1 dex for both wavebands. The discrepancy between model and observation for the UV bands was also reported in the radiation transfer models of M 51 (De Looze et al. 2014), M 31 (Viaene et al. 2017), M 81 (Verstocken et al. 2019), and M 33 (Williams et al. 2019), as well as for edge-on galaxies (e.g. De Looze et al. 2012a,b; Mosenkov et al. 2016, 2018). UV bands are hard to fit because the SED in this spectral region depends sensitively on all the different components: the effects of dust extinction are more pronounced, the shape of the extinction curve is less well-determined and the shape of the intrinsic SEDs is very sensitive to the assumed population ages. Several studies have shown that age-selective attenuation may have a significant effect on the bump strength (Silva et al. 1998; Granato et al. 2000) at $0.22 \mu\text{m}$, characteristic of the dust attenuation. For example, the MAPPINGS III template seems to induce an inverse UV slope with respect to observations, making it very hard to accurately determine the age of the very young stellar populations. Another and as-yet un-quantified uncertainty arises from THEMIS, which predicts that the UV extinction is sensitive to the a-C nano-particle population (Jones et al. 2013) and that this dust component varies with the local ISRF. These effects may result, in part, in the observed discrepancies in the UV bands (especially for the NUV band).

Another notable discrepancy seen in all galaxies, with the exception of M 95, is the overestimation of the 2MASS bands, with the worst fitted bands being: the 2MASS J for NGC 1365 with a difference of -0.18 dex, and 2MASS K_s for M 83 and M 100 with a difference of -0.2 dex and -0.13 dex, respectively. The 2MASS bands for those three galaxies are less sensitive to more diffuse emission and the 2MASS flux determination is therefore restricted to smaller regions, resulted in lower NIR flux density measurements. Furthermore, even though the predicted MIR-FIR luminosities are fitted by the models

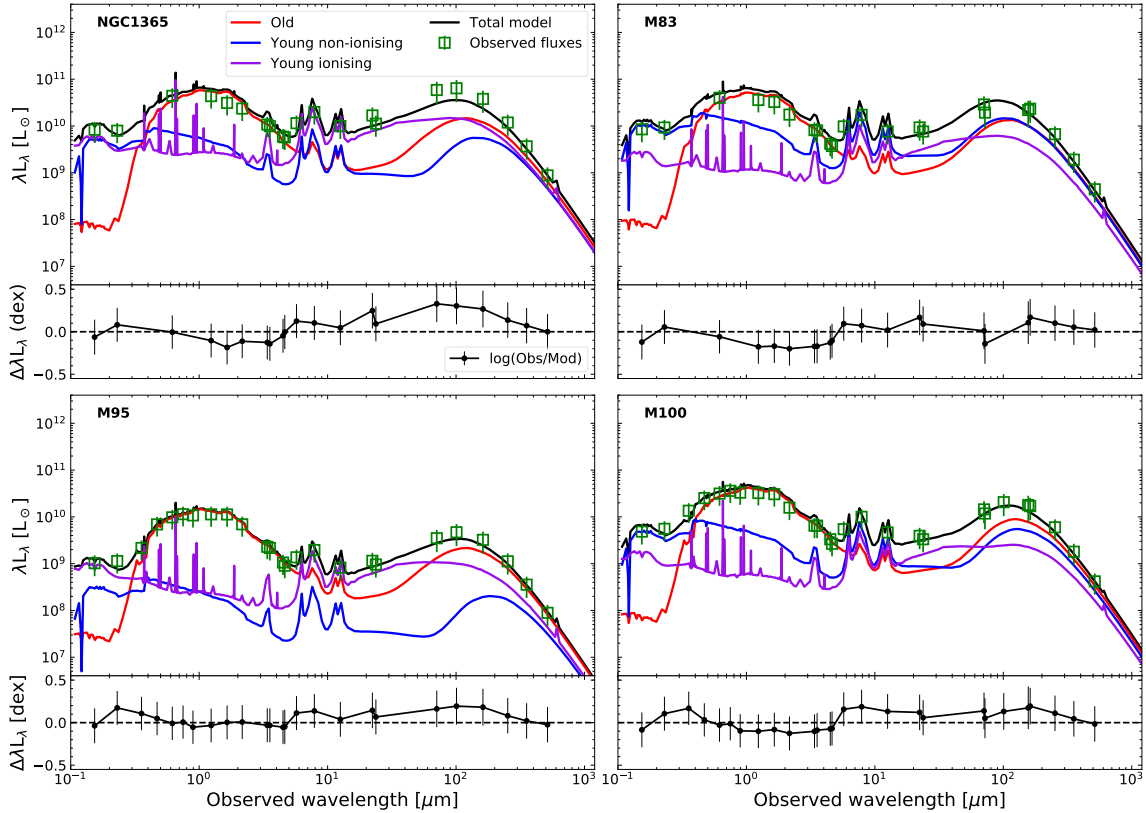


Figure 6.2: The top panel of each sub-figure shows the panchromatic SED of the respective galaxy. The black line is the best-fitting radiative transfer model, run at high-resolution. The green square points are the observed integrated luminosities measured for each galaxy (see Table 6.2). The red, blue, and violet lines represent the SEDs for simulations with only one stellar component: old, young non-ionising, and young ionising stellar population, respectively. The interstellar dust component is still present in these simulations. The bottom panel of each sub-figure shows the difference in dex between the observations and the best-fitting model.

within the uncertainties, they fall short in relation to the observations in that wavelength range, especially for NGC 1365, which has a difference for the peak of the dust emission at $100 \mu\text{m}$ around 0.3 dex.

To obtain an estimate of the uncertainty for each one of the free parameters we build their PDFs. The probability is proportional to $\exp(-\chi^2/2)$. Figure 6.3 shows the PDFs of the free parameters from the second batch of simulations for all four galaxies. The best-fitted values are marked by a dashed red line, with the actual values given in Table 6.4. In all cases (except the $L_{\text{yni, FUV}}$ of NGC 1365), the best-fitted value is either the same as the most probable value of the parameter or it takes the second most probable value. For some parameters an asymmetric distribution is seen, for example in the $L_{\text{yni, FUV}}$ of M 83 and M 100 (values of $L_{\text{yni, FUV}}$ higher than the best-fitted value were also explored and have close to zero probability). The FUV emission of the young non-ionising stars dominates this particular region of the SED of M 83 and M 100 (blue curve in Fig. 6.2), leading to a better constraint on the $L_{\text{yni, FUV}}$ parameter. On the other hand, the $L_{\text{yni, FUV}}$ of M 95 has a flat distribution, leading to a poor constraint on

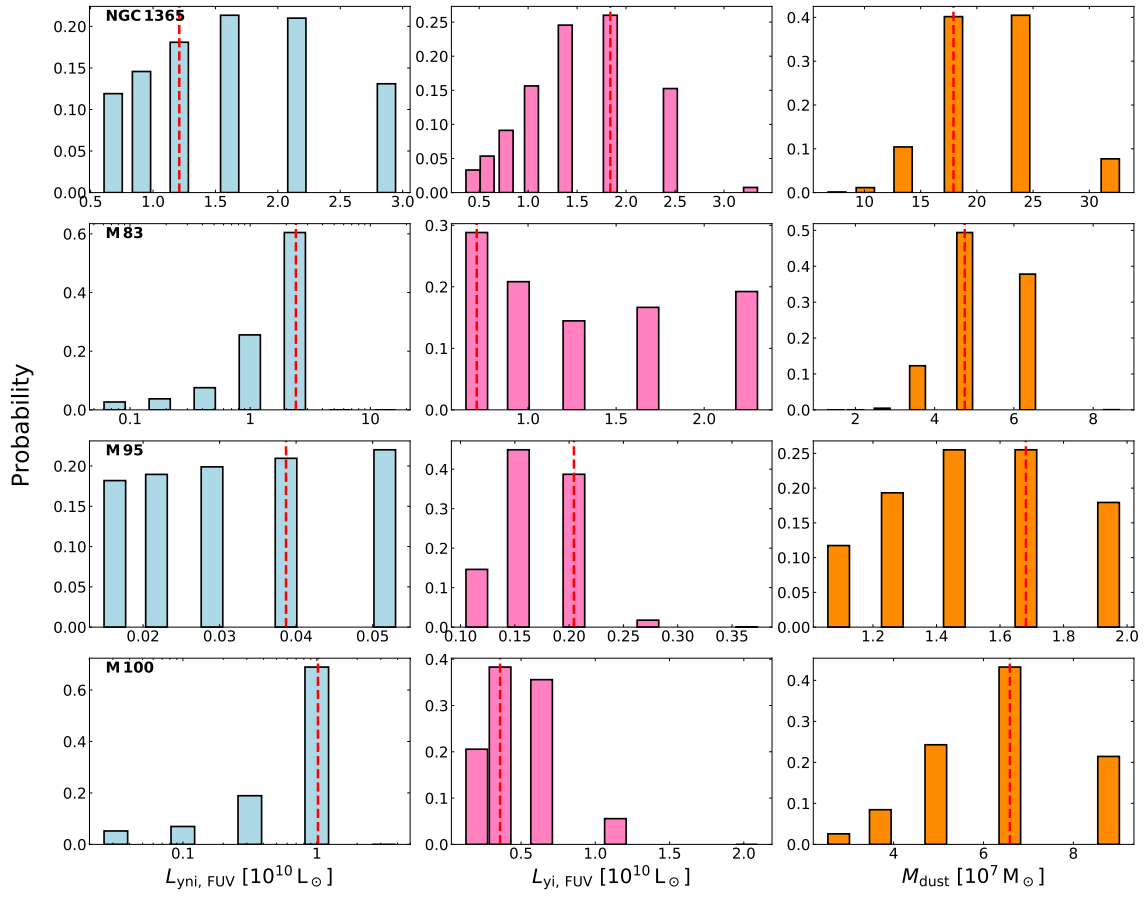


Figure 6.3: PDFs of the three free parameters in our model optimisation: the intrinsic FUV luminosity from the young non-ionising stellar component, $L_{\text{yni, FUV}}$ (left), the intrinsic FUV luminosity from the young ionising stellar component, $L_{\text{yi, FUV}}$ (middle), and the total dust mass, M_{dust} (right). Dashed red lines are the parameter values for the best-fitting model.

the parameter. The PDFs of the parameters that resemble a normal distribution suggest that the parameters are constrained fairly well.

Overall, the two fitted luminosities always end up being below the initial guess, while the dust mass always ends up being higher. To be more specific, despite the fact that the best-fitted values of the $L_{\text{yi, FUV}}$ are below the initial guess, they are still comparable with the initial guess values (marginally within the uncertainties, with M 100 as the only exception), while the best-fitted values of the $L_{\text{yni, FUV}}$ take much lower values than the initial guess. The lower FUV emission from the young non-ionising stellar population could partially explain the lower MIR-FIR emission in the final SED models. The most notable difference between the best-fitted and initial guess values is the total dust mass, where the best-fitted value for all galaxies is approximately two times larger than the one derived by CIGALE.

6.4.2 Image comparison

Another way to validate our results and understand the discrepancies in the integrated luminosities shown in Fig. 6.2, is to compare model and observations at spatially resolved scales. Figures 6.4, 6.5, 6.6, and 6.7 show a selection of representative wavebands across the spectrum of M 83, NGC 1365, M 95, and M 100, respectively. The bands were fitted with SKIRT, and were selected to demonstrate how well the model reproduces the observed images across the different wavelength regimes (from top to bottom: UV, optical, NIR, MIR, FIR, submm). The most efficient way to visualise any difference between observations (first column) and simulations (second column) is by computing a residual image (third column),

$$\text{residual} = 100 \times \left(\frac{\text{observation} - \text{model}}{\text{observation}} \right) \%. \quad (6.1)$$

Positive values (in red) mean that the model underestimates the observed emission. On the other hand, negative values (in blue) mean that the model overestimates the observations. The fourth column shows a kernel density estimation (KDE) of the residual values, normalised to 1 at the peak. Overall, there is a good agreement between model and observations in all four galaxies, with the majority of the model pixels within 50% of their observed counterpart. At this point, we stress that the model images are not directly used in the optimisation procedure (we only fit to the measured global fluxes). We focus primarily on M 83 to describe the cause of any discrepancies between observations and simulations, applicable for the rest three aforementioned galaxies.

In detail, the FUV emission in the model of M 83 compares quite well with the observations, with the majority of the pixel residuals being near 0%. However, the model overestimates the FUV emission across the spiral arms and bar region, with residuals lower than -50%, whereas it underestimates the FUV emission in the central and star-forming regions (red points within the spiral arms). As mentioned in Sect. 6.4.1, there is a certain challenge in modelling the UV bands because all the different components (stellar and dust) affect, in one way or another, the total emission we observe.

A very good match between model and observation is seen for the optical image in the R_C band. The model is an accurate representation of the observed image, with very few residuals below -50% in the spiral arms, and few positive residuals at the edges of the image due to low S/N. The IRAC 3.6 μm residual map shows a smooth distribution without many sharp features, with deviations remaining mostly within the spiral arms and partially in the inter-arm regions (i.e. the model overestimates the observations, with the peak of the distribution of the residual values being around 40%). This somewhat confirms that the old stellar component in our radiation transfer simulations represents the old stellar population adequately. Interestingly enough, the pixel residuals for all three galaxies with high star-formation activity (M 83, NGC 1365, and M 100) display a systematic offset, with the model predicting higher emission despite the fact that we directly determine the normalisation of the old stellar component from the IRAC 3.6 μm band (see the IRAC 3.6 μm image comparison in Figs. 6.4, 6.5, and 6.7). In the 3D model of M 51 (De Looze et al. 2014), a similar offset was observed with the model

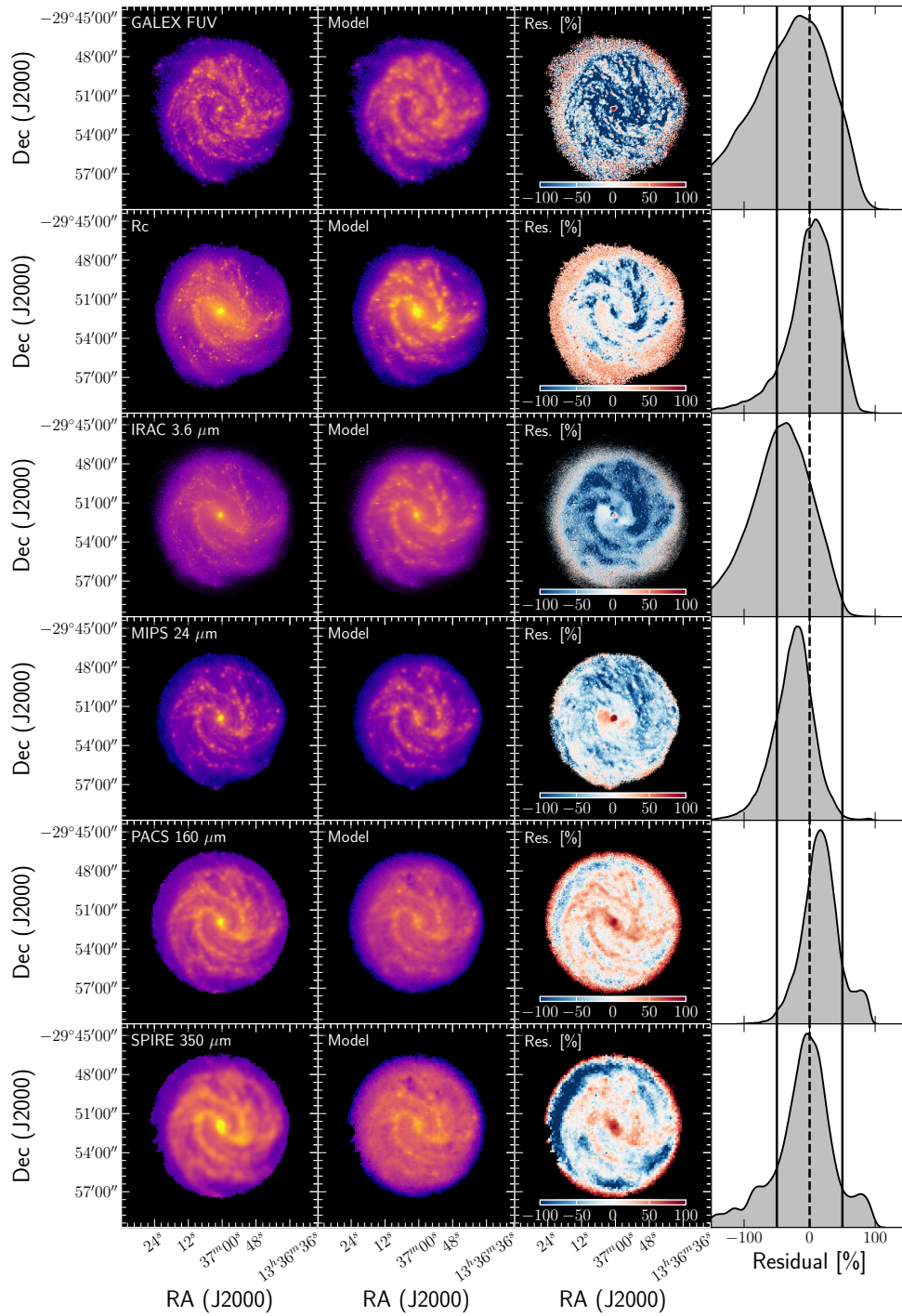


Figure 6.4: Comparison of the simulated images with observations in selected wavebands for M 83. First column shows the observed images, second column the simulated images, third column the maps of the relative residuals between observed and simulated images, and last column shows the KDE of the distributions of the residual pixel values. The simulated images have the same pixel mask as the observed images. The colour coding of the first two columns is in log scale and reflects a normalised flux density. The selected wavebands are: GALEX FUV, R_C , IRAC $3.6 \mu\text{m}$, MIPS $24 \mu\text{m}$, PACS $160 \mu\text{m}$, and SPIRE $350 \mu\text{m}$.

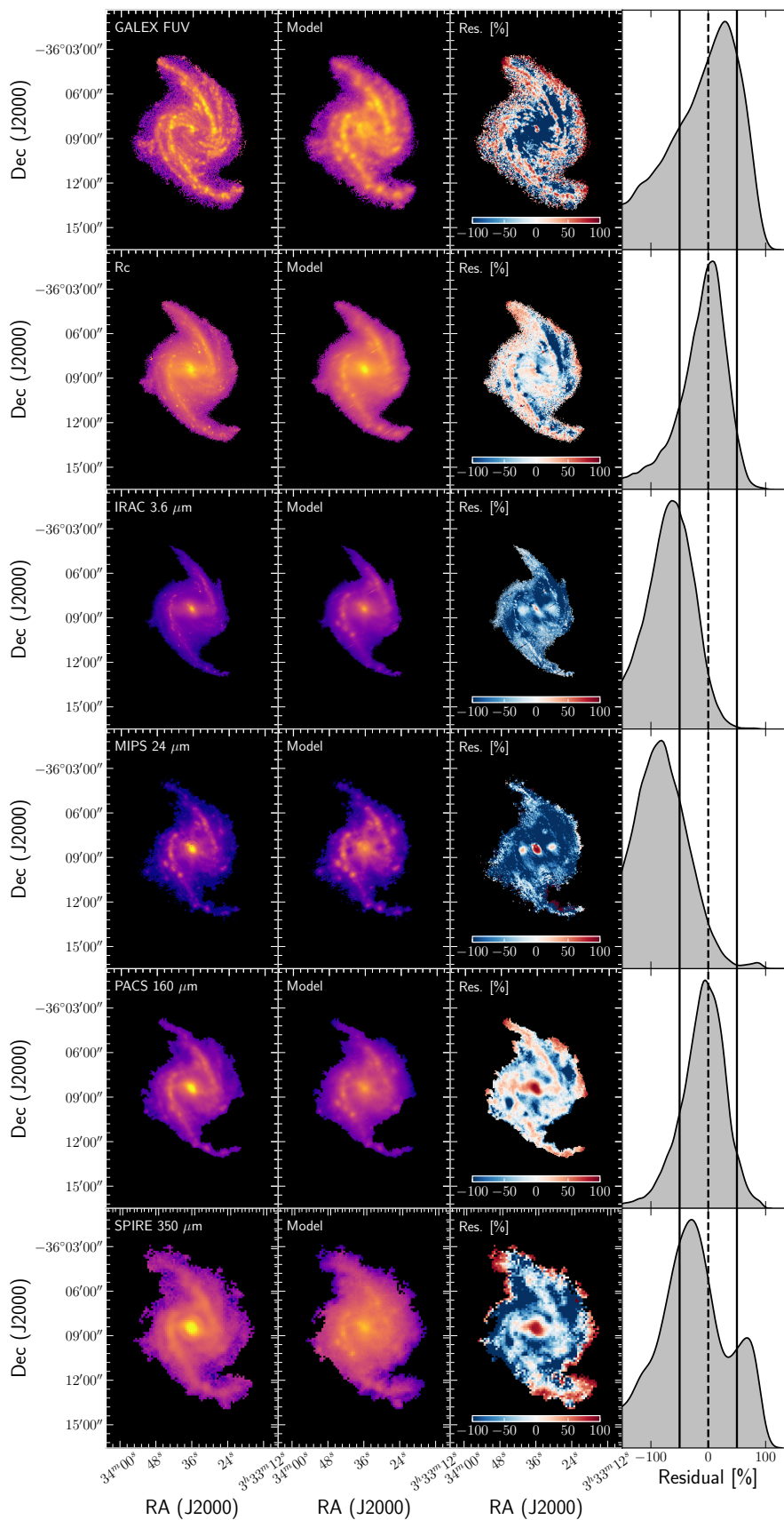


Figure 6.5: Same as Fig. 6.4 for NGC 1365

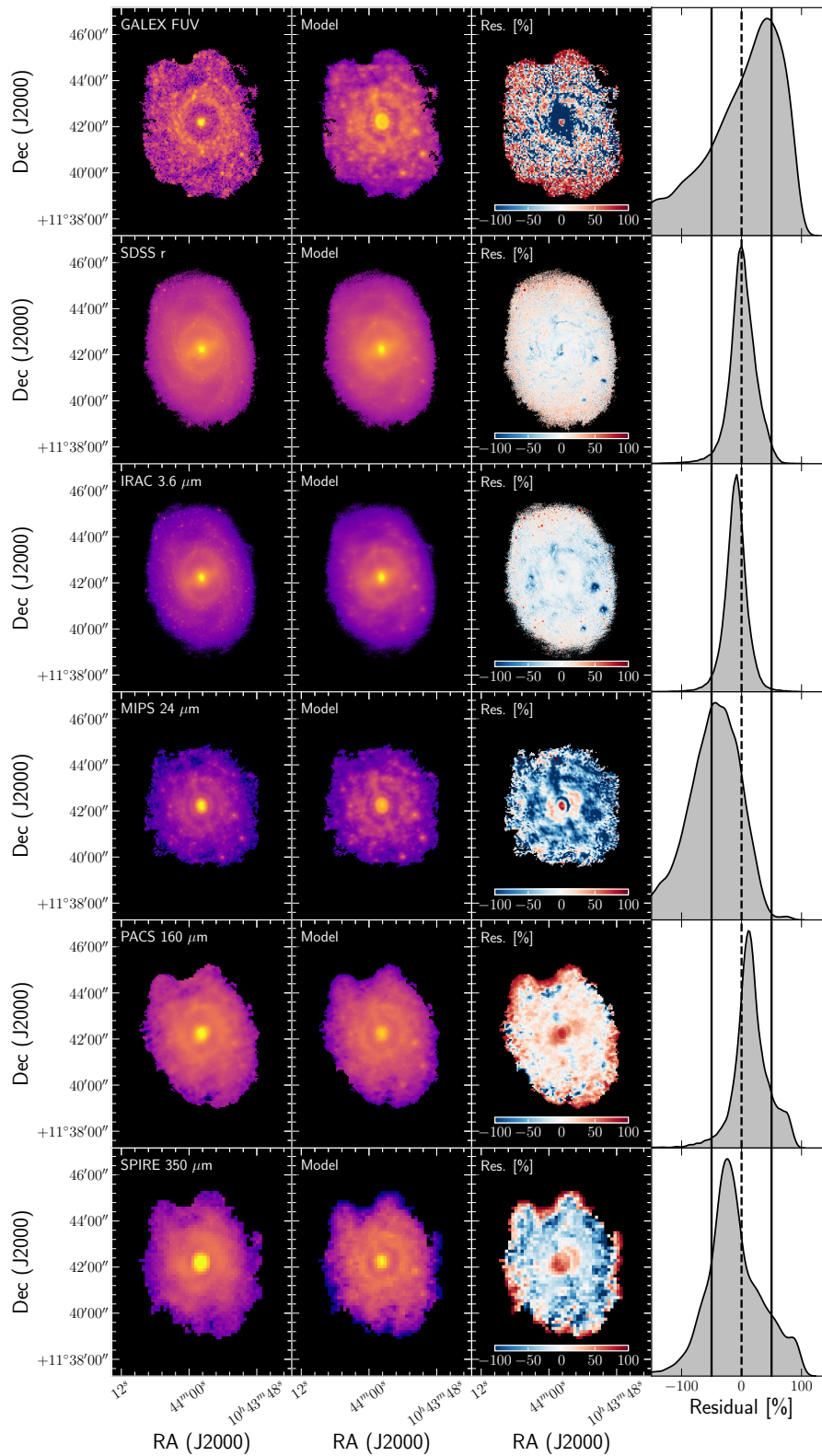


Figure 6.6: Same as Fig. 6.4 for M 95 but with the SDSS r observation used instead of R_C .

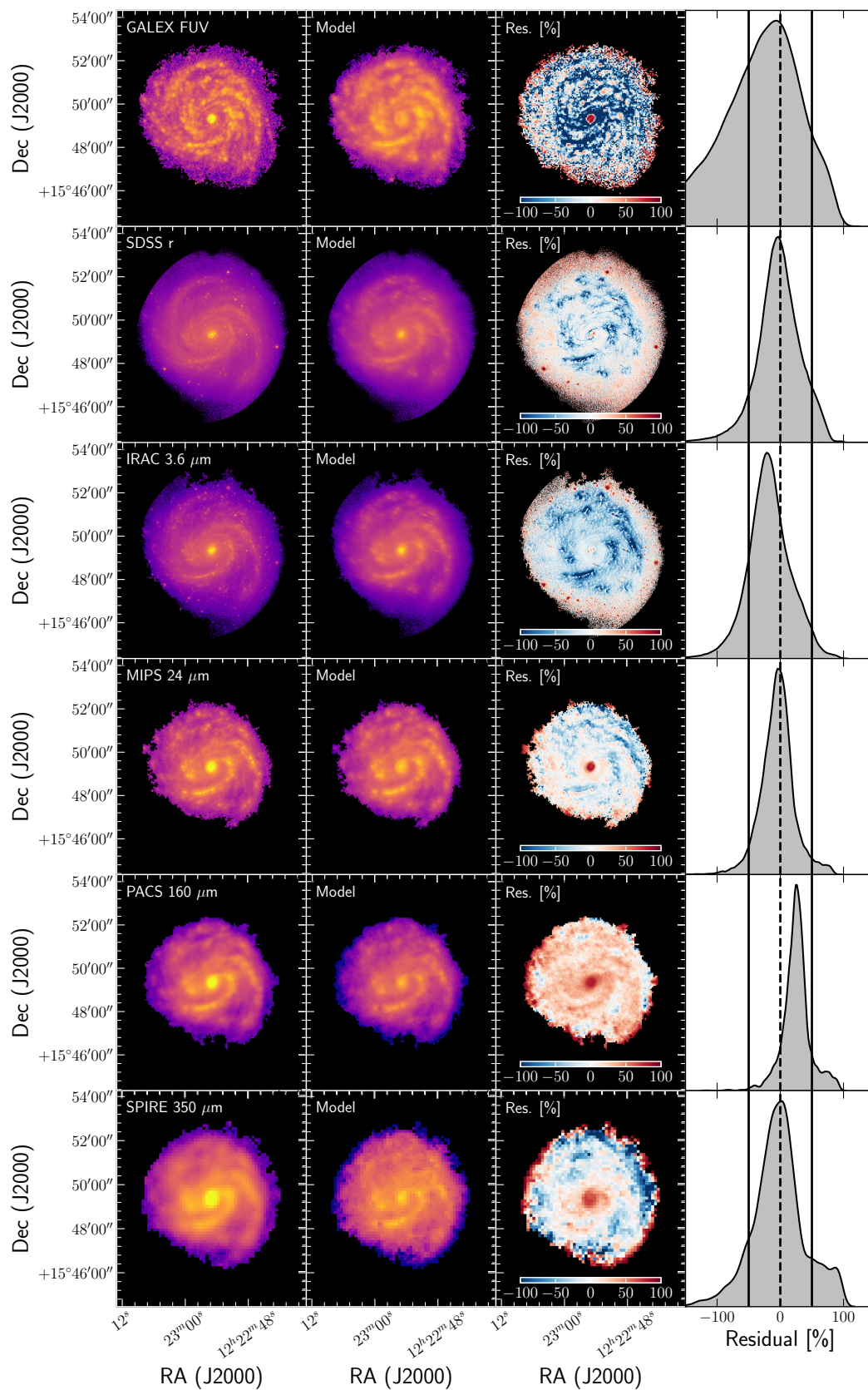


Figure 6.7: Same as Fig. 6.4 for M 100 but with the SDSS *r* observation used instead of R_C .

predicting lower values for that band instead. On the other hand, in the 3D models of low star-forming galaxies like M 95 (see the IRAC $3.6\ \mu\text{m}$ image comparison in Fig. 6.6), M 81 (Verstocken et al. 2019), M 31 (Viaene et al. 2017), and M 33 (Williams et al. 2019), model and observations are in excellent agreement. The excess $3.6\ \mu\text{m}$ emission may arise from young stars in the spiral arms that contribute light even at these wavelengths. There may also be a contribution from aromatic features emitting at this wavelength. Together these contaminants can explain the differences between model and observations.

Moving on to the MIR, FIR, and submm regimes, simulated images and observations are in good agreement, with residual values having a narrow distribution peaking within $\pm 20\%$. The residual map of MIPS $24\ \mu\text{m}$ exhibits some strong features indicative of the contributions by hot dust and aromatic features of clumpy areas in the outer regions of the spiral arms. In the cases of Photodetector Array Camera and Spectrometer (PACS; Poglitsch et al. 2010) $160\ \mu\text{m}$ and the Spectral and Photometric Imaging REceiver (SPIRE; Griffin et al. 2010) $350\ \mu\text{m}$ wavebands, the model underestimates the dust emission mainly in the spiral arms and bar region, with the diffuse dust in the inter-arm regions accurately being represented in our model.

In addition, when we try to understand the differences between simulations and observations, we need to take into consideration several effects that could potentially increase the level of the observed residuals in Figs. 6.4, 6.5, 6.6, and 6.7. First, the appearance of a significant level of residuals can be attributed to deprojection effects. Due to the deprojection procedure, the brightest regions are smeared out in the direction of deprojection. Then the light is smeared out in the vertical direction creating a blurring-like effect (for example, see the FUV and R_c model images in Figs. 6.4, 6.5, and 6.7). Another cause, responsible for a substantial fraction of residuals, is the fact that we combine multiple images, of different resolutions, to generate the input maps of the stellar and dust components in our models. Simulated images thus have a complex point spread function (PSF) and are not convolved by a single beam, in contrast with observed images.

A certain degree of difficulty also exists when modelling the star-forming regions in detail which probably adds up to the observed discrepancies. For star-forming regions, a spherical shell geometry and an isotropic emission is implemented here. Those models result in a higher level of attenuation per unit dust mass than other models where a clumpy or asymmetric geometry is assumed (Witt & Gordon 1996, 2000; Városi & Dwek 1999; Indebetouw et al. 2006; Whelan et al. 2011). Of course the effect described here is more pronounced in the UV regime, where the young ionising stars are relatively more luminous.

Finally, the largest discrepancies can be seen for NGC 1365, for the IRAC $3.6\ \mu\text{m}$ and MIPS $24\ \mu\text{m}$ wavebands. The model overestimates the observations with absolute residuals higher than 50%, especially for MIPS $24\ \mu\text{m}$, where the model overestimates the flux densities up to 100%, with the extremely bright AGN in the centre as a possible cause. In the fourth panel of Fig. 6.1a (young ionising stellar disc), an Airy ring effect is still visible, despite our efforts to subtract the AGN emission (PSF) from the original image by employing 2D decomposition with GALFIT (Peng et al. 2010). To be more specific, since AGN is a point source we convolved it with the PSF for the MIPS $24\ \mu\text{m}$

image. We assumed a model for that galaxy that includes an AGN, a Sérsic bulge, a Ferrers bar and an exponential disc, and then we subtracted the modelled AGN from the original image. Nevertheless, the residuals of the remaining wavebands and galaxies are still more or less within 50%, and with very narrow residual distributions, indicating that our simulations are accurate representations of the observed data.

6.5 Discussion

6.5.1 Attenuation law

An important caveat in SED fitting codes is the use of idealised attenuation curves, converted from extinction laws that do not fully incorporate the effect of the relative geometries expected to be found between dust and stars. In a recent effort to address this caveat, [Buat et al. \(2018\)](#) measured the shape of the attenuation curves of star-forming galaxies by employing two different recipes: a flexible Calzetti attenuation law ([Noll et al. 2009](#)) and a two power-law recipe based on the one inferred by [Charlot & Fall \(2000\)](#). Both recipes take the shape of the attenuation curve and the relative attenuation of young and old stellar populations as free parameters. [Buat et al. \(2018\)](#) found that the [Charlot & Fall \(2000\)](#) recipe is able to better reproduce the results from radiative transfer models, and [Buat et al. \(2019\)](#) proposed a new modified Calzetti attenuation law with that specific goal in mind. From our radiative transfer simulations we can shed light on the impact of the relative geometry between the different stellar populations and the diffuse dust to the observed galaxy SEDs by reconstructing realistic dust attenuation curves. In order to determine the global attenuation curves we use the observed SED of the best-fitting model and the stellar spectrum we reconstruct for each galaxy. In [Fig. 6.8](#) we present the attenuation curves of the galaxies in our sample, derived from the 3D modelling with SKIRT. A face-on orientation (inclination angle 0°) was assumed for all galaxies. We complement the attenuation curves with those derived for M 81 from [Verstocken et al. \(2019\)](#) and M 77 from [Viaene et al. \(2019, submitted, see also Chap. 7\)](#). The attenuation curves of NGC 1365, M 83, M 95, M 100, M 81, and M 77 have been normalised to the V -band attenuation by: 0.27, 0.47, 0.22, 0.32, 0.09, and 1.03, respectively. We find a steep increase of attenuation towards the UV wavelengths due to absorption by small grains. A broad absorption bump is also evident with a peak around $0.22 \mu\text{m}$. The values of the V -band attenuation indicate that the galactic discs are optically thin if galaxies were to be seen face-on. This explains the steeper slopes in the UV wavelengths and the stronger $0.22 \mu\text{m}$ bumps in relation to the normalised THEMIS extinction curve ([Witt & Gordon 2000](#)).

The observed curves are the combination of the attenuation by diffuse dust as modelled by the dust mass input map, and the attenuation by dust in star-forming regions. The dust in the star-forming clouds is incorporated in the MAPPINGS III SED templates ([Groves et al. 2008](#)), which were used to represent the ionising stellar component. The MAPPINGS III attenuation law is directly provided by [Groves et al. \(2008\)](#), while the diffuse dust attenuation curve is a combination of the THEMIS extinction law ([Jones et al. 2013, 2017; Köhler et al. 2014](#)) and the relative geometry between stars and dust.

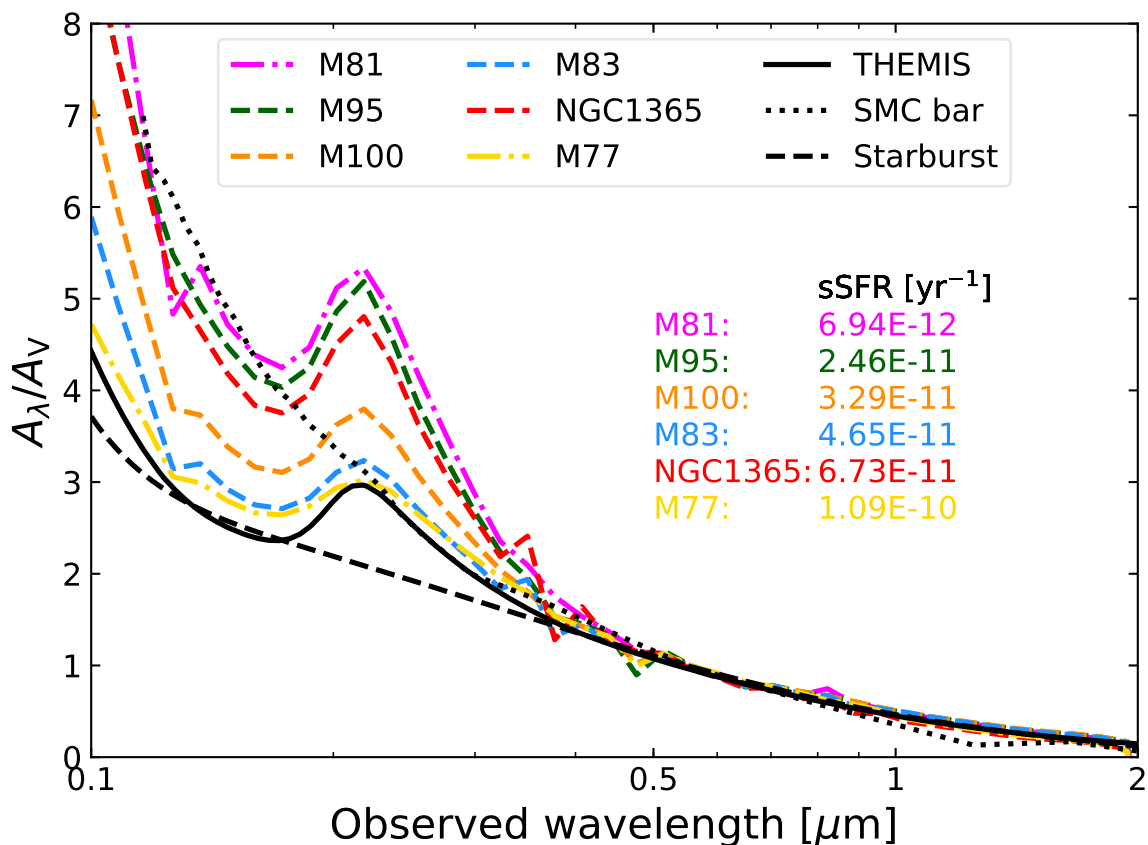


Figure 6.8: Compilation of attenuation laws derived from our models on a face-on view (0° inclination angle), normalised to the V-band attenuation. In addition to the attenuation curves derived for the galaxy sample of this study, we provide the attenuation curves of M 81 from [Verstocken et al. \(2019\)](#), and M 77 from [Viaene et al. \(2019\)](#), submitted, see also Chap. 7). Several literature measurements are shown as well: solid black curve: THEMIS extinction law ([Jones et al. 2013, 2017](#); [Köhler et al. 2014](#)), dotted black line: extinction curve of SMC bar ([Gordon et al. 2003](#)), dashed black line: attenuation law of starburst galaxies ([Calzetti et al. 2000](#)). The median values of the sSFR for every galaxy is also given in increasing order, as derived from our simulations.

In Fig. 6.8, we also plot the extinction curve of the THEMIS dust model (solid black line), which was used in all six studied galaxies. In addition, for comparison purposes, we provide literature measurements of the extinction law for the SMC bar region from [Gordon et al. \(2003\)](#) (dotted black line), and the attenuation law of starburst galaxies from [Calzetti et al. \(2000\)](#) (dashed black line). Moreover, we show the median values of the sSFR for every galaxy in increasing order derived from our simulations (see Sect. 6.5.3 on how we compute the sSFR).

At optical and NIR wavelengths ($\lambda \geq 0.4 \mu\text{m}$) all attenuation curves are in agreement, but this is expected since we normalised them with the V-band. At shorter wavelengths ($\lambda < 0.4 \mu\text{m}$), the curves begin to diverge. The UV bump in all six galaxies covers quite an extended range, with the peak of the bump varying over 2 orders of magnitude, despite the fact that all galaxies in our collective study share the exact same grain properties (i.e. the THEMIS extinction curve for the standard MW case was used in every model).

The diversity of the bump strength can be linked directly to the sSFR (a measure of the current to past star formation in galaxies) of each system (Kriek & Conroy 2013; Reddy et al. 2015). A weakened UV bump implies that an extra amount of radiation is filling in the bump either by UV photons from unobscured young stars or by light scattered into the line-of-sight (Narayanan et al. 2018). Of course, a reduced UV bump can also arise from opposing processes: intense UV radiation destroying the carriers in low density regions, and the bump carriers accreting onto big grains in high density regions, however these processes are not incorporated in the model so they cannot explain the differences in the attenuation curves.

With the exception of NGC 1365, we find a correlation between the sSFR and the shape of the attenuation curve, suggesting an age-dependent extinction curve. M 81 and M 95, two low sSFR galaxies exhibit a strong, almost identical UV bump, whereas galaxies of higher sSFR, for example M 83 and M 77, have a weaker UV bump. Contrarily, NGC 1365, a galaxy of high sSFR, presents a strong bump similar to M 81 and M 95. This behaviour suggests that most of the UV light emitted in the star-forming regions of NGC 1365 is heavily obscured by dust resulting in the strong bump feature we observe here. Another notable result is the presence of a UV bump in all attenuation curves, despite the claims made by some other authors in the past that bump-free attenuation curves, such as the Calzetti et al. (2000) curve, could arise even with dust that has a normal UV bump in the extinction curve. We confirm that as long as the UV bump in the extinction curve is represented as a true absorption feature, the corresponding attenuation laws must have a bump, although it may appear weakened.

Beyond the UV bump, our model curves steadily increase and fall somewhere between the starburst idealised attenuation law and the SMC extinction curve. It is interesting to notice here that stronger bumps seem to sit on steeper slopes. This result is well known and is attributed to the star-dust geometry (Witt & Gordon 1996; Narayanan et al. 2018). Narayanan et al. (2018) have shown that steeper slopes may arise either by a large fraction of obscured young stars or by a significant fraction of unobscured old stars. Consequently, galaxies with older stellar populations exhibit steeper attenuation curves. On the other hand, flatter attenuation curves are the result of a more complex geometry where more of the starlight is decoupled from dust. Based on our results we hereby confirm that galaxies of high sSFR values have shallower attenuation curves and weaker UV bumps.

6.5.2 Dust heating

A relevant quantity that holds information about the stellar energy absorbed by dust in a galaxy, and that is based on the assumption of energy balance, is the fraction of dust to bolometric luminosity (dust-heating fraction). Bianchi et al. (2018) defined this quantity as f_{abs} . With the use of radiative transfer modelling we can calculate this quantity not only on global scales but also on local scales. On global scales the dust-heating fraction is:

Table 6.6: $f_{\text{abs}}^{\text{SKIRT}}$, $f_{\text{abs}}^{\text{CIGALE}}$ (Bianchi et al. 2018), and the mean global f_{young} , as well as the mean f_{young} in the bulge and bar region; the regions are defined in Fig. 6.9 with a solid red circle and a dashed blue ellipse, respectively.

Galaxy ID	$f_{\text{abs}}^{\text{SKIRT}}$ [%]	$f_{\text{abs}}^{\text{CIGALE}}$ [%]	f_{young} [%]		
			Global	Bulge	Bar
NGC 1365	44	53 ± 21	68 ± 15	40 ± 14	66 ± 13
M 83	43	53 ± 9	64 ± 15	32 ± 12	59 ± 12
M 95	26	28 ± 4	47 ± 16	46 ± 12	43 ± 17
M 100	33	38 ± 4	57 ± 13	34 ± 12	46 ± 12

$$f_{\text{abs}}^{\text{SKIRT}} = \frac{L_{\text{dust}}}{L_{\text{stars}} + L_{\text{dust}}}, \quad (6.2)$$

where L_{stars} is the observed stellar emission and L_{dust} is the total dust luminosity, computed by integrating the SEDs presented in Fig. 6.2. For each galaxy we have calculated $f_{\text{abs}}^{\text{SKIRT}}$ and we have compared them with $f_{\text{abs}}^{\text{CIGALE}}$ produced in Bianchi et al. (2018) (see Table 6.6). The $f_{\text{abs}}^{\text{SKIRT}}$ fractions we obtain are slightly lower than, but compatible with, those obtained by Bianchi et al. (2018). In Bianchi et al. (2018) the authors provide the mean $f_{\text{abs}}^{\text{CIGALE}}$ values for 814 DustPedia galaxies, divided into 6 groups, according to their morphology classification (Hubble stage, T). The mean $f_{\text{abs}}^{\text{CIGALE}}$ value of the corresponding morphological bin (Sb-Sc; $2.5 \leq T < 5.5$) that our galaxy sample falls into is $32.8 \pm 13.9\%$. This value is in very good agreement with the mean value of $f_{\text{abs}}^{\text{SKIRT}}$ ($36.5 \pm 7.4\%$) of the rather small group of galaxies in our study. In any case, our modelling gives us the opportunity to better characterise which stellar population is the dominant dust-heating source in each galaxy, and how significant the contribution of old stars is, on a spatially resolved manner.

From our simulations it is possible to retrieve the absorbed energy in each dust cell (originating from the different stellar populations in the model), and thus to quantify the dust-heating fraction from the young non-ionising and young ionising stellar populations (hereafter, we will refer to the heating fraction by the young non-ionising and young ionising stellar populations simply as young heating fraction or f_{young}). We obtain the young heating fraction through:

$$f_{\text{young}} = \frac{L_{\text{yni}}^{\text{abs}} + L_{\text{yi}}^{\text{abs}}}{L_{\text{total}}^{\text{abs}}}. \quad (6.3)$$

where $L_{\text{yni}}^{\text{abs}}$ and $L_{\text{yi}}^{\text{abs}}$ are the luminosities of the young non-ionising and young ionising stellar populations absorbed by dust, respectively, and $L_{\text{total}}^{\text{abs}}$ is the total stellar luminosity absorbed by dust.

In Fig. 6.9, the left panel of each sub-figure shows the dust-heating map of the face-on

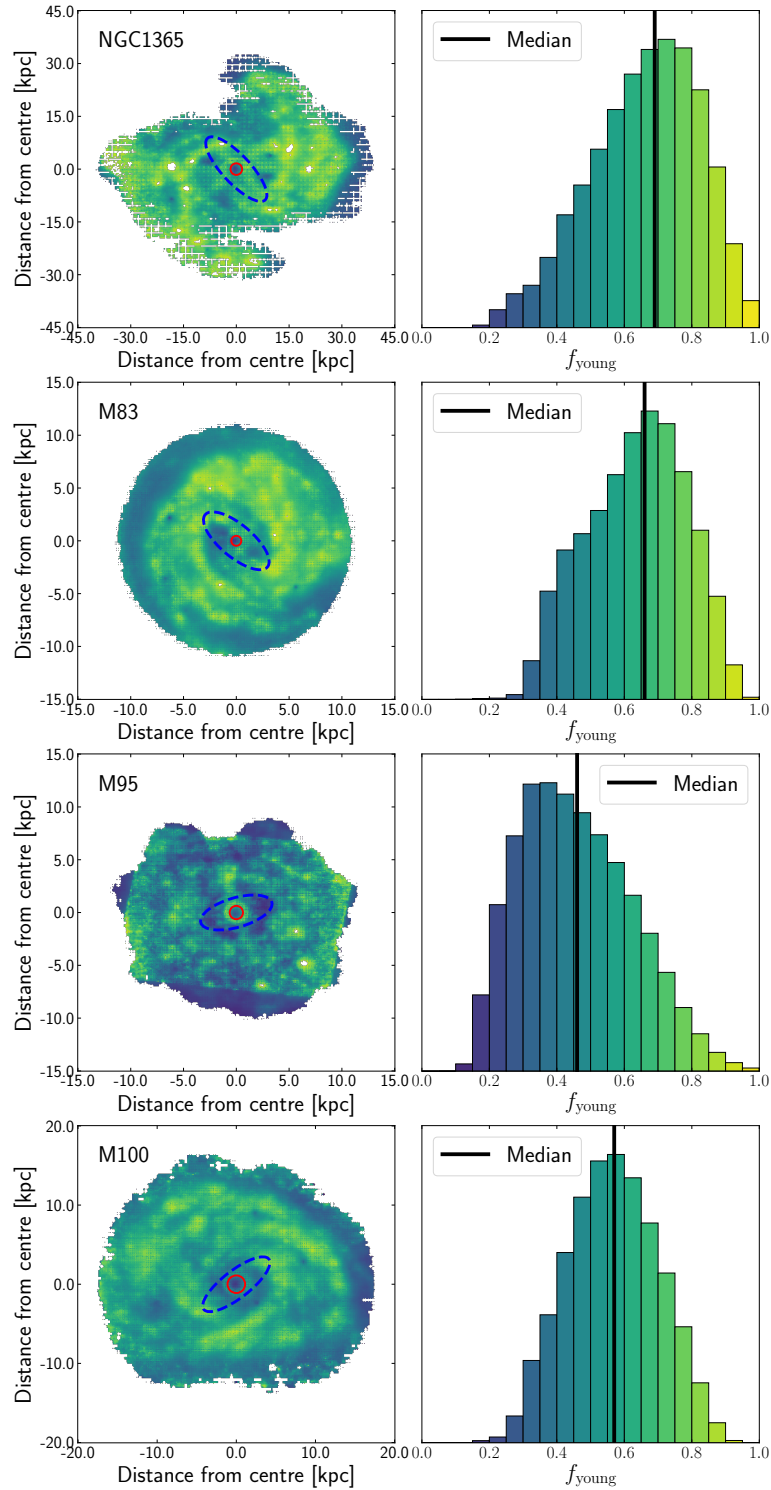


Figure 6.9: Left panel of each sub-figure: Face-on view of the heating fraction by young non-ionising and young ionising stellar populations (Equation 6.3), as obtained from the 3D dust cell distribution, for each galaxy. The bulge region of every galaxy is indicated with a solid red circle and the bar region with a dashed blue ellipse (see text for more details). Right panel of each sub-figure: Distribution of the dust cell heating fractions, weighted by dust mass. The histogram also denotes the colour coding of the map on the left. The solid black line shows the median value.

view of each galaxy. The bulge and bar regions are denoted with a solid red circle and a dashed blue ellipse, respectively. The parameters used to define these regions were retrieved from the S⁴G database (Salo et al. 2015). We define the bulge radius as $2 \times R_e$. Salo et al. (2015) used a modified Ferrers profile to model the bar. The histogram in the right panel of each sub-figure displays the young heating fraction distribution within the dust cells, weighted by the dust mass. For NGC 1365 we find that on average, 68% of the dust heating (or dust emission) originates from the radiation produced by the young stellar populations. M 83 shows also a high f_{young} with a mean value of 64%, while in the cases of M 95 and M 100 the young and old stellar populations contribute approximately to one half each, with mean young heating fractions around 47% and 57%, respectively. However, in the case of M 95 the mode of the distribution is shifted to a much lower value ($\sim 37\%$) compared to the mean and median values. From the dust-heating maps of NGC 1365, M 83, and M 100 we can see that the star formation is for the most part concentrated in the spiral arms. In the case of M 95 the bulk of the dust is heated by the old stellar population, with few sites of star formation remaining in the circumnuclear ring and in the outer ring of molecular gas that surrounds the stellar bar.

We find that the mean f_{young} within the bulge region of every galaxy does not exceed $\sim 46\%$ (see Table 6.6). As expected, the old stellar population is the dominant dust-heating source in the central region of each galaxy (see also, De Looze et al. 2014; Viaene et al. 2017; Verstocken et al. 2019). Regarding the bar, although we do not treat the bar of each galaxy as a different component in our modelling, we can still extract basic information of its properties by looking at the young heating fraction, the radial profiles (see Fig. 6.10) and the dust temperature (see Sect. 6.5.4). In the bar region, the mean young heating fractions are: $\sim 66\%$, $\sim 59\%$, $\sim 43\%$, and $\sim 46\%$ for NGC 1365, M 83, M 95, and M 100 respectively, with the higher value being for the galaxy with the longest bar (NGC 1365; bar length of 24 kpc), while the lower value being for the galaxy with the shorter bar (M 95; bar length of 7 kpc). These fractions imply that the radiation field in the bar is caused by a mix of old and young stellar populations, both ‘equally’ contributing to the dust heating. The young heating fractions for every galaxy and each region are given in Table 6.6.

Furthermore, Fig. 6.10 depicts the radial profiles of the young heating fractions. Each point represents a dust cell in our simulations. Following the running median (dashed black line) an interesting pattern appears. It is immediately evident, that all galaxies showcase a narrow central peak where the bulge region ends and the bar starts. This peak is followed by a local minimum in the young heating fraction and then an outer maximum which interestingly coincides with the bar truncation point. Then, the running median of f_{young} in the galactic disc slowly declines or remains constant. This pattern is clearer for M 95 with a strong peak at 1 kpc distance, possibly due to the nuclear starburst and the inner star-forming ring that connects the bulge with the bar. Moreover, M 95 reaches a second minimum in the bar inner region indicating the suppression of star formation due to gas depletion or gas re-distribution. For example, James et al. (2009) have shown the lack of H α emission in the bar region of M 95, and long-slit spectroscopy showed that any diffuse emission from that region is associated with post-AGB stars (James & Percival 2015). In a recent study, George et al. (2019) presented evidence of suppressed star formation in the bar inner region of M 95 due to gas inflows

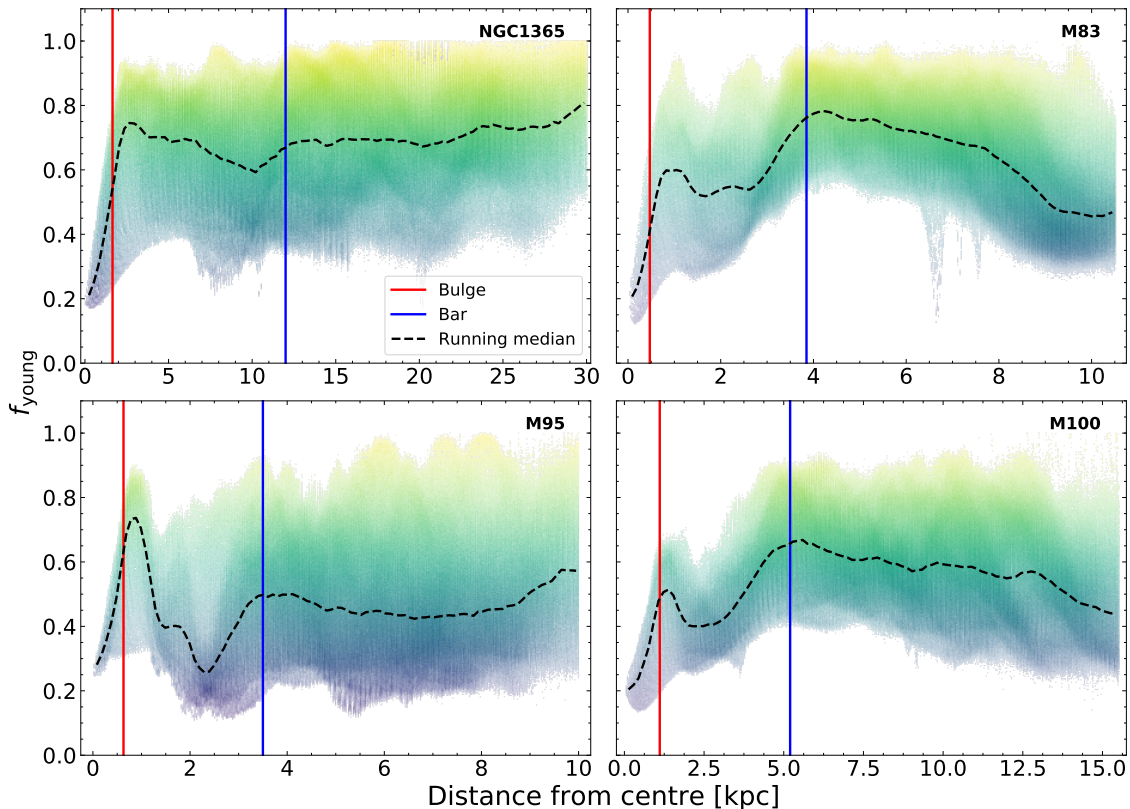


Figure 6.10: Distribution of f_{young} calculated for every galaxy with galactocentric distance. Each point represents a dust cell and it is colour-coded according to f_{young} . The level of transparency indicates the points density. The radius of the bulge is indicated with a vertical red line while the vertical blue line denotes the outer truncation radius of the Ferrers-bar. The dashed black line is the running median through the data points.

to the nuclear region. On the other hand, the pattern we describe here is less prominent in the case of NGC 1365 possibly due to the enhanced star-forming activity close to the central area (Fazeli et al. 2019), but also due to the higher levels of star formation in the bar inner region.

James et al. (2009) reported the same pattern while studying the effects of bars on the radial distributions of $H\alpha$ and R-band light for more than 300 nearby galaxies. James et al. (2009) have shown (see their Fig. 8) that the mean $H\alpha$ profiles (tracing the SFR) for galaxies with a clear optical bar and of Hubble stages T , between 3 and 5, have the same visible pattern as the one we observe here. They concluded as we do, that the bar component is responsible for the distinctive profiles seen in Fig. 6.10, since a similar pattern is absent in the radial profiles of unbarred galaxies (for example, see the radial profile of M 81; Verstocken et al. 2019).

In summary, our analysis indicates that the central regions and the two diametrically opposed ends of the bar are places of enhanced star formation while the bar inner region is mostly populated by more evolved stars. Even though the galaxy sample studied here is too small for any formal statistical analysis, we can confirm that bars have a clear effect on the variation of the f_{young} radial profile. Of course, bars are not axisymmetric

and therefore any effect caused by them will only arise in a diluted form, in any of the radial profiles. Furthermore, a dynamical origin of the presence of low-age stars in the bar central and outer regions cannot be excluded. [Wozniak \(2007\)](#) have shown that the regions of enhanced star formation inside the bar are due to the accumulation of young stellar populations trapped on elliptical-like orbits along the bar. In any case, the distinct bar-induced features in the young heating fraction profiles suggest that the bars are prompting star formation that would not otherwise be happening ([James et al. 2009](#)).

6.5.3 Correlation between young heating fraction and sSFR

In this section we report a strong relation between the young heating fraction and the sSFR. According to [Ciesla et al. \(2014\)](#), sSFR is a measure of the hardness of the UV radiation field, providing an interesting and unique insight on the ratio of the current over the past star-forming activity of a galaxy. [De Looze et al. \(2014\)](#) have shown the existence of a strong correlation between the sSFR and the dust mass fraction heated by the young stellar populations for M 51. This correlation was further confirmed in the radiation transfer models of M 31 ([Viaene et al. 2017](#)) and M 81 ([Verstocken et al. 2019](#)). Radiation transfer models aside, others have found the same relationship at both local galaxy samples ([Viaene et al. 2016](#); [Nersesian et al. 2019b](#)) and intermediate redshift (z) galaxies ([Leja et al. 2019](#)).

Figure 6.11 shows the relative contribution from the young stellar populations to the dust heating responsible for the TIR emission as was calculated for each dust cell and for all four galaxies of this study, as a function of \log sSFR. Additionally, we include the data of the radiation transfer models of M 77 ([Viaene et al. 2019](#), see also Chap. 7) and M 81 ([Verstocken et al. 2019](#)). In total, the plot of Fig. 6.11 contains more than 15 million data points. To estimate the stellar masses we used the IRAC $3.6 \mu\text{m}$ luminosities and the prescription provided by [Oliver et al. \(2010\)](#). We converted the intrinsic FUV luminosity of the young stellar populations to SFR using the prescription provided in [Kennicutt & Evans \(2012\)](#). To calculate the sSFR in every data cell, we simply divided the SFR with the stellar mass. To fit the relationship of Fig. 6.11, we used the function given in [Leja et al. \(2019\)](#) (see their Equation 2) which yields the following relation:

$$f_{\text{young}} = \frac{1}{2} \left[1 - \tanh \left(a \log \left(\text{sSFR}/\text{yr}^{-1} \right) + bz + c \right) \right]. \quad (6.4)$$

where $a = -0.87$ and $c = -9.3$. Since the galaxies in our sample lie in the local Universe ($z < 0.01$) we used $z = 0$. For comparison purposes, we provide the best-fitted power-laws of: M 31 ([Viaene et al. 2017](#)), M 51 ([De Looze et al. 2014](#)), and the relations derived by [Leja et al. \(2019\)](#) for a sample of galaxies from the 3D-HST catalogues at redshift $0.5 < z < 2.5$. Due to the overlap of colours, we present the data of the radiation transfer models of each galaxy separately in Fig. 6.12, and fit the bulk of the data cells using both Equation 6.4 and a power-law. The best-fitted parameters are given in Table 6.7 along with the Spearman's rank correlation coefficient (ρ). The strong correlation between the two quantities is justified by the fact that ρ takes values

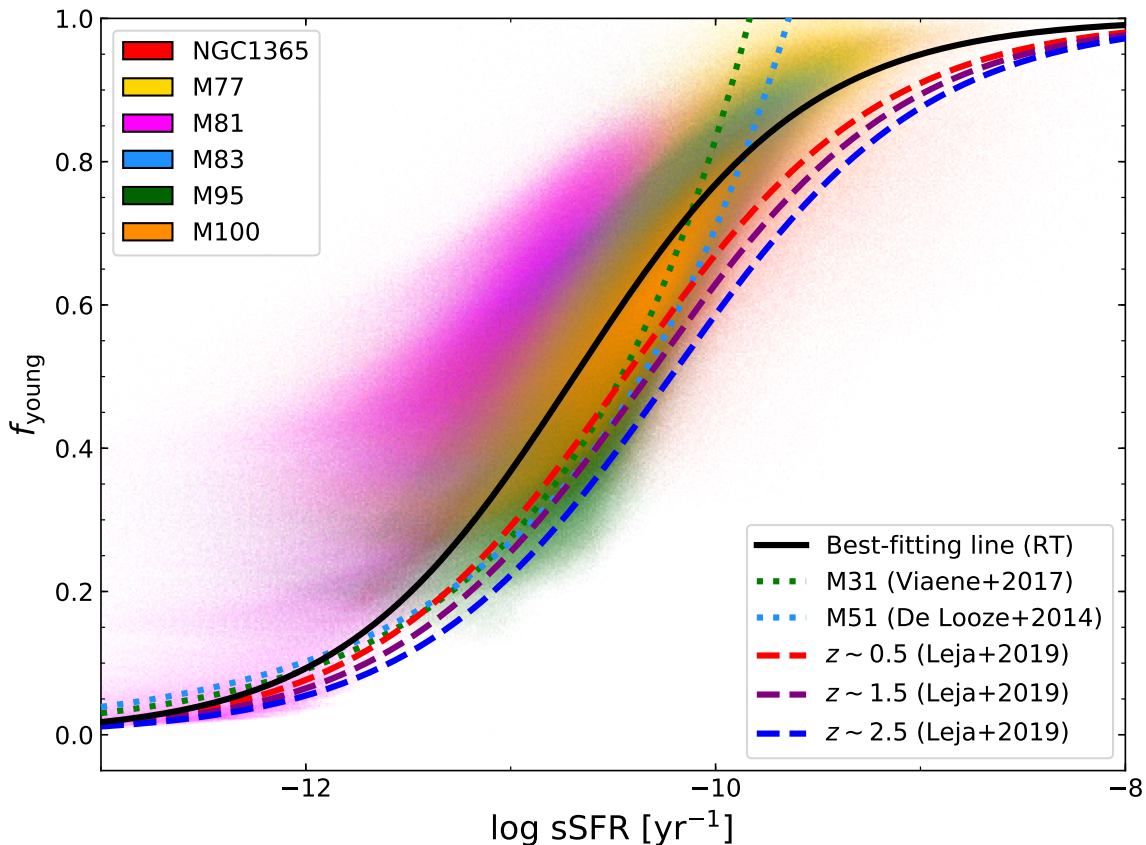


Figure 6.11: Relation between sSFR and f_{young} , shown for the radiation transfer models of: NGC 1365, M 83, M 95, M 100; M 81 (Verstocken et al. 2019); and M 77 (Viaene et al. 2019, see also Chap. 7). Each galaxy dataset is assigned with a different colour indicated in the upper left corner of the figure. The solid black line shows the fit from Equation 6.4 through all data cells of every galaxy (RT). For comparison purposes we also provide the best-fitted power-laws of: M 31 (dotted green line, Viaene et al. 2017); M 51 (dotted cyan line, De Looze et al. 2014); and the relations derived by Leja et al. (2019) for a sample of galaxies from the 3D-HST catalogues at three redshift bins: $z \sim 0.5$ (dashed red line), $z \sim 1.5$ (dashed purple line), and $z \sim 2.5$ (dashed blue line).

≥ 0.80 . The only exception is NGC 1365 with $\rho = 0.75$, however the correlation still remains strong. The best-fitting power-law for M 81 was given in Verstocken et al. (2019). An interesting result we notice here is that the slope of the power-law becomes more and more flat as the bulk of data cell values shifts towards higher sSFR and f_{young} values.

It is immediately evident that there is an increasing trend between the young heating fraction in each dust cell and the sSFR in all cases. Cells of high sSFR ($> 10^{-10} \text{ yr}^{-1}$) are primarily heated by the young stellar populations, whereas the contribution of the old population becomes more and more significant for cells with low sSFR ($\leq 10^{-10} \text{ yr}^{-1}$). The bulk of data points of every galaxy are concentrated more or less in the same region of the diagram, with the sSFR spanning three orders of magnitude. Our results are in accordance with the relations produced by the radiation transfer models of M 31 and M 51 despite the overall differences and assumptions made in the studies of Viaene et al.

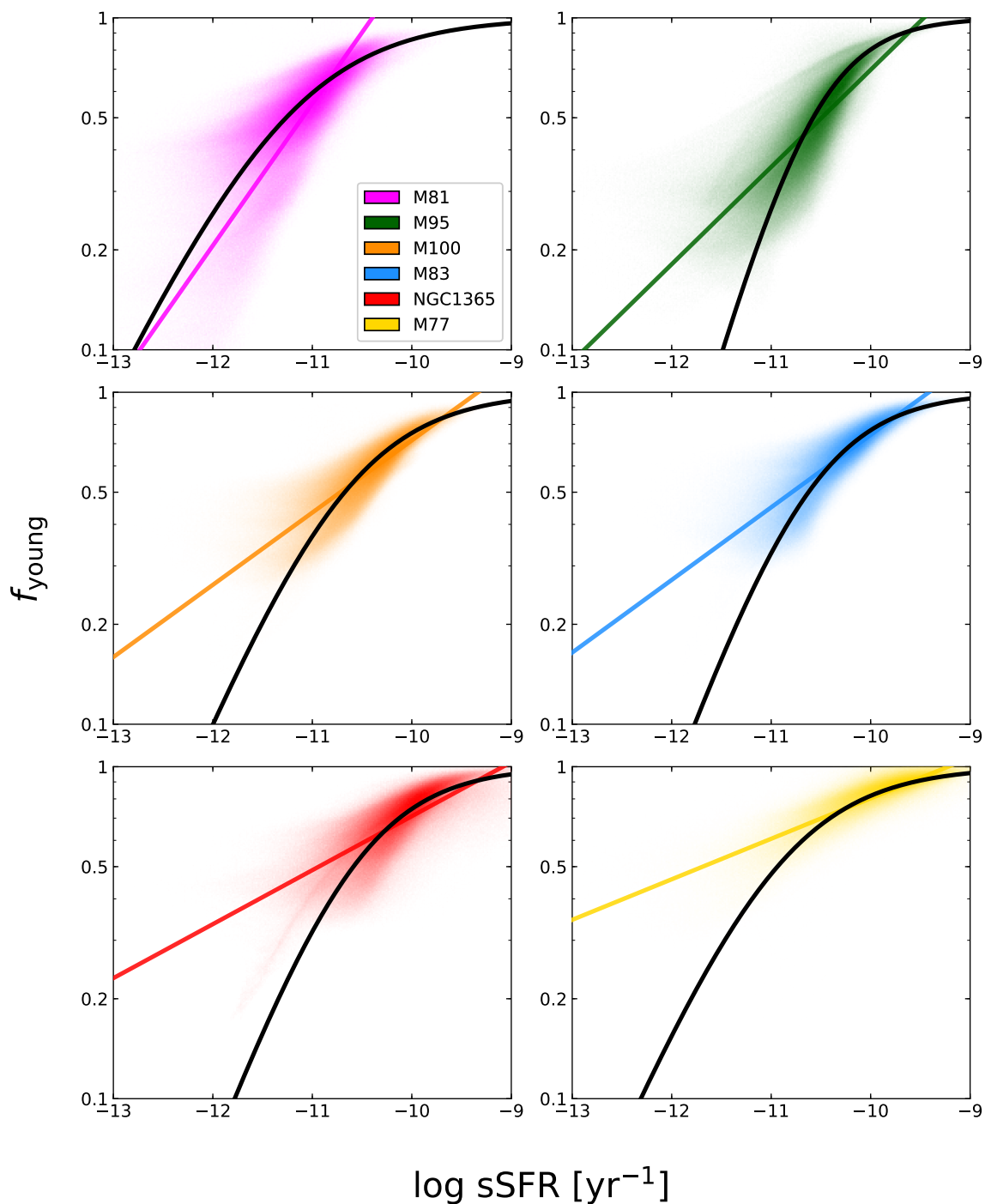


Figure 6.12: Relation between sSFR and f_{young} , shown for the radiation transfer models of: NGC 1365, M 83, M 95, M 100; M 81 (Verstocken et al. 2019); and M 77 (Viaene et al. 2019, see also Chap. 7). Each galaxy dataset is assigned with a different colour indicated in the lower right corner of the first panel. The solid black line shows the fit from Equation 6.4 through the bulk of data cells of every galaxy. Each coloured line shows the best-fitting power-law through the bulk of data cells of every galaxy.

Table 6.7: Relations between sSFR and f_{young} . The relationship in Fig. 6.12 is fitted with a power-law: $y = ax + b$; where $y = \log f_{\text{young}}$, $x = \log [\text{sSFR}/\text{yr}^{-1}]$, a is the slope and b is the intercept of the best-fitting line, and ρ is the Spearman's rank correlation coefficient. The relationship is also fitted with Equation 6.4.

Galaxy ID	$y = ax + b$		Spearman's coef.	Equation 6.4	
	a	b	ρ	a	c
NGC 1365	0.16	1.48	0.75	-0.92	-9.74
M 77	0.12	1.13	0.84	-0.80	-8.75
M 81	0.43	4.45	0.85	-0.72	-8.11
M 83	0.22	2.06	0.85	-0.96	-10.2
M 95	0.29	2.79	0.80	-1.21	-12.8
M 100	0.22	2.04	0.84	-0.83	-8.86

(2017) and De Looze et al. (2014), respectively (i.e. different ages of the young stellar populations and different methods of estimating the sSFR). The derived relationship, in principle, will enable us to quantify the young heating fraction based on sSFR measurements in other galaxies and can be applied to calibrate the energy fraction of the old stellar population in global SED modelling.

Furthermore, we find very good agreement with the relations derived by Leja et al. (2019) at different redshifts. The authors fitted the data of more than $\sim 50,000$ galaxies from the 3D-HST catalogues at redshifts $0.5 < z < 2.5$. Galaxies at those redshifts are massive and obscured star formation is the main agent of star formation (Whitaker et al. 2017). The authors used the PROSPECTOR- α physical model (Leja et al. 2017) to fit the galaxy SEDs. The model includes a flexible non-parametric star-formation history (SFH), a two-component dust attenuation model with a flexible age-dependent Charlot & Fall (2000) attenuation curve, a model accounting for the MIR emission from AGN torii, and dust emission via energy balance. In their study, the young heating fraction is defined as the relevant fraction of $L_{\text{UV+IR}}$ emitted by the young stars (≤ 100 Myr), while a Chabrier (2003) IMF was used. After fitting the data, the authors reported lower SFRs and higher stellar masses than those found by previous studies in the literature for galaxies at $0.5 < z < 2.5$. They infer that the cause for this offset in both quantities is the contribution from the old stars (> 100 Myr), implying an older, less active Universe. Here we notice that the relation yielded by Equation 6.4 shifts towards higher sSFR values with increasing redshift (from the solid black line to the dashed blue line). It is also worth noting that for a fixed sSFR value the f_{young} decreases with increasing redshift. To some degree the shift of the sSFR- f_{young} relation towards higher sSFR values with increasing redshift can be attributed to the increased SFR, at least in the regime $0.5 < z < 1.5$. In addition, Leja et al. (2019) showed that the old stellar populations in high-redshifts ($1.5 < z < 2.5$) are relatively younger and on average more luminous, contributing more to the dust heating, which explains the decrease in f_{young} with redshift.

The concluding remarks in [Leja et al. \(2019\)](#) agree quite well with the picture we draw here by studying the properties of local galaxies on resolved scales, as we also infer that the older stellar population has a more prominent role on the heating of the diffuse dust. The relation between the sSFR and the relative fraction of dust heated by the star-forming regions or by the old stellar populations has now been observed in a wide range of galaxy types and using various modelling approaches. Our analysis showcases the importance of a consistent modelling approach in order to derive safe conclusions when comparing different datasets. With that in mind, further investigation of the relationship discussed here, both in global and resolved scales, will allow for a better understanding of the scatter in the sSFR- f_{young} relation.

6.5.4 Dust temperature

Light originating from star-forming regions acts as an important dust-heating source and thus one should expect to find a trend between regions of high dust temperatures and increased levels of star formation. Moreover, several studies have shown a dependence of the FIR surface brightness colours (i.e. indicators of dust temperature), with radius ([Bendo et al. 2010, 2012](#)). In the left column of [Fig. 6.13](#) we plot the dust temperature (T_{dust}) as a function of the deprojected galactocentric radius in kpc. Again, each point on each panel of this plot represents a dust cell in our simulations, colour-coded according to f_{young} . The bulge radius is indicated with a vertical red line while the outer truncation radius of the Ferrers-bar profile is indicated with the vertical blue line. From our analysis it is possible to determine how much the old stellar bulge and the composite stellar populations of the bar and disc structures affect the temperature of the diffuse dust.

Here we should make clear to the reader that the dust temperatures are only those of the diffuse dust and thus interpretation of the results should be considered with caution. Including the dense dust clouds in the star-forming regions, which they are subgrid properties of the MAPPINGS III templates, could add a significant amount of unusually high SFR and temperature values.

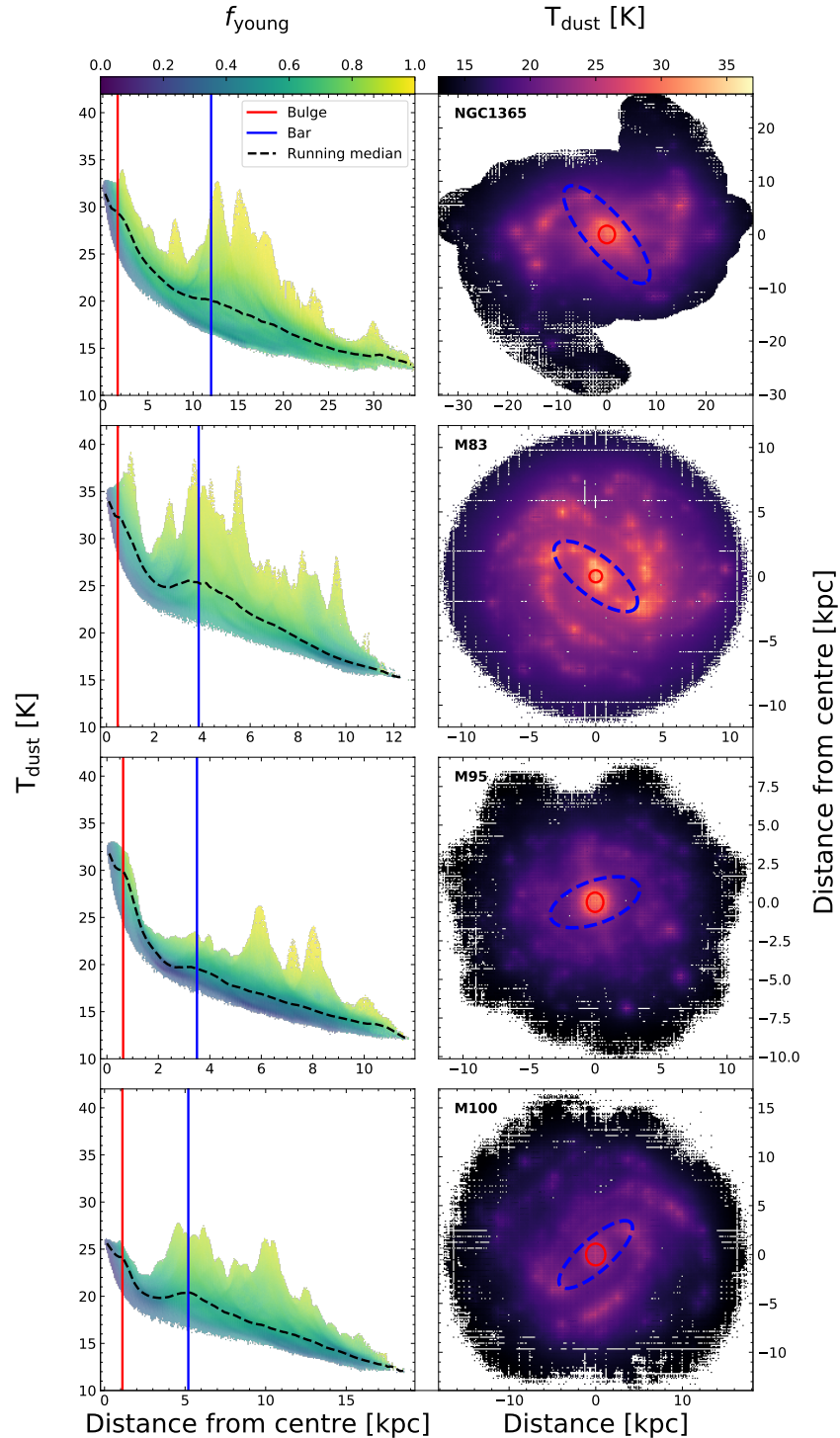
The diffuse dust temperature of each dust cell in our simulations was approximated through the strength of the ISRF (U). First we calculated U by integrating the mean intensity of the radiation field J_{λ} of each cell over the wavelength range 8-1000 μm . Then we normalised with the ISRF, estimated by [Mathis et al. \(1983\)](#) for the solar neighbourhood ($\sim 5 \times 10^{-6} \text{ W/m}^2$). Assuming that dust is heated by an ISRF with a Milky-Way like spectrum ([Mathis et al. 1983](#)) we employed the following equation to approximate the dust temperatures of the diffuse dust:

$$T_{\text{dust}} = T_{\text{o}} U^{1/(4+\beta)}, \quad (6.5)$$

([Nersesian et al. 2019b](#), and references therein). Here, $T_{\text{o}} = 18.3 \text{ K}$ which is the dust temperature measured in the solar neighbourhood, and β is the dust emissivity index, which, for the THEMIS dust model, gives the value of 1.79.

Overall, temperatures range from 13-37 K with a decreasing trend towards the outermost regions of each galaxy, with several peaks and fluctuations which coincide with the

Figure 6.13: Left column: distribution of the temperature of the diffuse dust with galactocentric distance. Each point represents a dust cell in our simulations. They are colour-coded according to f_{young} . The level of transparency indicates the point density. The bulge radius is indicated with a vertical red line while the vertical blue line denotes the outer truncation radius of the Ferrers-bar. The dashed black line is the running median through the data points. Right column: face-on view of the dust temperatures as obtained from the 3D dust cell distribution, for each galaxy. The bulge region is indicated with a solid red circle and the bar region with a dashed blue ellipse.



appearance of high young heating fractions. These peaks are star-forming regions in the spiral arms or in the galactic disc, with the harsh UV radiation by the young populations heating the dust grains to high temperatures (25-37 K). Again, if we follow the running median line, a distinct pattern is seen in all galaxies. Dust temperature peaks at the centre of each galaxy and then sharply declines until a plateau is reached, approximately at 20-25 K (even with a rising trend, more clearly visible in the cases of M 83 and M 100). At the point where the bar is truncated, this plateau is followed by a continuous decline. These results are consistent with those obtained in previous studies on the T_{dust} radial trends of nearby spiral galaxies (Pohlen et al. 2010; Sauvage et al. 2010; Boquien et al. 2011; Xilouris et al. 2012; Bendo et al. 2012; Galametz et al. 2012). Here we see again the possible effect of the bar to the T_{dust} radial profile, since the plateau (or shoulder) is seen in the bar inner region. The average T_{dust} in the bulge region of NGC 1365, M 83, M 95, and M 100 is warmer than the average T_{dust} in the bar by 25%, 22%, 28%, and 16%, respectively. We measured the global dust temperatures for NGC 1365, M 83, M 95, and M 100 to be 19.2 ± 3.8 K, 21.8 ± 3.6 K, 17.5 ± 3.0 K, and 17.6 ± 2.6 K, respectively. The average dust temperature of our galaxy sample is 19.0 ± 1.7 K. According to Nersesian et al. (2019b), the average dust temperature for Sb-Sc type galaxies is 22.2 ± 3.0 K and compares fairly well with the mean dust temperature derived here for our galaxy sample.

Taking advantage of the information given by f_{young} , it is apparent that the emission of the old stellar population is directly responsible for the high dust temperatures at the nuclear region of each galaxy. This behaviour is expected since bulges are regions of extremely high radiation density produced by old stars. For example, several studies concluded that early-type galaxies (which tend to be more concentrated than spirals and their ISRF is governed by old stellar emission) have on average warmer dust temperatures than late-type galaxies (e.g. Skibba et al. 2011; Nersesian et al. 2019b). The old stellar population is also responsible for the lower dust temperatures in the bar and disc inner regions, as opposed to the higher temperatures there which are driven by star formation. In the right column of Fig. 6.13 we plot the dust temperature maps, to get a better visual view of the results discussed here. The bulge and the bar regions are indicated with a solid red circle and a dashed blue ellipse, respectively. Indeed, from this plot it is evident that the dust temperature is enhanced near the nucleus and along the spiral arms near star-forming regions. On the other hand, in the inter-arm and outermost regions of each galaxy, the diffuse dust is much colder. This radial trend mostly is a consequence of the diluted ISRF and possibly due to fewer young stellar populations at larger radii. The bars are not prominent in the temperature maps (with the exception of M 83). More specifically in the case of M 95, which has an inner and an outer star-forming ring with the bar acting as a bridge between them, we see that dust temperature in the inner ring ranges from 25-33 K, while the dust temperatures of the outer ring drops to 15-25 K. The old stellar population is the dominant heating agent of the diffuse dust in the outer ring of M 95, and the young stellar populations are dominating the dust-heating process in the inner ring.

6.6 Conclusions

We have constructed detailed 3D radiative transfer models using the state-of-the-art Monte Carlo code SKIRT, for four late-type barred spiral galaxies (NGC 1365, M 83, M 95, M 100), with the purpose of investigating the dust-heating processes and to assess the influence of the bar on the heating fraction. Our models have been validated by comparing the simulated SEDs with the observational data across the entire UV to submm wavelength range, yielding a best-fitting description of each galaxy. Here we list our main results:

- ◆ We provide global attenuation curves for NGC 1365, M 83, M 95, M 100, M 81, and M 77, and we confirm the dependence of the shape of the observed attenuation curve with the star-to-dust geometry and the level of star-formation activity. The strength of the UV bump and the slope of the attenuation curve correlate with the sSFR of a galaxy and the degree of complexity of the star-to-dust geometry.
- ◆ For the full sample, 36.5% of the bolometric luminosity is absorbed by dust. This average fraction is in line with the mean values determined by [Bianchi et al. \(2018\)](#), for the particular morphological group (Sb-Sc) that our galaxies fall into.
- ◆ We find that the old stellar population has a more active role in the process of dust heating. This result hints that the use of infrared luminosity as a proxy for the star-formation activity in star-forming galaxies should be used with caution. The global f_{young} fractions for NGC 1365, M 83, M 95, and M 100 are 68%, 64%, 47%, and 57%, respectively. We find that the old stellar population is the dominant heating source in the bulge region, while both old and young stellar populations are equally responsible for the dust heating in the bar region.
- ◆ We confirm a strong link between f_{young} and the sSFR which was previously reported in the radiative transfer model analysis of M 51 ([De Looze et al. 2014](#)), M 31 ([Viaene et al. 2017](#)), and M 81 ([Verstocken et al. 2019](#)), as well as in studies of ([Nersesian et al. 2019b](#)) for the DustPedia galaxy sample and [Leja et al. \(2019\)](#) for the 3D-HST galaxy sample, and provide a relation to calibrate the contribution of the old stellar population to dust heating in global SED modelling.
- ◆ We confirm that the central regions and the two diametrically opposed ends of the bar are places of enhanced star formation and show that the bar in those galaxies affects the radial profiles of the f_{young} and dust temperature. On average, the diffuse dust temperatures at the central regions of galaxies are warmer than those at the bar regions, while T_{dust} decreases towards the outer parts of galaxies. The old stellar population is exclusively responsible for the warmer T_{dust} at the bulge and the colder T_{dust} across the galactic disc of galaxies. The young stellar populations are responsible for the warmer T_{dust} in the spiral arms and near the star-forming dust clouds. The average dust temperature of our galaxy sample is 19.0 ± 1.7 K and is comparable to the mean values derived by [Nersesian et al. \(2019b\)](#), for the particular morphological group (Sb-Sc) that our galaxies fall into.

The full description of our framework and the results of the radiation transfer modelling of M 81 are presented in [Verstocken et al. \(2019\)](#), while the modelling results of a galaxy with the addition of an AGN component, NGC 1068 (M 77) will be presented in [Viaene et al. \(2019\)](#), see also Chap. 7). The continuation of the 3D radiation transfer modelling in a statistically significant sample of nearby spatially resolved galaxies, which have been modelled in a homogeneous way, will allow us to better understand the scatter in the $\text{sSFR}-f_{\text{young}}$ relation but also to investigate the properties of dust (e.g. composition, size distribution, etc.) and possible variations in the dust-heating processes among different galaxy types in the local Universe.

AGN-powered dust heating in NGC 1068

The analysis and results of this chapter appear in **S. Viaene, A. Nersesian**, J. Fritz, S. Verstocken, M. Baes, S. Bianchi, V. Casasola, L. P. Cassará, C. J. R. Clark, I. De Looze, P. De Vis, W. Dobbels, M. Galametz, F. Galliano, A. P. Jones, S. C. Madden, A. V. Mosenkov, A. Trčka, E. M. Xilouris, and N. Ysard, 2019, ‘High-resolution, 3D radiative transfer modelling IV. AGN-powered dust heating in NGC 1068’, *A&A*, *submitted*.

7.1 Introduction

Dust can be found in all star-forming galaxies, and even in a significant fraction of ETGs ([Smith et al. 2012a](#); [di Serego Alighieri et al. 2013](#)). Dust grains play a vital role in the formation of stars by shielding and catalysing the creation of molecules such as H₂ and CO, and by regulating the gas temperature. Due to this close connection with both stars and gas, dust is increasingly used as a tool to study the evolution of galaxies through time.

Dust and gas are strongly intertwined in the ISM and usually follow a metallicity dependent gas-to-dust ratio ([Sandstrom et al. 2013](#); [Rémy-Ruyer et al. 2014](#)). As such, dust emission can not only be used to trace its own mass, but also the total mass of the ISM ([Eales et al. 2012](#); [Scoville et al. 2014](#); [Hughes et al. 2017](#)). Accurate dust mass measurements are an important extra metric for evolutionary studies of ISM in galaxies, as neutral gas is hard to detect beyond the local Universe, and molecular gas tracers rely on empirical conversion factors. The most obvious effect of dust is of course its capacity to absorb and scatter UV and optical light. In the local Universe, roughly one third of starlight is absorbed by dust grains ([Skibba et al. 2011](#); [Viaene et al. 2016](#); [Bianchi et al. 2018](#)). This absorbed energy is re-emitted again at MIR-mm wavelengths where it can even be observed up to high redshifts with telescopes such as ALMA and *Herschel*. Dust is therefore also a popular star-formation tracer across cosmic time (see e.g. [da Cunha](#)

et al. 2010; Madau & Dickinson 2014; Casey et al. 2014; Scoville et al. 2015).

The big caveat to using dust as a tracer of either ISM mass or the SFR, is the conversion of FIR-submm emission into either of these quantities. At this point, it becomes important how the dust grains are heated to their equilibrium temperature. In practice, the most common assumption is that of a single heating source (e.g. star formation) producing a single radiation field, which is then parametrized with a single -average-temperature component. Dust masses can then be estimated from a MBB function (Hildebrand 1983) or a dust emission template (e.g. Dale et al. 2001; Draine et al. 2014). In reality however, dust in galaxies is a mix of grain types and sizes, with multiple temperatures, and multiple heating sources. A more accurate determination of dust masses (and thus total ISM masses) require more complex models for the dust emission. Such models also benefit the determination of the SFR from dust emission. In this case it is important to only count the absorbed energy from new stars that is re-emitted by dust.

The main dust heating sources in galaxies have been qualitatively derived from correlations of dust emission with SFR or stellar mass tracers (Galametz et al. 2010; Boquien et al. 2011; Bendo et al. 2012; Foyle et al. 2013; Hughes et al. 2014) or from panchromatic models for a galaxy's SED (Groves et al. 2012; Aniano et al. 2012; Dale et al. 2012; Mentuch Cooper et al. 2012; Ciesla et al. 2014; Rémy-Ruyer et al. 2015; Boquien et al. 2016; Viaene et al. 2016). The broadest of such studies was performed by Nersesian et al. (2019b) as they modelled the global SED of 814 nearby galaxies of different morphologies. They found a wide range in the individual contributions of dust heating sources, with a significant and often dominant contribution of the old stellar populations (see Sect. 5.11.1). In a dedicated resolved study, (Bendo et al. 2015) mapped the dust heating sources for 24 nearby face-on spiral galaxies. They found that in some galaxies the dust is predominantly heated by star formation, while some are heated by the old stellar population. Most galaxies however again show an ambiguous heating pattern with energy from both young and older stars contributing to the dust emission.

In a pioneering study by De Looze et al. (2014), high resolution 3D radiative transfer simulations were used to model the dust heating in M 51. The novelty in this study was to infer realistic, non-axisymmetric distributions for both stars and dust from observed broad band images. They found a strong wavelength dependence in the dust heating, with an overall contribution of 37% from the old stellar populations. A similar model was created for the Andromeda galaxy (M 31) by Viaene et al. (2017). They found that the old stellar populations dominate the dust heating (91% globally), even in the main star-forming ring of M 31. This effect was attributed to the large and old bulge of Andromeda. Most recently, M 33 was also modelled in this way, finding old population heating contributions between 50 and 80% (Williams et al. 2019). In the context of the DustPedia project (Davies et al. 2017), we have set up a best-practice framework for such radiative transfer modelling and applied it to M 81 (Verstocken et al. 2019) and to a set of nearby star-forming spirals (M 83, M 95, M 100 and NGC 1365; Nersesian et al. 2019a, see also Chap. 6).

All these studies assume a stellar origin for the energy absorbed by dust. In the radiative transfer models, three stellar populations are needed to match the observed panchro-

matic SED and images: an old (5-12 Gyr) stellar component, a non-ionising (~ 100 Myr) component, and a population of ongoing obscured star formation. While this is acceptable for many star-forming spiral galaxies, there is evidence for other sources of dust heating. Dust grains can gain energy by capturing hot electrons, protons or even ions (Jones 2004). In the latter two cases this can also partially destroy a grain (a process called sputtering). As such, cosmic rays produced by recent supernovae may be a secondary dust heating mechanism following recent star formation. In a similar way, hot gas can produce a flux of energetic electrons which directly heat the dust grains (Bocchio et al. 2013).

Another potential dust heating source is the accretion disc around supermassive black holes. In galaxies hosting an AGN, the accretion disc certainly heats the dusty torus surrounding it and produces strong MIR emission (see e.g. Fritz et al. 2006). However, higher dust temperatures and anomalously bright nuclear FIR emission is found for galaxies hosting an AGN (Wu et al. 2007; Bendo et al. 2012; Kirkpatrick et al. 2012; Verstappen et al. 2013; Kirkpatrick et al. 2015; Roebuck et al. 2016). This circumstantial evidence suggests that the accretion disc may be powerful enough to heat ISM dust beyond the torus. Schneider et al. (2015) investigated this phenomenon using radiative transfer simulations of a $z \sim 6$ quasar, and found that the AGN may contribute 30-70% to the heating of diffuse dust. While this may be an extreme case, it shows that AGN can contribute to the FIR-submm SED in galaxies. This effect influences the total mass and SFR estimates of galaxies hosting an AGN, but is not taken into account by SED fitting models.

The goal of this study is to address the question of AGN powered dust heating in the local Universe. We choose to take a quantitative approach to separate the contributions of star formation, old stellar populations and AGN. Therefore, we will focus on a single galaxy, but construct a detailed model based on 3D radiative transfer simulations as originally outlined in De Looze et al. (2014); Viaene et al. (2017), and now perfected in the DustPedia framework (Verstocken et al. 2019; Nersesian et al. 2019a).

This study focuses on NGC 1068 (M 77), a nearby ($D = 10.1$ Mpc) Seyfert 2 SAb galaxy (Osterbrock & Martel 1993). This AGN has no broad-line emission features, despite being a nearly face-on ($i = 28^\circ.1$) disc galaxy. Instead, optical polarimetry reveals broad reflection lines (Antonucci & Miller 1985). These observations suggest that the accretion disc is obscured by the torus for an observer on Earth. VLBI measurements of a H₂O megamaser (Greenhill et al. 1996) confirm that the torus is in fact seen edge-on. Recent ALMA observations of the core of NGC 1068 reveal a complex ISM, with the torus being more inclined $34 - 66^\circ$ at larger radii (García-Burillo et al. 2016). The orientation of the torus suggests that the accretion disc is in effect beaming its radiation straight into the galactic disc, which makes NGC 1068 a well-suited target to study AGN-powered dust heating. In addition, the galaxy is actively forming stars in its inner regions and hosts a relatively quiescent outer disc ((D'Agostino et al. 2018). We can thus also compare the relative importance of stellar heating mechanisms to each other, and to the AGN contribution.

7.2 Data

This investigation relies mostly on broad-band imaging from the DustPedia database¹ (Davies et al. 2017). This comprehensive database contains the 875 nearby (< 40 Mpc) galaxies that were observed by the *Herschel Space Observatory*. It includes uniformly reduced PACS and SPIRE maps, and broad-band images from major ground and space-based survey telescopes up to the UV. In addition, they provide aperture-matched photometry in the UV-mm. For more details on the image processing and photometry we refer to Clark et al. (2018).

In particular, for NGC 1068, we make use of UV maps from GALEX (Martin et al. 2005), optical images from SDSS (York et al. 2000), MIR observations from WISE (Wright et al. 2010), and submm data from HERSCHEL (Pilbratt et al. 2010). We don't rely on the standard photometry of DustPedia in this case, as our model will focus on a different aperture. We thus repeated the photometry measurements based on these new apertures. The AGN in NGC 1068 is especially bright in the MIR. Images from $3.4 \mu\text{m}$ till $24 \mu\text{m}$ are severely distorted by the PSF signature of their respective instruments. This virtually renders any morphological study impossible in this wavelength domain. We note that the images are not over-exposed in the MIR, meaning the integrated flux measurements are still useful and will serve as the most important constraint on the AGN model.

There are only two *Spitzer*-IRAC bands ($3.6 \mu\text{m}$ and $4.5 \mu\text{m}$) for NGC 1068 in DustPedia. They unfortunately have strong blooming artefacts and do show signs of an over-exposed centre. We thus prefer the WISE images, which are of comparatively much better quality in this case, and cover a wider wavelength range ($3.4 \mu\text{m} - 22 \mu\text{m}$). The *Spitzer*-MIPS bands don't have artefacts, but are still heavily PSF dominated (especially at $24 \mu\text{m}$). Moreover, the PACS bands surpass them in spatial resolution. For these reasons we do not include any *Spitzer* observations in our sample.

The 2MASS observations (also in the DustPedia database) turned out to be too shallow to capture the entire disc of NGC 1068. We instead use the UKIDSS (Lawrence et al. 2007) *H* and *K* band observations which are deeper and have better spatial resolution. Most importantly, the *H* band is the reddest band without a significant PSF signature and will be vital to determine the spatial distribution of the old stellar populations. For a similar reason, we will also use the narrow-band $\text{H}\alpha$ map of NGC 1068 (Knapen et al. 2004). The map will be an important constraint on the spatial distribution of the ongoing star formation in the absence of usable $22 \mu\text{m}$ or $24 \mu\text{m}$ images. We discuss this in more detail in the next section.

7.3 Model preparation

Our modelling strategy closely follows the prescriptions outlined in Verstocken et al. (2019), which, in turn were based on the work by De Looze et al. (2014). Here, we limit

¹<http://dustpedia.astro.noa.gr>

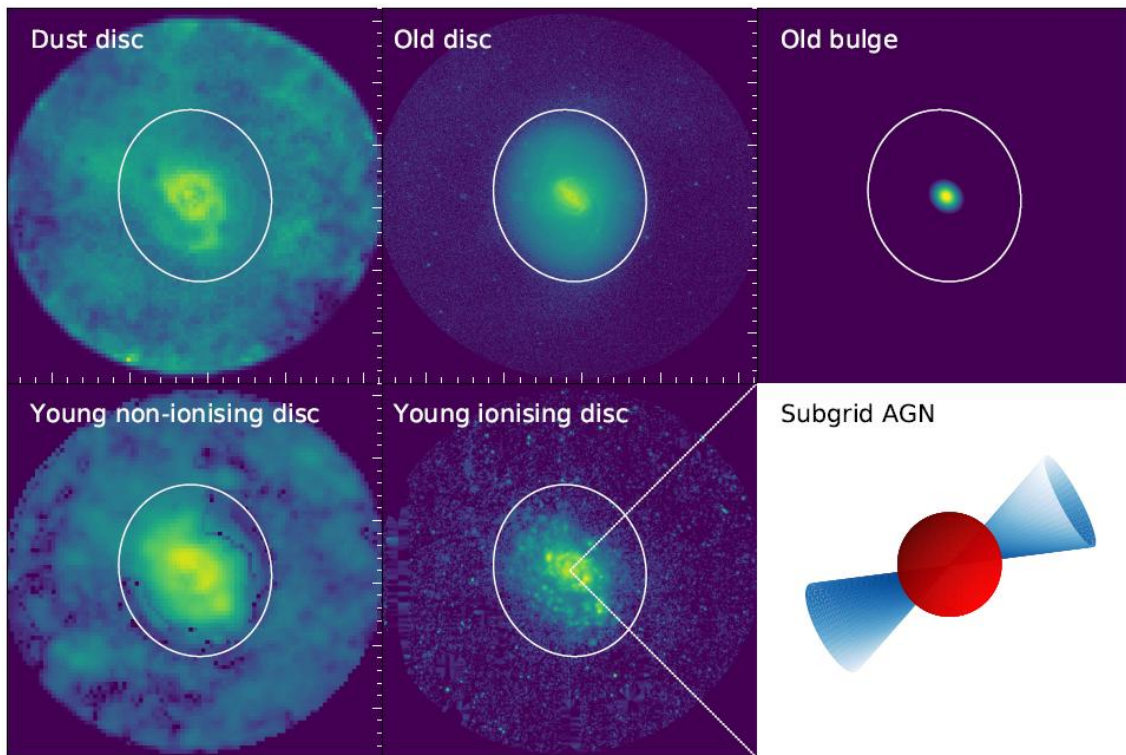


Figure 7.1: 2D representations used as input morphologies for the 3D geometries for the model of NGC 1068. The old bulge and AGN model are based on analytical prescriptions while the other morphologies are derived from observed imagery. The model is only evaluated within the white ellipse to ensure a sufficient signal-to-noise ratio.

ourselves to a brief description at each modelling step and highlight where we deviate from [Verstocken et al. \(2019\)](#). The requirements for a panchromatic, 3D and resolved radiative transfer fit are three stellar components and one dust component. Each of these stellar components have a 3D spatial distribution associated to them, and a template shape for their SED. The dust component also requires a 3D geometry, plus the choice of a dust mix with associated optical properties. While geometries were mostly analytical density profiles in the past, it is now possible to derive them from observations directly. This allows the use of non-axisymmetric and more clumpy distributions for stars and dust, leading to more realistic models.

The most obvious way to trace the dust morphology is through a map of the dust mass surface density. However, this requires resolved SED fitting up to the SPIRE 350 μm band and drastically limits the working resolution. However, the input dust distribution doesn't need to be normalised as the total dust mass will be a free parameter. We therefore construct a map of FUV attenuation, which also traces the dust distribution but importantly attains higher spatial resolution. The A_{FUV} map is shown in Fig. 7.1 labelled as the dust disc. To convert this to a 3D density distribution, we simply deproject the 2D image, and stretch the emission in each deprojected pixel out into the vertical (z -axis) direction according to an exponential profile. We set the scalelength of this exponential profile to 76 pc, which is half that of the old stellar scale height as suggested by [\(De Geyter et al. 2014\)](#). For the spectral properties of dust absorption, scattering and

emission we adopt the THEMIS dust model for diffuse MW dust (Ysard et al. 2015; Jones et al. 2017), in line with our other DustPedia studies.

We split the stellar components into three age groups. The old stellar population contains stars that are much older than 100 Myr, and therefore no longer contribute to the classic SFR tracers (Kennicutt & Evans 2012). Typically, one can trace this component best with either WISE 3.4 μm or IRAC 3.6 μm observations. However, in the case of NGC 1068, these images are dominated by the PSF shape and don't provide clear morphological information. We therefore rely on the UKIDSS H band to trace the old stellar component. The additional advantage of using this shorter waveband is that the AGN contamination in the centre is minimal. We perform a bulge/disc decomposition on the H band image to further split the geometry into a Sérsic bulge and a disc. The bulge model (the only analytical density profile) is already 3-dimensional by construction. The disc is deprojected in the same way as the dust map, but now given an exponential scale height of 151 pc, which is $1/8.26$ of the scale length as suggested by (De Geyter et al. 2014). The second stellar component is a young non-ionising stellar population with average age of 100 Myr and is based on the GALEX FUV map. This map was then deprojected and given an exponential scale height equal to the dust scale height.

The third stellar component models the ongoing star formation in the form of young (10 Myr) ionising stars still in their birth clouds. As these stars heat their surrounding dust to high temperatures, they can in principle be traced by a MIR continuum tracer such as the WISE 22 μm or MIPS 24 μm band. Again, these images for NGC 1068 are dominated by the PSF pattern and only useful to extract a global flux. To trace the ongoing star formation, we instead use the narrow-band continuum subtracted $H\alpha$ emission. This image still has an unusually bright nucleus. D'Agostino et al. (2018) showed that the AGN is responsible for $\sim 24\%$ of the $H\alpha$ emission in the galaxy. To mitigate this effect, we mask out the nuclear $H\alpha$ peak and employ the `astropy` routine `interpolate_replace_nans`² to infer the $H\alpha$ emission from the surrounding disc. Note that this procedure preserves the exponential flux profile of the $H\alpha$ disc. The resulting image is converted to a 3D geometry by deprojecting it and assuming an exponential scale height of 38 pc, which is half that of the dust scale height and represents the embedded nature of the star-forming regions.

An important novelty is the addition of an AGN in our model. Radiative transfer simulations of accretion discs surrounded by a dusty torus have been done in the past (see e.g. Nenkova et al. 2008; Stalevski et al. 2012). However, given the enormous difference in scale between the torus and the galactic disc, it is not useful to solve the transfer of radiation in the same simulation. As such, we construct a subgrid model for the AGN in NGC 1068. The two AGN emission components (the accretion disc and the dusty torus) are both modelled as point-like sources located at the centre of the galaxy.

The accretion disc spectrum is modelled as a composition of power-laws with indexes varying as a function of the wavelength. We used the Schartmann et al. (2005) prescription, which combines observed and theoretical evidences and is quite commonly used as a heating source in radiative transfer models for dusty torii in AGN. Its emission peaks at UV-optical wavelengths and its normalisation (or, equivalently, its total luminosity) is

²<http://docs.astropy.org/en/stable/convolution/>

strictly related to the one of torus model. A part of the radiation of the accretion disc is blocked locally by dust within the torus. We have implemented this as an anisotropic (cone-shaped) emission profile with an opening angle of 40° around the polar direction (see Fig. 7.1, bottom right panel). The orientation of the accretion disc is such that it beams directly into the galactic disc, with the obscured part pointing to the observer, as expected for a Type-2 Seyfert galaxy like NGC 1068.

As for the torus dust emission, we resorted to the model grid from Fritz et al. (2006) in the upgraded version described in Feltre et al. (2012). We assume the torus emission to be isotropic, which is a fair approximation given that its MIR radiation is far more optically thin than the obscured accretion disc (see also Fig. 7.1, bottom right panel). From the Feltre et al. (2012) grid, we adopt the model that most closely resembles the one that Fritz et al. (2006) used to fit to NGC 1068. It has an optical depth of $\tau_{\text{eq}}(9.7 \mu\text{m}) = 6$, with a torus full opening angle of 140° , an outer-to-inner ratio of 10, and the dust density parameters $\gamma = 4$ and $\beta = -1$ (see Equation 3 of Fritz et al. 2006, for a detailed explanation of these parameters). The AGN model is normalised by the WISE $4.6 \mu\text{m}$ luminosity since this wavelength is particularly sensitive to the presence of very hot dust. It is not the goal of this investigation to further constrain the torus or accretion disc properties. We simply require a realistic subgrid implementation for the AGN. As such the total luminosity is the only free parameter of the AGN component (with a fixed ratio between accretion disc and torus luminosity).

7.4 Radiative transfer SED fitting

The different components described in the previous section define the framework for our model of NGC 1068. Radiative transfer simulations are computationally demanding, so the free parameters in this model need to be limited. We therefore rely on well-informed estimates for the spatial and spectral distribution of each component as outlined above. The normalisation of each component is left as a free parameter. The dust density distribution is normalised by the total dust mass, M_{dust} . The spatial and spectral distribution of the young non-ionising (yni) and young ionising (yi) stellar populations are normalised by their FUV luminosity: $L_{\text{FUV}}^{\text{yni}}$ and $L_{\text{FUV}}^{\text{yi}}$, respectively. The old stellar components are normalised together (assuming a fixed bulge-to-disc ratio) by their total luminosity in the H band: L_H^{old} . Finally, the subgrid AGN SED is normalised by the total emission of accretion disc and torus at $4.6 \mu\text{m}$: $L_{4.6}^{\text{AGN}}$. Here again the ratio between disc and torus luminosity is fixed to guarantee the internal energy balance. In total, the model thus has five free parameters.

We make use of SKIRT (Baes et al. 2011; Baes & Camps 2015) to perform the radiative transfer calculations in the 3D simulation space. The stellar and AGN components serve as sources of radiation. The dust component acts as a sink of UV-optical-NIR radiation, which is then reprocessed and emitted at longer wavelengths. Light is also anisotropically scattered by the dust grains. SKIRT can perform these simulations in a highly efficient way thanks to multiple optimisation techniques for the transfer of radiation towards the observer (Baes et al. 2011), effective quantisation of the dust density distribution using a binary tree dust grid (Saftly et al. 2014), and support for various types of parallel

computing (Verstocken et al. 2017). As a result, the radiation transfer is evaluated in a set of 3D dust cells of variable volume, but roughly equal in mass. This allows us to investigate the energy balance in 3D in Sect. 7.6.

For each set of these parameters, a different energy balance will occur globally but also per dust cell in the simulation. Our goal is to find the optimal combination of free parameters that reproduce the observations. Despite the efficiency of SKIRT, this is not a trivial task. We therefore run a suite of low resolution simulations and use the global broadband SED of NGC 1068 as observational constraint since it is efficient to generate the synthetic, line-of-sight model fluxes. With a dust grid of 1.3×10^6 cells we reach an effective resolution of 44 pc in each dimension. Each simulation has 134 wavelengths, and 10^6 photon packages per wavelength. Doing so, each set of parameters can be evaluated in under one hour (on average) on a 16 CPU node.

With each point in the 5D parameter space taking 16 CPU hours, it becomes impractical to run a classic nonlinear fitting algorithm. We therefore adopt the same two-step fitting approach as for the other DustPedia-modelled galaxies (Verstocken et al. 2019; Nersesian et al. 2019a, see Chap. 6). In a first run, we explore a wide parameter space, sparsely sampled around a well motivated initial guess. For each parameter set, the observed and model broadband SED is compared by summing the χ^2 metric, where each wavelength regime (UV, optical, NIR, MIR, FIR and submm) is given equal weight to the total squared sum (see Verstocken et al. 2019, for a detailed description).

The parameter values for each fit can then be weighted by $\exp(-\chi^2/2)$ to sample the probability density distribution. As an initial guess, we use the global properties derived by Nersesian et al. (2019b) which are based on SED modelling with CIGALE (Boquien et al. 2019). They find

$$\begin{cases} M_{\text{dust}}^{\text{CIGALE}} = (1.71 \pm 0.23) \times 10^7 M_{\odot} \\ \text{SFR}^{\text{CIGALE}} = 13.4 \pm 3.6 M_{\odot} \text{ yr}^{-1} \\ A_{\text{FUV}}^{\text{CIGALE}} = 3.64 \pm 0 : 31 \end{cases} \quad (7.1)$$

This dust mass can directly be used as an initial guess. From the SFR, we compute an initial guess for the UV luminosity of the ionising stellar populations. The A_{FUV} can be used to deredden the observed FUV luminosity, which we assume here for simplicity as the sum of the ionising and non-ionising stellar components. Furthermore, we use the observed H band luminosity as an initial guess for the total (bulge and disc) old stellar populations as this band is relatively free from other contributions. For the AGN torus, our initial guess normalisation was set at $2.50 \times 10^{35} \text{ W } \mu\text{m}^{-1}$ and tied to that is an accretion disc luminosity $0.48 \times 10^{35} \text{ W } \mu\text{m}^{-1}$. As such, we construct the initial parameter set for the model as listed in Table 7.1.

For galaxies without a strong AGN, radiative transfer fits with three parameters (M_{dust} , $L_{\text{FUV}}^{\text{ni}}$, and $L_{\text{FUV}}^{\text{i}}$) are sufficient. The challenge of adding an AGN is that the MIR SED becomes even more convoluted and difficult to decode into separate contributions. For this reason we not only have $L_{4.6}^{\text{AGN}}$ as a free parameter, but also L_H^{old} . An adequate

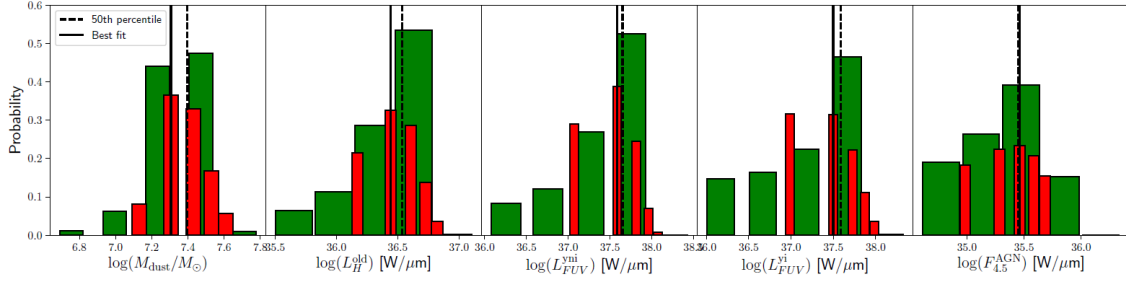


Figure 7.2: Probability density distributions for the free parameters in our model configuration. The green distribution corresponds to the first batch of models. The parameter grid was refined based on this batch. After the second fit iteration, the red distributions are found. The median values of the second batch are indicated with vertical dashed lines. The solid vertical lines indicate the values for the model with the lowest overall χ^2 .

coverage of this parameter space thus requires many more sample points. We build a sparse but wide 5D Cartesian parameter grid around our initial guesses. The grid spans more than one order of magnitude in M_{dust} , $L_{4.6}^{\text{AGN}}$, and L_H^{old} , and more than two orders of magnitude in $L_{\text{FUV}}^{\text{ni}}$, and $L_{\text{FUV}}^{\text{yi}}$. Each dimension is uniformly sampled (in log space) with 5 points during this first run, which already amounts to 3,215 simulations.

The resulting probability distributions of the first batch is shown in Fig. 7.2 by the green histograms. These have a clear peak for all free parameters which importantly doesn't occur at the edge of the sampled space. This means that we are already able to put coarse constraints on all parameters. The most probable values (50th percentile of the PDFs) are summarised in Table 7.1.

Based on the distributions of the first batch, we can narrow the parameter space significantly and adopt a finer sampling. We ensure that over 90% of the probability is captured in the parameter space for the second batch. We again use 5 sample points per parameter, but now uniformly distributed in linear space. The probability distributions for this second batch of 3,125 simulations are also shown in Fig. 7.2 (red histograms). The distribution again show a clear peak, with the exception of $L_{\text{FUV}}^{\text{yi}}$. It seems we are reaching the limit of precision by which we can constrain this parameter. The PDF for $L_{4.6}^{\text{AGN}}$ is also rather broad for the second batch. The parameter values for the best-fitting model (lowest χ^2) lie close to the most probable parameters (50th percentile values) and are listed together in Table 7.1. These value also correspond well with our initial guess. We conclude that at this point the free parameters of our model are reasonably constrained. Adding another iteration would again require significant computational resources and not significantly reduce the uncertainties. In the next section, we analyse the best-fitting model in further detail.

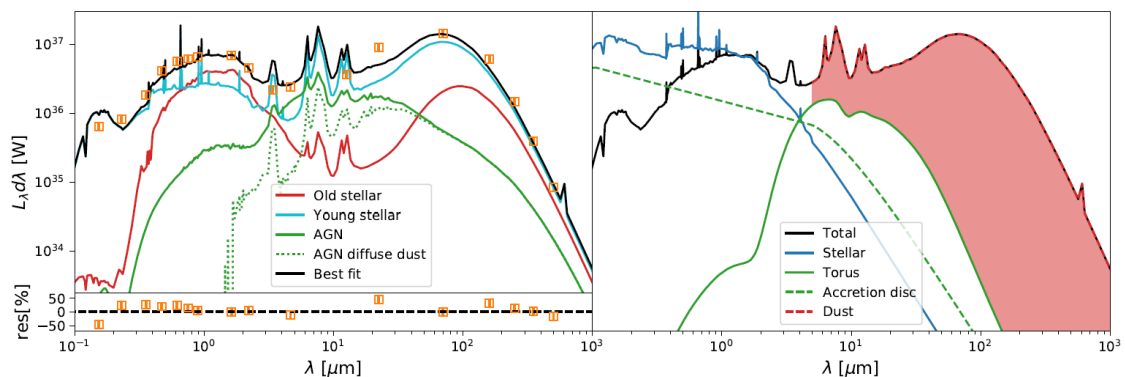


Figure 7.3: SEDs from the best-fit model for NGC 1068. Left: the global SED (black line) fits the observed (orange) broad band fluxes. The corresponding residuals are shown in the bottom panel. Additional lines represent models with only one stellar component, but with the same dust distribution. In particular, the green line shows the total emission for a model with only the AGN and the dust component. The green dotted line then corresponds to only the light reprocessed by the diffuse dust in this simulation. Right: breakdown of the global SED (black line) in the total intrinsic (unattenuated) stellar SED (blue), and the AGN emission mode along the line-of-sight (solid green line). The accretion disc is not visible along the line-of-sight ($i = 28^\circ.1$), but the edge-on ($i = 90^\circ$) view is shown by the dashed green line. The shaded red area represents the energy emitted by the dust after absorbing radiation from the stellar and AGN component.

7.5 A 3D high-resolution model for NGC 1068

The best-fit model obtained in the previous section forms the basis for our dust heating analysis. We first produce a higher quality version of the best-fit model by shooting five times as many photons per wavelength (5×10^6), and almost twice the number of wavelength points (252). To separate the contributions of each source of radiation, each simulation is run again with the same dust distribution, but only one source: the old (bulge and disc), young (non-ionising and ionising discs) and AGN (accretion disc and torus) component. This process takes another 1,280 CPU hours. The resulting SED is shown in Fig. 7.3 (left panel, black line).

Globally, our model follows the observed SED fairly well. The main stellar and dust peak match the datapoints closely. There are, however, several points of discrepancy. First, the FUV point is overestimated by the model, while the NUV point is underestimated. This issue has been noted before in galaxies with a significant contribution of the MAPPINGS III templates (De Looze et al. 2014; Verstocken et al. 2019; Nersesian et al. 2019a). This signature in the template for ionising stellar populations is amplified by a broad bump in the THEMIS attenuation curve. Nersesian et al. (2019a) compared the attenuation curve (normalised to A_V) of our model to their galaxies and to the THEMIS MW extinction curve. They found that NGC 1068 exhibits the flattest attenuation curves of the sample and lies closest to the MW reference.

Also driven by the dust model are the strong aromatic peaks in the MIR SED in Fig. 7.3.

Table 7.1: Overview of the free parameters of our model setup together with their initial guess values. After each fitting batch, the 50th percentile corresponds to the most probable value for that fit. The uncertainties on the percentiles are derived as half of the sampling of the coarse parameter grid. The last column lists the parameter values for the model with the lowest overall χ^2 .

Parameter	Initial guess	Batch 1 (50th pct)	Batch 2 (50th pct)	Best fit
$\log(M_{\text{dust}}/M_{\odot})$	7.23	$7.43^{+0.15}_{-0.19}$	$7.40^{+0.11}_{-0.12}$	7.31
$\log(L_H^{\text{old}}/W\mu\text{m}^{-1})$	36.65	$36.64^{+0.17}_{-0.25}$	$36.54^{+0.15}_{-0.19}$	36.44
$\log(L_{\text{FUV}}^{\text{yni}}/W\mu\text{m}^{-1})$	37.56	$37.85^{+0.25}_{-0.32}$	$37.65^{+0.21}_{-0.28}$	37.58
$\log(L_{\text{FUV}}^{\text{yi}}/W\mu\text{m}^{-1})$	37.46	$37.76^{+0.22}_{-0.33}$	$37.59^{+0.23}_{-0.31}$	37.50
$\log(L_{4.6}^{\text{AGN}}/W\mu\text{m}^{-1})$	35.47	$35.63^{+0.30}_{-0.32}$	$35.45^{+0.16}_{-0.24}$	35.46

The adopted emission model was calibrated on diffuse dust in the MW. The strength of the MIR emission features is often reduced in AGN compared to star-forming galaxies (see e.g. [Sales et al. 2010](#)) although this may be attributed to dilution by the bright MIR continuum ([Alonso-Herrero et al. 2014](#)). MIR spectra of NGC 1068 do reveal line emission even close to the nucleus ([Mason et al. 2006](#); [Howell et al. 2007](#)) due to ongoing star formation there. We did not wish to skew our model by fitting to wavebands that contain such a peak and therefore don't include the WISE $3.4 \mu\text{m}$ and $12 \mu\text{m}$ flux in the χ^2 weighting. The MIR continuum of the model does follow the slope of the observed data points.

A third discrepant point is the WISE $22 \mu\text{m}$ flux, which is underestimated by the model. We looked into models with a stronger AGN contribution, but these lift at the same time also the MIR continuum. Changing the ratio between the stellar components also did not improve the situation without introducing discrepancies at other wavelengths. The observed WISE $22 \mu\text{m}$ flux in our aperture does come out higher than the MIPS $24 \mu\text{m}$ flux (not shown). Part of this discrepancy can thus be attributed to the observational uncertainty, but still our model seems unable to capture the exact SED shape in the MIR. This may partly be due to the subgrid implementation of the torus. A non-isotropic torus model or a more clumpy one could boost the emission at $22 \mu\text{m}$ in the AGN SED (see [Feltre et al. 2012](#)). However, as indicated earlier, it is not the goal of this study to further constrain the torus properties themselves, but instead we focus on how radiation escaping the AGN affects the host galaxy.

In the left panel of [Fig. 7.3](#) are the SEDs for separate simulations for the old SSPs, the young (non-ionising and ionising) SSPs, and the AGN. The diffuse dust is now heated solely by the components that are present in the simulation. The dominance of the young stellar population (blue line) is immediately clear. It lies well above the other components in the UV, MIR and FIR regime. This is already an indication that the FIR flux is powered by ongoing star formation. The second most luminous SED comes from the old bulge and disc component, although it only really dominates in the NIR. Still it seems to contribute some energy to the submm emission. Finally, there is the AGN

(accretion disc and torus) emission, which is only significant in the MIR, but does not dominate the global SED in any regime. An important observation here, however, is the broad tail of the AGN SED in the submm. This is not direct emission from the AGN, but light reprocessed by the diffuse dust in the galaxy (see green dotted line in Fig. 7.3). This already indicates that there is AGN feedback on the surrounding ISM. However, the effect is rather small as the dust emission lies typically one order of magnitude below the emission generated by the old or young components.

In the right panel of Fig. 7.3 we decompose SED into its main constituents: stars, AGN and dust. It is again evident that the AGN does not dominate the galaxy at any wavelength at this global scale. We compute a bolometric luminosity $L_{\text{AGN}}^{\text{bol}} = 0.6 \times 10^{10} L_{\odot}$, compared to $L_{\text{dust}}^{\text{bol}} = 7.4 \times 10^{10} L_{\odot}$. For the total observed SED, the bolometric luminosity is $L_{\text{tot}}^{\text{bol}} = 11.4 \times 10^{10} L_{\odot}$. Following Bianchi et al. (2018) we can compute $f_{\text{abs}} = L_{\text{dust}}^{\text{bol}}/L_{\text{tot}}^{\text{bol}} = 0.65$ the fraction of stellar light that is reprocessed into dust emission. Our estimate corresponds well with the 0.68 they find from a CIGALE model of the global SED.

To further assess the quality of our model, we generate synthetic images. We convolve the 3D datacube produced by SKIRT using the spectral response curves of five representative broadband filters across the SED. We did not convolve the images with a corresponding PSF as it is difficult to determine the kernel. The SKIRT images blend the different PSFs of their input geometries and the resolution of the dust grid. As such we simply compare the spectrally convolved model images with their observed counterparts in Fig. 7.4 and indicate the PSF as a yellow circle. We also produce residual maps corresponding to (observation – model)/observation, and plot the KDE for the pixel distributions in these residual maps.

The model images reproduce the observed counterparts within a factor of two. Visually the correspondence is quite good in the UV, optical and NIR maps. However, the residuals reveal significant asymmetries corresponding to the spiral arms. This is because we don't resolve the dust extinction at sufficient resolution. The effect is worst in the SDSS g band image, where the spatial resolution is the highest. In this band the flux is also systematically underestimated by the model as highlighted by the KDE plot. In the NIR, there are two strong positive residual features on opposite sides of the galaxy. They correspond to star-forming regions which are over-luminous in the model (represented by the ionising component). Globally, though, the NIR regime shows the best correspondence with the observations.

The model FIR images do not show the bright central area, but instead peak sharply in the nucleus. This can mainly be attributed to the difference in PSF, but the model also underestimates the flux in the centre (while matching the total flux in the FIR regime). We speculate that this may be due to an insufficient central dust density in the input map. The current dust geometry map is based on pixel-by-pixel determinations of A_{FUV} . This relies on the calibrations of Cortese et al. (2008), which derive the stellar age bin from the FUV– r colour. It is possible that the AGN emission in NGC 1068 can locally skew these age estimates, resulting in a less reliable A_{FUV} estimate in the centre of the galaxy. We have tried to fit a model where the dust geometry followed more closely the PACS $70\mu\text{m}$ map. This dust map is more centrally peaked than the current one based

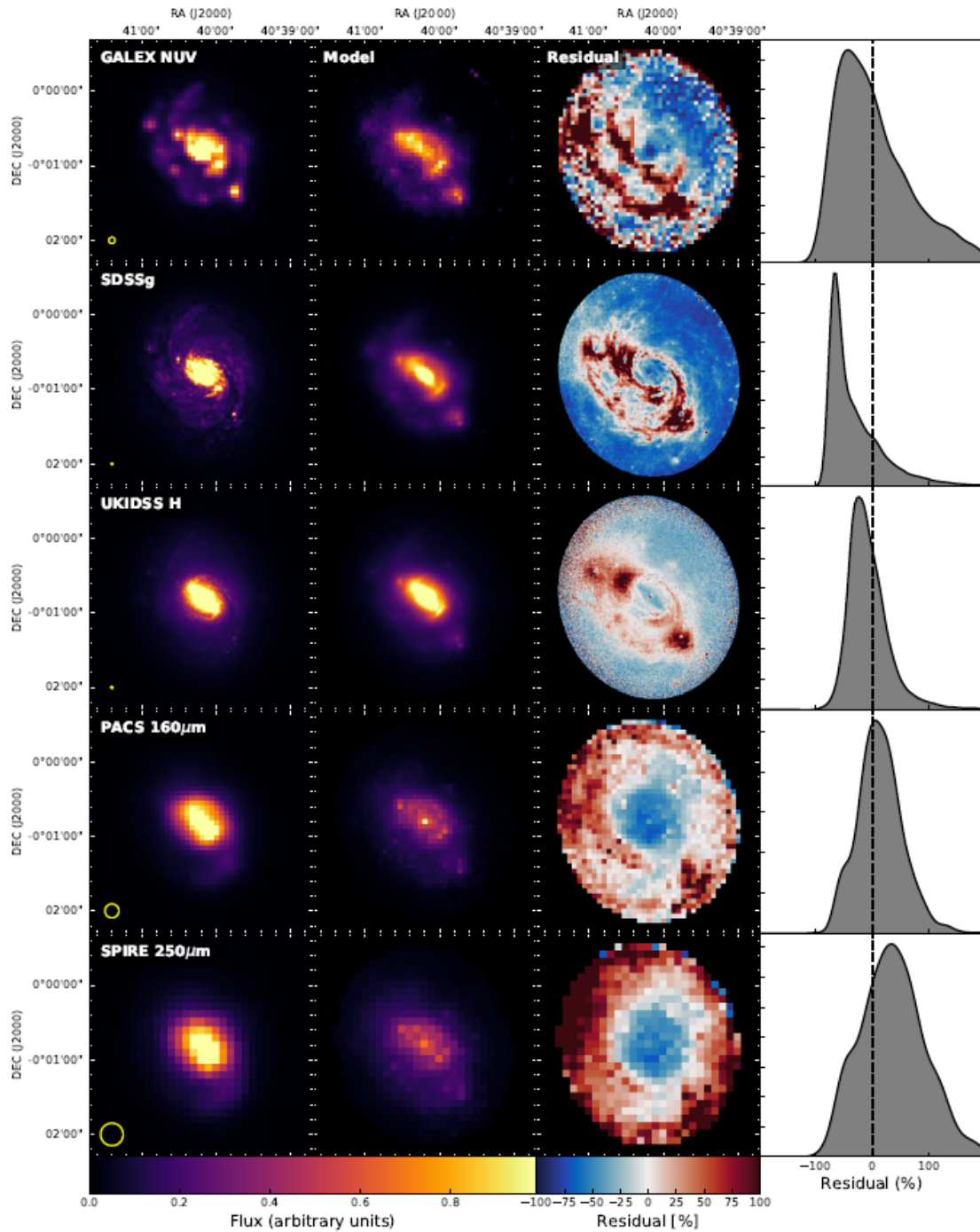


Figure 7.4: Spatial comparison of our best-fit model to observed broad-band images (left column). The second column contains the model images. Note that the model images are not convolved by any PSF and only hold the intrinsic model PSF (a composite of the input images). Residual images are shown in the third column. Corresponding residual distributions are represented by KDE plots in the right column.

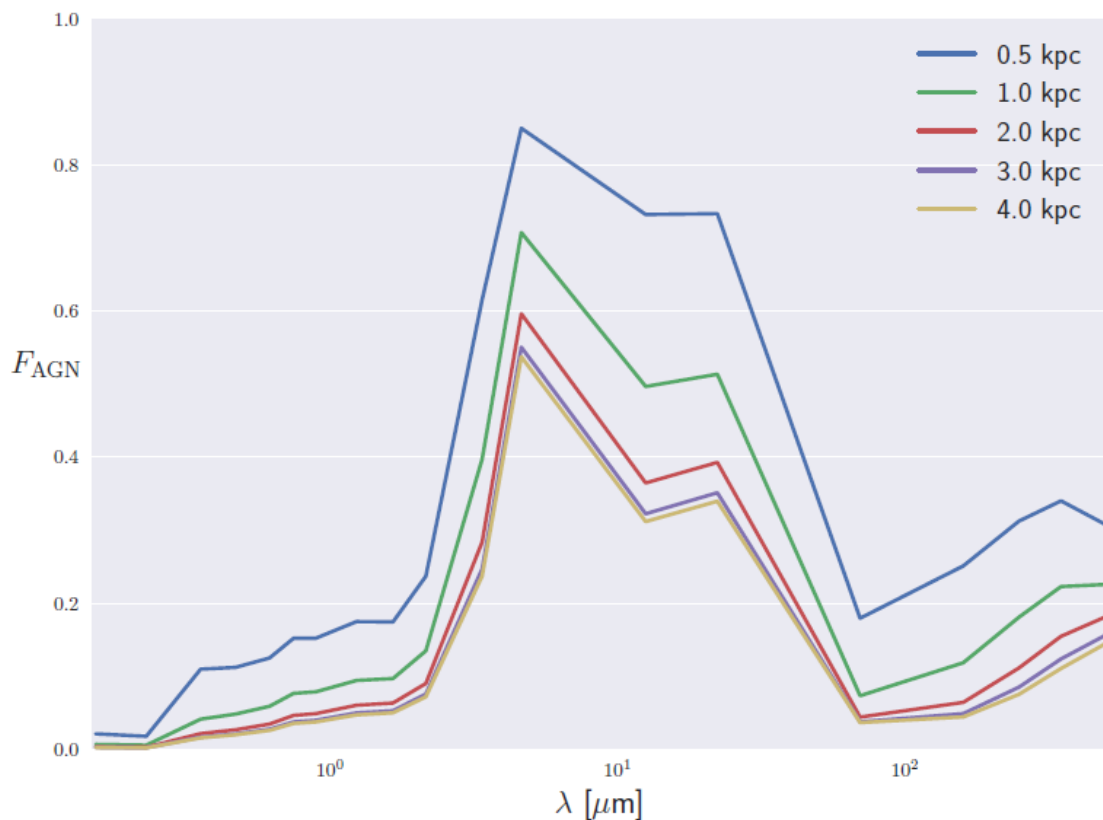


Figure 7.5: Fraction of emission originating from the AGN component to the total emission per band, F_{λ}^{AGN} . Different lines correspond to different concentric elliptical apertures.

on A_{FUV} . However, this alternative map caused severe attenuation in the UV and optical bands, and too much dust emission in the FIR.

The global SED shape was also less fitting to the observed global fluxes. We therefore don't present this alternative model here. While it seems using the dust map based on A_{FUV} has its downsides, it appears to be the best working solution. Knowing the qualities and caveats to the best-fitting model, we analyse the dust heating sources and energy balance in NGC 1068 in the next section. The global SED of our model further allows to estimate the AGN light contamination in NGC 1068. We therefore compute the emission ratio between the total and the AGN-only simulation (still including the same dust component) in each band, F_{λ}^{AGN} . It is useful to quantify this contribution since several broad band colours or luminosities are used to directly derive physical properties of galaxies. An adequate correction for star-forming galaxies containing an AGN is necessary before applying such recipes. Fig. 7.5 shows F_{λ}^{AGN} for all bands in our dataset, and for several concentric elliptical apertures. As expected, there is a general increase in AGN light ratio towards the innermost regions of the galaxy. F_{λ}^{AGN} averages to only 0.05 inside a 4 kpc major axis radius and across all wavebands. In the innermost aperture (0.5 kpc) this average increases to 0.18.

Along the wavelength axis, all apertures exhibit the same behaviour. There is virtually no

AGN contamination in the UV bands and only minor contamination in the optical bands ($F_{\lambda}^{\text{AGN}} = 0.02 - 0.15$). There is a strong increase in the NIR and the peak F_{λ}^{AGN} is reached in the WISE 4.6 μm band and varies from 0.54 within 4 kpc to 0.85 within the inner 0.5 kpc. The peak actually extends well into the MIR, but drops off quickly towards the PACS 70 μm band. In the FIR, an interesting positive slope points to an increasing contribution with increasing wavelength. The intrinsic AGN (disc and torus) emission model does not have this behaviour, as is evident from the right panel in Fig. 7.3. This is actually an indirect effect as AGN light is reprocessed by the diffuse dust. It is important to realise that even SPIRE bands can thus be contaminated by the AGN.

7.6 Dust heating sources

The main advantage of 3D radiative transfer simulations is the inherent information on the energy balance in every dust cell. Our model, based on NGC 1068, contains the absorbed energy in each cell and thus summarises how the dust in that cell is heated before re-emitting this energy at longer wavelengths. In line with our previous work (Verstocken et al. 2019; Nersesian et al. 2019a, see Chap. 6), we make use of the total (wavelength-integrated) absorbed energy per stellar component and per volume element (dust cell). We focus on two quantities: f_{young} , the combined heating fraction of the young (non-ionising and ionising) component, and f_{AGN} , the AGN heating fraction. They reflect dust heating through ongoing star formation and through AGN emission, respectively, and are defined as

$$f_{\text{young}} = \frac{L_{\text{yni}}^{\text{abs}} + L_{\text{yi}}^{\text{abs}}}{L_{\text{tot}}^{\text{abs}}}, \quad (7.2)$$

$$f_{\text{AGN}} = \frac{L_{\text{AGN}}^{\text{abs}}}{L_{\text{tot}}^{\text{abs}}}.$$

These quantities are computed per dust cell, where the L_k^{abs} refer to the absorbed luminosity for component k . Given the set-up of our model, the old stellar component (bulge and disc) makes up the remainder of the absorbed energy per dust cell: $L_{\text{tot}}^{\text{abs}} = L_{\text{yni}}^{\text{abs}} + L_{\text{yi}}^{\text{abs}} + L_{\text{AGN}}^{\text{abs}} + L_{\text{old}}^{\text{abs}}$. Figure 7.6 summarises the dust heating fraction of both the young and the AGN components. The left panels show a cut through the mid-plane of dust cells in a face-on view of the galaxy model. The colour coding is set by the histograms on the right and reflect the dust heating fractions by the young and AGN component, respectively. The histograms contain all dust cells (including the ones above and below the mid-plane). Globally, a median $f_{\text{young}} = 0.83$ was found, which underlines the dominance of star formation as a heating source in this galaxy model. In contrast, the AGN effect is minor with a median $f_{\text{AGN}} = 0.004$.

More detail is visible on a local level in Fig. 7.6. The young component peaks in a ring around the centre, and in two zones above and below it. These structures can also be distinguished in optical images of NGC 1068 and are associated with intense star formation (see the ionising disc map in Fig. 7.1 or the NUV map in Fig. 7.4). The base

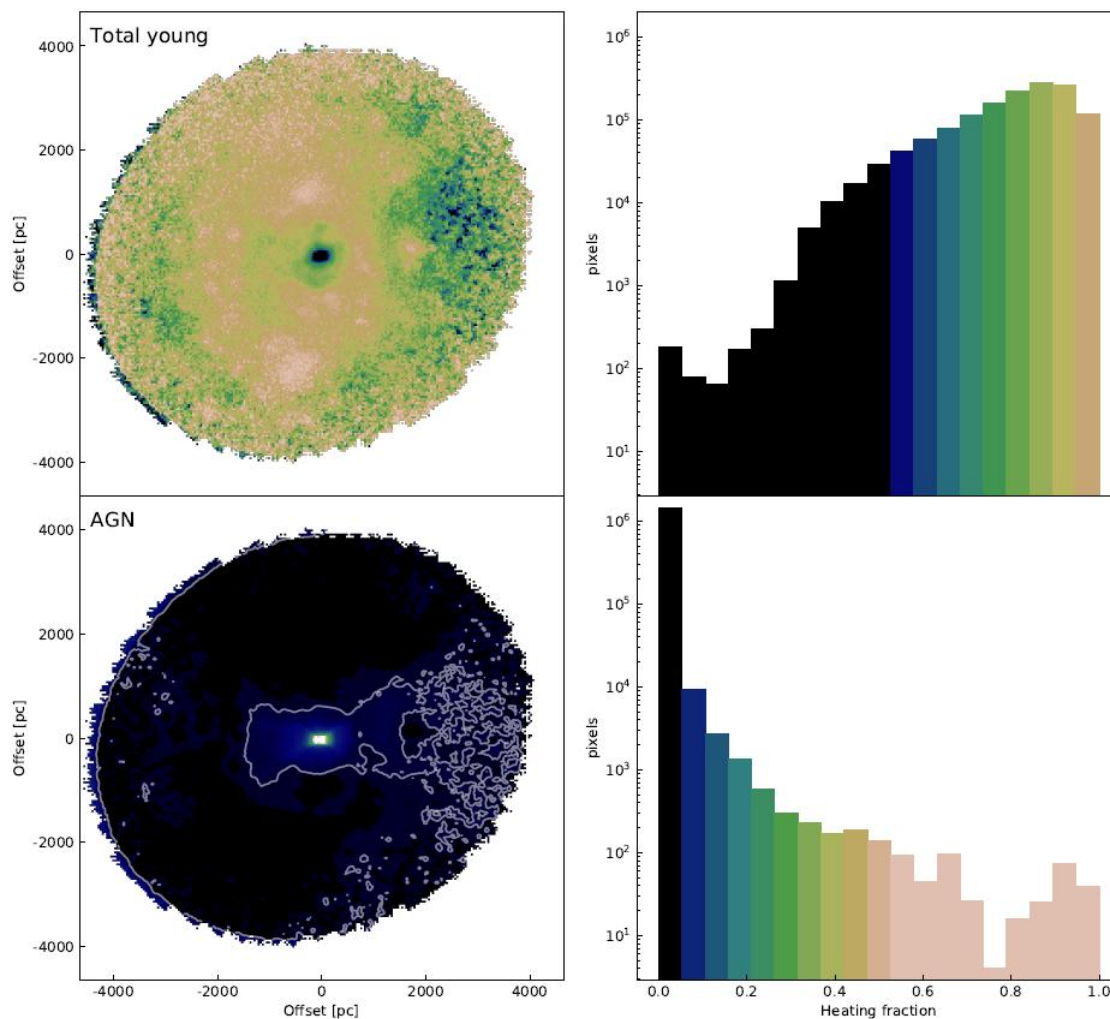


Figure 7.6: Dust heating fractions in a slice through the mid-plane of the face-on view of our model (left panels). The colour code is set on the histograms on the right. The histograms contain all dust cells (including the ones above and below the mid-plane). Top row corresponds to f_{young} and bottom row to f_{AGN} . The white contour corresponds to the 0.4% level in f_{AGN} and highlights an asymmetry in the heating of dust in the disc.

level of f_{young} remains high across the disc, but drops below 0.5 in some patches at larger radii. This is where the ongoing star formation fades and the radiation field created by the old stellar population takes over in heating the dust.

Quite remarkable is the central dip in f_{young} , which spatially correlates with the peak in f_{AGN} in the bottom left panel of Fig. 7.6. The central ~ 0.5 kpc is the main zone of influence of the AGN. Here, the dust heating even dominates that of the surrounding star-forming disc. The f_{AGN} map also shows a clear directional preference for the AGN heating (roughly along the horizontal axis Fig. 7.6). The main direction is guided by our implementation of the AGN accretion disc, beaming straight into the disc with a conical opening angle of 40° (see Sect. 7.3). The map also shows a slight left-right asymmetry (highlighted by the white contour), where the AGN radiation is able to reach out further towards the right side of the map. This is again because the star-forming disc fades off

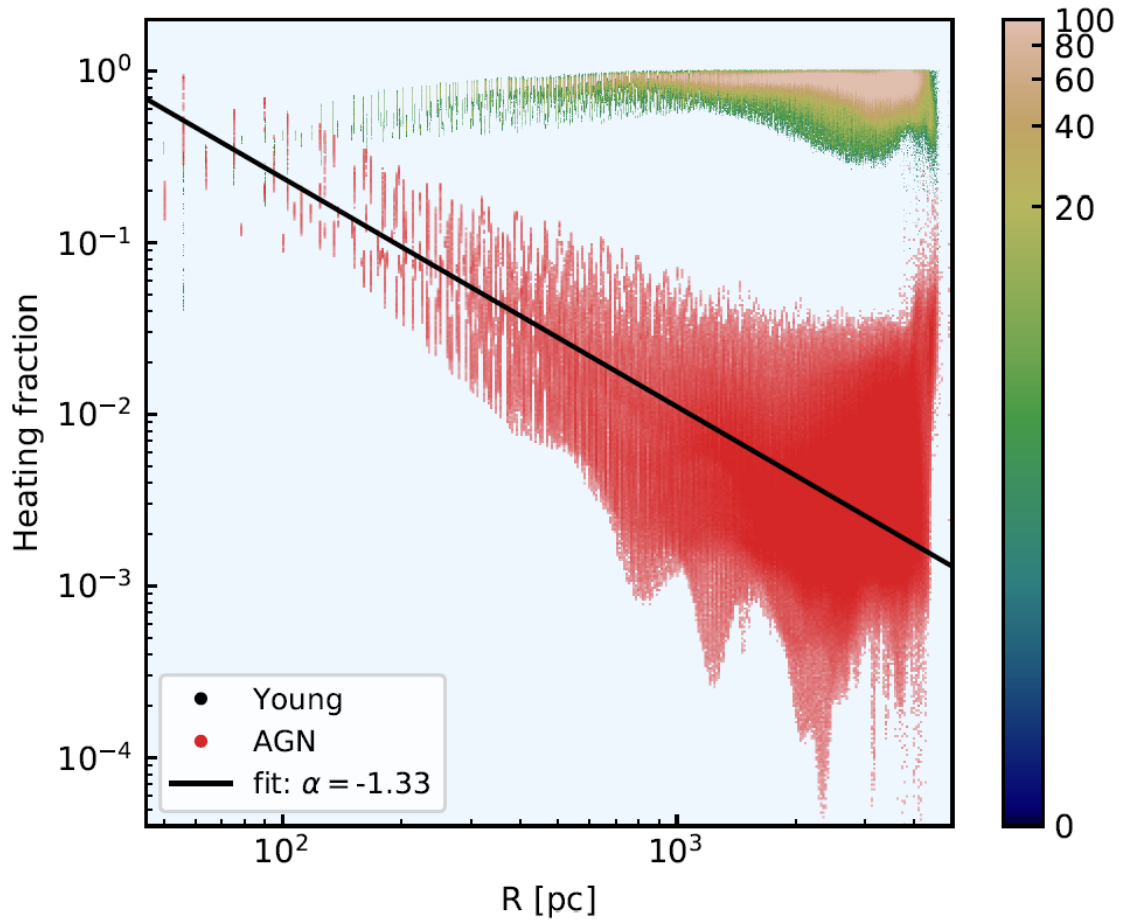


Figure 7.7: Scatter density plots showing the radial profiles of the dust heating fraction. The colour bar corresponds to the density in points of f_{young} . The red points correspond to f_{AGN} . The power-law fit of Equation 7.3 is shown as a black line.

more quickly in that direction. At the very left side of the map, an arc of blue pixels is visible. Here, no stellar sources are present due to the deprojection during model setup. The analytical emission model for the AGN does reach out to these radii, causing an edge-effect. We note that this is a minor effect ($< 5\%$).

To further quantify the AGN-powered dust heating, we plot the radial profiles of f_{AGN} and f_{young} in Fig. 7.7. Despite the azimuthal averaging, we see the same trend of Fig. 7.6 reoccurring. The ongoing star formation dominates the dust heating in most of the dust cells in the disc with fractions between 60 and 95% and with appreciable scatter at every radius. The radial distribution for f_{AGN} exhibits a steep decline from the centre towards the outskirts. The slight increase in f_{AGN} beyond 4 kpc relates to the edge-effect also be noted on the left side of the f_{AGN} map. We can approximate the radial decline of the AGN heating fraction quite well with a power law:

$$f_{\text{AGN}} = 0.0113 \left(\frac{R}{\text{kpc}} \right)^{-1.33}. \quad (7.3)$$

In the above fit we excluded data points inside the inner 50 pc to avoid limited sampling and our spatial resolution limit. We also excluded the points beyond 3 kpc to avoid the influence of the edge-effect. The power law thus only holds within these radial limits. Our analysis suggests that AGN-powered dust heating is appreciable ($> 5\%$) inside the inner few 100 pc, and remains at the percentage-level throughout the galaxy.

7.7 Discussion and summary

We have created a radiative transfer model based on observed imagery of NGC 1068. This galaxy contains an extended old disc and a smaller star-forming disc with spiral arms and an inner bar. NGC 1068 also bears an AGN and its accretion disc appears to be edge-on while the galaxy is roughly face-on. As such, the accretion disc beams directly into the star-forming disc. This particular configuration makes the galaxy an ideal target to investigate a scenario where the AGN heats diffuse dust beyond its torus. While there is circumstantial evidence for such AGN-powered dust heating in the local universe (Wu et al. 2007; Bendo et al. 2012; Kirkpatrick et al. 2012; Verstappen et al. 2013; Kirkpatrick et al. 2015; Roebuck et al. 2016), this is, to our knowledge, the first time a full 3D radiative transfer fit was performed to a star-forming galaxy with an AGN.

The complex geometry of structure of NGC 1068 makes it difficult to disentangle the main components of our model. We used linear combinations of observed broad and narrow band images to obtain the purest possible 2D maps of old, non-ionising and ionising stellar populations. The main challenge was to construct a dust mass map at a workable resolution. We deviated from the standard recipes provided by Verstocken et al. (2019) as we could not use bands that are dominated by the instrumental PSF signature (notably the MIR). Our model can reproduce the global SED of NGC 1068 and many of the resolved features (see Fig. 7.3 and Fig. 7.4). However, it is less successful in retrieving the FIR wavebands due to a slight shortage of dust mass towards the centre. Adding more dust in these areas would increase the heating fraction of the AGN and would produce a less favourable fit to the global SED. With these caveats in mind, our model should be seen as a representation of a star-forming galaxy, based on NGC 1068. The subsequent dust heating results are therefore still realistic.

Our best-fit radiative transfer model has a dust mass and SFR which are in line with a classic CIGALE SED fit (Table 7.1 and Nersesian et al. 2019b). The AGN in our model has a bolometric luminosity of $L_{\text{bol}}^{\text{AGN}} = 2.35 \times 10^{43} \text{ erg s}^{-1}$, which is somewhat lower than previous AGN models for NGC 1068 (e.g. Lopez-Rodriguez et al. 2018). This could in part be due to our assumption of an isotropic point source for the subgrid implementation of the AGN torus. The AGN in NGC 1068 is in any case quite weak for Seyfert 2 galaxies (see e.g. Lusso et al. 2012). It is thus possible that the reported AGN dust heating fractions are on the low end of the potential spectrum. Still, even for this relatively weak AGN, we find percentage-level dust heating out to 4 kpc from the centre. In the inner 500 pc, however, the heating fraction rises quickly above 10% and peaks at 80% in the inner resolution element of our simulation (40 pc). This is also reflected in the contribution of AGN light to each broadband flux in NGC 1068 (Fig. 7.5). Even in the SPIRE bands there is contamination in the emission due to reprocessed AGN energy.

Globally, we find that most of the dust in the NGC 1068 model is heated by ongoing star formation. The median of this fraction is 83% when all dust cells are considered. This corresponds to a reduction of the L_{dust} -derived SFR from $11.8 M_{\odot} \text{ yr}^{-1}$ in the full model to $8.4 M_{\odot} \text{ yr}^{-1}$ in the model where only young (non-ionising and ionising) stellar populations heat the dust. These estimates were obtained using the [Kennicutt & Evans \(2012\)](#) conversion from L_{dust} to SFR. Relatively speaking, this is a fairly small correction as NGC 1068 is the galaxy with the highest f_{young} in our project sample (containing M 81 and four barred spirals M 83, M 95, M 100, and NGC 1365). This is clearly shown already in Fig. 6.11 of Chap. 6, where we plotted f_{young} as a function of sSFR. The dust cells of our model lie in line with the general increasing trend that other star-forming galaxies exhibit. Here, SFR and stellar mass were computed per dust cell, already taking into account the fact that not all dust emission arises from the young stellar populations.

Most of the additional energy to heat the dust actually comes from the old stellar populations $\sim 17\%$ in our model, with only a negligible part from the AGN (on global scales). However, Fig. 7.6 clearly shows that there are significant local differences. In the extreme case, considering the dust cells in the inner 100 pc, the median heating fractions average out at 29% and 38% for the young and for the AGN heating sources, respectively. The remaining energy can be attributed to the small bulge of old stars. FIR-based SFR indicators or dust mass estimates which include this part of the galaxy are thus susceptible to significant bias both due to the AGN and to the radiation field generated by the old stellar populations.

This study is the third in a series after [Verstocken et al. \(2019\)](#) and [Nersesian et al. \(2019a, Chap. 6\)](#) where we investigated the effect of dust heating in face-on large galaxies in the DustPedia database. The novelty of this study is that we added an AGN in the model as a source of radiation. We have pushed our models to the limit by requiring high-resolution images from FUV to submm wavelengths, and by fitting 3D radiative transfer simulations to these data. We are thus for the first time able to actually quantify the dust heating fraction for separate heating sources in a sample of galaxies. Our main conclusion is that star formation alone is inadequate to explain the observed FIR emission. In all cases, a significant contribution of the old stellar population is needed.

In the particular case of NGC 1068, a low-luminosity AGN is also required to match the observations. In systems hosting a stronger AGN or in quasars, the AGN-powered heating of the diffuse dust will be even higher. Hence, simply removing a (fitted) AGN torus component from the FIR flux will still lead to an overestimation of the SFR of the host galaxy. These findings, in particular the necessity for multiple heating sources, should be considered when building the next generation of galaxy SED modelling tools.

Part V

Summary and conclusions

Summary and conclusions

The goal of this thesis was to refine our knowledge about the dust properties in the local Universe and to investigate the interaction between dust and the stellar radiation field. Towards this goal, we combined theory and simulation, paired with well-calibrated multiwavelength imaging and flux data, which are available in the DustPedia archive. We used physically motivated models and state-of-the-art astrophysical tools to derive the intrinsic properties of stars and dust for the DustPedia galaxy sample. This investigation opened the path to a detailed understanding of several effects caused by the complex interplay of starlight and dust, such as attenuation and dust heating, in different types of galaxies. The main conclusions of this thesis are summarised here.

In Chap. 5, we have performed panchromatic (UV-submm) SED modelling of the DustPedia galaxies. For the first time, we were able to determine the dust heating fraction by the old and young stellar populations in such a large, and statistically significant sample of local galaxies. The morphology of galaxies varies from pure ellipticals to ‘typical’ spirals to irregulars, with an average of 50 objects in each morphology class. In order to extract information on their baryonic content (stars and dust) we use the SED fitting code CIGALE adapted so as to include the recently developed dust model THEMIS (Jones et al. 2017). For each galaxy we retrieve estimates of the stellar mass, the current SFR, the dust mass, and the dust temperature, while the stellar populations in each galaxy and their role in the dust heating is investigated by deriving the luminosity produced by the old and the young stellar populations separately. Complementary information on the atomic gas mass (M_{HI}) for a subsample of 711 galaxies is also provided for each galaxy (De Vis et al. 2019). For comparison, we derived the global dust properties (mass and temperature) in an independent way, by fitting the FIR-submm part of the SED ($\lambda \geq 100 \mu\text{m}$) with a MBB properly scaled to account for the THEMIS dust physics.

We have shown how the mass of stars, dust, and atomic gas, as well as the SFR and the dust temperature vary between galaxies of different morphologies and have provided recipes to estimate these parameters given their Hubble stage (T). We have found a

mild correlation between the mass fraction of the small a-C(:H) grains with the sSFR. On average, young stars are very efficient in heating the dust, with absorption fractions reaching as high as $\sim 77\%$ of the total unattenuated luminosity of this population. On the other hand, the maximum absorption fraction of old stars is $\sim 24\%$. Dust heating in ETGs is mainly due to old stars, up to a level of $\sim 90\%$. Young stars progressively contribute more for 'typical' spiral galaxies and they become the dominant source of dust heating for Sm-type and irregular galaxies, with $\sim 60\%$ of their luminosity contributing to that purpose. The dust temperature, calculated by scaling the strength of the ISRF intensity derived by CIGALE, is higher for ETGs (~ 30 K) compared to LTGs where a drop by ~ 10 K is observed, followed by a sharp rise back to ~ 30 K for Sm-Irr type galaxies. Finally, we have found a strong correlation of the dust heating fraction by young stars with morphology and the sSFR. The results of this study can be used as reference for subsequent studies in the local Universe.

In Part IV, we have constructed detailed 3D stellar and dust radiative transfer models for nearby galaxies, using the state-of-the-art Monte Carlo code SKIRT and exploring the capabilities of inverse radiative transfer. Our goal was to analyse the contribution of the different stellar populations to the dust heating, and to quantify the fraction directly related to young stellar populations, both globally and on local scales. In Chap. 6, we have constructed detailed 3D radiative transfer models, for four late-type barred spiral galaxies (NGC 1365, M 83, M 95, M 100), with the purpose of investigating the dust-heating processes and to assess the influence of the bar on the heating fraction. Our models have been validated by comparing the simulated SEDs with the observational data across the entire UV to submm wavelength range, yielding a best-fitting description of each galaxy. We have derived global attenuation laws for each galaxy and have confirmed that galaxies of high specific sSFR have shallower attenuation curves and weaker UV bumps. On average, 36.5% of the bolometric luminosity is absorbed by dust in our galaxy sample. Moreover, the bar structure clearly affects the radial profiles of the dust-heating fraction by the young stellar populations, and the dust temperature. We have found that the young stellar populations are the main contributors to the dust heating, donating, on average $\sim 59\%$ of their luminosity to this purpose throughout the galaxy. This dust-heating fraction drops to $\sim 53\%$ in the bar region and $\sim 38\%$ in the bulge region where the old stars are the dominant contributors to the dust heating. We also have found a strong link between the heating fraction by the young stellar populations and the sSFR.

In Chap. 7, we have investigated the effect of diffuse dust heating in NGC 1068 with the inclusion of an AGN component. This additional dust heating source further contaminates the broadband fluxes on which classic galaxy modelling tools rely to derive physical properties. We have fitted a realistic model to the observations of NGC 1068. We have quantified the contribution of the various dust heating sources in each 3D dust cell and have found a median value of 83% for the star-formation component. The AGN contribution is measurable at the percentage level in the disc, but quickly increases in the inner few 100 pc, peaking at 80%. This is the first time the phenomenon of an AGN heating the diffuse dust beyond its torus was quantified in a nearby star-forming galaxy. NGC 1068 only contains a weak AGN, meaning this effect can be stronger in galaxies with a more luminous AGN. This could significantly impact the derived SFRs and ISM

masses for such systems. Overall, the results presented in Part [IV](#) reveal the importance of non-local heating and provide a valuable insight in the dust heating mechanisms. In addition, inferring a realistic geometry between the stars and dust results in a better representation of the attenuation properties in galaxies, which leads up to more accurate estimates of the intrinsic stellar properties.

Bibliography

- Alonso-Herrero, A., Ramos Almeida, C., Esquej, P., et al. 2014, [MNRAS](#), **443**, 2766
- Alton, P. B., Xilouris, E. M., Misiriotis, A., Dasyra, K. M., & Dumke, M. 2004, [A&A](#), **425**, 109
- Aniano, G., Draine, B. T., Calzetti, D., et al. 2012, [ApJ](#), **756**, 138
- Antonucci, R. R. J. & Miller, J. S. 1985, [ApJ](#), **297**, 621
- Assef, R. J., Stern, D., Noirot, G., et al. 2018, [ApJS](#), **234**, 23
- Auld, R., Bianchi, S., Smith, M. W. L., et al. 2013, [MNRAS](#), **428**, 1880
- Baes, M. & Camps, P. 2015, [Astronomy and Computing](#), **12**, 33
- Baes, M., Clemens, M., Xilouris, E. M., et al. 2010a, [A&A](#), **518**, L53
- Baes, M. & Dejonghe, H. 2001, [MNRAS](#), **326**, 733
- Baes, M., Fritz, J., Gadotti, D. A., et al. 2010b, [A&A](#), **518**, L39
- Baes, M., Trčka, A., Camps, P., et al. 2019, [MNRAS](#), **484**, 4069
- Baes, M., Verstappen, J., De Looze, I., et al. 2011, [ApJS](#), **196**, 22
- Baldry, I. K., Balogh, M. L., Bower, R. G., et al. 2006, [MNRAS](#), **373**, 469
- Bamford, S. P., Nichol, R. C., Baldry, I. K., et al. 2009, [MNRAS](#), **393**, 1324
- Bendo, G. J., Baes, M., Bianchi, S., et al. 2015, [MNRAS](#), **448**, 135
- Bendo, G. J., Boselli, A., Dariush, A., et al. 2012, [MNRAS](#), **419**, 1833
- Bendo, G. J., Wilson, C. D., Pohlen, M., et al. 2010, [A&A](#), **518**, L65
- Bettoni, D., Galletta, G., & García-Burillo, S. 2003, [A&A](#), **405**, 5
- Bianchi, S. 1999, [Modelling the Far-Infrared emission in spiral galaxies](#), PhD thesis, -

- Bianchi, S. 2007, *A&A*, 471, 765
- Bianchi, S. 2008, *A&A*, 490, 461
- Bianchi, S., Davies, J. I., & Alton, P. B. 2000, *A&A*, 359, 65
- Bianchi, S., De Vis, P., Viaene, S., et al. 2018, *A&A*, 620, A112
- Blanton, M. R., Eisenstein, D., Hogg, D. W., Schlegel, D. J., & Brinkmann, J. 2005, *ApJ*, 629, 143
- Bocchio, M., Jones, A. P., & Slavin, J. D. 2014, *A&A*, 570, A32
- Bocchio, M., Jones, A. P., Verstraete, L., et al. 2013, *A&A*, 556, A6
- Bocchio, M., Micelotta, E. R., Gautier, A. L., & Jones, A. P. 2012, *A&A*, 545, A124
- Boquien, M., Buat, V., & Perret, V. 2014, *A&A*, 571, A72
- Boquien, M., Burgarella, D., Roehlly, Y., et al. 2019, *A&A*, 622, A103
- Boquien, M., Calzetti, D., Aalto, S., et al. 2015, *A&A*, 578, A8
- Boquien, M., Calzetti, D., Combes, F., et al. 2011, *AJ*, 142, 111
- Boquien, M., Kennicutt, R., Calzetti, D., et al. 2016, *A&A*, 591, A6
- Boselli, A., Ciesla, L., Buat, V., et al. 2010a, *A&A*, 518, L61
- Boselli, A., Ciesla, L., Cortese, L., et al. 2012, *A&A*, 540, A54
- Boselli, A., Cortese, L., Boquien, M., et al. 2014, *A&A*, 564, A66
- Boselli, A., Eales, S., Cortese, L., et al. 2010b, *PASP*, 122, 261
- Bron, E., Le Bourlot, J., & Le Petit, F. 2014, *A&A*, 569, A100
- Bruzual, G. & Charlot, S. 2003, *MNRAS*, 344, 1000
- Buat, V., Corre, et al. 2019, arXiv e-prints [[arXiv:1902.09435](https://arxiv.org/abs/1902.09435)]
- Buat, V., Boquien, M., Małek, K., et al. 2018, *A&A*, 619, A135
- Buat, V. & Xu, C. 1996, *A&A*, 306, 61
- Buitrago, F., Trujillo, I., Conselice, C. J., & Häußler, B. 2013, *MNRAS*, 428, 1460
- Calzetti, D. 2013, *Star Formation Rate Indicators*, ed. J. Falcón-Barroso & J. H. Knapen, 419
- Calzetti, D., Armus, L., Bohlin, R. C., et al. 2000, *ApJ*, 533, 682
- Calzetti, D., Kennicutt, R. C., Engelbracht, C. W., et al. 2007, *ApJ*, 666, 870
- Calzetti, D., Wu, S.-Y., Hong, S., et al. 2010, *ApJ*, 714, 1256

- Camps, P. 2016, [Monte Carlo radiative transfer simulations of galaxies using numerically generated models](#), PhD thesis, Ghent University
- Camps, P. & Baes, M. 2015, [Astronomy and Computing](#), **9**, 20
- Camps, P., Baes, M., & Saftly, W. 2013, [A&A](#), **560**, A35
- Camps, P., Misselt, K., Bianchi, S., et al. 2015, [A&A](#), **580**, A87
- Cappellari, M., Emsellem, E., Krajnović, D., et al. 2011, [MNRAS](#), **413**, 813
- Cardelli, J. A., Clayton, G. C., & Mathis, J. S. 1989, [ApJ](#), **345**, 245
- Casasola, V., Bettoni, D., & Galletta, G. 2004, [A&A](#), **422**, 941
- Casasola, V., Bianchi, S., De Vis, P., et al. 2019, [A&A](#), submitted, submitted
- Casasola, V., Cassarà, L. P., Bianchi, S., et al. 2017, [A&A](#), **605**, A18
- Casasola, V., Hunt, L. K., Combes, F., García-Burillo, S., & Neri, R. 2011, [A&A](#), **527**, A92
- Casey, C. M. 2012, [MNRAS](#), **425**, 3094
- Casey, C. M., Narayanan, D., & Cooray, A. 2014, [Phys. Rep.](#), **541**, 45
- Cassarà, L. P., Xilouris, E. M., Nersesian, A., et al. 2019, [A&A](#), in preparation, in preparation
- Chabrier, G. 2003, [PASP](#), **115**, 763
- Chang, Y.-Y., van der Wel, A., da Cunha, E., & Rix, H.-W. 2015, [ApJS](#), **219**, 8
- Charlot, S. & Fall, S. M. 2000, [ApJ](#), **539**, 718
- Chevallard, J. & Charlot, S. 2016, [MNRAS](#), **462**, 1415
- Ciesla, L., Boquien, M., Boselli, A., et al. 2014, [A&A](#), **565**, A128
- Ciesla, L., Boselli, A., Elbaz, D., et al. 2016, [A&A](#), **585**, A43
- Ciesla, L., Charmandaris, V., Georgakakis, A., et al. 2015, [A&A](#), **576**, A10
- Ciesla, L., Elbaz, D., & Fensch, J. 2017, [A&A](#), **608**, A41
- Clark, C. J. R., Verstocken, S., Bianchi, S., et al. 2018, [A&A](#), **609**, A37
- Clayton, D. D. & Nittler, L. R. 2004, [ARA&A](#), **42**, 39
- Cluver, M. E., Jarrett, T. H., Hopkins, A. M., et al. 2014, [ApJ](#), **782**, 90
- Cole, S., Lacey, C. G., Baugh, C. M., & Frenk, C. S. 2000, [MNRAS](#), **319**, 168
- Combes, F., García-Burillo, S., Casasola, V., et al. 2013, [A&A](#), **558**, A124

- Combes, F., García-Burillo, S., Casasola, V., et al. 2014, *A&A*, **565**, A97
- Compiègne, M., Verstraete, L., Jones, A., et al. 2011, *A&A*, **525**, A103
- Conselice, C. J. 2014, *ARA&A*, **52**, 291
- Conselice, C. J., Blackburne, J. A., & Papovich, C. 2005, *ApJ*, **620**, 564
- Cortese, L., Boselli, A., Franzetti, P., et al. 2008, *MNRAS*, **386**, 1157
- Cortese, L., Ciesla, L., Boselli, A., et al. 2012, *A&A*, **540**, A52
- Cortese, L., Fritz, J., Bianchi, S., et al. 2014, *MNRAS*, **440**, 942
- Croxall, K. V., Smith, J. D., Wolfire, M. G., et al. 2012, *ApJ*, **747**, 81
- Cutri, R. M., Skrutskie, M. F., van Dyk, S., et al. 2003, VizieR Online Data Catalog, **2246**
- da Cunha, E., Charlot, S., & Elbaz, D. 2008, *MNRAS*, **388**, 1595
- da Cunha, E., Eminian, C., Charlot, S., & Blaizot, J. 2010, *MNRAS*, **403**, 1894
- D'Agostino, J. J., Poetrodjojo, H., Ho, I. T., et al. 2018, *MNRAS*, **479**, 4907
- Dale, D. A., Aniano, G., Engelbracht, C. W., et al. 2012, *ApJ*, **745**, 95
- Dale, D. A., Helou, G., Contursi, A., Silbermann, N. A., & Kolhatkar, S. 2001, *ApJ*, **549**, 215
- Dale, D. A., Helou, G., Magdis, G. E., et al. 2014, *ApJ*, **784**, 83
- Dartois, E., Marco, O., Muñoz-Caro, G. M., et al. 2004a, *A&A*, **423**, 549
- Dartois, E., Muñoz Caro, G. M., Deboffle, D., & d'Hendecourt, L. 2004b, *A&A*, **423**, L33
- Dartois, E., Muñoz Caro, G. M., Deboffle, D., Montagnac, G., & D'Hendecourt, L. 2005, *A&A*, **432**, 895
- Davies, J. I., Baes, M., Bianchi, S., et al. 2017, *PASP*, **129**, 044102
- Davies, J. I., Bianchi, S., Cortese, L., et al. 2012, *MNRAS*, **419**, 3505
- Davies, J. I., Nersesian, A., Baes, M., et al. 2019, *A&A*, **626**, A63
- Davies, L. J. M., Driver, S. P., Robotham, A. S. G., et al. 2016, *MNRAS*, **461**, 458
- Davis, T. A., Young, L. M., Crocker, A. F., et al. 2014, *MNRAS*, **444**, 3427
- De Geyter, G., Baes, M., Camps, P., et al. 2014, *MNRAS*, **441**, 869
- De Geyter, G., Baes, M., De Looze, I., et al. 2015, *MNRAS*, **451**, 1728
- De Looze, I., Baes, M., Bendo, G. J., et al. 2012a, *MNRAS*, **427**, 2797

- De Looze, I., Baes, M., Fritz, J., & Verstackpen, J. 2012b, *MNRAS*, **419**, 895
- De Looze, I., Fritz, J., Baes, M., et al. 2014, *A&A*, **571**, A69
- De Lucia, G., Weinmann, S., Poggianti, B. M., Aragón-Salamanca, A., & Zaritsky, D. 2012, *MNRAS*, **423**, 1277
- de Vaucouleurs, G. 1959, *Handbuch der Physik*, **53**, 275
- de Vaucouleurs, G., de Vaucouleurs, A., Corwin, H. G., et al. 1995, *VizieR Online Data Catalog*, **7155**
- De Vis, P., Dunne, L., Maddox, S., et al. 2017, *MNRAS*, **464**, 4680
- De Vis, P., Jones, A., Viaene, S., et al. 2019, *A&A*, **623**, A5
- Declair, M., De Looze, I., Boquien, M., et al. 2019, *MNRAS*, **486**, 743
- Desert, F.-X., Boulanger, F., & Puget, J. L. 1990, *A&A*, **237**, 215
- Devereux, N. A. & Young, J. S. 1990, *ApJ*, **350**, L25
- di Serego Alighieri, S., Bianchi, S., Pappalardo, C., et al. 2013, *A&A*, **552**, A8
- Disney, M., Davies, J., & Phillipps, S. 1989, *MNRAS*, **239**, 939
- Draine, B. T. 2003, *ARA&A*, **41**, 241
- Draine, B. T., Aniano, G., Krause, O., et al. 2014, *ApJ*, **780**, 172
- Draine, B. T., Dale, D. A., Bendo, G., et al. 2007, *ApJ*, **663**, 866
- Draine, B. T. & Lee, H. M. 1984, *ApJ*, **285**, 89
- Draine, B. T. & Li, A. 2001, *ApJ*, **551**, 807
- Draine, B. T. & Li, A. 2007, *ApJ*, **657**, 810
- Dressler, A. 1980, *ApJ*, **236**, 351
- Dressler, A., Thompson, I. B., & Sheckman, S. A. 1985, *ApJ*, **288**, 481
- Driver, S. P., Hill, D. T., Kelvin, L. S., et al. 2011, *MNRAS*, **413**, 971
- Dunne, L., Gomez, H. L., da Cunha, E., et al. 2011, *MNRAS*, **417**, 1510
- Dwek, E., Arendt, R. G., Fixsen, D. J., et al. 1997, *ApJ*, **475**, 565
- Dwek, E., Galliano, F., & Jones, A. 2009, in *Astronomical Society of the Pacific Conference Series*, Vol. 414, *Cosmic Dust - Near and Far*, ed. T. Henning, E. Grün, & J. Steinacker, **183**
- Eales, S., Smith, M. W. L., Auld, R., et al. 2012, *ApJ*, **761**, 168
- Eisenstein, D. J., Weinberg, D. H., Agol, E., et al. 2011, *AJ*, **142**, 72

- Eskew, M., Zaritsky, D., & Meidt, S. 2012, [AJ](#), **143**, 139
- Fanciullo, L., Guillet, V., Aniano, G., et al. 2015, [A&A](#), **580**, A136
- Farrah, D., Bernard-Salas, J., Spoon, H. W. W., et al. 2007, [ApJ](#), **667**, 149
- Fazeli, N., Busch, G., Valencia-S., M., et al. 2019, [A&A](#), **622**, A128
- Fazio, G. G., Hora, J. L., Allen, L. E., et al. 2004, [ApJS](#), **154**, 10
- Feltre, A., Hatziminaoglou, E., Fritz, J., & Franceschini, A. 2012, [MNRAS](#), **426**, 120
- Fitzpatrick, E. L. & Massa, D. 2007, [ApJ](#), **663**, 320
- Fitzpatrick, E. L. & Massa, D. 2009, [ApJ](#), **699**, 1209
- Foyle, K., Natale, G., Wilson, C. D., et al. 2013, [MNRAS](#), **432**, 2182
- Fritz, J., Franceschini, A., & Hatziminaoglou, E. 2006, [MNRAS](#), **366**, 767
- Fumagalli, M., Krumholz, M. R., Prochaska, J. X., Gavazzi, G., & Boselli, A. 2009, [ApJ](#), **697**, 1811
- Gadotti, D. A. 2009, [MNRAS](#), **393**, 1531
- Gadotti, D. A., Baes, M., & Falony, S. 2010, [MNRAS](#), **403**, 2053
- Gail, H. P., Zhukovska, S. V., Hoppe, P., & Tieloff, M. 2009, [ApJ](#), **698**, 1136
- Galametz, M., Kennicutt, R. C., Albrecht, M., et al. 2012, [MNRAS](#), **425**, 763
- Galametz, M., Kennicutt, R. C., Calzetti, D., et al. 2013, [MNRAS](#), **431**, 1956
- Galametz, M., Madden, S., Galliano, F., et al. 2009, [A&A](#), **508**, 645
- Galametz, M., Madden, S. C., Galliano, F., et al. 2010, [A&A](#), **518**, L55
- Galliano, F., Galametz, M., & Jones, A. P. 2018, [ARA&A](#), **56**, 673
- García-Burillo, S., Combes, F., Ramos Almeida, C., et al. 2016, [ApJ](#), **823**, L12
- Gavazzi, G., Boselli, A., Pedotti, P., Gallazzi, A., & Carrasco, L. 2002, [A&A](#), **396**, 449
- George, K., Joseph, P., Mondal, C., et al. 2019, [A&A](#), **621**, L4
- Giovanelli, R. & Haynes, M. P. 1985, [ApJ](#), **292**, 404
- Gomez, H. L., Clark, C. J. R., Nozawa, T., et al. 2012, [MNRAS](#), **420**, 3557
- Gordon, K. D., Clayton, G. C., Misselt, K. A., Landolt, A. U., & Wolff, M. J. 2003, [ApJ](#), **594**, 279
- Granato, G. L., Lacey, C. G., Silva, L., et al. 2000, [ApJ](#), **542**, 710
- Greenhill, L. J., Gwinn, C. R., Antonucci, R., & Barvainis, R. 1996, [ApJ](#), **472**, L21

- Griffin, M. J., Abergel, A., Abreu, A., et al. 2010, [A&A](#), **518**, L3
- Groves, B., Dopita, M. A., Sutherland, R. S., et al. 2008, [ApJS](#), **176**, 438
- Groves, B., Krause, O., Sandstrom, K., et al. 2012, [MNRAS](#), **426**, 892
- Groves, B. A., Dopita, M. A., & Sutherland, R. S. 2004, [ApJS](#), **153**, 9
- Han, Y. & Han, Z. 2014, [ApJS](#), **215**, 2
- Helou, G., Soifer, B. T., & Rowan-Robinson, M. 1985, [ApJ](#), **298**, L7
- Hildebrand, R. H. 1983, [QJRAS](#), **24**, 267
- Hinz, J. L., Rieke, G. H., Gordon, K. D., et al. 2004, [ApJS](#), **154**, 259
- Hirashita, H. & Kuo, T.-M. 2011, [MNRAS](#), **416**, 1340
- Ho, L. C., Filippenko, A. V., & Sargent, W. L. W. 1997, [ApJS](#), **112**, 315
- Houck, J. R., Weedman, D. W., Le Floch, E., & Hao, L. 2007, [ApJ](#), **671**, 323
- Howell, J. H., Mazzarella, J. M., Chan, B. H. P., et al. 2007, [AJ](#), **134**, 2086
- Hubble, E. 1982, The realm of the nebulae
- Hughes, T. M., Baes, M., Fritz, J., et al. 2014, [A&A](#), **565**, A4
- Hughes, T. M., Foyle, K., Schirm, M. R. P., et al. 2015, [A&A](#), **575**, A17
- Hughes, T. M., Ibar, E., Villanueva, V., et al. 2017, [MNRAS](#), **468**, L103
- Hunt, L. K., De Looze, I., Boquien, M., et al. 2019, [A&A](#), **621**, A51
- Indebetouw, R., Whitney, B. A., Johnson, K. E., & Wood, K. 2006, [ApJ](#), **636**, 362
- Inoue, A. K. 2011, [MNRAS](#), **415**, 2920
- James, P. A., Bretherton, C. F., & Knapen, J. H. 2009, [A&A](#), **501**, 207
- James, P. A. & Percival, S. M. 2015, [MNRAS](#), **450**, 3503
- James, P. A. & Percival, S. M. 2016, [MNRAS](#), **457**, 917
- Jones, A. P. 2004, in *Astronomical Society of the Pacific Conference Series*, Vol. 309, *Astrophysics of Dust*, ed. A. N. Witt, G. C. Clayton, & B. T. Draine, 347
- Jones, A. P. 2012a, [A&A](#), **540**, A1
- Jones, A. P. 2012b, [A&A](#), **540**, A2
- Jones, A. P. 2012c, [A&A](#), **542**, A98
- Jones, A. P., Duley, W. W., & Williams, D. A. 1990, [QJRAS](#), **31**, 567

- Jones, A. P., Fanciullo, L., Köhler, M., et al. 2013, *A&A*, 558, A62
- Jones, A. P. & Habart, E. 2015, *A&A*, 581, A92
- Jones, A. P., Köhler, M., Ysard, N., Bocchio, M., & Verstraete, L. 2017, *A&A*, 602, A46
- Jones, A. P., Ysard, N., Köhler, M., et al. 2014, *Faraday Discussions*, 168, 313
- Kamenetzky, J., McCray, R., Indebetouw, R., et al. 2013, *ApJ*, 773, L34
- Kaneda, H., Onaka, T., Sakon, I., et al. 2008, *ApJ*, 684, 270
- Kauffmann, G., White, S. D. M., Heckman, T. M., et al. 2004, *MNRAS*, 353, 713
- Kennicutt, R. C., J. 1983, *AJ*, 88, 483
- Kennicutt, R. C., J., Bothun, G. D., & Schommer, R. A. 1984, *AJ*, 89, 1279
- Kennicutt, R. C., Calzetti, D., Aniano, G., et al. 2011, *PASP*, 123, 1347
- Kennicutt, R. C. & Evans, N. J. 2012, *ARA&A*, 50, 531
- Kennicutt, Jr., R. C. 1998, *ARA&A*, 36, 189
- Kennicutt, Jr., R. C., Armus, L., Bendo, G., et al. 2003, *PASP*, 115, 928
- Kennicutt, Jr., R. C., Hao, C.-N., Calzetti, D., et al. 2009, *ApJ*, 703, 1672
- Kirkpatrick, A., Pope, A., Alexander, D. M., et al. 2012, *ApJ*, 759, 139
- Kirkpatrick, A., Pope, A., Sajina, A., et al. 2015, *ApJ*, 814, 9
- Knapen, J. H., Pérez-Ramírez, D., & Laine, S. 2002, *MNRAS*, 337, 808
- Knapen, J. H., Sharp, R. G., Ryder, S. D., et al. 2010, *MNRAS*, 408, 797
- Knapen, J. H., Stedman, S., Bramich, D. M., Folkes, S. L., & Bradley, T. R. 2004, *A&A*, 426, 1135
- Kodama, T., Smail, I., Nakata, F., Okamura, S., & Bower, R. G. 2001, *ApJ*, 562, L9
- Köhler, M., Jones, A., & Ysard, N. 2014, *A&A*, 565, L9
- Köhler, M., Stepnik, B., Jones, A. P., et al. 2012, *A&A*, 548, A61
- Köhler, M., Ysard, N., & Jones, A. P. 2015, *A&A*, 579, A15
- Kriek, M. & Conroy, C. 2013, *ApJ*, 775, L16
- Kroupa, P. 2001, in *Astronomical Society of the Pacific Conference Series*, Vol. 228, *Dynamics of Star Clusters and the Milky Way*, ed. S. Deiters, B. Fuchs, A. Just, R. Spurzem, & R. Wielen, 187
- Kylafis, N. D. & Bahcall, J. N. 1987, *ApJ*, 317, 637

- Lauberts, A. & Valentijn, E. A. 1989, *The Messenger*, [56](#), [31](#)
- Lawrence, A., Warren, S. J., Almaini, O., et al. 2007, *MNRAS*, [379](#), [1599](#)
- Leitherer, C., Li, I.-H., Calzetti, D., & Heckman, T. M. 2002, *ApJS*, [140](#), [303](#)
- Leja, J., Johnson, B. D., Conroy, C., et al. 2019, *ApJ*, [877](#), [140](#)
- Leja, J., Johnson, B. D., Conroy, C., van Dokkum, P. G., & Byler, N. 2017, *ApJ*, [837](#), [170](#)
- Lenz, D., Hensley, B. S., & Doré, O. 2017, *ApJ*, [846](#), [38](#)
- Li, A. & Draine, B. T. 2001, *ApJ*, [554](#), [778](#)
- Li, A. & Draine, B. T. 2002, *ApJ*, [572](#), [232](#)
- Li, A. & Greenberg, J. M. 1997, *A&A*, [323](#), [566](#)
- Lindblad, P. O. 1999, *A&A Rev.*, [9](#), [221](#)
- Lindblad, P. O., Hjelm, M., Hoegbom, J., et al. 1996, *A&AS*, [120](#), [403](#)
- Liszt, H. 2014a, *ApJ*, [783](#), [17](#)
- Liszt, H. 2014b, *ApJ*, [780](#), [10](#)
- Lo Faro, B., Buat, V., Roehlly, Y., et al. 2017, *MNRAS*, [472](#), [1372](#)
- Lopez-Rodriguez, E., Fuller, L., Alonso-Herrero, A., et al. 2018, *ApJ*, [859](#), [99](#)
- Lusso, E., Comastri, A., Simmons, B. D., et al. 2012, *MNRAS*, [425](#), [623](#)
- Madau, P. & Dickinson, M. 2014, *ARA&A*, [52](#), [415](#)
- Madden, S. C., Rémy-Ruyer, A., Galametz, M., et al. 2013, *PASP*, [125](#), [600](#)
- Makarov, D., Prugniel, P., Terekhova, N., Courtois, H., & Vauglin, I. 2014, *A&A*, [570](#), [A13](#)
- Małek, K., Buat, V., Roehlly, Y., et al. 2018, *A&A*, [620](#), [A50](#)
- Maraston, C. 2005, *MNRAS*, [362](#), [799](#)
- Marks, M., Kroupa, P., Dabringhausen, J., & Pawlowski, M. S. 2012, *MNRAS*, [422](#), [2246](#)
- Martin, D. C., Fanson, J., Schiminovich, D., et al. 2005, *ApJ*, [619](#), [L1](#)
- Mason, R. E., Geballe, T. R., Packham, C., et al. 2006, *ApJ*, [640](#), [612](#)
- Mathis, J. S., Mezger, P. G., & Panagia, N. 1983, *A&A*, [128](#), [212](#)
- Matsuura, M., Dwek, E., Barlow, M. J., et al. 2015, *ApJ*, [800](#), [50](#)

- Mattsson, L., De Cia, A., Andersen, A. C., & Zafar, T. 2014, [MNRAS](#), **440**, 1562
- Mattsson, L. & Höfner, S. 2011, [A&A](#), **533**, A42
- Mazzalay, X., Saglia, R. P., Erwin, P., et al. 2013, [MNRAS](#), **428**, 2389
- Meidt, S. E., Schinnerer, E., van de Ven, G., et al. 2014, [ApJ](#), **788**, 144
- Mentuch Cooper, E., Wilson, C. D., Foyle, K., et al. 2012, [ApJ](#), **755**, 165
- Misiriotis, A. & Bianchi, S. 2002, [A&A](#), **384**, 866
- Misiriotis, A., Popescu, C. C., Tuffs, R., & Kylafis, N. D. 2001, [A&A](#), **372**, 775
- Morgan, H. L. & Edmunds, M. G. 2003, [MNRAS](#), **343**, 427
- Morrissey, P., Conrow, T., Barlow, T. A., et al. 2007, [ApJS](#), **173**, 682
- Mosenkov, A. V., Allaert, F., Baes, M., et al. 2018, [A&A](#), **616**, A120
- Mosenkov, A. V., Allaert, F., Baes, M., et al. 2016, [A&A](#), **592**, A71
- Mosenkov, A. V., Baes, M., Bianchi, S., et al. 2019, [A&A](#), **622**, A132
- Moss, C. & Whittle, M. 1993, [ApJ](#), **407**, L17
- Narayanan, D., Conroy, C., Davé, R., Johnson, B. D., & Popping, G. 2018, [ApJ](#), **869**, 70
- Natale, G., Tuffs, R. J., Xu, C. K., et al. 2010, [ApJ](#), **725**, 955
- Nenkova, M., Sirocky, M. M., Ivezić, Ž., & Elitzur, M. 2008, [ApJ](#), **685**, 147
- Nersesian, A., Verstocken, S., Viaene, S., et al. 2019a, [A&A](#), Forthcoming, Forthcoming
- Nersesian, A., Xilouris, E. M., Bianchi, S., et al. 2019b, [A&A](#), **624**, A80
- Neugebauer, G., Habing, H. J., van Duinen, R., et al. 1984, [ApJ](#), **278**, L1
- Nguyen, H., Dawson, J. R., Miville-Deschênes, M.-A., et al. 2018, [ApJ](#), **862**, 49
- Noeske, K. G., Weiner, B. J., Faber, S. M., et al. 2007, [ApJ](#), **660**, L43
- Noll, S., Burgarella, D., Giovannoli, E., et al. 2009, [A&A](#), **507**, 1793
- Norris, B. R. M., Tuthill, P. G., Ireland, M. J., et al. 2012, [Nature](#), **484**, 220
- Oemler, Augustus, J. 1974, [ApJ](#), **194**, 1
- Oliver, S., Frost, M., Farrah, D., et al. 2010, [MNRAS](#), **405**, 2279
- Ormel, C. W., Paszun, D., Dominik, C., & Tielens, A. G. G. M. 2009, [A&A](#), **502**, 845
- Ossenkopf, V. 1993, [A&A](#), **280**, 617

- Osterbrock, D. E. & Martel, A. 1993, [ApJ](#), **414**, 552
- Ostriker, J. P. & Tremaine, S. D. 1975, [ApJ](#), **202**, L113
- Pastrav, B. A., Popescu, C. C., Tuffs, R. J., & Sansom, A. E. 2013a, [A&A](#), **553**, A80
- Pastrav, B. A., Popescu, C. C., Tuffs, R. J., & Sansom, A. E. 2013b, [A&A](#), **557**, A137
- Pendleton, Y. J. & Allamandola, L. J. 2002, [ApJS](#), **138**, 75
- Peng, Y.-j., Lilly, S. J., Kovač, K., et al. 2010, [ApJ](#), **721**, 193
- Pilbratt, G. L., Riedinger, J. R., Passvogel, T., et al. 2010, [A&A](#), **518**, L1
- Pinte, C., Ménard, F., Duchêne, G., & Bastien, P. 2006, [A&A](#), **459**, 797
- Planck Collaboration, Abergel, A., Ade, P. A. R., et al. 2011a, [A&A](#), **536**, A24
- Planck Collaboration, Ade, P. A. R., Aghanim, N., et al. 2015, [A&A](#), **576**, A104
- Planck Collaboration, Ade, P. A. R., Aghanim, N., et al. 2011b, [A&A](#), **536**, A1
- Poglitsch, A., Waelkens, C., Geis, N., et al. 2010, [A&A](#), **518**, L2
- Pohlen, M., Cortese, L., Smith, M. W. L., et al. 2010, [A&A](#), **518**, L72
- Popescu, C. C., Misiriotis, A., Kylafis, N. D., Tuffs, R. J., & Fischera, J. 2000, [A&A](#), **362**, 138
- Popescu, C. C. & Tuffs, R. J. 2002, in *Reviews in Modern Astronomy*, Vol. 15, *Reviews in Modern Astronomy*, ed. R. E. Schielicke, 239
- Psychogyios, A. 2018, [Galaxy morphology in different environments](#), PhD thesis, University of Crete
- Reach, W. T., Bernard, J.-P., Jarrett, T. H., & Heiles, C. 2017a, [ApJ](#), **851**, 119
- Reach, W. T., Heiles, C., & Bernard, J.-P. 2015, [ApJ](#), **811**, 118
- Reach, W. T., Heiles, C., & Bernard, J.-P. 2017b, [ApJ](#), **834**, 63
- Reddy, N. A., Kriek, M., Shapley, A. E., et al. 2015, [ApJ](#), **806**, 259
- Rémy-Ruyer, A., Madden, S. C., Galliano, F., et al. 2014, [A&A](#), **563**, A31
- Rémy-Ruyer, A., Madden, S. C., Galliano, F., et al. 2015, [A&A](#), **582**, A121
- Rho, J., Jarrett, T. H., Reach, W. T., Gomez, H., & Andersen, M. 2009, [ApJ](#), **693**, L39
- Rieke, G. H., Young, E. T., Engelbracht, C. W., et al. 2004, [The Astrophysical Journal Supplement Series](#), **154**, 25
- Roebuck, E., Sajina, A., Hayward, C. C., et al. 2016, [ApJ](#), **833**, 60

Bibliography

- Roehlly, Y., Burgarella, D., Buat, V., et al. 2014, in *Astronomical Society of the Pacific Conference Series*, Vol. 485, *Astronomical Data Analysis Software and Systems XXIII*, ed. N. Manset & P. Forshay, [347](#)
- Rowlands, K., Gomez, H. L., Dunne, L., et al. 2014, *MNRAS*, [441](#), [1040](#)
- Sadavoy, S., Matsuura, M., Armus, L., et al. 2019, *BAAS*, [51](#), [66](#)
- Saftly, W., Baes, M., & Camps, P. 2014, *A&A*, [561](#), [A77](#)
- Saftly, W., Baes, M., De Geyter, G., et al. 2015, *A&A*, [576](#), [A31](#)
- Saftly, W., Camps, P., Baes, M., et al. 2013, *A&A*, [554](#), [A10](#)
- Sales, D. A., Pastoriza, M. G., & Riffel, R. 2010, *ApJ*, [725](#), [605](#)
- Salim, S., Boquien, M., & Lee, J. C. 2018, *ApJ*, [859](#), [11](#)
- Salo, H., Laurikainen, E., Laine, J., et al. 2015, *ApJS*, [219](#), [4](#)
- Salpeter, E. E. 1955, *ApJ*, [121](#), [161](#)
- Sandstrom, K. M., Leroy, A. K., Walter, F., et al. 2013, *ApJ*, [777](#), [5](#)
- Satyapal, S., Abel, N. P., & Secret, N. J. 2018, *ApJ*, [858](#), [38](#)
- Sauvage, M., Sacchi, N., Bendo, G. J., et al. 2010, *A&A*, [518](#), [L64](#)
- Schartmann, M., Meisenheimer, K., Camenzind, M., Wolf, S., & Henning, T. 2005, *A&A*, [437](#), [861](#)
- Schaye, J., Crain, R. A., Bower, R. G., et al. 2015, *MNRAS*, [446](#), [521](#)
- Schmidt, M. 1959, *ApJ*, [129](#), [243](#)
- Schneider, R., Bianchi, S., Valiante, R., Risaliti, G., & Salvadori, S. 2015, *A&A*, [579](#), [A60](#)
- Scoville, N., Aussel, H., Sheth, K., et al. 2014, *ApJ*, [783](#), [84](#)
- Scoville, N., Sheth, K., Aussel, H., et al. 2015, *arXiv e-prints*, [arXiv:1505.02159](#)
- Serra Díaz-Cano, L. & Jones, A. P. 2008, *A&A*, [492](#), [127](#)
- Sérsic, J. L. 1963, *Boletin de la Asociacion Argentina de Astronomia La Plata Argentina*, [6](#), [41](#)
- Sheth, K., Regan, M., Hinz, J. L., et al. 2010, *PASP*, [122](#), [1397](#)
- Siebenmorgen, R. & Kruegel, E. 1992, *A&A*, [259](#), [614](#)
- Silva, L., Granato, G. L., Bressan, A., & Danese, L. 1998, *ApJ*, [509](#), [103](#)
- Skibba, R. A., Engelbracht, C. W., Dale, D., et al. 2011, *ApJ*, [738](#), [89](#)

- Skrutskie, M. F., Cutri, R. M., Stiening, R., et al. 2006, *AJ*, 131, 1163
- Slavin, J. D., Dwek, E., & Jones, A. P. 2015, *ApJ*, 803, 7
- Smith, J. D. T., Draine, B. T., Dale, D. A., et al. 2007, *ApJ*, 656, 770
- Smith, M. W. L., Eales, S. A., Gomez, H. L., et al. 2012a, *ApJ*, 756, 40
- Smith, M. W. L., Gomez, H. L., Eales, S. A., et al. 2012b, *ApJ*, 748, 123
- Smith, M. W. L., Vlahakis, C., Baes, M., et al. 2010, *A&A*, 518, L51
- Soifer, B. T. & Neugebauer, G. 1991, *AJ*, 101, 354
- Springel, V., White, S. D. M., Jenkins, A., et al. 2005, *Nature*, 435, 629
- Stahler, S. W. & Palla, F. 2005, *The Formation of Stars*, 865
- Stalevski, M., Fritz, J., Baes, M., Nakos, T., & Popović, L. Č. 2012, *MNRAS*, 420, 2756
- Steinacker, J., Baes, M., & Gordon, K. D. 2013, *ARA&A*, 51, 63
- Steinacker, J., Henning, T., Bacmann, A., & Semenov, D. 2003, *A&A*, 401, 405
- Stepnik, B., Abergel, A., Bernard, J. P., et al. 2003, *A&A*, 398, 551
- Strateva, I., Ivezić, Ž., Knapp, G. R., et al. 2001, *AJ*, 122, 1861
- Taylor, E. N., Hopkins, A. M., Baldry, I. K., et al. 2011, *MNRAS*, 418, 1587
- Telesco, C. M. & Harper, D. A. 1980, *ApJ*, 235, 392
- Teuben, P. J., Sanders, R. H., Atherton, P. D., & van Albada, G. D. 1986, *MNRAS*, 221, 1
- Tielens, A. G. G. M. 2008, *ARA&A*, 46, 289
- Todini, P. & Ferrara, A. 2001, *MNRAS*, 325, 726
- Tomczak, A. R., Quadri, R. F., Tran, K.-V. H., et al. 2014, *ApJ*, 783, 85
- Trčka, A., Baes, M., Camps, P., et al. 2019, *MNRAS*, submitted, submitted
- Turner, J. L., Ho, P. T. P., & Beck, S. 1987, *ApJ*, 313, 644
- van Velzen, S., Falcke, H., Schellart, P., Nierstenhöfer, N., & Kampert, K.-H. 2012, *A&A*, 544, A18
- Városov, F. & Dwek, E. 1999, *ApJ*, 523, 265
- Véron-Cetty, M.-P. & Véron, P. 2006, *A&A*, 455, 773
- Verstappen, J., Fritz, J., Baes, M., et al. 2013, *A&A*, 556, A54
- Verstocken, S., Baes, M., Nersesian, A., et al. 2019, *A&A*, submitted, submitted

- Verstocken, S., Van De Putte, D., Camps, P., & Baes, M. 2017, [Astronomy and Computing](#), **20**, 16
- Viaene, S. 2016, [The panchromatic interplay between starlight and dust in Andromeda and the Local Universe](#), PhD thesis, Ghent University
- Viaene, S., Baes, M., Bendo, G., et al. 2016, [A&A](#), **586**, A13
- Viaene, S., Baes, M., Tamm, A., et al. 2017, [A&A](#), **599**, A64
- Viaene, S., Nersesian, A., Fritz, J., et al. 2019, [A&A](#), submitted, submitted
- Vidali, G., Roser, J. E., Manicò, G., & Pirronello, V. 2004, [Advances in Space Research](#), **33**, 6
- Vika, M., Ciesla, L., Charmandaris, V., Xilouris, E. M., & Leboutellier, V. 2017, [A&A](#), **597**, A51
- Visvanathan, N. & Sandage, A. 1977, [ApJ](#), **216**, 214
- Wang, Y., Pearce, F., Knebe, A., et al. 2018, [ApJ](#), **868**, 130
- Wen, X.-Q., Wu, H., Zhu, Y.-N., et al. 2013, [MNRAS](#), **433**, 2946
- Werner, M. W., Roellig, T. L., Low, F. J., et al. 2004, [ApJS](#), **154**, 1
- Whelan, D. G., Johnson, K. E., Whitney, B. A., Indebetouw, R., & Wood, K. 2011, [ApJ](#), **729**, 111
- Whitaker, K. E., Bezanson, R., van Dokkum, P. G., et al. 2017, [ApJ](#), **838**, 19
- Whitaker, K. E., Franx, M., Bezanson, R., et al. 2015, [ApJ](#), **811**, L12
- White, S. D. M. & Rees, M. J. 1978, [MNRAS](#), **183**, 341
- Willett, K. W., Schawinski, K., Simmons, B. D., et al. 2015, [MNRAS](#), **449**, 820
- Williams, T. G., Baes, M., De Looze, I., et al. 2019, [MNRAS](#), **487**, 2753
- Witt, A. N. & Gordon, K. D. 1996, [ApJ](#), **463**, 681
- Witt, A. N. & Gordon, K. D. 2000, [ApJ](#), **528**, 799
- Wozniak, H. 2007, [A&A](#), **465**, L1
- Wright, E. L., Eisenhardt, P. R. M., Mainzer, A. K., et al. 2010, [AJ](#), **140**, 1868
- Wu, H., Zhu, Y.-N., Cao, C., & Qin, B. 2007, [ApJ](#), **668**, 87
- Xilouris, E. M., Byun, Y. I., Kylafis, N. D., Paleologou, E. V., & Papamastorakis, J. 1999, [A&A](#), **344**, 868
- Xilouris, E. M., Tabatabaei, F. S., Boquien, M., et al. 2012, [A&A](#), **543**, A74

- Xu, C. & Buat, V. 1995, *A&A*, 293 [[astro-ph/9411101](#)]
- York, D. G., Adelman, J., Anderson, Jr., J. E., et al. 2000, *AJ*, 120, 1579
- Ysard, N., Köhler, M., Jones, A., et al. 2015, *A&A*, 577, A110
- Zabel, N., Davis, T. A., Smith, M. W. L., et al. 2019, *MNRAS*, 483, 2251
- Zhang, Z.-Y., Romano, D., Ivison, R. J., Papadopoulos, P. P., & Matteucci, F. 2018, *Nature*, 558, 260
- Zubko, V., Dwek, E., & Arendt, R. G. 2004, *ApJS*, 152, 211